Sediment provenance and weathering history of different continental margins in SE Asia : examples from South China Sea

Junfei Chen

Ecole Doctorale SIReNa
Centre de Recherches Pétrographique
et Géochimique (CNRS-CRPG)

Thèse

Présentée et soutenue publiquement pour l'obtention du titre de

DOCTEUR DE l'UNIVERSITE DE LORRAINE

Mention : Géosciences

par **Junfei CHEN**

Sous la direction de Albert GALY and Chao LI

Enregistrement sedimentaire de l'alteration continentale sur les marges du SE Asiatique : exemples dans la mer de Chine du Sud

soutenance publiquement le 15 Novembre 2024

Membres du jury :

Directeur(s) de thèse :	**Albert GALY**	**Professeur, CRPG-CNRS-UL, Nancy**
	Chao LI	**Associé Professeur, Tongji Université, Shanghai (CHN)**
Président de jury :	**Shiming WAN**	**Professeur, Institute of Oceanology, Chinese Academy of Science, Qingdao, Shangdong (CHN)**
Rapporteurs :	**Christophe COLIN**	**Professeur, Université Paris-Saclay, Orsay**
	Yibo YANG	**Professeur, Institute of Tibetan Plateau Research, Chinese Academy of Science, Beijing (CHN)**
Examinateurs :	**Pascale HUYGHE**	**Professeur, Université Grenoble Alpes, Grenoble**
	Viviane ROUMAZEILLES	**Directeur de Recherche, Université Lille, Villeneuve d'Ascq**
	Shiming WAN	**Professeur, Institute of Oceanology, Chinese Academy of Science, Qingdao, Shangdong (CHN)**
	Shouye YANG	**Professeur, Tongji Université, Shanghai (CHN)**

Résumé

Le plateau de la Sonde, qui fait partie du sud de la mer de Chine méridionale (SCS), est situé dans une région tropicale caractérisée par une tectonique stable depuis le Quaternaire. Elle a examiné des échantillons de sédiments fluviaux dans des régions sources potentielles, des sédiments du fond marin et des carottes du plateau de la Sonde (ST13) et du talus (18288-2), à l'aide d'analyses élémentaires et isotopiques. Elle a analysé l'évolution des sources de sédiments depuis la dernière déglaciation et les changements induits sur le cycle du carbone par plateau de la Sonde pendant les périodes de haut et de bas niveau de la mer. En particulier, elle a exploré les changements relatifs de l'intensité de l'altération des silicates entre les périodes glaciaires et interglaciaires dans le sud de la SCS. Elle a également calculé le taux de consommation de CO_2 atmosphérique par l'altération des silicates depuis la dernière déglaciation et identifié les facteurs contrôlant ce taux.

Les principales observation et conclusions de ce travail sont les suivantes :

Les grandes rivières dominent les sources actuelles de sédiments marins. La composition isotopique Sr-Nd des sédiments du plateau continental de la Sonde et du sud du SCS ressemble étroitement à celle des sédiments des grandes rivières du nord (Mékong, Fleuve Rouge), ce qui indique que les sédiments marins actuels sont principalement contrôlés par de grandes rivières à fort flux de sédiments.

Les changements du niveau de la mer ont imposé des changements dans les transferts et la nature des sédiments dans le sud du SCS depuis la fin du dernier maximum glacière (LGM). Les valeurs $^{87}Sr/^{86}Sr$ et εNd des sédiments du stade I (0-12.5 Ka) de 18288-2 et les sédiments de ST13 sont dans la gamme de celles du golfe de Beibuwan, du plateau de la Sonde et des sédiments au large de la péninsule indochinoise. Les valeurs $^{87}Sr/^{86}Sr$ et εNd des sédiments du stade II (12.5-16.5 Ka) de 18288-2 sont assez proches de celles des sédiments au large de la péninsule indochinoise. La composition isotopique des sédiments du stade III (16.5-18.5 Ka) de 18288-2 est proche de la gamme de distribution isotopique des sédiments offshore de Bornéo.

Quatre facteurs suivants contrôlent les changements de provenance des sédiments des niveaux marins élevés et bas : le changements du niveau de la mer, les flux fluviaux et distance de transport, les courants océaniques, et les changemens climatiques.

Les changements d'intensité d'altération enregistrés par les sédiments des carottes

ST13 et 18288-2 sur les différentes périodes géologiques nécessitent la détermination des contributions de diverses sources par l'analyse de provenance. Les différences de consommation de CO_2 par l'altération des silicates au cours de la période glaciaire et de l'Holocène ont été calculées quantitativement sur la base des différences d'intensité d'altération et relative à la consommation de CO_2 entre le stade I (fin de la LGM à début de la déglaciation), le stade II (fin de la déglaciation) et le stade III (Holocène) pour les sédiments de la carotte 18288-2. Les changements entre le stade I et le stade III sont minimes. Pour le stade II, la consommation de CO_2 était comprise entre - 44 et 14×10^9 mol/an, selon la présence ou non de matériel de Bornéo dans la source. En supposant un taux moyen de consommation de CO_2 de 191×10^3 mol/km^2/an pendant l'Holocène (stade III) basé sur des données publiées précédemment sur les taux d'altération terrestre autour du SCS, avec une superficie moyenne de terres altérables de $1,76 \times 10^6$ km^2 dans la zone d'étude, nous avons estimé la consommation moyenne de CO_2 pendant l'Holocène à 336×10^9 mol/an. La consommation de CO_2 pendant les stades I et II a été calculée à 300-350 $\times 10^9$ mol/an, ce qui suggère que la consommation de CO_2 par l'altération des silicates dans le sud du SCS est restée relativement constante depuis la fin du LGM.

Abstract

The Sunda Shelf, as part of southern South China Sea (SCS), is in a low-latitude tropical region, with stable tectonics since the Quaternary. During glacial lowstand, the Sunda Shelf was exposed and connected to surrounding land, forming the Sunda Continent, which is the most important geographical change in the low-latitude regions during the Quaternary. How did the exposure of the shelf during glacial-interglacial cycles alter the sediment "source-sink" processes in the southern SCS? Did the increased land available for weathering reactions due to shelf exposure affect atmospheric CO_2 concentrations? Research on these questions remains limited.

This study focuses on the Sunda Shelf of southern SCS and surrounding lands. It examined samples both from the land and marine with geochemical methods. analyzed the evolution of sediment sources in the southern SCS since the last deglaciation and the changes in the "source-sink" role of the Sunda Shelf during of high and low sea levels periods. Explored the relative changes in silicate weathering intensity between glacial and interglacial periods in the southern SCS. It also calculated the atmospheric CO_2 consumption rate by silicate weathering since the last deglaciation and identified the factors controlling this rate.

The main findings and conclusions are as follows:

(1) Large rivers dominate the present-day marine sediment sources on the southern Sunda shelf of the southern SCS. The Sr-Nd isotopic composition of sediments from the Sunda Shelf and southern SCS closely resembles that of sediments from northern large rivers, indicating that present-day marine sediments are mainly controlled by large rivers with high sediment flux.

(2) Sea level changes controlled the shifts in sediment source-to-sink processes in the southern SCS since late LGM. During the glaciation, low sea levels exposed the shelf, with large paleo-river systems. Sediments were directly transported to the slope through these paleo-channels. As sea levels rose, the shelf was gradually submerged, reducing material from southern small island rivers while increasing input from major rivers in the northern shelf. During the Holocene highstand, the Mekong River became the primary sediment source for the Sunda Shelf. It is indicated that sea level changes dictated shifts in source areas and sedimentary centers, while climate, ocean currents, and sediment flux jointly influenced sediment provenance in the southern SCS.

（3）The ($^{234}U/^{238}U$) ratio revealed the ongoing active erosion of equatorial tropical islands during glacial periods. It was found that tropical islands near the equator experienced slightly weaker precipitation compared to the Holocene. Materials that had undergone early erosion or had been retained for extended periods were shallowly eroded and remobilized to the slope via paleo-rivers. This indicated that the tropical islands in the southern SCS remained actively eroded during glacial periods.

（4）Shelf exposure during glacial periods compensated for the reduced CO_2 consumption rates by silicate weathering due to decreased precipitation, thereby maintaining the overall balance of CO_2 consumption flux since the LGM. Calculations of major elements in core sediments indicated that atmospheric CO_2 consumption flux in the southern SCS has remained nearly constant since the LGM, although silicate weathering rates during glacial periods were only half of those in the Holocene. The increased area available for weathering reactions during glacial periods compensated for the reduced silicate chemical weathering rates, thus controlling the long-term balance of atmospheric CO_2 consumption flux. It was revealed that changes in precipitation are the primary factor controlling variations in silicate weathering and CO_2 consumption rates, while the roles of temperature and lithology require further evidenc

Résumé étendu

Le plateau de la Sonde, qui fait partie du sud de la mer de Chine méridionale (SCS), est situé dans une région tropicale caractérisée par une tectonique stable depuis le Quaternaire. Au Nord, de grands fleuves drainant le continent, et des rivières plus petites des îles du sud apportent chaque année d'importantes quantités de sédiments terrestres dans cette mer (Fig 1). La région connaît des températures élevées et des précipitations abondantes. Lors de la dernière glaciation, le plateau de la Sonde a été exposé et connecté aux terres environnantes, formant le continent de la Sonde, ce qui constitue le changement géographique le plus important des régions équatoriales au cours du Quaternaire (Fig. 2).

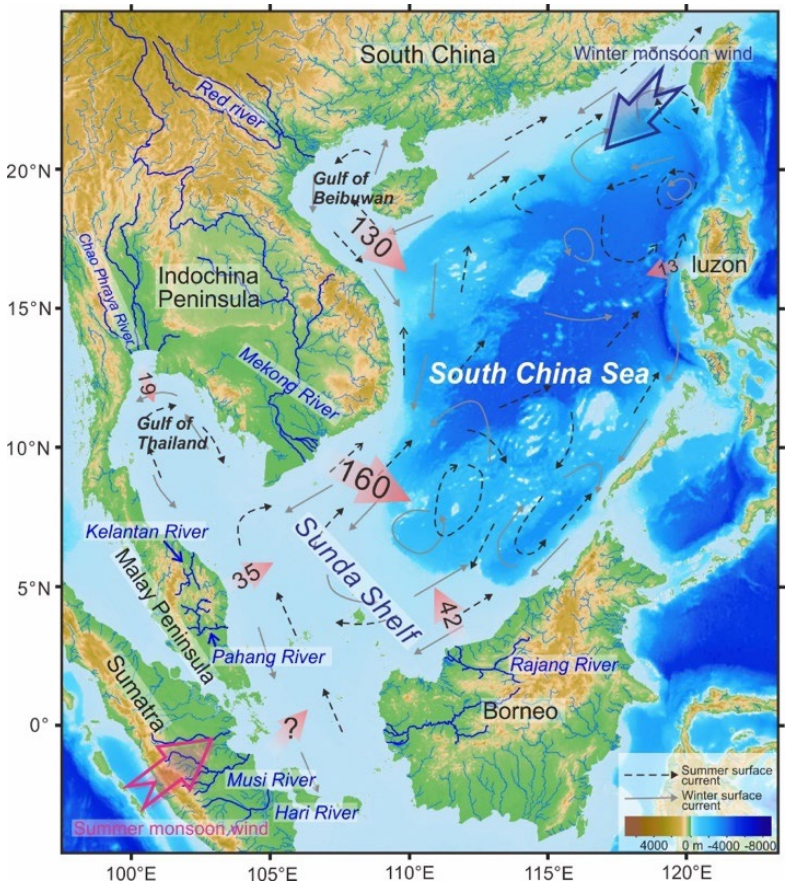

Fig. 1 Schéma géographique de la mer de Chine méridionale (SCS), et flux sédimentaires des principaux fleuves et courant de surface (les flèches roses indiquent le flux sédimentaire annuel des fleuves, en Mt/an ; Milliman and Farnsworth, 2011)

On peut se demander comment l'exposition du plateau au cours des cycles glaciaires-interglaciaires a-t-elle modifié les processus de sédimentation et d'altération

dans le sud de la SCS ? L'augmentation des terres soumises aux réactions d'altération en raison de l'exposition du plateau a-t-elle eu un impact sur la concentration atmosphérique de CO_2 ? Les informations sur ces questions restent limitées. Cependant, ces questions peuvent être importantes pour comprendre les différentes rétroactions entre l'altération continentale, déclenchée par l'exposition des plateaux tropicaux en raison de la baisse du niveau de la mer, et le cycle du carbone. L'étude de l'évolution historique des concentrations atmosphériques de CO_2 et de ses forçages est essentielle pour comprendre les changements climatiques mondiaux mais aussi pourraient améliorer les prédictions des tendances climatiques futures.

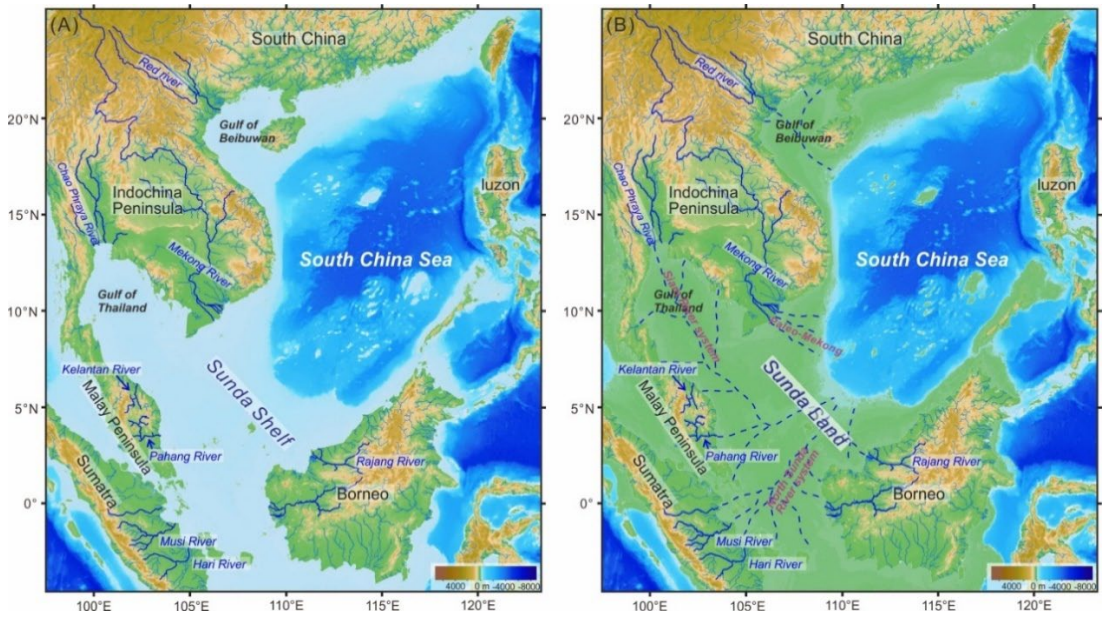

Fig. 2 Géographie du SCS pendant les périodes de haut niveau de la mer (A) et de bas niveau de la mer (B) (Sathiamurthy and Voris, 2006; Voris, 2000).

Cette étude porte sur le plateau de la Sonde du sud de la SCS et les terres environnantes. Elle a examiné des échantillons de sédiments fluviaux dans des régions sources potentielles, des sédiments du fond marin et des carottes du plateau de la Sonde (ST13) et du talus (18288-2), à l'aide de méthodes géochimiques, notamment des analyses élémentaires et isotopiques (Fig 3). Elle a analysé l'évolution des sources de sédiments dans le sud de la SCS depuis la dernière déglaciation et les changements induits sur le cycle du carbone par plateau de la Sonde pendant les périodes de haut et de bas niveau de la mer. En particulier, elle a exploré les changements relatifs de l'intensité de l'altération des silicates entre les périodes glaciaires et interglaciaires dans

le sud de la SCS. Elle a également calculé le taux de consommation de CO_2 atmosphérique par l'altération des silicates depuis la dernière déglaciation et identifié les facteurs contrôlant ce taux.

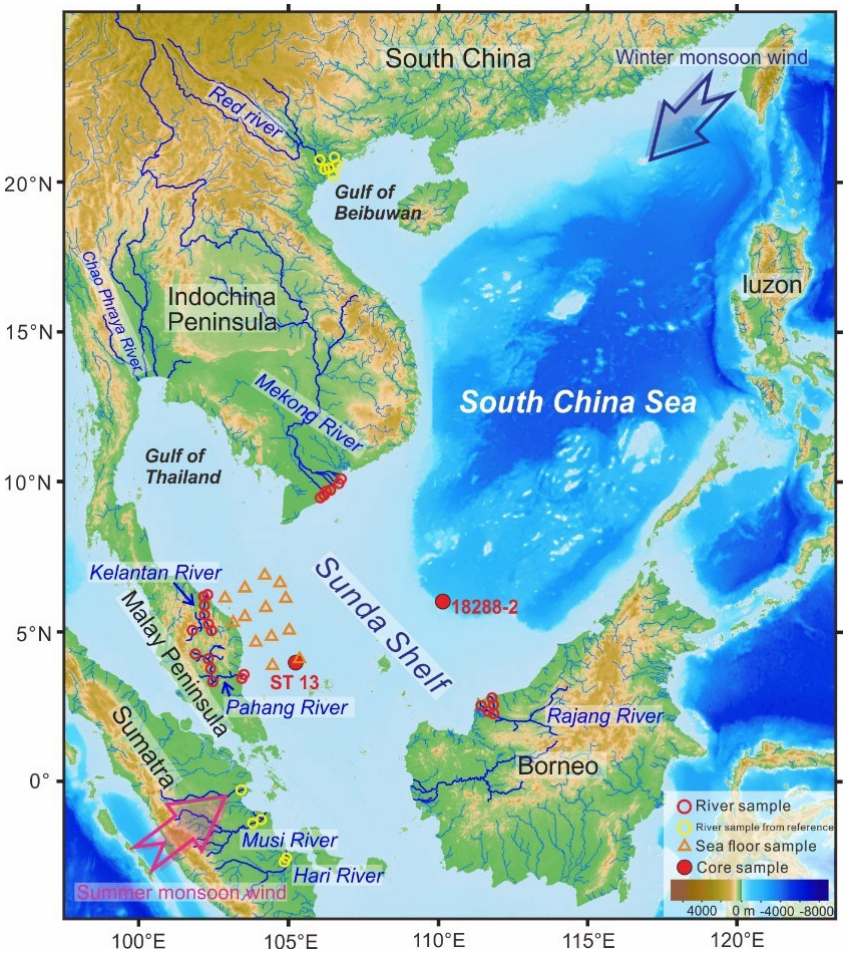

Fig. 3 Localisation des différents types d'échantillons collectés dans cette étude

Les principales observation et conclusions de ce travail sont les suivantes :

(1) Les grandes rivières dominent les sources actuelles de sédiments marins sur le plateau continental de la Sonde dans le sud du SCS (e.g. Milliman and Farnsworth, 2011). Les sources potentielles dans la partie sud de la mer de Chine méridionale comprennent principalement le fleuve Rouge en Chine méridionale, le fleuve Mékong dans la péninsule indochinoise, les rivières de la péninsule malaisienne, les rivières de Sumatra et les rivières de Bornéo. Ces systèmes fluviaux peuvent être divisés en deux catégories : les grands fleuves représentés par le fleuve Mékong au nord et les petits fleuves des îles du sud comme le fleuve Pahang dans la péninsule malaisienne et le fleuve Rajang à

Bornéo. Ces fleuves sont contrôlés par une taille de bassin, une topographie et un climat différent, induisant des flux de sédiment différents dans l'océan. Les terres du nord de la SCS sont situées sur un bloc continental stable, et le bassin versant contient de grandes plaines inondables de cours moyen et inférieur, principalement caractérisées par des roches crustales. Alors que les îles du sud de la SCS sont situées dans une zone de limite de plaque active. Par exemple, Sumatra a des activités volcaniques actives depuis l'Holocène, donc en plus des roches sédimentaires, on y trouve également des matériaux du manteau largement répartis. La différence de lithologie entre les terres du sud et du nord contrôle les caractéristiques géochimiques des sédiments fluviaux, en particulier la composition des isotopes Sr et Nd. Les sédiments des rivières autour du SCS montrent un rapport $^{87}Sr/^{86}Sr$ croissant et des valeurs εNd décroissantes du sud au nord, ce qui indique que les sédiments du sud intègrent une composante mantellique, tandis que les sédiments du nord sont principalement d'origine crustale (Fig 4). La composition isotopique Sr-Nd des sédiments du plateau continental de la Sonde et du sud du SCS ressemble étroitement à celle des sédiments des grandes rivières du nord, ce qui indique que les sédiments marins actuels sont principalement contrôlés par de grandes rivières à fort flux de sédiments. Cependant, les sédiments fluviaux et les sédiments marins ne correspondent pas toujours en termes de compositions élémentaires (Ti, Mg, Na, Ca, Fig. 5) ou d'autres indicateurs, il faut donc faire preuve de prudence lors de l'utilisation de sédiments fluviaux et de leur signature radiogénique comme seuls critères pour retracer les sources de sédiments marins.

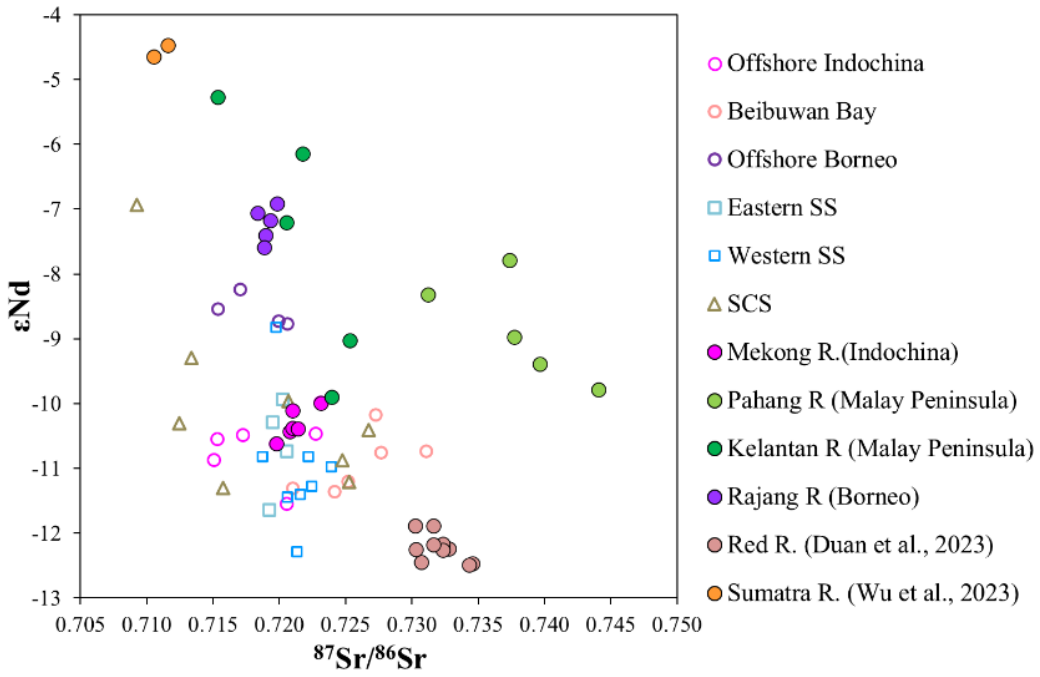

Fig. 4 Comparaison des isotopes Sr-Nd entre les sédiments fluviaux (symboles pleins) et marins (symboles ouverts).

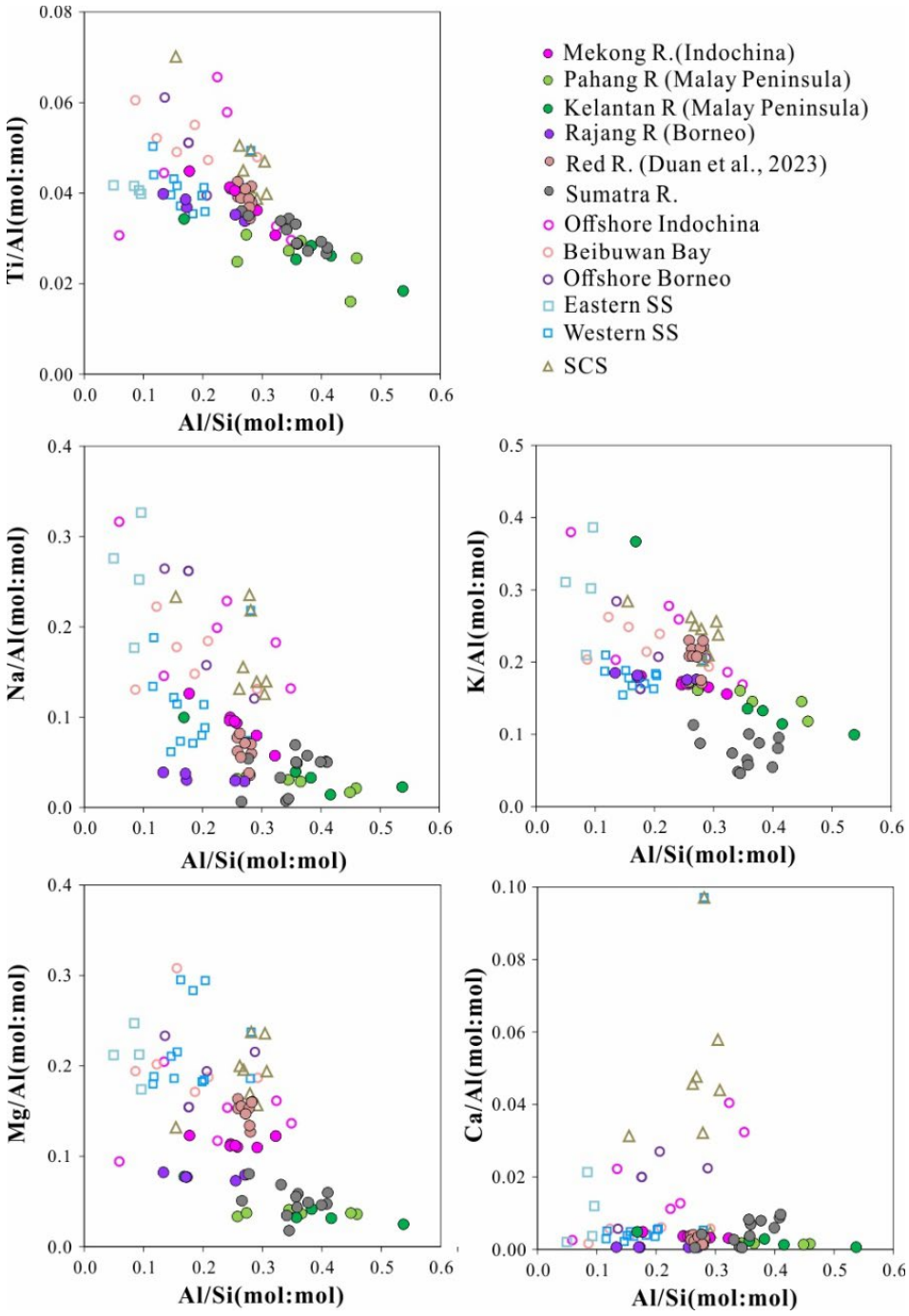

Fig. 5 Relation entre les ratios des éléments majeurs dans les sédiments fluviaux (symboles pleins) et marins (symboles ouverts). Ti et Mg sont enrichis dans les roches mantelliques. Cependant, certains de ces éléments majeurs sont sensible à l'altération (Ca, Mg, Na, K) et tous sont sensibles au tri minéralogique lors du transport.

(2) Les changements du niveau de la mer ont imposé des changements dans les transferts et la nature des sédiments dans le sud du SCS depuis la fin du dernier maximum glacière (LGM). Lors de la dernière période glacière, les bas niveaux de la mer ont exposé le plateau, permettant à de grands systèmes

paléo-fluviaux de se développer.

Nous avons comparé les valeurs $^{87}Sr/^{86}Sr$ et εNd des sédiments récents des carottes ST13 et 18288-2 avec celles des sédiments marins du fond marin pour compenser le problème de représentativité insuffisante de l'échantillonnage des sédiments fluviaux (Fig. 6). Les sédiments marins sont mélangés de manière plus homogène que les sédiments fluviaux en raison d'un temps de transport plus long et de recyclage plus significatif. Les valeurs $^{87}Sr/^{86}Sr$ et εNd des sédiments du stade I (0-12.5 Ka) de 18288-2 et les sédiments de ST13 sont dans la gamme de celles du golfe de Beibuwan, du plateau de la Sonde et des sédiments au large de la péninsule indochinoise. Les valeurs $^{87}Sr/^{86}Sr$ et εNd des sédiments du stade II (12.5-16.5 Ka) de 18288-2 sont assez proches de celles des sédiments au large de la péninsule indochinoise. La composition isotopique des sédiments du stade III (16.5-18.5 Ka) de 18288-2 est proche de la gamme de distribution isotopique des sédiments offshore de Bornéo. Contrairement aux sédiments fluviaux, il n'existe pas de données publiées sur les valeurs $^{87}Sr/^{86}Sr$ et εNd des sédiments offshore de Sumatra. Cependant, sur la base du contexte géologique et de la lithologie de Sumatra, on peut en déduire que ses sédiments offshore présenteront de faibles valeurs $^{87}Sr/^{86}Sr$ et des valeurs élevées εNd. Comme la plupart de ces sédiments du fond marin proviennent des rivières les plus proches, en comparant les caractéristiques $^{87}Sr/^{86}Sr$ et εNd des sédiments des carottes et des sédiments du fond marin, des conclusions sur la provenance des carottes peuvent être obtenues.

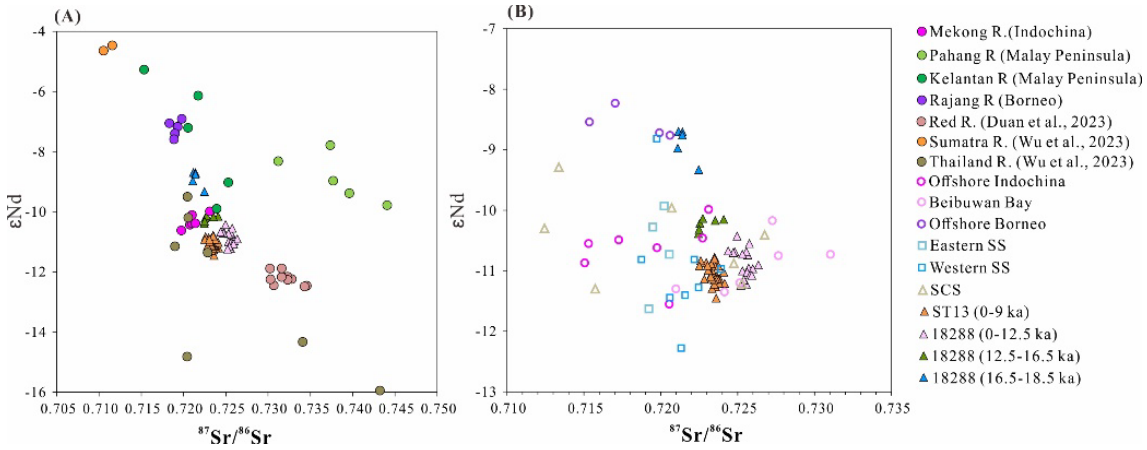

Fig. 6 Caractéristiques isotopiques $^{87}Sr/^{86}Sr$ et εNd des sédiments des périodes Holocène à LGM (carottes ST13 et 18288-2) et des sédiments fluviaux (A), ou des sédiments du fond marin (B).

Après une analyse approfondie, on estime que les quatre facteurs suivants contrôlent les changements de provenance des sédiments des niveaux marins élevés et bas :

i. Changements du niveau de la mer. Depuis le LGM, la montée du niveau de la mer a modifié la configuration terre-mer du plateau continental de la Sonde et du sud du SCS. Pendant les périodes de bas niveau de la mer, le plateau continental de la Sonde était exposé sous forme d'une vaste plaine, développant de nombreux systèmes paléo-fluviaux (Fig 2). Ces rivières transportaient des matériaux érodés des îles du sud du SCS et du plateau directement vers la pente et les eaux profondes, le centre de dépôt étant principalement situé sur le bord du plateau continental et la pente. À mesure que le niveau de la mer est remonté, la transgression marine a provoqué le retrait de l'estuaire fluvial, déplaçant le centre de dépôt vers l'intérieur du plateau. En raison de la pente douce du plateau continental de la Sonde, inférieure à 0,03° (Hanebuth et al., 2003; Tjia and Kuala, 1980), seules des particules relativement fines ont pu être maintenues en suspension et transportées vers la pente et les eaux profondes par le courant de surface pendant cette période. Par conséquent, les sédiments sur la pente ont diminué, tandis que les sédiments sur le plateau continental ont augmenté. Pendant les périodes de haut niveau de la mer, les rivières ont transporté des sédiments vers l'estuaire, où la plupart d'entre eux se sont accumulés près du rivage. Une plus petite partie a été transportée sur de longues distances par les courants océaniques, permettant aux matériaux provenant de grands fleuves comme le Mékong et la rivière Rouge de se déposer sur les pentes et dans les zones d'eau profonde.

ii. Flux fluvial et distance de transport. Actuellement, les recherches sur le flux de sédiments des rivières du SCS du nord qui se jettent dans le SCS sont approfondies, tandis que les études sur les rivières des îles du sud sont relativement rares. Le flux actuel de sédiments du Mékong est de 150 Mt/an, ce qui domine les sources potentielles du SCS du sud. Le fleuve Rouge suit avec 110 Mt/an. Cependant, en raison de sa plus grande distance par rapport au plateau de la Sonde et au SCS du sud, et de l'influence du tri hydrodynamique, la plupart des sédiments du fleuve

Rouge ne sont pas transportés loin dans l'océan. Seule une petite fraction des particules fines du fleuve Rouge ou du golfe de Beibuwan atteint le SCS du sud. Par rapport au Mékong et au fleuve Rouge, les flux de sédiments des autres rivières insulaires sont très faibles, ce qui rend difficile leur apport de sédiments aux zones de pente et d'eau profonde. Les recherches indiquent que les sédiments des petites rivières insulaires, comme la péninsule malaisienne, s'accumulent principalement près du rivage le long de la côte (Wu et al., 2019) et ne sont pas transportés sur de longues distances. Par conséquent, pendant les périodes de haut niveau de la mer, les grands fleuves comme le Mékong sont les principales sources de matériaux pour le plateau de la Sonde.

iii. Courants océaniques. Le SCS est situé dans la région de la mousson du sud-est de l'Asie. Les courants de surface océaniques sont affectés par la mousson avec des différences saisonnières. La mousson du sud-ouest prévaut en été, formant un système de courant océanique tournant dans le sens des aiguilles d'une montre à la surface du SCS, tandis que la mousson du nord-est prévaut en hiver, formant un système de courant océanique de surface dans le sens trigonométrique. Les moussons d'été et d'hiver forment un fort courant de bordure ouest à la limite occidentale du SCS près de la terre, transportant ainsi des sédiments de la rivière Rouge et des matériaux recyclés du fond du plateau vers la pente et les profondeurs marines.

iv. Changement climatique. À l'heure actuelle, le SCS est influencé par les moussons, ce qui se traduit par des températures généralement élevées et des précipitations abondantes. Les fortes précipitations intensifient l'érosion et l'altération des roches, ce qui conduit à un apport accru de sédiments en provenance des principaux bassins fluviaux. Pendant les périodes glaciaires, les températures mondiales diminuent et les régimes de précipitations changent. Les recherches actuelles indiquent que, comme le SCS du sud est proche de l'équateur et de la source de la mousson du sud-ouest, les zones de Sumatra et de Bornéo abritaient encore des forêts tropicales humides pendant les périodes glaciaires. En revanche, la partie centrale des zones exposées du plateau continental et de la péninsule d'Indochine a vu principalement se développer des savanes

(Sun et al., 2000; Wang et al., 2009). Cela suggère que pendant les périodes glaciaires, les précipitations sur le plateau continental du sud étaient plus élevées que dans les zones terrestres du nord. Par conséquent, pendant les périodes glaciaires, les îles du sud ont connu une érosion physique plus intense en raison des précipitations abondantes. Les roches et les sédiments de surface ont été érodés, fournissant un apport important de sédiments dans la mer. Des systèmes paléo-fluviaux bien développés ont transporté ces sédiments jusqu'au talus continental. De plus, la zone de latitude 5°-30°N est sujette aux tempêtes tropicales, qui provoquent des ouragans et de forts courants de marée, perturbant ou remobilisant les sédiments de surface dans les eaux peu profondes. Étant donné la profondeur moyenne du plateau de 50 à 70 m, les sédiments de surface du golfe de Beibuwan, du plateau offshore de la péninsule indochinoise et du plateau nord de la Sonde sont remobilisés pendant les saisons de tempêtes. Ces matériaux de remobilisation sont des sédiments à grains fins, qui peuvent être transportés sur de longues distances par les courants océaniques. Les recherches actuelles montrent qu'environ 30 à 50 % des sédiments à grains fins déposés dans l'estuaire du fleuve Yangtze et dans le delta submergé sont remobilisés et transportés vers le plateau de la mer de Chine orientale et le creux d'Okinawa (Liu et al., 2007; Xu et al., 2012).

3. Les enregistrements de l'estuaire du Changjiang au cours des 14 derniers ka, combinés aux données publiées sur la température, les précipitations, le pollen et l'activité humaine dans le bassin versant du Changjiang, indiquent que depuis 14 ka, les sédiments de l'estuaire du Changjiang proviennent principalement des zones d'érosion du cours supérieur de ce fleuve avec une certaine contribution des plaines inondables des parties moyennes et du cours inférieur depuis 4 ka. L'âge d'ouverture du système isotopique $^{234}U/^{238}U$ (appelé âge de communition en anglais, t_{com}) montre une corrélation significative avec les proxys de température, précipitations, pollen de végétation à feuilles persistantes et activité humaine (Fig. 7). L'étude révèle que de la période Bølling-Allerød au milieu de l'Holocène, les changements climatiques ont contrôlé les processus de mobilisation des sédiments dans le bassin versant du Changjiang, le t_{com} des sédiments montrant un modèle

cyclique de valeurs plus récentes et plus anciennes. Pendant les périodes froides et sèches, la valeur t_{com} des sédiments est plus élevée, suggérant une érosion du bassin versant moins profonde et plus faible et des processus de transport des sédiments plus lents. En revanche, pendant les périodes chaudes et humides, les plus faibles valeurs de t_{com} des sédiments indiquent une érosion plus forte du bassin versant et des processus de transport des sédiments plus rapides (Fig. 7). Depuis la fin de l'Holocène, des précipitations fréquentes ont entraîné des inondations dans le cours moyen et inférieur du fleuve, provoquant l'érosion locale des sédiments plus anciens des plaines inondables. De plus, au cours des 2 derniers ka, des activités humaines (par exemple la déforestation et l'agriculture) ont entraîné une érosion anthropique locale des sols des plaines inondables (Fig. 7 A et F ; Annexe 1 : Chen et al., 2024).

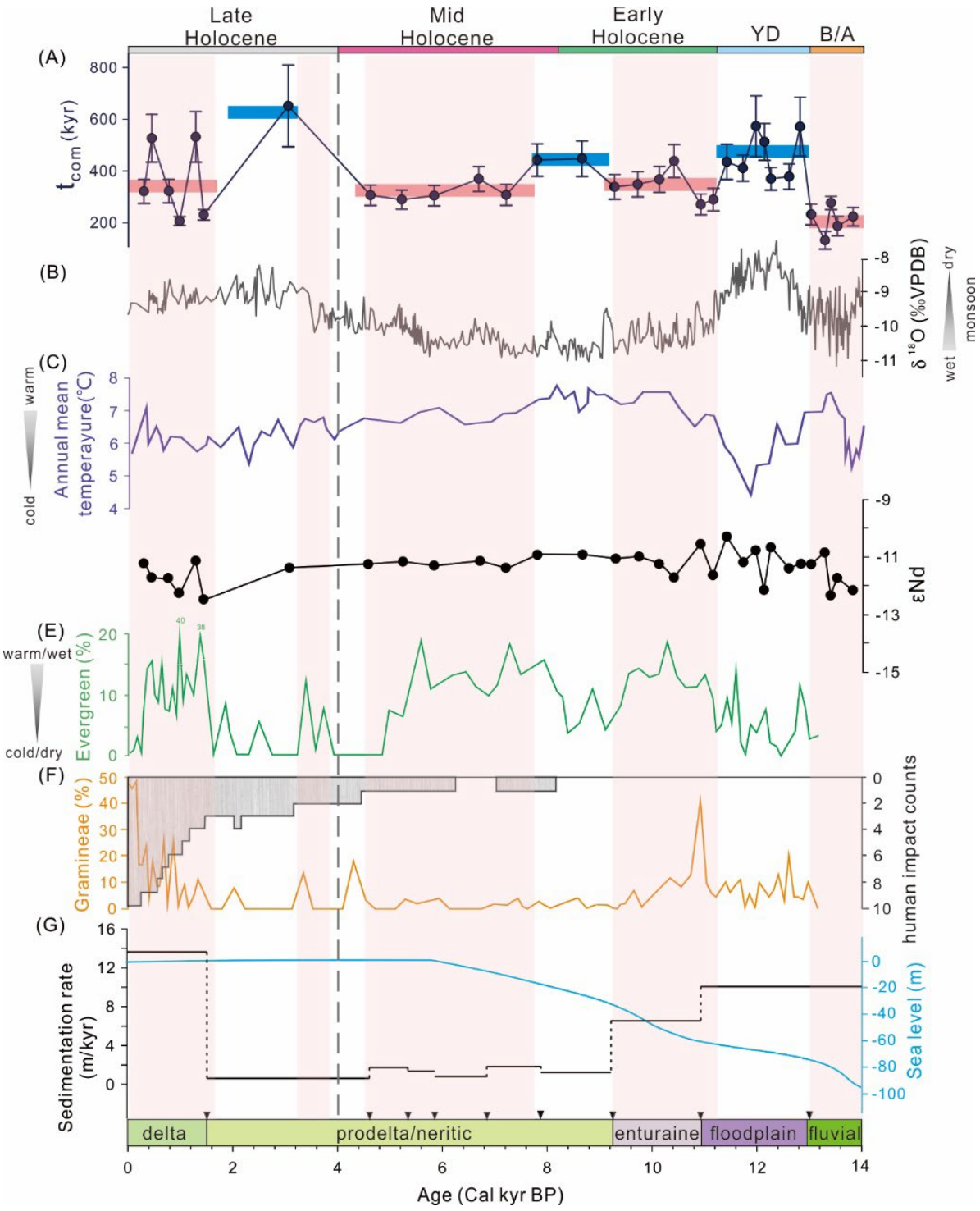

Fig.7 Variations temporelles de (A) tcom, les barres bleues et rouges représentent la valeur moyenne de t_{com} pendant les périodes froides et chaudes, respectivement. (B) stalagmite $\delta^{18}O$ de la grotte de Sanbao (Cheng et al., 2016), (C) Température moyenne annuelle dans le cours moyen du bassin versant de Changjiang (Zhu et al., 2008), (D) εNd, (E) Teneur en pollen de conifères et périodes climatiques à partir des données polliniques (les bandes roses représentent les périodes chaudes et humides) (Yi et al., 2003), (F) Teneur en pollen de graminées (Yi et al., 2003) et facteur d'impact (Wang et al., 2010). (G) taux de sédimentation et faciès sédimentaires du noyau CM97, et niveau de la mer de Chine orientale depuis 14 ka. Les triangles noirs représentent les points de datation AMS^{14}C.

L'analyse des t_{com} des sédiments des carottes du plateau de la Sonde (ST13) et du talus (18288-2) révèle une érosion active continue des îles tropicales équatoriales pendant les périodes glaciaires. En combinant l'analyse de provenance avec les conditions climatiques du sud du SCS pendant les périodes glaciaires, les îles tropicales proches de l'équateur ont connu des précipitations légèrement plus faibles par rapport à l'Holocène (Fig 8). Les faibles variations de t_{com} indiquent que les îles tropicales du sud du SCS sont restées activement érodées pendant les périodes glaciaires.

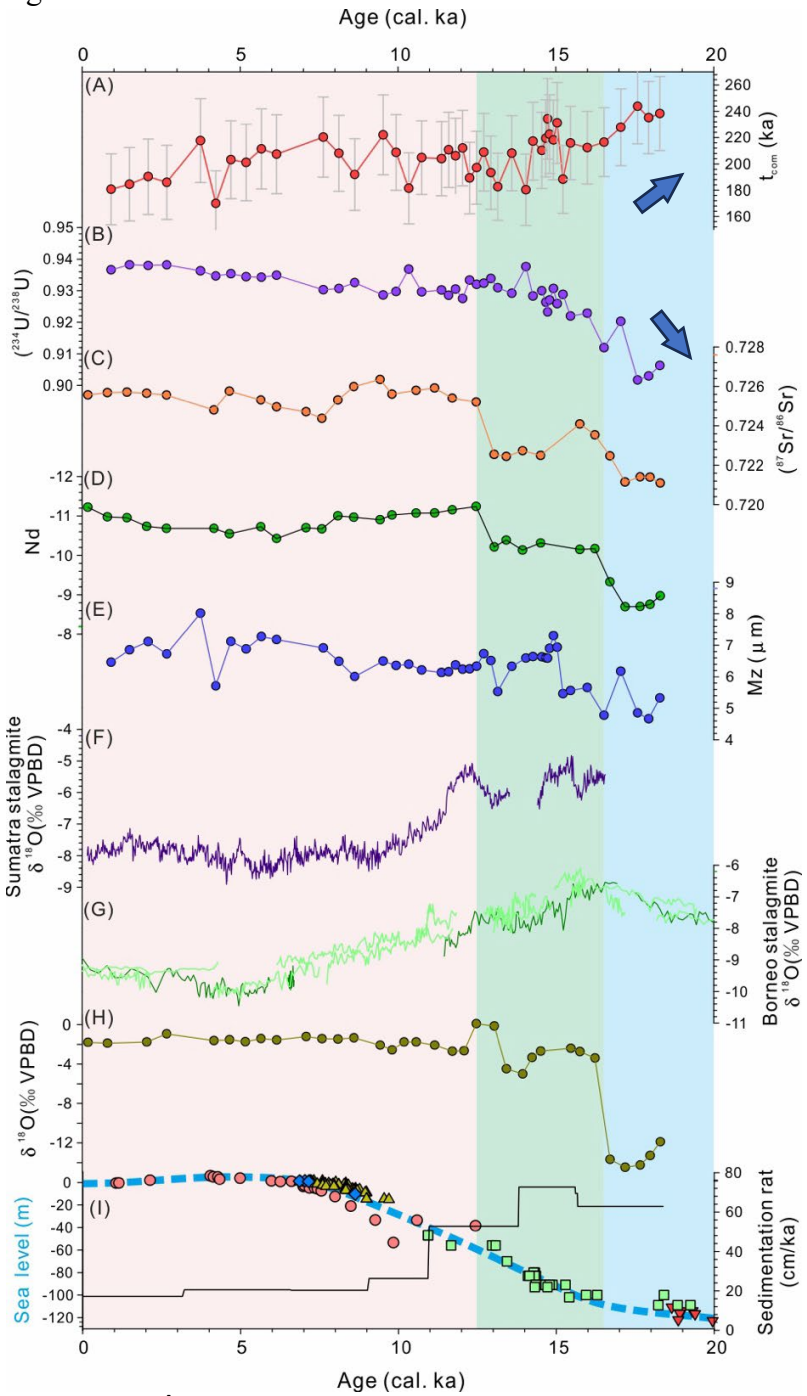

Fig. 8 Carotte 18288-2 (A) Âge de fragmentation (t_{com}) , (B) ($^{234}U/^{238}U$), (C) Rapport $^{87}Sr/^{86}Sr$, (D)

Valeur εNd (E) Taille médiane des grains des composants inférieurs à 50 μm, (F) Valeur $\delta^{18}O$ des stalagmites de la grotte de Tangga à Sumatra (Wurtzel et al., 2018), (G) Valeur $\delta^{18}O$ des stalagmites de la grotte du parc national de Gunung Buda dans le nord de Bornéo (Partin et al., 2007), (H) Valeur $\delta^{18}O$ du carbonate dans les sédiments en vrac de la carotte 18288-2, (I) Changements du niveau de la mer dans le SCS depuis 20 ka (Bird et al., 2007; Geyh et al., 1979; Hanebuth et al., 2000; Hanebuth et al., 2009; Hesp et al., 1998) et le taux de sédimentation de la carotte 18288-2.

4. Les changements d'intensité d'altération enregistrés par les sédiments des carottes ST13 et 18288-2 sur les différentes périodes géologiques nécessitent la détermination des contributions de diverses sources par l'analyse de provenance. En considérant un élément chimique, X, sensible à l'intensité d'altération, sa teneur est calculée en fonction de la chimie des sédiments récents, ce qui donne la valeur théorique de l'élément X dans le sédiment altéré avec une intensité identique à l'actuel (X_{mix}). La différence entre la valeur mesurée de l'élément X dans la carotte (X_{core}) et la valeur de mélange (X_{mix}) est indiquée par $\Delta X = X_{core} - X_{mix}$. Si $\Delta X > 0$, cela suggère une intensité d'altération réelle plus faible par rapport à la valeur de mélange théorique ; si $\Delta X < 0$, cela indique une intensité d'altération plus forte ; et si $\Delta X = 0$, l'intensité d'altération est comparable à la valeur de mélange théorique. En comparant les valeurs ΔX sur différentes périodes, on peut déduire les changements d'intensité d'altération au fil du temps. Nous utilisons le rapport X/Al dans les calculs pour éliminer l'effet de la taille des grains et tri minéralogique lors du transport. Une simulation de Monte Carlo pour l'estimation des proportions pour différentes combinaisons des sources implique que les valeurs ΔX/Al de la carotte 18288-2 permettent seulement deux combinaisons possibles pour la source (18288-2 (0-12,5 ka) + Sumatra avec ou sans Bornéo offshore, possibilité 2 et 3 dans la Fig. 9).

Ainsi, les différences de consommation de CO_2 par l'altération des silicates au cours de la période glaciaire et de l'Holocène ont été calculées quantitativement sur la base des différences d'intensité d'altération. Nous avons calculé la différence relative de consommation de CO_2 entre le stade I (fin de la LGM à début de la déglaciation), le stade II (fin de la déglaciation) et le stade III (Holocène) pour les sédiments de la carotte 18288-2. Les changements entre le stade I et le stade III sont minimes, avec des différences de 1,6 à 1,7 × 10^9 mol/an, en fonction de la présence ou non de Bornéo dans la source des sédiments. Cela indique que la consommation de CO_2 par l'altération des silicates dans ces deux stades était presque identique. Pour le

stade II, la consommation de CO_2 était comprise entre - 44 et 14 × 10^9 mol/an, selon la présence ou non de matériel de Bornéo dans la source. En supposant un taux moyen de consommation de CO_2 de 191 × 10^3 mol/km^2/an pendant l'Holocène (stade III) basé sur des données publiées précédemment sur les taux d'altération terrestre autour du SCS (Li et al., 2014), avec une superficie moyenne de terres altérables de 1,76 × 10^6 km^2 dans la zone d'étude, nous avons estimé la consommation moyenne de CO_2 pendant l'Holocène à 336 × 10^9 mol/an. La consommation de CO_2 pendant les stades I et II a été calculée à 300-350 × 10^9 mol/an, avec des différences minimes entre les stades, ce qui suggère que la consommation de CO_2 par l'altération des silicates dans le sud du SCS est restée relativement constante depuis la fin du LGM. L'impact du plateau exposé sur l'altération des silicates doit également être pris en compte. Lorsque le niveau de la mer était au plus bas pendant la période glaciaire, la zone de plateau exposée était à son maximum (Fig. 10B).

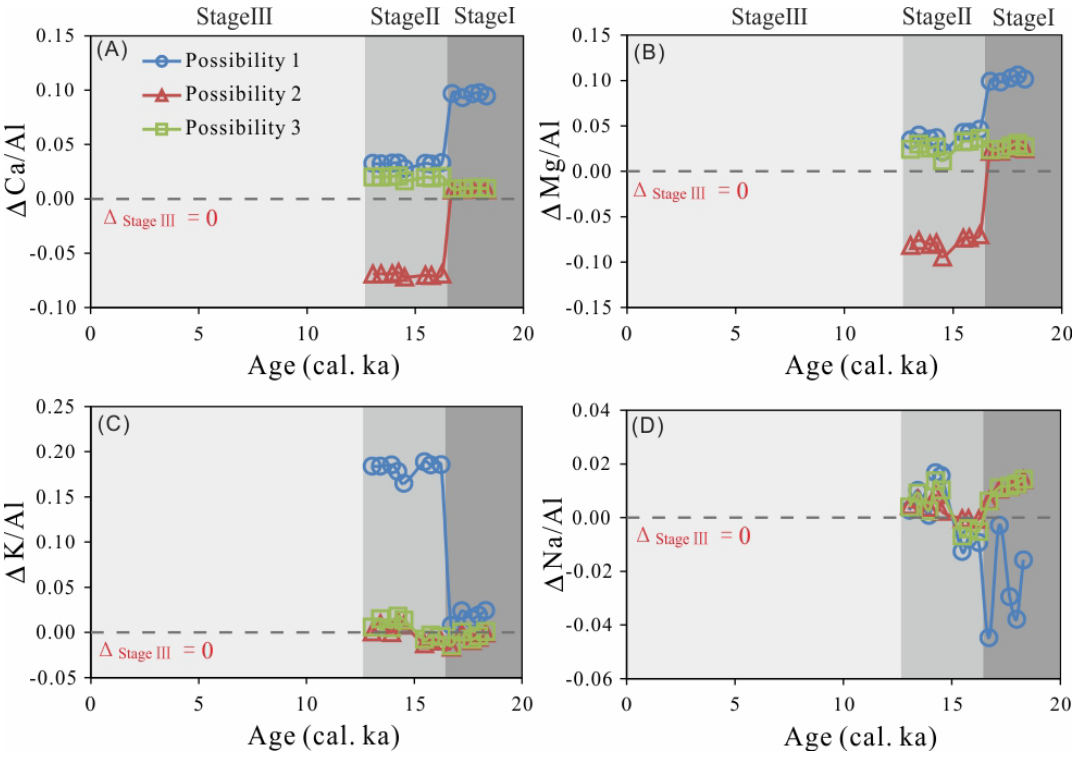

Fig. 9 Différences entre le rapport des éléments et les lignes de mélange théoriques à différents stades des sédiments de la carotte 18288-2.

Ainsi, l'exposition des plateaux pendant les périodes glaciaires a compensé la réduction des taux de consommation de CO_2 par l'altération des silicates due à la diminution des précipitations, maintenant ainsi l'équilibre global du flux de

consommation de CO_2 depuis le LGM. Les calculs des éléments majeurs dans les sédiments ont indiqué que le flux de consommation de CO_2 atmosphérique dans le sud du SCS est resté presque constant depuis le LGM, bien que les taux d'altération des silicates pendant les périodes glaciaires n'aient été que la moitié de ceux de l'Holocène. L'augmentation de la surface disponible pour les réactions d'altération pendant les périodes glaciaires a compensé la réduction des taux d'altération chimique des silicates, contrôlant ainsi l'équilibre à long terme du flux de consommation de CO_2 atmosphérique. Il a été révélé que le changement dans la quantité de précipitations est le principal facteur contrôlant les variations de l'altération des silicates et des taux de consommation de CO_2, tandis que les rôles de la température et de la lithologie nécessitent des preuves supplémentaires.

En résumé, cette étude a reconstitué les changements dans les processus depuis les sources jusqu'aux puits sédimentaires sur le plateau de la Sonde du sud de la SCS depuis la dernière déglaciation, a réévalué l'impact de l'exposition du plateau glaciaire sur l'altération des silicates et la consommation de CO_2 dans les régions tropicales de basse latitude, et a identifié les facteurs contrôlant l'altération des silicates et les taux de consommation de CO_2 atmosphérique.

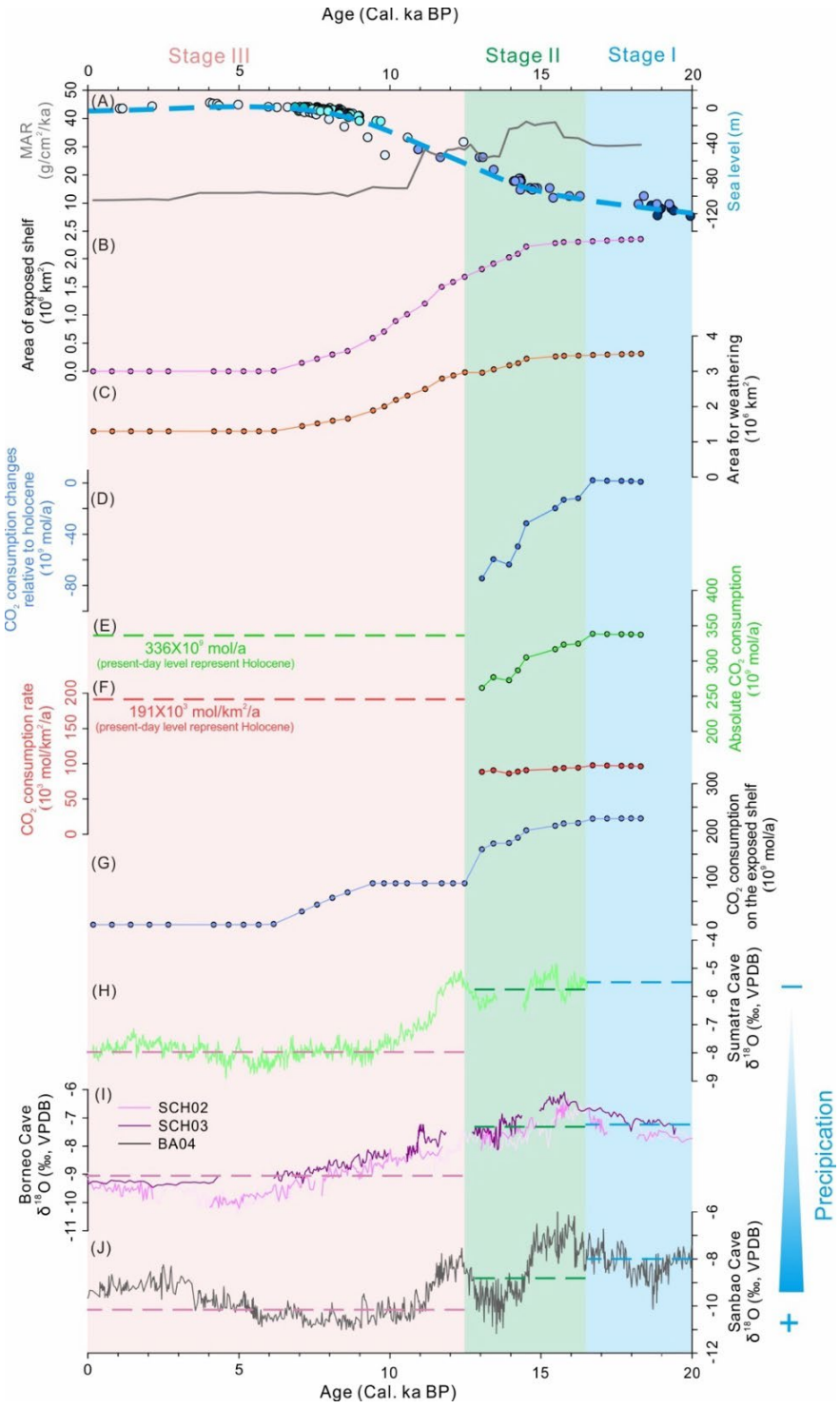

Fig. 10 Le graphique montre les enregistrements de l'altération des silicates et de la consommation de CO_2 du noyau 18288-2 depuis la dernière déglaciation. (A) Taux d'accumulation de la masse sédimentaire (MAR) et changement du niveau de la mer depuis 20 ka BP (Bird et al., 2007; Geyh et al., 1979; Hanebuth et al., 2000; Hanebuth et al., 2009; Hesp et al., 1998), (B) Superficie du plateau exposé depuis la dernière déglaciation (Sathiamurthy and Voris, 2006); (C) Superficie totale des terres pour la réaction d'altération depuis la dernière déglaciation (terre et plateau exposé) (Milliman and Farnsworth, 2011; Sathiamurthy and Voris, 2006). (D) Différences de consommation de CO_2 lors de l'altération des silicates entre les stades I et II par rapport au stade III. (E) La consommation absolue de CO_2 par l'altération des silicates depuis la dernière déglaciation, stade I (Holocène) est de 336×10^9 mol/a calculée par le taux de (F). (F) Taux de consommation de CO_2 par l'altération des silicates depuis la dernière déglaciation, le taux du stade I est de 119×10^3

mol/km^2/a (Li et al., 2014). (G) Consommation de CO_2 par l'altération des silicates sur le plateau exposé depuis la dernière déglaciation. (H) Valeurs $\delta^{18}O$ des stalagmites de la grotte de Tangga, Sumatra (Wurtzel et al., 2018). (I) Valeurs $\delta^{18}O$ des stalagmites du parc national de Gunung Buda, au nord de Bornéo (Partin et al., 2007). (J) Valeurs $\delta^{18}O$ des stalagmites de la grotte de Sanbao, montagne Shengnongjia dans la partie moyenne du Changjiang, Chine (Cheng et al., 2016).

Mots clés: plateau continental de la Sonde, mer de Chine méridionale, de la source au puits, altération chimique des silicates, cycle du carbone, ($^{234}U/^{238}U$), variations du niveau de la mer

Références:

Bird, M.I., Fifield, L.K., Teh, T.S., Chang, C.H., Shirlaw, N., Lambeck, K., 2007. An inflection in the rate of early mid-Holocene eustatic sea-level rise: A new sea-level curve from Singapore. Estuarine, Coastal and Shelf Science 71, 523-536.

Chen, J., Li, C., Galy, A., Wang, H., Yang, C., Yang, S., 2024. Uranium-series comminution ages constrain large catchment erosion and its response to climate change: A case study from the Changjiang. Earth and Planetary Science Letters 625.

Cheng, H., Edwards, R.L., Sinha, A., Spotl, C., Yi, L., Chen, S., Kelly, M., Kathayat, G., Wang, X., Li, X., Kong, X., Wang, Y., Ning, Y., Zhang, H., 2016. The Asian monsoon over the past 640,000 years and ice age terminations. Nature 534, 640-646.

Geyh, M.A., Kudrass, H.R., Streif, H., 1979. Sea-level changes during the late Pleistocene and Holocene in the Strait of Malacca. Nature 278, 441-443.

Hanebuth, T., Stattegger, K., Grootes, P.M., 2000. Rapid flooding of the Sunda Shelf: A late-glacial sea-level record. Science 288, 1033-1035.

Hanebuth, T.J.J., Stattegger, K., Bojanowski, A., 2009. Termination of the Last Glacial Maximum sea-level lowstand: The Sunda-Shelf data revisited. Global and Planetary Change 66, 76-84.

Hanebuth, T.J.J., Stattegger, K., Schimanski, A., Lüdmann, T., Wong, H.K., 2003. Late Pleistocene forced-regressive deposits on the Sunda Shelf (Southeast Asia). Marine Geology 199, 139-157.

Hesp, P.A., Hung, C.C., Hilton, M., Ming, C.L., M, I., Turner, S., 1998. A First Tentative Holocene Sea-Level Curve for Singapore. Journal of Coastal Research 14, 308-314.

Li, S., Lu, X.X., Bush, R.T., 2014. Chemical weathering and CO(2) consumption in the Lower Mekong River. Sci Total Environ 472, 162-177.

Liu, J.P., Xu, K.H., Li, A.C., Milliman, J.D., Velozzi, D.M., Xiao, S.B., Yang, Z.S., 2007. Flux and fate of Yangtze River sediment delivered to the East China Sea. Geomorphology 85, 208-224.

Milliman, J.D., Farnsworth, K.L., 2011. River Discharge to the Coastal Ocean-A Global Synthesis. Cambridge University Press United Kingdom.

Partin, J.W., Cobb, K.M., Adkins, J.F., Clark, B., Fernandez, D.P., 2007. Millennial-scale trends in west Pacific warm pool hydrology since the Last Glacial Maximum. Nature 449, 452-455.

Sathiamurthy, E., Voris, H.K., 2006. Maps of Holocene Sea level transgression and submerged lakes on the Sunda Shelf. The Natural History Journal of Chulalongkorn University Supplement 2, 1153-1167.

Sun, X.J., Li, X., Luo, Y.L., Chen, X.D., 2000. The vegetation and climate at the last glaciation on the emerged continental shelf of the South China Sea. Palaeogeogr Palaeocl 160, 301-316.

Tjia, H.D., Kuala, L., 1980. The Sunda Shelf, Southeast Asia. Zeitschrift für Geomorphologie 24, 405-427.

Voris, H.K., 2000. Maps of Pleistocene sea levels in Southeast Asia: shorelines, river systems and time durations. J Biogeogr 27, 1153-1167.

Wang, X.M., Sun, X.J., Wang, P.X., Stattegger, K., 2009. Vegetation on the Sunda Shelf, South China Sea, during the Last Glacial Maximum. Palaeogeogr Palaeocl 278, 88-97.

Wang, Y., Liu, X., Herzschuh, U., 2010. Asynchronous evolution of the Indian and East Asian Summer Monsoon indicated by Holocene moisture patterns in monsoonal central Asia. Earth-Science Reviews 103, 135-153.

Wu, K., Liu, S., Kandasamy, S., Jin, A., Lou, Z., Li, J., Wu, B., Wang, X., AbdRahim Mohamed, C., Shi, X., 2019. Grain-size effect on rare earth elements in Pahang River and Kelantan River, Peninsular Malaysia: Implications for sediment provenance in the southern South China Sea. Cont Shelf Res 189.

Wurtzel, J.B., Abram, N.J., Lewis, S.C., Bajo, P., Hellstrom, J.C., Troitzsch, U., Heslop, D., 2018. Tropical Indo-Pacific hydroclimate response to North Atlantic forcing during the last deglaciation as recorded by a speleothem from Sumatra, Indonesia. Earth and Planetary Science Letters 492, 264-278.

Xu, K., Li, A., Liu, J.P., Milliman, J.D., Yang, Z., Liu, C.-S., Kao, S.-J., Wan, S., Xu, F., 2012. Provenance, structure, and formation of the mud wedge along inner continental shelf of the East China Sea: A synthesis of the Yangtze dispersal system. Marine Geology 291-294, 176-191.

Yi, S., Saito, Y., Zhao, Q.H., Wang, P.X., 2003. Vegetation and climate changes in the Changjiang (Yangtze River) Delta, China, during the past 13,000 years inferred from pollen records. Quaternary Science Reviews 22, 1501-1519.

Zhu, C., Chen, X., Zhang, G., Ma, C., Zhu, Q., Li, Z., Xu, W., 2008. Spore-pollen-climate factor transfer function and paleoenvironment reconstruction in Dajiuhu, Shennongjia, Central China. Science Bulletin 53, 42-49.

Extended abstract

The Sunda Shelf, as part of southern South China Sea (SCS), is located in a low-latitude tropical region, with stable tectonics since the Quaternary. Large rivers from the northern mainland and smaller rivers from southern islands annually transport significant terrestrial clastic sediments into the sea. The region experiences high temperatures and abundant rainfall. During glacial lowstand, the Sunda Shelf was exposed and connected to surrounding land, forming the Sunda Continent, which is the most important geographical change in the low-latitude regions during the Quaternary. How did the exposure of the shelf during glacial-interglacial cycles alter the sediment "source-sink" processes in the southern SCS? Did the increased land available for weathering reactions due to shelf exposure affect atmospheric CO_2 concentrations? Research on these questions remains limited. However, the weathering feedback triggered by the exposure of tropical shelves due to glacial sea-level decline may play a crucial role in the glacial carbon cycle. Investigating the historical evolution of atmospheric CO_2 concentrations and their driving mechanisms is vital for understanding global climate change and predicting future climate trends.

This study focuses on the Sunda Shelf of southern SCS and surrounding lands. It examined samples from major river sediments in potential source regions, seafloor sediments, and cores from the Sunda Shelf (ST13) and slope (18288-2), with geochemical methods, including elemental and isotopic analyses. This study analyzed the evolution of sediment sources in the southern SCS since the last deglaciation and the changes in the "source-sink" role of the Sunda Shelf during high and low sea levels periods. The study explored the relative changes in silicate weathering intensity between glacial and interglacial periods in the southern SCS. It also calculated the atmospheric CO_2 consumption rate by silicate weathering since the last deglaciation and identified the factors controlling this rate.

The main findings and conclusions are as follows:

(1) Large rivers dominate the present-day marine sediment sources on the southern Sunda shelf of the southern SCS. Sediments from rivers around the SCS show an increasing $^{87}Sr/^{86}Sr$ ratio and decreasing εNd values from south to north, indicating that southern sediments are mantle-derived, while northern sediments are primarily crustal. The Sr-Nd isotopic composition of sediments from the Sunda Shelf and southern SCS closely resembles that of sediments from northern large rivers,

indicating that present-day marine sediments are mainly controlled by large rivers with high sediment flux. However, river sediments and marine sediments do not always correspond in elemental composition or other proxies, so caution is required when using river sediments as end-members for tracing marine sediment sources.

(2) Sea level changes controlled the shifts in sediment source-to-sink processes in the southern SCS since late Last Glacial Maximum (LGM). During the late LGM to early last deglaciation, low sea levels exposed the shelf, allowing large paleo-river systems to develop. Sediments from the Mekong River and islands of southern shelf were directly transported to the slope through these paleo-channels. As sea levels rose, the shelf was gradually submerged, reducing material from southern small island rivers while increasing input from major rivers in the northern shelf. During the Holocene highstand, the Mekong River became the primary sediment source for the Sunda Shelf, while the slope and deepwater areas were also influenced by sediments from the Red River and the Gulf of Beibuwan. It is indicated that sea level changes dictated shifts in source areas and sedimentary centers, while climate, ocean currents, and sediment flux jointly influenced sediment provenance in the southern SCS.

(3) The ($^{234}U/^{238}U$) ratio revealed the ongoing active erosion of equatorial tropical islands during glacial periods. By combining provenance analysis with the climatic conditions of the southern SCS during glacial periods, it was found that tropical islands near the equator experienced slightly weaker precipitation compared to the Holocene. Materials that had undergone early erosion or had been retained for extended periods were shallowly eroded and remobilized to the slope via paleo-rivers. This indicated that the tropical islands in the southern SCS remained actively eroded during glacial periods.

(4) Shelf exposure during glacial periods compensated for the reduced CO_2 consumption rates by silicate weathering due to decreased precipitation, thereby maintaining the overall balance of CO_2 consumption flux since the LGM. Calculations of major elements in core sediments indicated that atmospheric CO_2 consumption flux in the southern SCS has remained nearly constant since the LGM, although silicate weathering rates during glacial periods were only half of those in the Holocene. The increased area available for weathering reactions during glacial periods compensated for the reduced silicate chemical weathering rates, thus controlling the long-term balance of atmospheric CO_2 consumption flux. It was revealed that changes in precipitation are the primary factor controlling variations in silicate weathering and

CO_2 consumption rates, while the roles of temperature and lithology require further evidence.

In summary, this study reconstructed the changes in sediment source-to-sink processes on the Sunda Shelf of the southern SCS since the Last deglaciation, reevaluated the impact of glacial shelf exposure on silicate weathering and CO_2 consumption in low-latitude tropical regions, and identified the factors controlling silicate weathering and atmospheric CO_2 consumption rates. This study potentially provides evidence for the hypothesis that low-latitude tropical regions being a driver of global climate change over glacial-interglacial timescales.

Key words: Sunda shelf, South China Sea, Source to sink, Silicate chemical weathering, Carbon cycle, Sea level changes, ($^{234}U/^{238}U$)

Acknowledgement

As I type these words, my doctoral research has been distilled into this slim volume, and I finally take up the pen to express my gratitude. Looking back 5 years ago, I started my doctoral career at Tongji University, and then spent more than 2 years studying at the University of Lorraine. Along the way, there have been joys and sorrows, but fortunately, I met many teachers, fellow students and families who cared for and helped me. In the moment of earning my doctoral degree, I would like to express my most sincere gratitude to them.

First and foremost, I must express my appreciation to my supervisors, Prof. Albert Galy and associate Prof. Chao Li. I vividly remember writing to Albert for the first time, expressing my desire to join his lab for joint training. I was fortunate to receive a positive response quickly, which allowed me to study in France for over two years. Albert is not only knowledgeable and broad-minded but also meticulous in his approach. He personally guided me through experiments in the clean room and often spent entire days with me in front of the equipment. He meticulously revised my thesis multiple times. I greatly benefited from our discussions, where he encouraged me to ask "why" and even to challenge his conclusions. Albert is an incredibly insightful scientist. Whenever I was lost in the chaos of tangled curves, he provided the inspiration needed to advance my research smoothly. Albert often reminded me, "You are doing science," telling me what true research is and how it should be conducted. His academic philosophy will serve as a guiding light on my future research journey. His profound insights and unwavering beliefs were the rudder and sails guiding me through the stormy seas, accompanying me as I navigated through waves and winds.

During my study in Tongji University, as the first PhD. student of Chao. He is not only a teacher, but also a friend. He introduced me to the fascinating world of geochemistry. I still remember the first time you took me to Lingang Campus, personally introducing me to each laboratory instrument and explaining the testing procedures. Also, he encouraged academic freedom, provided me with various research opportunities, and supported my participation in academic activities beyond the campus, from which I greatly benefited. What’s more, Chao is also very concerned about students' daily lives. We often have dinner together, and he often teaches us life experience. Therefore, I am very grateful to him for providing me with so much help and support during the five years of my doctoral studies.

I would like to extend my heartfelt appreciate to Prof. Christian France-Lanord at CRPG-CNRS-UL. During the coffee break, I often gained many unexpected scientific research surprises from chatting with him. He gave me step-by-step guidance on stable isotope analysis and taught me how to draw inferences from one example to another to understand the working principle of the mass spectrometer. I would also like to express my appreciation to my thesis monitor committee, Prof. Mary Ford from CRPG, Prof. Christophe Colin from the Université Paris-Saclay, and Prof. Cédric Carpentier from the GeoRessources, they give many helpful and useful suggestions during the studies. I would like to thank Yves Marrocchi, Laurie Reisberg, Thomas Rigaudier, Catherine Zimmermann, Aimeryc Schumacher, Damien Cividini and other teachers for their kind guidance and help during my studies and experiments in the CRPG. I also need to thank the teachers in CMS group at Tongji University, they gave me a lot of beneficial suggestions and kind help during my thesis management, laboratory work and also my daily life. First is Prof. Shouye Yang, who is the PI of CMS group. He often analyzed problems for me from the perspective of an elder, provided advice, and created various conditions for my research. He always encouraged me to think deeply about why I need to do these experiments? what are the scientific problems? Often a few words can enlighten me and benefit me a lot. In addition, Dr. Xiangtong Huang, Dr. Ni Su, Dr. Juan Xu, Jiahuan Du in CMS group give me a lot of help and guidance during my research.

I also would like to extend my profound gratitude to the teachers and fellow students who accompanied me have a happy life in France, they are Dr. Jun Zhong from Tianjin University, Dr. Zhengliang Yu from ITPRCAS, Xiaobai Ruan, Aswin, Chenyang Jin, Xiaoyu Zhou, Feng Li. Additionally, I want to express my gratitude to all senior and junior fellow students in TJ-CMS research group, including Chengfan Yang, Zhongya Hu, Kai Deng, Hui Wang, Chi Zhang, Qiang Hao, Fang Cao, Zhifei Duan, Nicholas Ng Chia Wei, Shuo Wang, Songyang Ma, Shijun Wang and so on. They have not only provided invaluable help throughout my doctoral journey but also brought me much joy and pleasure.

I would like to express my deepest gratitude to my families, who have silently accompanied me all along. They are the strong pillars supporting me on my journey, always there to affirm and uphold me during moments of doubt and setback. From my childhood to the present, my parents have done everything within their power to provide me with the best educational and living conditions. They have never pressured me to

excel above others, but rather hoped for my happiness and well-being. They have been, and will always be, the warmest refuge and harbor for me, no matter where life takes me. I can no longer hear grandma's voice on the other end of the phone. The ruthless disease did not let you see me put on a doctoral cap. You always accompanied me since I was a child and gave me warm and steadfast love. When I was helpless, I used to look up, and I knew that you had always been with me as the brightest star in the night. I would like to dedicate this thesis to you, and I will always miss you.

This work was funded by National Natural Science Foundation of China. Great thanks to the support from China Scholarship Council, who provided 24 months funding for my stay in France, also appreciate CRPG-CNRS for 2 months funding and experimental expense.

Now, as I stand on the cusp of culminating my educational journey, I am only at the gate of scientific research. This journey has been one of storms weathered and miles traveled, with an unrelenting road that stretches towards the horizon. So, last but not least, I need to thank myself, brave the storm, spare no effort. My heart swells with appreciation for the love and support I have received from all. May I continue to forge ahead with unyielding determination, and as I unfurl the sails once more, may I venture forth into the boundless expanse that lies between the mountains and the seas.

Finally, my favorite Ci-poetry *Xingxiangzi, unbosoming myself* by Shi Su from Song Dynasty (A.D.960-A.D.1279), I try to translate into English, for you all:

On a clear night, the moonlight shines like silver. As you pour the wine, make sure the cup is full. The pursuit of fame and fortune is fleeting and exhausting. Life passes quickly, like a horse in a crack, a spark from a stone, or a fleeting dream.

Although I possess literary talent, who truly understands when I speak? I prefer to be carefree and enjoy simple pleasures. When will I return to a life of leisure, with just a zither, a jug of wine, and a stream of clouds?

Contents

Chapter 1 Introduction

1.1 Background

1.1.1 Research background

The scientific understanding and evolutionary dynamics of Earth's habitability are key frontier issues in 21st-century science. The Earth's surface is a crucial component of its habitability, and we strive to understand the interactions between its various spheres. Weathering processes connect the physical and chemical processes across these spheres (Fig. 1.1) (Frings and Buss, 2019). Terrestrial silicate weathering processes consume atmospheric CO_2. Among the weathering of different minerals such as silicates, carbonates, and sulphides, silicate weathering acts as a net carbon sink in the weathering-carbon cycle (Frings, 2019; Walker et al., 1981). It is estimated that the global annual CO_2 emission is 10×10^{12} mol/yr, with silicate rock weathering consuming approximately 0.144 Gt of atmospheric CO_2 at a flux of about 11.7×10^{12} mol/yr. This mechanism plays a significant role in global climate change and the carbon cycle (Gaillardet et al., 1999a). Globally, low-latitude regions account for over 60% of the CO_2 flux consumed by chemical weathering (Hartmann et al., 2009), highlighting the crucial role of tropical weathering in the global carbon cycle. Studying the historical evolution of atmospheric CO_2 concentrations and their driving mechanisms is important for understanding global climate change and predicting future climate trends (Ganopolski et al., 2016). Polar ice core records show that CO_2 concentrations during glacial periods were approximately 80-90 ppmv lower than during interglacial periods, a reduction of nearly one-third (Luthi et al., 2008). Why did atmospheric CO_2 concentrations decrease significantly during glacial periods compared to interglacial periods? Where did the lost atmospheric carbon go during the glacial periods? What mechanisms drive the coupled changes in "ice" and "carbon"? These questions form the basis of the well-known "glacial atmospheric CO_2 mystery" (Sigman and Boyle, 2000).

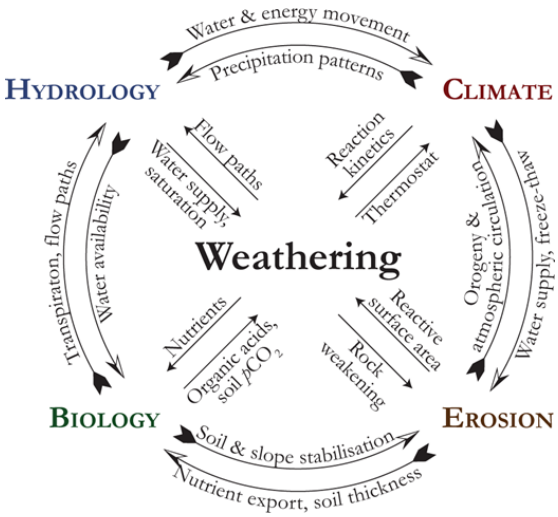

Fig. 1.1 The relationship between weathering and spheres of the Earth's surface (Frings and Buss, 2019)

The Sunda Shelf of the southern SCS is located in the low-latitude tropical region between the Eurasian continent and the Pacific Ocean. Its unique location is crucial for understanding environmental evolution mechanisms, particularly regarding ocean-continent and high-latitude to low-latitude interactions (Wang et al., 2014b). The Sunda Shelf, also known as the "Great Asian Bank", covers an area of approximately 2.37×10^6 km^2, making it the largest continental shelf outside the polar regions (Sathiamurthy and Voris, 2006). The region has experienced tectonic stability, abundant rainfall, and rapid sedimentation over the past few centuries. Notably, the low-gradient (1:9000) muddy depositional areas have preserved extensive stratigraphic records (Fig. 1.2A). During glacial periods, sea levels dropped, exposing the Sunda Shelf and connecting it with surrounding lands and islands to form the "Sunda Land", representing the most significant geographical change in the tropical region during glacial times (Tjia and Kuala, 1980; Tjia and Liew, 1996). Large paleo-river systems developed on the exposed shelf (Fig. 1.2B) (Solihuddin, 2014; Voris, 2000), directly transporting eroded and weathered sediments from surrounding lands and islands to the slope and southern SCS. This transport process differs between high and low sea levels, complicating sediment sources due to shifts in the source-to-sink dynamics during glacial and interglacial cycles. It is estimated that during the Last Glacial Maximum (LGM), the global continental shelf area exposed due to sea-level decline was 22.3×10^6 km^2, approximately 15% of the Earth's total land area. Of this newly exposed land, 39% ($\sim8.6\times10^6$ km^2) was located in tropical regions where temperature and precipitation fluctuations were relatively minor during the glacial period (Kump et al., 2000; Ludwig

et al., 1999). “The present is the key to the past”, the weathering feedback caused by the exposure of tropical shelves during glacial lowstand likely played a significant role in the glacial carbon cycle. Therefore, did the Sunda Shelf's role reversal from a source during glacial to a sink during interglacial periods affect the transmission of environmental signals from land to ocean? Did the exposure of the shelf enhance silicate weathering, thereby influencing atmospheric CO_2 flux during glacial periods? This study will address these fundamental questions by analyzing terrestrial and marine sediments using sedimentological and geochemical methods to investigate sediment transport processes and silicate weathering history on the Sunda Shelf of the southern SCS since the late LGM, thereby exploring differences in atmospheric CO_2 consumption by silicate weathering between glacial and interglacial periods.

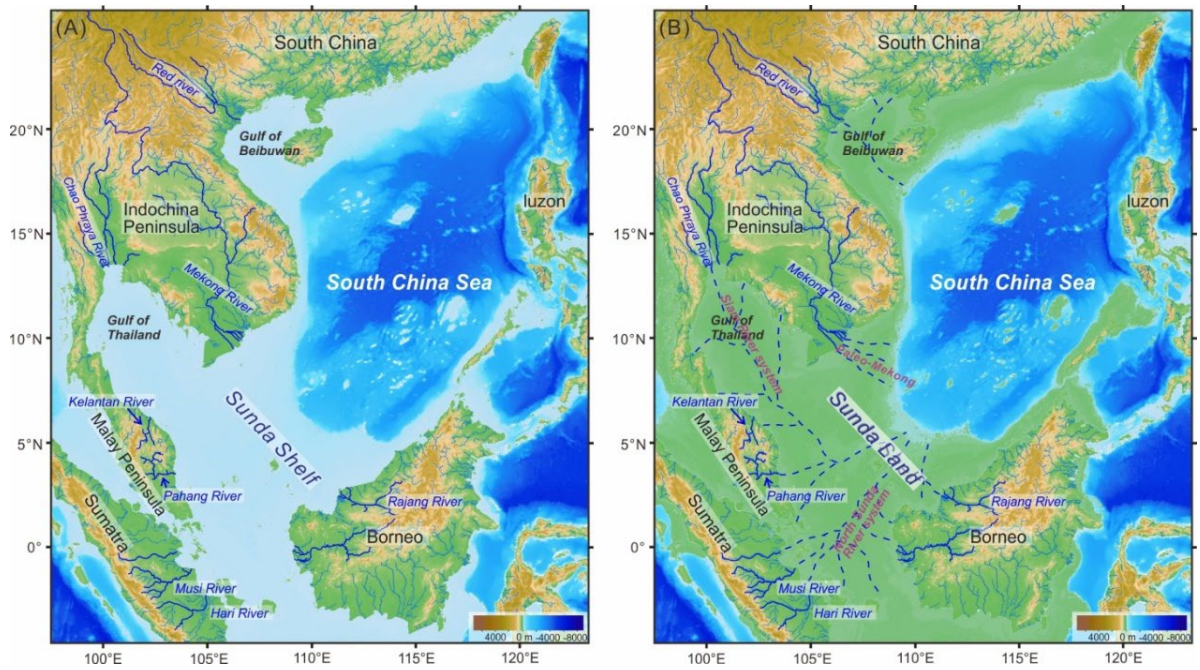

Fig. 1.2 Geomorphic patterns of the SCS during high sea level (A) and low sea level (B) periods (Sathiamurthy and Voris, 2006; Solihuddin, 2014; Voris, 2000).

1.1.2 Research questions and objectives

Considering the limitations and significance of two major scientific issues-namely, the source-to-sink processes of sediments on the Sunda Shelf of the southern SCS, and the silicate weathering history and its role in atmospheric CO_2 consumption since the LGM. This study focuses on the Sunda Shelf of the southern SCS and the surrounding lands and island. The research employs geochemical methods, anzlyzing sediments from major rivers from surrounding lands, seafloor sediments, and marine core sediments from the shelf and slope. Combing with published sedimentological and

mineralogical studies and guided by the principle of "present is the key to the past", This research aims to address the following three key questions:

(1) By comparing trace elements and Sr-Nd isotopes in river sediments from surrounding lands, seafloor sediments, and marine core sediments to identify the sources of sediments on the Sunda Shelf of the southern SCS since the late LGM (18.5 ka). Also, we reconstructed sediment source-to-sink transitions during highstand and lowstand, and the factors controlling sediment provenance evolution.

(2) Based on the Sr-Nd isotope analysis of sediment provenance, this study will try to apply U-series disequilibrium methods to slope core sediments. This approach helps to reconstruct the erosion processes of small tropical island rivers during glacial periods, revealing the relationship between glacial erosion and climate in these regions.

(3) Calculating the relative changes in silicate weathering intensity and CO_2 consumption rates between the glacial period and the Holocene using major element data, indicating the impact of shelf exposure during glacial periods on silicate weathering and CO_2 consumption, exploring the factors controlling CO_2 consumption rate by silicate chemical weathering in low-latitude tropical regions during glacial and interglacial periods.

This study is funded by the Natural Science Foundation of China, 'The impact of Sunda Shelf exposure on sediment transfer processes and chemical weathering archive since late Pleistocene (No. 42076063)', National Key R&D Program 'Late Cenozoic weathering, sedimentation patterns and carbon sink effects of the Asian continental margin (No. 2022YFF0800504)' and China Scholarship Council (No. 202106260083). I participated in literature research, sample collection, laboratory analysis, data processing, chart drawing, paper writing, etc. The specific physical workload is shown in Table 1.1.

Table 1.1 Statistics of physical workload of the paper

No.	Samples	Types	Lab. work	Amounts	Lab.	Operator
1			wet sieving and pretreatment	22	SKLMG *	Nicholas Ng Chia Wei, Junfei Chen
2	river sediments	<50 μm component	grain size	22	NJU**	Junfei Chen, Nicholas Ng Chia Wei
3			major and trace elements	22	SKLMG	Nicholas Ng Chia Wei, Junfei Chen, Zhifei Duan

4			Sr and Nd isotope	22	SKLMG	Nicholas Ng Chia Wei, Junfei Chen, Zhifei Duan
5			U isotope	22	SKLMG	Nicholas Ng Chia Wei, Junfei Chen, Zhifei Duan
6			major and trace elements	31	CRPG***	Junfei Chen
7		bulk-AcAc****	Sr and Nd isotope	31	CRPG	Junfei Chen
8			carbonate and $\delta^{18}O$, $\delta^{13}C$	38	CRPG	Junfei Chen
9		bulk	major and trace elements	38	CRPG	Junfei Chen
10			carbonate and $\delta^{18}O$, $\delta^{13}C$	38	CRPG	Junfei Chen
11	sea floor sediments		wet sieving and pretreatment	13	SKLMG	Nicholas Ng Chia Wei, Junfei Chen
12			grain size	13	NJU	Nicholas Ng Chia Wei, Junfei Chen
13		<50 μm component	major and trace elements	13	SKLMG	Nicholas Ng Chia Wei, Junfei Chen, Zhifei Duan
14			Sr and Nd isotope	13	SKLMG	Nicholas Ng Chia Wei, Junfei Chen, Zhifei Duan
15			U isotope	13	SKLMG	Nicholas Ng Chia Wei, Junfei Chen, Zhifei Duan
16			major and trace elements	13	CRPG	Junfei Chen
17		bulk-AcAc	Sr and Nd isotope	8	CRPG	Junfei Chen
18			carbonate and $\delta^{18}O$, $\delta^{13}C$	13	CRPG	Junfei Chen
19		bulk	major and trace elements	13	CRPG	Junfei Chen
20			carbonate and $\delta^{18}O$, $\delta^{13}C$	13	CRPG	Junfei Chen
21	core ST13	core observation and sampling		150	SKLMG	Junfei Chen
22		foraminifera selection and AMS^{14}C dating		11	SKLMG and BETA	Junfei Chen
23		^{210}Pb dating		9	SKLMG	Junfei Chen
24		<50 μm component	grain size	41	NJU	Junfei Chen
25			wet sieving and pretreatment	41	SKLMG	Junfei Chen
26			major and trace elements	41	SKLMG	Junfei Chen
27			Sr and Nd isotope	41	SKLMG	Junfei Chen
28			U isotopes	41	SKLMG	Junfei Chen
29		bulk-AcAc	major and trace elements	40	CRPG	Junfei Chen
30			Sr and Nd isotope	35	CRPG	Junfei Chen
31			carbonate and $\delta^{18}O$, $\delta^{13}C$	41	CRPG	Junfei Chen
32		bulk	carbonate and $\delta^{18}O$, $\delta^{13}C$	41	CRPG	Junfei Chen
33		sampling		69	SKLMG	Junfei Chen

34		foraminifera selection and AMS^{14}C dating		8	SKLMG and BETA	Junfei Chen
35			grain size	44	NJU	Junfei Chen, Hui Wang
36			wet sieving and pretreatment	44	SKLMG	Junfei Chen
37		<50 μm component	major and trace elements	44	SKLMG	Junfei Chen
38	core 18288-2		Sr and Nd isotope	44	SKLMG	Junfei Chen
39			U isotope	44	SKLMG	Junfei Chen
40			major and trace elements	35	CRPG	Junfei Chen
41		bulk-AcAc	Sr and Nd isotope	30	CRPG	Junfei Chen
42			carbonate and $\delta^{18}O$, $\delta^{13}C$	34	CRPG	Junfei Chen
43		bulk	carbonate and $\delta^{18}O$, $\delta^{13}C$	34	CRPG	Junfei Chen

Note: *SKLMG: State Key Laboratory of Marine Geology, Tongji University, China

**NJU: Nanjing University

***CRPG: Centre de Recherches Pétrographiques et Géochimiques, CNRS, Université de Lorraine, France

**** bulk-AcAc: bulk sediments after acetic acid leaching

1.1.3 Thesis structure

This thesis primarily employs geochemical methods to study the sediment source-to-sink processes and silicate weathering history, with atmospheric CO_2 consumption of the Sunda Shelf in the southern SCS since the last deglaciation. The thesis is structured into eight chapters, with Chapters 4 to 7 comprising the core content. Chapter 1 provides a general introduction to the research background, and reviews the history of source-to-sink processes and silicate weathering studies in the southern SCS. It also outlines the primary research questions and objectives of this study. Chapter 2 describes the geological background of the southern SCS, including its geographical location, tectonics, sedimentology, and lithology, as well as the ocean currents and climate. Chapter 3 details the samples in this study and the research methods employed. Chapter 8 summarizes the key findings of this research, discusses the limitations, and presents future plans and perspectives. The key questions raised in Section 1.1.2 are addressed in detail in Chapters 4 to 7.

Chapter 4 primarily analyzed the elemental and isotopic compositions of river and seafloor sediments around the southern SCS, and explored the sources of marine sediments in this multi-source context and their controlling factors. The chapter discussed the importance of lithology in the source area on the geochemical

composition of sediments and highlighted the need for caution when using river sediment geochemistry as a comparative end-member for marine sediment sources.

Chapter 5 used the core sediments of the Sunda Shelf and slope as research objects, analyzed the trace elements and Sr-Nd isotope composition of sediments in the southern SCS since the last deglaciation. It revealed shifts in sediment provenance and source-to-sink processes between the glacial lowstand and interglacial highstand. The primary factors driving these changes were identified as sea level changes and monsoon-induced precipitation variations. Chapters 4 and 5 address key questions (1).

Chapter 6 compared the geomorphology of the southern SCS during the low sea level of the glacial period, when the Sunda Shelf was exposed, with the present-day geomorphology of the Changjiang catchment. It introduced a new approach using ($^{234}U/^{238}U$) and Comminution Ages in core sediments to reveal that tropical islands experienced strong erosion during the glacial period as precipitation being a controlling factor. This chapter addresses key question 2, and portions of the content have been published in *Earth and Planetary Science Letters*.

Chapter 7 calculated relative changes in weathering intensity and atmospheric CO_2 consumption flux in the southern SCS since the last deglaciation using the major elemental composition of terrigenous detrital components in core sediments. It quantified the rate of atmospheric CO_2 consumption by silicate weathering during different periods, revealing the significant impact of shelf exposure during glacial periods on weathering processes in the low-latitude tropics and indicating the factors that control silicate weathering rates.

To avoid repeated citations in each chapter, all references have been consolidated and listed collectively in the "References" section.

1.2 State of the art

1.2.1 Study of sediments “source to sink” of the Sunda shelf and the southern SCS

More than 300 years BC, the ancient Greek philosopher Plato posed a question that we continue to ponder today: "Where do I come from?" Similarly, when we pick up a handful of sand from a river or the sea, we instinctively ask: "Where did they come from?" Rocks, when eroded or weathered in source areas, break down into sediment particles or dissolve into solutes. These materials are then transported and ultimately deposited in sedimentary basins or depositional areas, a process known as the "source-

to-sink (S2S)" system (Fig 1.3) (Allen, 1997; Allen, 2008; Anthony and Julian, 1999; Carter et al., 2010). Rocks break into fine particles in source areas and are transported by different forces to be deposited in lakes or oceans. During this process, these particles may have temporarily resided within weathering profiles in the source area or trapped on floodplains. Consequently, the sediment eventually found in the “sink” may record environmental evolution information beyond our imagination (Romans et al., 2016). The environmental signals recorded in sediments can be transformed, phase-shifted, or lagged by the internal dynamics of the routing system, due to changes in transport pathways. Therefore, it is crucial to thoroughly study the provenance and transport processes of sink sediments to better understand the environmental signals they preserve. This is how we might "see a world in a grain of sand," as poet William Blake suggested.

Fig. 1.3 Sediment “source to sink” process. The dotted lines represent the transport routes of sediments; large circles indicate that sediments are stored in the floodplain for a long time, and small circles indicate that sediments are stored for a short time during the transport process (Allen, 2008).

The SCS, the largest marginal sea in the low-latitude region of the Western Pacific, is situated near the southeastern Eurasian continent and the Pacific island arcs. Since the Neogene, terrigenous clastic components have accounted for 80% of the marine sediments in the SCS (Milliman and Farnsworth, 2011). Current research on the SCS primarily focuses on its northern and western regions, with limited studies on the southern part, which is closer to the equator (e.g. Liu et al., 2007b; Liu et al., 2003; Sang et al., 2022; Wang et al., 2021). Compared to the northern SCS, the surrounding landforms and sediment sources of the southern region are more complex. More importantly, the southern SCS features the Sunda Shelf, the largest shallow continental shelf in the low-latitude tropics, characterized by shallow waters and gentle slopes (Hanebuth et al., 2003; Tjia and Kuala, 1980). During the glacial low sea level periods, the Sunda Shelf was exposed as a vast plain, connecting with the surrounding lands, forming what is known as the "Sunda Land" (Hanebuth et al., 2003; Hanebuth et al., 2011).

Current research on sediment sources in the southern SCS mainly relies on comparing clay minerals composition between river and marine sediments. Clay minerals, as typical weathering products at the Earth's surface, can indicate earth surface chemical weathering processes and provide semi-quantitative assessments of sediment transport (Huang et al., 2021; Liu et al., 2016b; Steinke et al., 2008). For the potential sediments sources of the SCS, the Red River and Mekong River basins in the Indochina Peninsula have high concentrations of illite and kaolinite, constituting about 70% of all clay minerals. Sediments from Thailand rivers are rich in smectite (42%) and kaolinite (32%), while those from the Malay Peninsula and Sumatra are predominantly kaolinite (78% and 57%, respectively). Borneo Rivers show varied clay mineral compositions: northern Borneo is dominated by illite (~60%), while western and eastern Borneo are dominated by kaolinite (~45%). Smectite dominates the river sediments of the Luzon Arc (87%) (Fig. 5.10A). By comparing the types and contents of clay minerals between the rivers and the seafloor sediments of the SCS (Fig. 5.10B), the transport processes and sources of clay minerals in different regions of the SCS were determined (Liu et al., 2016b). Research on sediment sources in the southern SCS during the Quaternary is even more limited. This study summarized all current studies on sediment sources from marine core sediments in the southern SCS, including the Sunda Shelf (Table 1.2). Currently, there is only one core located at the central Sunda shelf studied sediment sources of the Sunda Shelf. Wu et al. (2023) indicate that since

the middle Holocene, sediments of the Sunda Shelf primarily originated from the Mekong River and Thailand rivers. Between 14-7.5 ka, sediment sources were mainly controlled by the Mekong River, while from 0 to7.5 ka, they were primarily influenced by Thailand rivers. The main factors affecting provenance changes are sea-level fluctuations and the East Asian monsoon. Research on core sediments in the southern SCS mainly focused on clay mineral content and composition. Pelejero et al. (1999) showed that sea-level changes control the exposure of the Sunda Shelf and the opening -closing of channels between the SCS and the southern tropical Indo-Pacific, which in turn affects whether sediments from the southern Indonesian archipelago can be transported to the SCS during highstand and lowstand. Steinke et al. (2008) initiated a more detailed study on sediment sources in the southern SCS, which revealed that glacial sediments originated from exposed shelf paleo-soil and Indonesian island material, while interglacial sediments came from northern Borneo. Huang et al. (2016) also used clay mineral data to show that glacial materials primarily consist of recycled exposed shelf material and sediments from the Mekong River and northern Borneo. In contrast, interglacial sediments mainly come from the Mekong River, northern Borneo, and the Indonesian archipelago. Sediment source changes were controlled by both sea level and monsoon. However, their study suggests that there may be no significant differences in sediment sources between glacial and interglacial periods, with the Mekong River and northern Borneo rivers consistently being the main sources for the southern SCS. Similarly, Jiwarungrueangkul et al. (2019) expanded on clay mineral analysis by adding grain size and major element proxies. Their study also confirmed that southern SCS sediments are primarily controlled by sea level and monsoon. The sources of interglacial sediments were consistent with Huang et al. (2016), while they proposed that glacial sediments mainly originated from islands surrounding the Sunda Shelf, such as the Malay Peninsula, Sumatra, and Borneo, with paleo-rivers transporting the sediments to the ocean. These limited studies suggest that the sediment sources in the southern SCS are highly complex, and no comprehensive conclusions have been reached. Moreover, research methods have been relatively narrow, focusing primarily on clay minerals. While clay minerals are a well-established indicator for tracing sediment sources, they are significantly influenced by hydrodynamic sorting. For example, studies have shown that in the Amazon River mouth, chlorite and illite particles are generally smaller than 20 μm, kaolinite is smaller than 8 μm, and smectite is smaller than 1 μm. As a result, the coarser chlorite and illite settle first, while smectite

can be transported over longer distances (Gibbs, 1977). Additionally, due to the different chemical property of clay minerals, kaolinite, when transported by rivers to estuaries, easily undergoes flocculation reactions with alkaline seawater and settles, resulting in lower kaolinite content in deep marine sediments (Liu et al., 2010). Therefore, caution is required when using clay minerals to trace the sources of marine sediments. There is an urgent need for more comprehensive studies on sediment sources in the southern SCS, incorporating additional geochemical methods, such as isotopic analysis.

Table 1.2 Studies of sediments sources since the Quaternary in the southern SCS

Area	Core name	Coordinate	Water depth (m)	Age (ka cal. BP)	Proxies	Sediments provenance		Controls	reference
Sunda Shelf	CJB01-64	104°58′06.54″E 5°59′53.49″N	62	~14	Clay minerals, trace elements and Sr-Nd isotopes	sediments provenances are Mekong River and Thailand rivers. 0-7.5 ka, controlled by Thailand river sediments; 7.5-14 ka, controlled by Mekong River sediments.		Sea level and East Asian monsoon	Wu et al. (2023)
	CJB01-75	105°31′50.94″E 4°54′40.52″N	80	~4					
Southern SCS	17961	112°19′E 8°30′N	1968	30	Clay minerals	Glacial	No sediments from archipelago of Indonesia	Sea level	Pelejero et al. (1999)
	17964	112°12′E 6°09′N	1556	23.5		Interglacial	Have sediments from archipelago of Indonesia		
	18284-3	110°32.42′E 5°32.50′N	226	17	Clay minerals	Glacial	exposed Sunda Shelf, archipelago of Indonesia.	Sea level	Steinke et al. (2008)
	18287-3	110°39.68′E 5°39.78′N	598			Interglacial	northern Borneo		
	CG2	110.1542°E 6.3928°N	1239	22	Clay minerals	Glacial	Sunda shelf, Mekong River, northern Borneo	Sea level, monsoon	Huang et al. (2016)
						Interglacial	archipelago of Indonesia, Mekong River, northern Borneo		
	MD05-2893	110°40.72′ E 6°06.07′ N	1183	17.2	Grain size, clay minerals, and major elements	Glacial	Malay Peninsula, Sumatra, and Thailand	Sea level, monsoon	Jiwarungrueangkul et al. (2019)
						Interglacial	Mekong River, northern Borneo, Sumatra		

1.2.2 Study of weathering history and carbon cycle of the Sunda Shelf and the southern SCS

(1) Carbon cycle and silicate chemical weathering

Atmospheric CO_2 is regulated by the earth's carbon cycle, which primarily consists of the organic carbon cycle and the silicate-carbonate inorganic carbon cycle. The silicate-carbonate cycle is the primary control mechanism for atmospheric CO_2 (Fig.

1.4)(Kasting, 2019), which can be broadly divided into two processes: sources and sinks. The "source" refers to the processes that produce CO_2, primarily including volcanic degassing, midocean ridge degassing, and the release of CO_2 from carbonate metamorphism, all of which involve the release of CO_2 from the Earth's interior into the atmosphere (Ruddiman, 2014):

$$CaCO_3 + SiO_2 \rightarrow CaSiO_3 + 2CO_2 \quad (1.1)$$

"Sink" refers to the process of consuming CO_2. It mainly refers to the process in which silicate rocks react with atmospheric CO_2 and water to form calcium and magnesium ions, bicarbonate and dissolved silicon (Berner, 1992a):

$$(Ca/Mg)SiO_3 + 2CO_2 + H_2O \rightarrow (Ca/Mg)_2+ + 2HCO_3^- + SiO_2 \quad (1.2)$$

Ions formed by the weathering of silicate rocks enter the ocean and combine with calcareous organisms in the ocean to form shells or skeletons, and carbonates precipitate:

$$(Ca/Mg)^{2+} + 2HCO_3^- \rightarrow (Ca/Mg)CO_3 + H_2O+ CO_2 \quad (1.3)$$

Therefore, combining chemical formulas (1.2) and (1.3), we can deduce the process of silicate rock from weathering to burial:

$$(Ca/Mg)SiO_3 + CO_2 \rightarrow (Ca/Mg)CO_3 + SiO_2 \quad (1.4)$$

From (1.4), the chemical weathering process of each 1 mol of calcium or magnesium ions consumes 1 mol of atmospheric CO_2. On the tectonic time scale, silicate weathering is equivalent to a "net carbon sink" (Berner, 1992a; Walker et al., 1981; West et al., 2005).

The chemical weathering process of carbonates consumes atmospheric CO_2, while the precipitation of marine calcium carbonate releases CO_2, so it can be considered a balanced process on a long-time scale (Berner et al., 1983).

$$CO_2 + CaCO_3 + H_2O \rightleftharpoons Ca^{2+} + 2HCO_3^- \quad (1.5)$$

The global geological carbon cycle is highly complex, collectively determining atmospheric CO_2 levels on a geological timescale. This study focuses on the silicate weathering process, which not only influences atmospheric CO_2 concentrations and thereby regulates temperature but is also affected by factors such as temperature, precipitation, and vegetation (Walker et al., 1981).

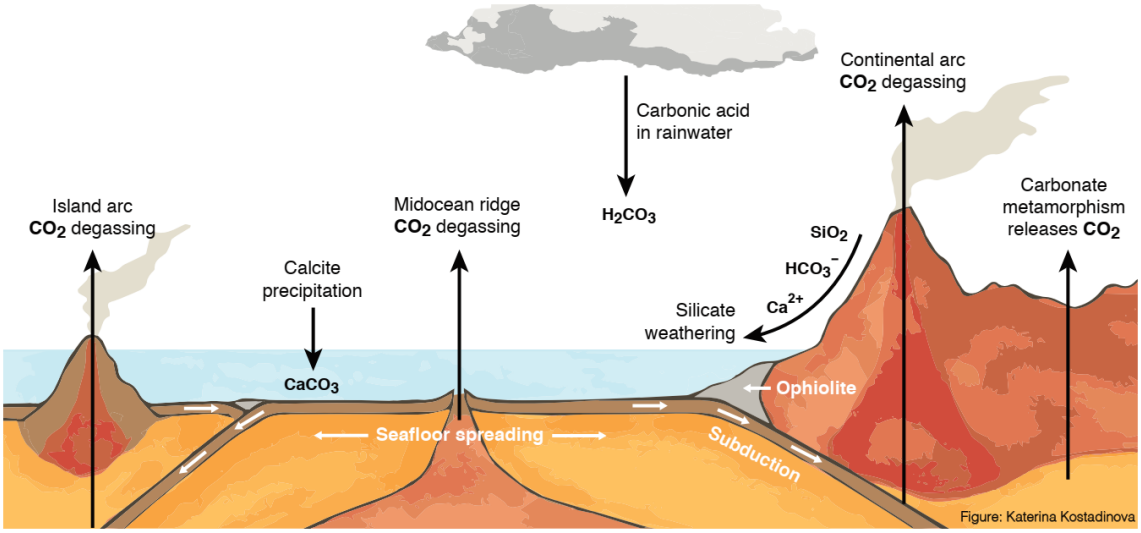

Fig.1.4 Schematic diagram of the silicate-carbonate cycle (Kasting, 2019)

(2) Research on weathering processes and carbon cycle in the southern SCS

The southern SCS, located at the edge of the East Asian continent in the southwestern Pacific, acts as a crucial link between ocean and land. It is one of the most active regions for land-sea interactions, and its paleoenvironmental evolution has a significant impact on global climate change (Wang, 1999). The southern SCS receives lots of terrigenous sediment from surrounding continents annually. The geochemical composition of these weathered products recorded valuable environmental evolution information, making it crucial for analyzing weathering processes and carbon cycle in low-latitude tropical regions. However, research on weathering processes and carbon cycling in this region remains limited. Wang et al. (2014b) summarized the history of sea surface temperature (SST) studies in the SCS, particularly the use of sediment geochemical proxies, which has significantly advanced paleoenvironmental research in the region. In 2017, the Chinese journal *Advances in Earth Science* published a special issue on the Sunda Shelf, where Wang (2017) proposed the hypothesis "Sunda Shelf—A Submerged Amazon Basin?". During glacial low sea levels, the shelf was exposed, possibly transforming the region's tropical forests into a significant tropical carbon sink comparable to the Amazon Basin. This hypothesis calls for a reevaluation of the global terrestrial carbon cycle. Subsequent studies have used pollen and other vegetation records preserved in core sediments to investigate the organic carbon cycle processes of the Sunda Shelf and the SCS (Cheng et al., 2023; Sun et al., 2000; Wang et al., 2009; Yu et al., 2023). However, research on the silicate-carbonate inorganic carbon cycle is limited. Ludwig et al. (1999) modelled the CO_2 consumption by terrestrial rock weathering during the present-day and the LGM. The result indicated opposite

differences between the northern and southern regions of the Sunda Shelf. In the north, including South China and the Indochina Peninsula, rock weathering currently consumes more CO_2 than during the LGM, while in the south, including Sumatra and Borneo, CO_2 consumption by weathering is lower than during the LGM. Due to limited research, the weathering processes in the Sunda Shelf remain difficult to estimate (Fig. 1.5). Therefore, the complex weathering processes in the SCS and their impact on CO_2 consumption require further attention. Some studies used the composition and content of clay minerals in river sediments from surrounding islands to reveal modern continent weathering processes (Liu et al., 2012; Liu et al., 2009). Regarding weathering processes during geological periods, Wan et al. (2017) proposed the "Enhanced weathering of tropical shelf during glacial periods" hypothesis using sediment records from cores 1143 and 1144 in the SCS. They suggested that intensified chemical weathering of tropical shelf during glacial periods could be a new mechanism for atmospheric CO_2 sequestration. The favorable conditions at low-latitude areas during glacial periods, including suitable temperature, humidity, extensive groundwater circulation, large mineral reaction surfaces, and sufficient time, would promote the re-weathering of exposed tropical shelf sediments, thereby affecting global carbon cycles and exacerbating glacial climate cooling. Zhao et al. (2024) revealed that chemical weathering intensity in the southern SCS over the past 21 ka has been controlled by sea level changes and monsoon evolution based on core MD05-2892 sediments. They found that physical erosion intensified on Sumatra and the Malay Peninsula during the glacial period, while chemical weathering increased on the Indochina Peninsula during the Holocene.

The South China Sea (SCS), situated in a low-latitude region between the largest continent and the largest ocean, holds a unique position that is crucial for understanding environmental evolution mechanisms, especially in terms of ocean-land or high-latitude to low-latitude interactions. The current hypothesis suggesting that global climate change is driven by low-latitude processes (Wang, 1999; Wang et al., 2014b) further underscores the importance of weathering processes and carbon cycling in the southern SCS. Therefore, this study will focus on investigating changes in silicate chemical weathering intensity and the factors controlling atmospheric CO_2 consumption rates in the Sunda Shelf of the southern SCS since the Last deglaciation.

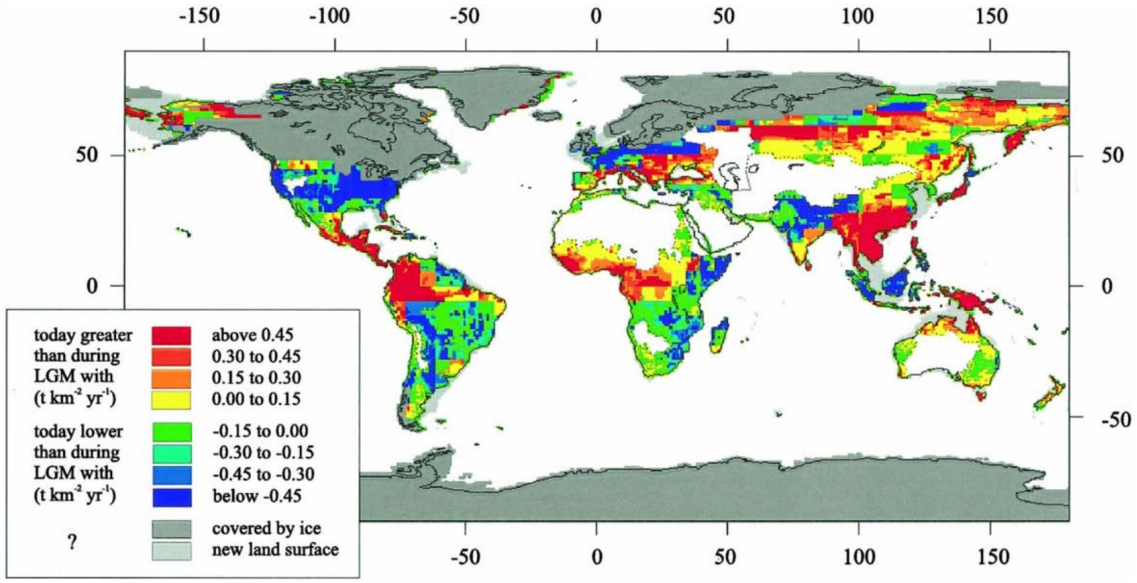

Fig. 1.5 Atmospheric CO consumption by rock weathering: differences between present-day and the LGM. The white parts of the continents are endoreic (Ludwig et al., 1999).

Chapter 2 Introduction of study area

2.1 Geographical location and rivers flowing into the sea

The Sunda Shelf is located at the southern SCS, which is at junction of the Pacific Ocean and the Indian Ocean (Fig. 2.1). It covers an area of more than 2.37×10^6 km^2, with a maximum width of 800 km. The average seafloor slope is less than 0.003° and the average water depth is 70-80 m (Hanebuth et al., 2003; Tjia and Kuala, 1980). It is the second largest shallow shelf in the world. The surrounding land includes the South China Continent, Indochina Peninsula, Malay Peninsula, Sumatra, Borneo and Luzon, etc., which constitute the Sunda Continent (Tjia and Kuala, 1980; Wang, 2017).

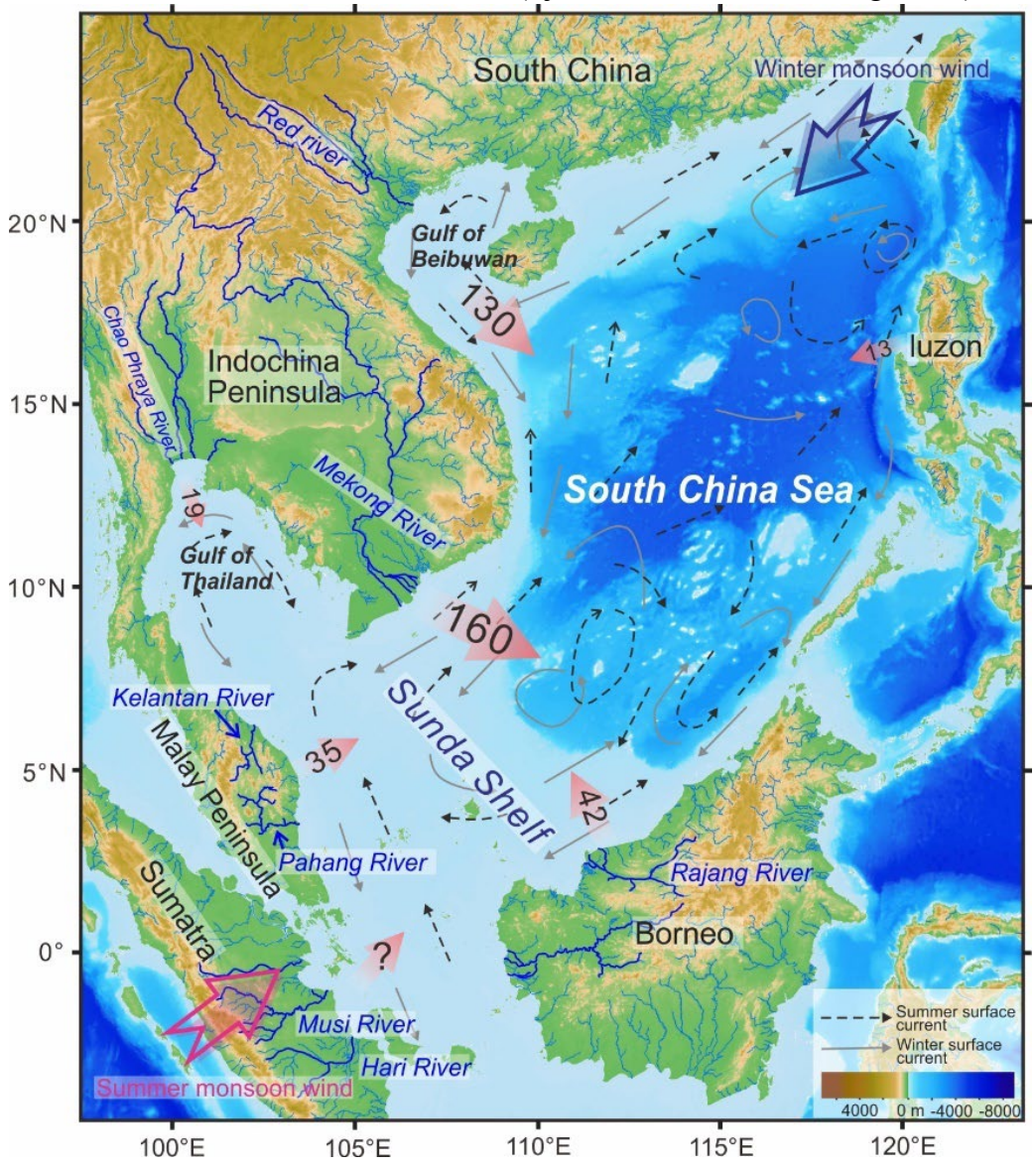

Fig. 2.1 Geographical pattern of the SCS, sediment flux of major rivers and surface current (pink arrows indicate annual sediment flux of rivers into the sea, unit: Mt/yr (Milliman and Farnsworth, 2011).

Rivers are the main way for terrestrial materials to enter the ocean. The river system entering the ocean around the Sunda Shelf is complex and can be divided into two categories: large rivers in the north land and small island rivers in the south and west. Large rivers in the north land include the Mekong River in the Indochina and the Red River in the South China, the Chao Phraya River in Thailand, and small island rivers include the Pahang River and the Kelantan River in the Malay Peninsula, the Hari River and the Musi River in Sumatra, and the Rajang River in Borneo (Table 2.1, Fig. 2.1).

The Mekong River is the largest river discharging into the southern SCS, originating from the Tibetan Plateau, it flows into the SCS from the southern part of the Indochina Peninsula. It is the world's ninth largest river and the largest in Southeast Asia, spanning 4148 km with a drainage area of up to 795,000 km², annually transporting approximately 150 Mt sediments to the ocean (Milliman and Farnsworth, 2011). The Red River originates in Yunnan Province and flows through northern Vietnam into the Gulf of Beibuwan, with a sediment discharge of up to 110 Mt/yr. In Thailand, the Chao Phraya and other three rivers primarily discharge into the Gulf of Thailand in the northwest Sunda Shelf, totally transporting over 19 Mt sediment annually. The Pahang and Kelantan Rivers are the largest rivers in the eastern Malay Peninsula, annually transporting approximately 35 Mt of sediment to the Sunda Shelf.

The rivers at the Sumatra and Borneo are poorly studied and there are few data about the discharge and sediments. According to estimates by Milliman et al.(1999), rivers flowing into the South China Sea from northeast Sumatra have an average annual sediment flux of approximately 459 Mt, while the major rivers of northwest Borneo contribute up to 498 Mt/yr. However, current observation shows that there is only about 30 Mt of sediment are discharged into the ocean annually of the Rajang River in northwest Borneo. Therefore, further studies are needed on the smaller island rivers in the southern South China Sea.

Table 2.1 Information of main rivers around the southern SCS in this study (Milliman and Farnsworth, 2011)

Area	River name	Area (10^3 km^2	Length (km)	Discharge (km^3/yr)	Total suspended sediments (Mt/yr)
Vietnam	Red	160	1100	120	130
Indochina Peninsula	Mekong	795	4800	550	160
	Kelantan	12	420	18	2.5

Malaysia peninsula	Pahang	19	320	18	3
Sumatra	Hari	50	490	46	-
	Musi	61	750	80	-
Borneo	Rajang	51	530	110	30

2.2 Tectonic and sedimentological characteristics

2.2.1 Tectonic characteristics of the SCS

The SCS is located at the intersection of the Tethys and circum-Pacific super-convergence zones, with unique tectonic features (Fig. 2.2). There are many differing opinions on its formation and tectonic evolution. The formation of the SCS was affected by the Eurasian, Pacific, and Indo-Australian plates. It expanded from approximately 34 to 15 Ma ago. Around 6.5 Ma, the collision of the Luzon Arc with the Asian continental margin initiated the episodic uplift of the Taiwan orogeny, restricting communication between the SCS and the ocean, thus establishing its semi-enclosed marginal sea configuration (Camanni and Ye, 2022; Franke et al., 2014; Li et al., 2022; Wu et al., 2016; Li et al., 2012; Wang and Jian, 2019; Yao et al., 2004).

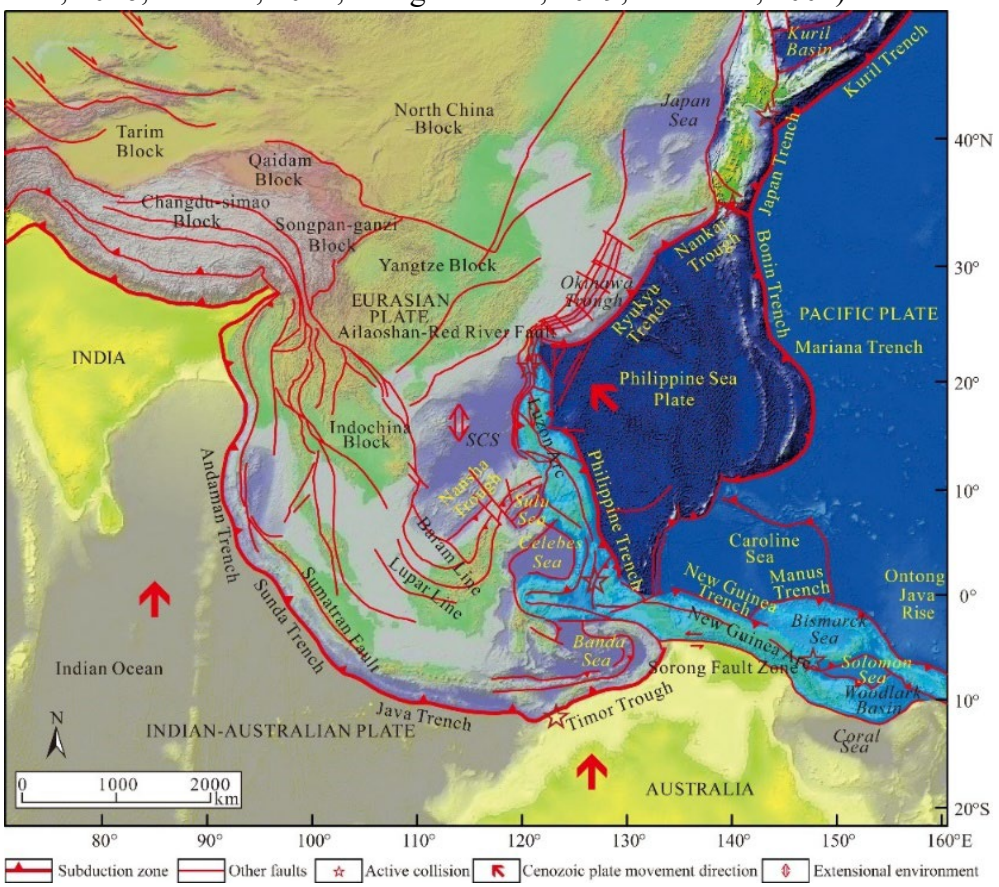

Fig. 2.2 Map showing the tectonic setting of the SCS and its surrounding areas (Li et al., 2022; Wu et al., 2016)

The southern SCS is bordered by Sumatra and Borneo to the south, the Philippine island arc to the east, and the Indochina Peninsula, Malay Peninsula to the west and South China to the north. Based on previous studies, the evolution of the SCS can be divided into the following stages (Fig. 2.3) (Li et al., 2022; Wu et al., 2016; Zhang et al., 2021), (1) The Liyue Movement (65-43 Ma) marked the beginning of tectonic activity in the SCS. Subduction rate of the Pacific plate decreased, the subduction zone retreated, and the South China continent experienced a series of rifting events, leading to the initial rifting phase and the formation of Cenozoic basin foundations. (2) The Xiwei Movement (43-30 Ma), the second tectonic event in the SCS. The Eurasian and Indian plates began to collide, some basins entered the initial rifting phase. Concurrently, the Paleo-SCS began to close, leading to the Sarawak Orogeny and the formation of the Zengmu Basin. The Liyue and Beikang basins experienced further rifting. (3) The Nanhai Movement (30-15.5 Ma) marked the third significant tectonic event. The Paleo-SCS accelerated its subduction and disappearance, while the new SCS began to expand. The central basin, southwest sub-basin and other basins opened sequentially, with intensified marine transgression accompanying the expansion. (4) From 15.5 Ma to the present, the fourth major tectonic event, the Nansha Movement, occurred. The subduction of the Paleo-SCS subducted and disappeared, and the expansion of the new SCS stopped. By the late Middle Miocene, stress reversal along regional strike-slip faults controlling the Sunda Shelf and Indochina block led some basins into a passive continental margin stage (Franke et al., 2014; Yao et al., 2004).

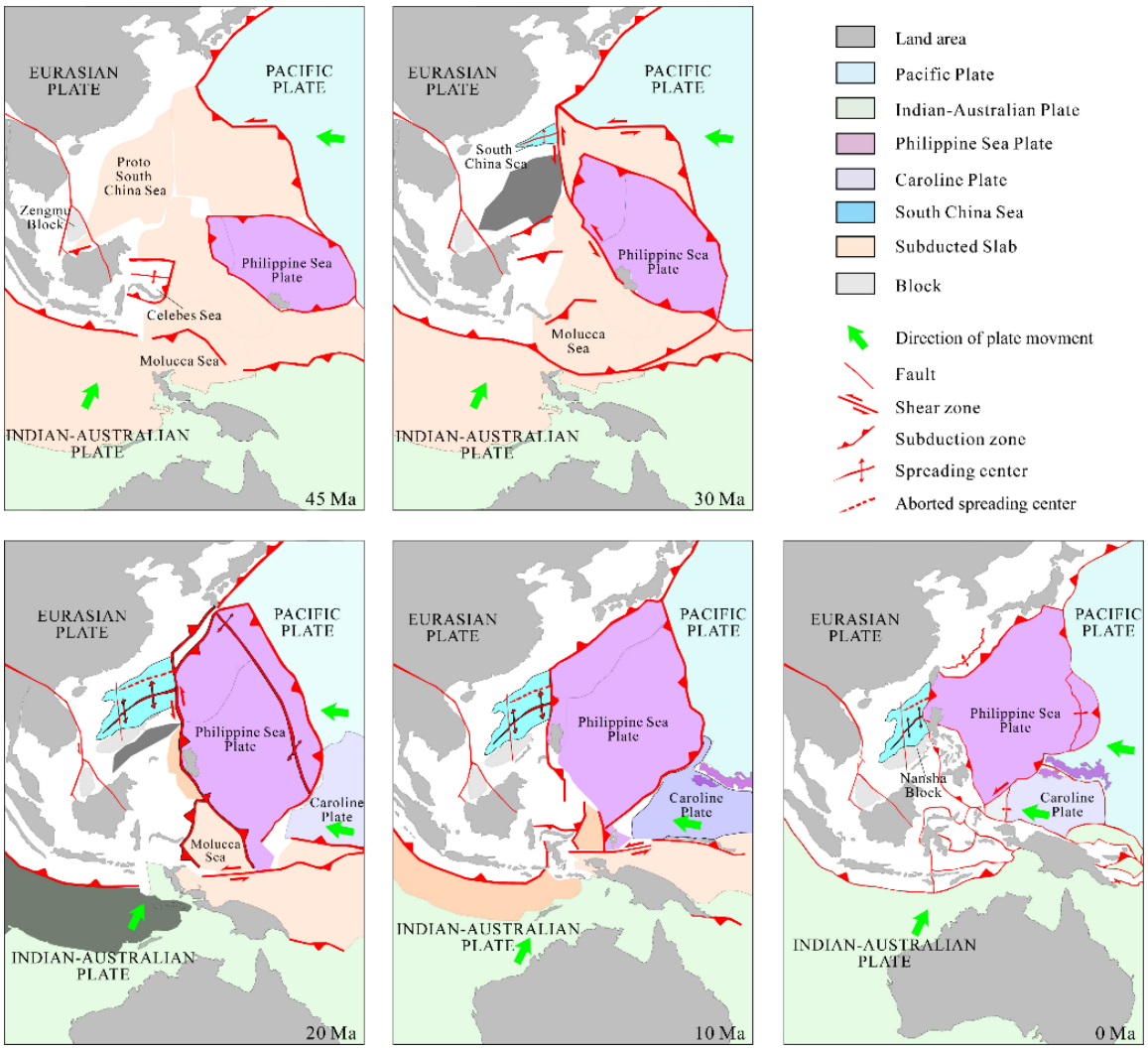

Figure2.3 Map showing the tectonic evolution of the SCS and its adjacent areas (Li et al., 2022; Wu et al., 2016)

2.2.2 Sedimentary characteristics of the southern SCS

The provenance of sediments of southern SCS are diverse and the sedimentation process is complex (Liu et al., 2016b). The sediment types mainly include terrigenous debris carried by surrounding rivers, biogenic calcareous and siliceous materials, volcanic eruption materials, minor atmospheric deposition materials and inputs from the Pacific Ocean, etc. (Fig. 2.4) (Wang et al., 2023). In addition, a three-dimensional diagram shows the main geomorphologic features of the SCS (Fig.2.5) will be helpful to explain the transportation of the submarine sediments. The southern SCS can be divided into the following sedimentary areas:

(1) Gulf of Beibuwan

Sediments carried by the Red River are the primary source of the Gulf of Beibuwan, predominantly forming a submerged delta. The sediments in this area are

generally fine-grained, mainly composed of sandy mud and mud. Muddy sediments develop in small areas on both sides of the river estuary. In shallow waters within 5 m depth, sandy deposits predominate. The delta front consists of silt deposits, silt-mud dominated most areas from the delta front to shelf (Duc et al., 2007).

(2) Offshore Indochina

Offshore Indochina mainly includes the offshore Mekong River delta and the narrow offshore shelf of Vietnam. The sedimentary environment is mainly the different scale submerged deltas. Nearshore areas close to the river mouth are dominated by gravel-bearing sediments, while most other areas are dominated by sandy materials. Grain size of sediment gradually decreases towards the southwest, with significant variations in sedimentation rates.

(3) Sunda shelf

The sediments of the Sunda Shelf are predominantly terrigenous clastic materials, with minor contributions from carbonate deposits such as corals and shells. This area can be divided into (I) gulf of Thailand, which is in the northwest of the Sunda Shelf, and it is a semi-enclosed shelf sea. The sediments in the Gulf of Thailand are generally fine-grained, with grain size ranging from 1.5 φ to 7.4 φ and an average value of 5.9 φ. The northern gulf and river estuary is mainly covered by silt, while the southern part is predominantly silt and sandy silt, and the central part is a muddy sediment zone. Qiao et al. (2015) indicates that the sediments in the Gulf of Thailand are primarily derived from rivers flowing into the sea from Thailand. The characteristics of the sediments in the central and southern parts are similar to those in the southern SCS, while the southwestern sediments are mainly sourced from coastal and island erosion.

(4) Southern and eastern Sunda shelf

The sediments near the shore are coarse while the sediments are fine away from the coast. The coastal and estuary areas on the east side of the Malay Peninsula are mainly sandy sediments. The middle of the shelf is affected by the Mekong delta resulting in sandy and silty sediments. The area of the offshore Sumatra is mainly muddy, and the content of coarse sandy sediments has decreased significantly during the Holocene.

(5) Eastern Sunda slope and deep sea

The slope is mainly covered with fine-grained sediments (Steinke et al., 2008). The western slope widely contains calcareous mud, silt, and siliceous-calcareous mud. Metal nodules are particularly abundant in these slope sediments, especially around the

Xisha Islands (Yin et al., 2019). The southern slope mainly contains calcareous mud and silt, siliceous mud, and siliceous-calcareous silt. The central basin is widely covered with siliceous clay and deep-sea clay, with minor amounts of siliceous clay, calcareous clay, and siliceous ooze and so on.

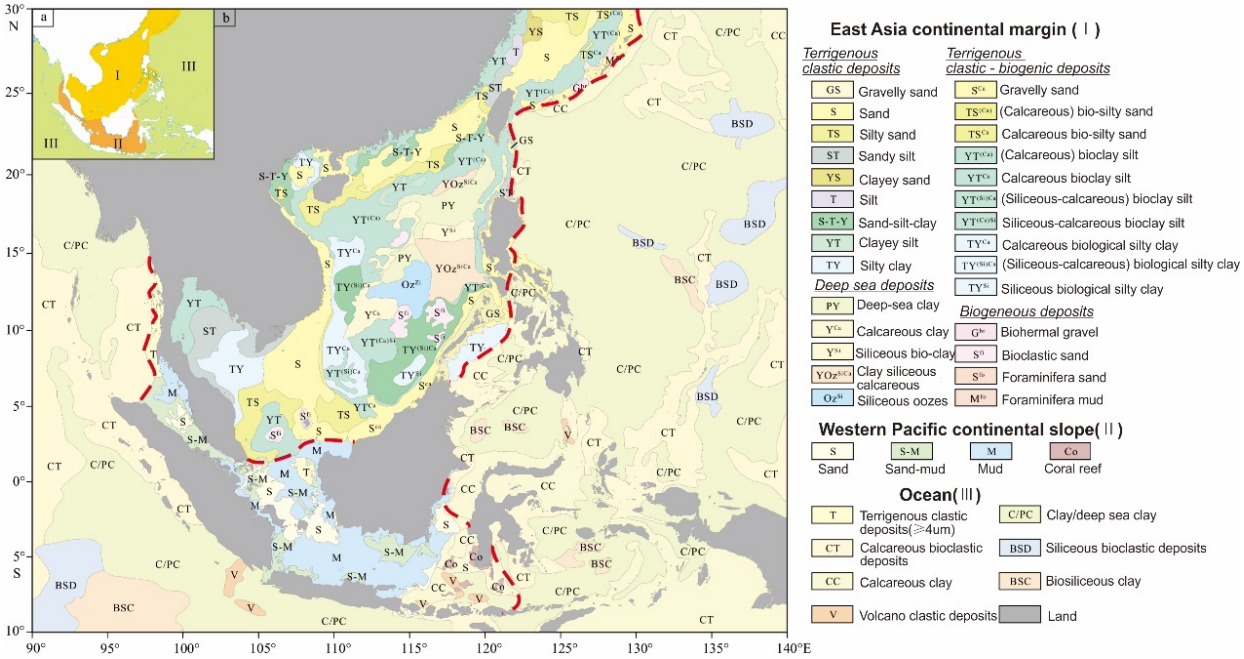

Fig. 2.4 Surface sediment type map of China-ASEAN seas and adjacent areas (a) schematic map of the sedimentary areas, (b) sediment type map (Wang et al., 2023).

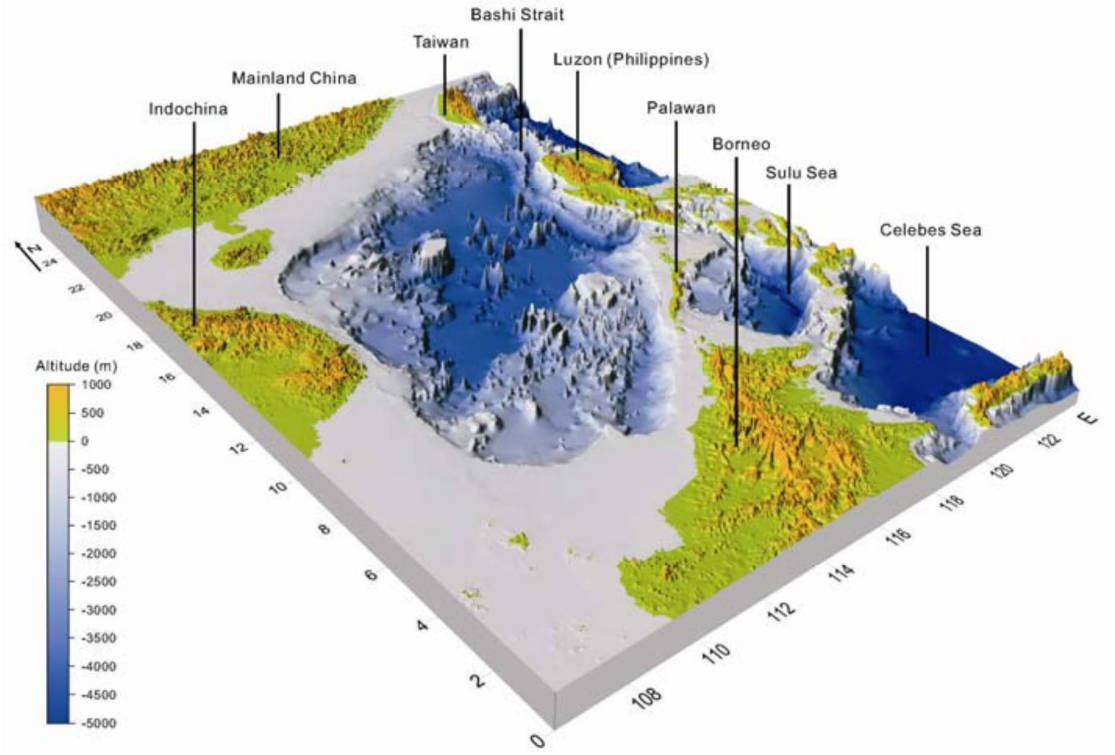

Fig. 2.5 Three-dimensional diagram shows the main geomorphologic features of the SCS (Wang and Li, 2009).

2.2.3 Lithological characteristics of the land around the SCS

The SCS and its surrounding lands have experienced stable tectonics during the Quaternary (Tjia and Liew, 1996). In the northern SCS, Indochina Peninsula predominantly features Quaternary deposits and Mesozoic sedimentary rocks. Coastal areas of Vietnam have various types of igneous rocks, including minor intrusions and extrusions. The western part of the Indochina Peninsula, near the Tibetan Plateau, contains small amounts of igneous and metamorphic rocks (Hartmann and Moosdorf, 2012) (Fig. 2.6).

The Malay Peninsula is characterized by Paleozoic to Mesozoic felsic plutonic rock, low grade metamorphic rocks, and Mesozoic sedimentary rocks, which are mainly mudstones, sandstones, and limestones (Hutchison, 1968, 2005). The northeastern part of Sumatra is mainly covered by Quaternary sediments and Paleogene to Neogene sedimentary rocks, while the southwestern part is predominantly composed of Quaternary intermediate to intermediate to mafic volcanic rocks due to continuous seismic and volcanic activity observed in the southwestern region until today (Feng et al., 2021), whereas the northeastern part is characterized by Quaternary sediments transported by rivers. Central Borneo is predominantly composed of Mesozoic sedimentary rocks, including sandstones, shales, and carbonates (Hutchison, 2005). The southwestern part of the island exposes felsic plutonic rocks, while other regions consist of Paleogene to Neogene sedimentary rocks and Quaternary sediments (Fig. 2.6).

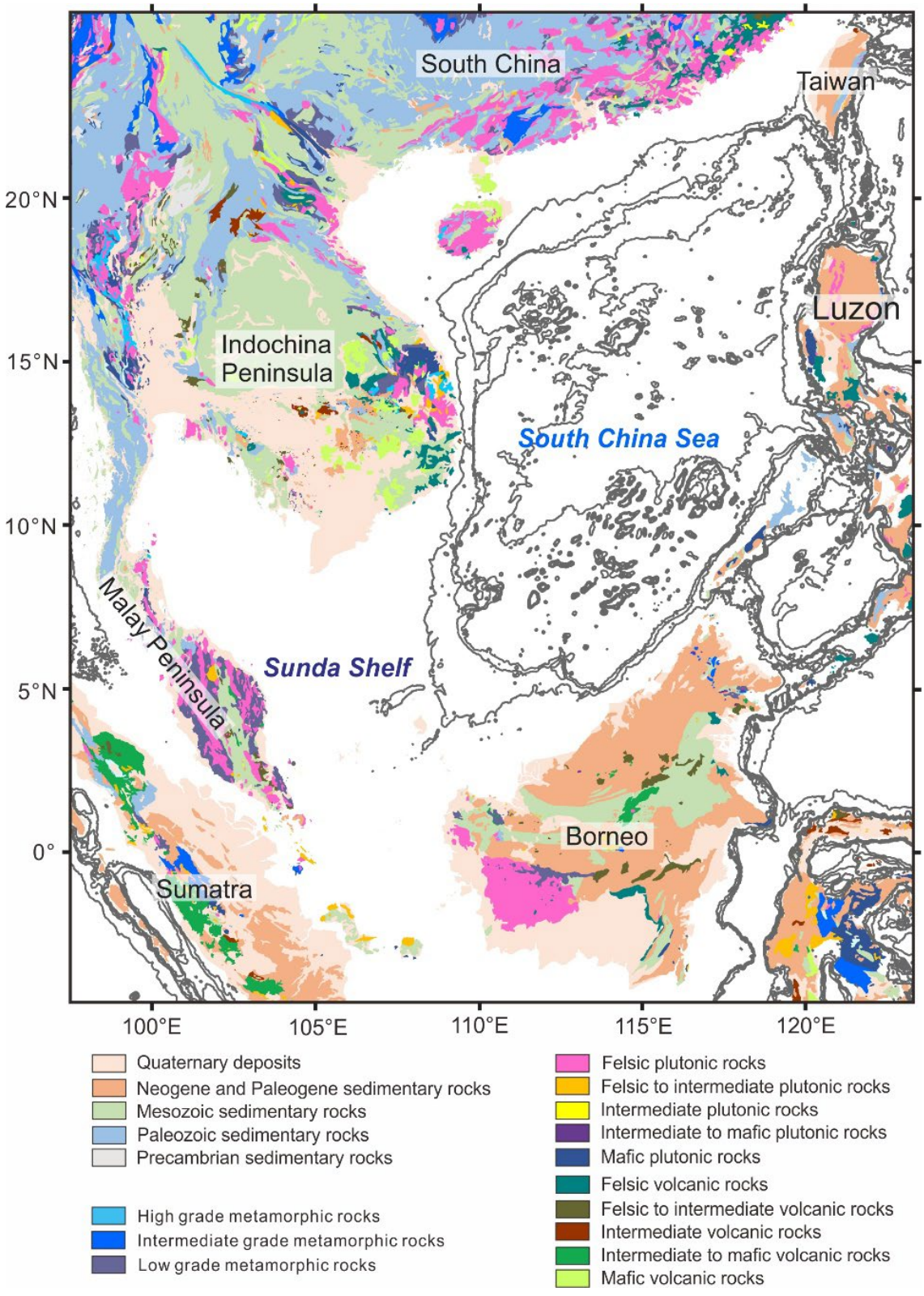

Fig. 2.6 Lithology of surrounding lands of the SCS, modified from geological database (Dürr et al., 2005; Hartmann and Moosdorf, 2012).

2.3 Surface current

The surface currents of the SCS are mainly controlled by the morphology of the semi-enclosed sea and the monsoon (Fang et al., 1998; Tangang et al., 2011). The morphology determines that the surface current can move in a circular manner. Affected by the monsoon, the surface current shows seasonal alternation (Fig. 2.1 and 2.7). During the summer, the prevailing southwest monsoon drives tropical Indian Ocean surface currents through the Malacca Strait and the Sunda Strait into the Sunda Shelf, which then flow through the Taiwan Strait and the Bashi Channel into the Pacific Ocean. In winter, driven by the northeast monsoon, colder Pacific currents flow through the Taiwan Strait and the Bashi Channel, across the Sunda Shelf, and exit through the Malacca Strait and the Sunda Strait into the Indian Ocean. The western boundary current is one of the most important surface currents in the SCS. In winter, a southward current flows along the western land boundary. In summer, a northward current flows along the western boundary of the southern SCS, turning eastward near the Vietnamese coast at around 12°N, which divides the summer currents into two systems: a cyclonic system in the north and an anticyclonic system in the south (Liu et al., 2016b; Wang et al., 2006) (Fig. 2.7).

Locally, in winter, the southern SCS is controlled by a cyclonic circulation and extends to the Sunda Shelf (Fang et al., 1998). A weak anticyclonic circulation may exist in the Palawan Trough area of the southeastern main current circulation. In summer, the southern SCS is occupied by the reversed anticyclonic circulation, and there is a weak local cyclonic circulation in the southwest of Palawan (Fig. 2.7).

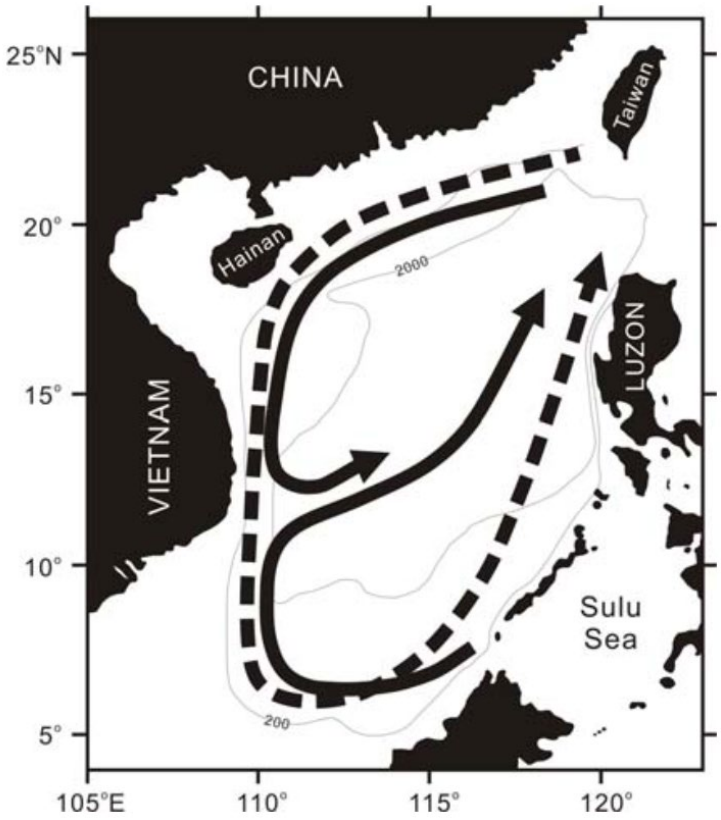

Fig. 2.7 Schematic diagram of the main surface currents in the SCS (solid lines are summer surface currents, and dotted lines are winter surface currents) (according to Fang et al., 1998).

2.4 Climate of the SCS

The SCS is located at southeastern Asia, the climate is controlled by the monsoon. In summer, a low-pressure system develops over the Asian continent due to land warming, leading to the flow of mild southwest winds across the SCS. In winter, a high-pressure system developed over the Asian continent due to land cooling, with northeast winds passing across the South China Sea (Fig. 2.1). Because the intertropical convergence zone (ITCZ) moves through the season changes (Fig. 2.8), precipitation in the southern and northern SCS shows opposite trends (Ayliffe et al., 2013; Wang et al., 2003). In the north, the average annual precipitation in South China and Indochina Peninsula is 1700-2000 mm, of which nearly 85-90% occurs in the summer monsoon season from May to September. In the south, the average annual precipitation in the Malay Peninsula, Sumatra, Borneo and other islands is 2500–3000 mm, with relatively uniform precipitation throughout the year. In the wet season (November to February of the following year), the precipitation increases by about 20% when the winter monsoon affects the region (Fig. 2.9). Since the SCS is located in the middle and low latitudes,

the temperature changes follow the latitude zonality, that is, the lower the latitude, the higher the temperature (Fig. 2.10). In subtropical areas such as the South China and the Indochina Peninsula, the temperature changes significantly with the seasons, with the highest average temperature in summer (July-August), about 20 ℃, and the lowest average temperature in winter (December-January), about 10 ℃. In tropical areas, such as the Malay Peninsula, Sumatra, Borneo and other southern lands, the annual average temperature is 27 ℃, the seasonal difference in Kuantan (Malay Peninsula) is less than 2.5 ℃, and the seasonal difference in Bandar Seri Begawan (Borneo) and Palembang (Sumatra) is less than 1.1 ℃, so there are no significant seasonal changes in the temperature of the southern SCS. In the central part of the SCS between the subtropical and tropical regions, such as Luzon Island and southern Indochina, the annual average temperature is stable at around 28 °C, with a seasonal temperature difference of about 5 °C in Manila (Luzon Island) and about 4 °C in Ho Chi Minh City (southern Indochina) (temperature and precipitation data from http://www.worldweather.org).

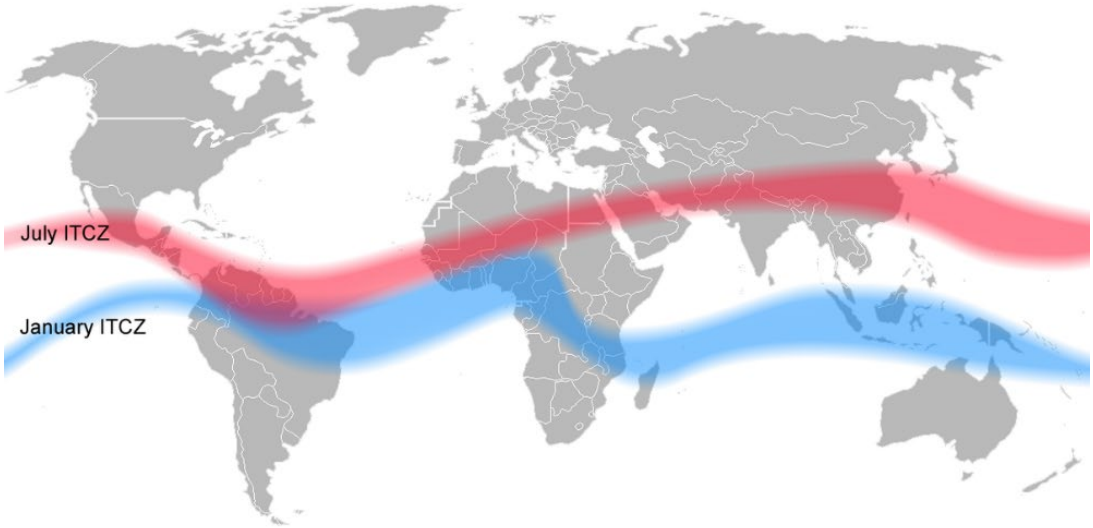

Fig. 2.8 Position of the intertropical convergence zone in January (in blue) and in July (in red). Source: Wikicommons. Author Mats Halldin, 13 Dec 2006.

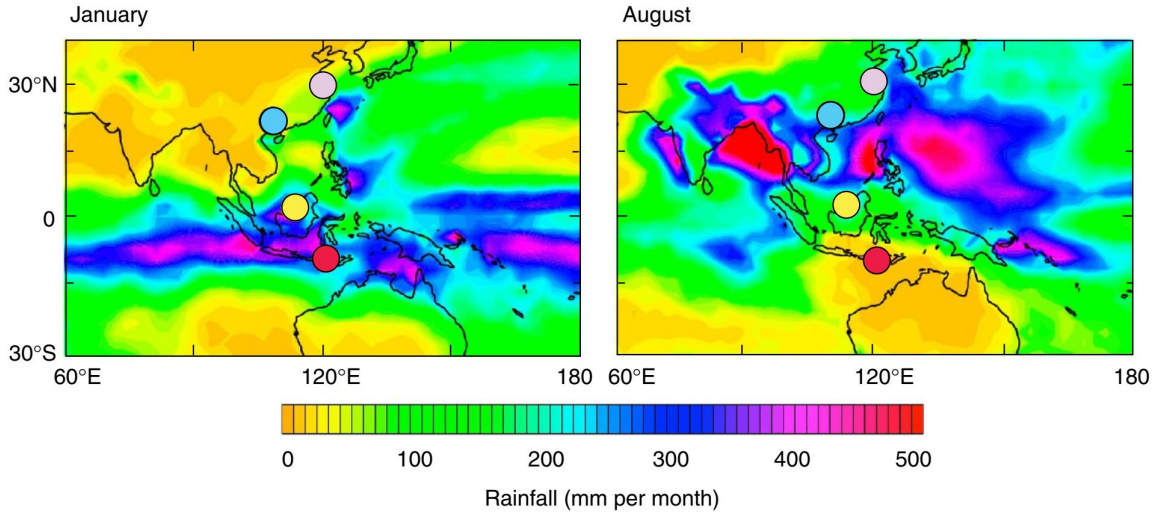

Fig.2.9 Mean precipitation in January and August in the South China Sea and surrounding areas (1979-1991, colored circles indicate sampling location for $\delta^{18}O$ isotope testing of stalagmites in different caves) (Ayliffe et al., 2013).

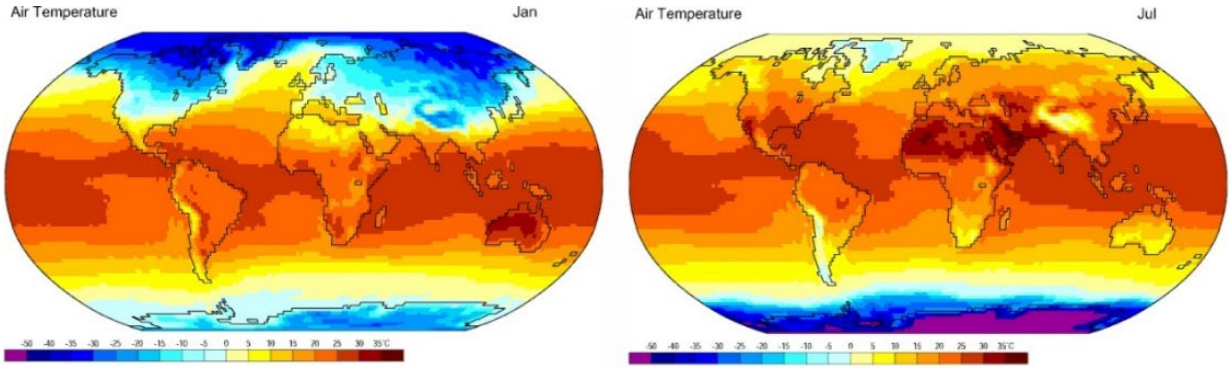

Fig. 2.10 Mean air temperature in January and July of the Earth's surface (1959-1997, Source of Original Modified Image: Climate Lab Section of the Environmental Change Research Group, Department of Geography, University of Oregon).

Chapter 3 Samples and methods

3.1 Introduction of samples

According to the object of this study, three major types of sediments were collected as research samples: (1) river sediments from the lands surrounding the southern SCS, (2) Sea floor sediments from the SCS, and (3) core ST13 sediments located at the middle of the Sunda Shelf and core 18288-2 sediments located at the eastern slope (Fig. 3.1).

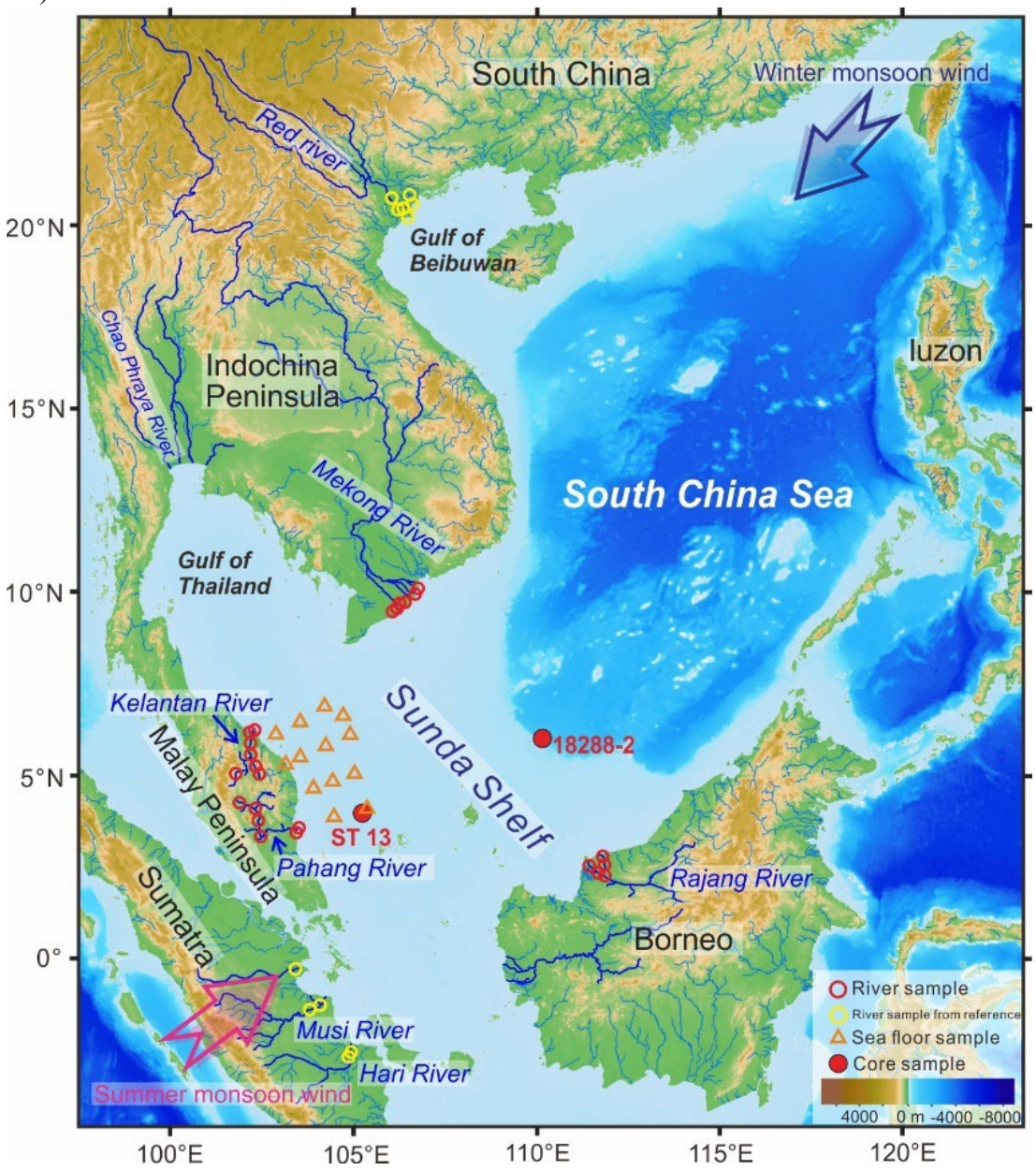

Fig. 3.1 Location of various types of samples collected in this study

3.1.1 River sediments and sea floor sediments

The river sediments mainly collected from Mekong River estuary in the Indochina Peninsula (number, N=7), the Kelantan River (N=7) and the Pahang River (N=7) in the Malay Peninsula, the Rajang River (N=5) in Borneo, and the published data of the Red River and Sumatra River (Duan et al., 2023; Liu et al., 2012; Wu et al., 2023) (Fig. 3.1). The Mekong River samples were collected in January 2005, the Kelantan River and the Pahang River samples were collected in August 2018, and the Rajang River samples were collected in February 2016. The river sediments are mainly composed of silt and mud. They were collected at locations where the river channel or floodplain is undisturbed and no significant human activity interference, and stored in a constant temperature environment of 4℃ in polyethylene sealed bags.

The 13 sediment samples of the Sunda shelf are mainly located in the western shelf and near shore Malay peninsula (Fig. 3.1), which were collected in the R/V Discovery Cruise of Tongji University and University of Terengganu, Malaysia in August 2018. The water depth of the sample collection area is about 60 m. The sample was mainly collected using a box grab sampler. The surface sediments of 0-10 cm are collected and stored in polyethylene sealed bags. The lithology of the samples ranges from coarse sand to mud, and some samples contain obvious marine biological debris such as shells. Other marine sediments elements and Sr-Nd isotope data were collected from published studies (Li et al., 2003; Liu et al., 2016; Wei et al., 2012).

3.1.2 Introduction and chronological framework of core ST13 of the shelf

The core ST13 (04°29.99′ N, 105°15.06′ N) is located in the middle of the Sunda Shelf (Fig. 3.1), with a water depth of 79 m and a length of 1.51 m (Fig. 3.3). It was collected by a gravity sampler during the R/V Discovery Cruise of Tongji University and University of Terengganu, Malaysia in August 2018. The core is mainly composed of brown muddy sediments. The moisture content increases from 15 cm to the top of the core, and obvious disturbances can be seen. There are varying amounts of white shells and other biological debris randomly distributed in the sediments. The samples were divided at a resolution of 1 cm and stored in a constant temperature environment of 4°C in polyethylene sealed bags.

The chronological framework of core ST13 is constrained by sediment ^{210}Pb and biological shell AMS^{14}C data. Nine samples were selected for AMS^{14}C dating. Complete planktonic foraminifera *G. ruber* (*Globianerinoides ruber*) and *G. sacculifer*

(*Globigerinoides sacculifer*) were selected. Each dating sample selected 600-800 shells or greater than or equal to 8 mg. The AMS^{14}C analysis was performed by Beta Laboratory in the United States (Table 3.1). The data were corrected to the local carbon reservoir age (-15±38) (Southon et al., 2002) using the Marine 20 dataset in Calib Rev 8.1.0 software (Heaton et al., 2020), and then the chronological framework was established using linear interpolation and extrapolation. From Table 3.1, the Calendar age of samples at 0-1cm is larger than the age of samples at 19-21cm. According to core analysis, the sediments at 0-15 cm from the top of the core were significantly disturbed and contained shells. There are two possible reasons for this disturbance: (1) The normal bioturbation by benthic organisms, might cause the mixing of materials deposited at different times. (2) Since the core was collected by gravity sampler, when the sampling tube came into contact with the seafloor sediments under the gravity, the huge impact force would cause local disturbance to the shallow seafloor sediments. This phenomenon is common in the process of marine drilling sampling. For long cores, the sediments at the top of the cores of about 30 cm are generally discarded to avoid this human impact. Therefore, eleven sediments were selected at 0-50 cm from the top of the core for ^{210}Pb testing. As can be seen from Fig. 3.2, the $^{210}Pb_{ex}$ content is very low, especially the 7th sample (22 cm) is less than 1 dpm/g, almost decaying completely, which means the age should be greater than 100 yr. There is an overall decay trend, but the segmentation is not obvious. The $^{210}Pb_{ex}$ values from the 1st sample to the 7th sample (0-22 cm) fluctuate greatly, and there is no decreasing law, indicating that this section is consistent with the analysis that the sediments are disturbed. Combining the AMS^{14}C and ^{210}Pb dating data, the ST13 core research started from 19 cm from the top, with a calendar age of 159±91 yr, and an age of 8286.5±84.5 yr at the bottom of the core, with an average sedimentation rate of about 20 cm/kyr (Fig. 3.3).

Table 3.1 AMS^{14}C data for chronology in core ST13

No.	Depth (cm)	Dating materials	Conventional AMS^{14}C age (yr BP)	Calendar age (cal yr BP)	1σ (yr)	sedimentation rate (cm/kyr)
4	0-1	*G.ruber+G.sacculifer*	2620 ± 30	2393.5	105.5	—
5	19-21	*G.ruber+G.sacculifer*	500 ± 30	159	91	—
6	42-43	*G.ruber+G.sacculifer*	3180 ± 30	3058	108	7.9
7	72-73	*G.ruber+G.sacculifer*	4110 ± 30	4247.5	110.5	25.2
8	105-107	*G.ruber+G.sacculifer*	6650 ± 30	7164	96	11.3
9	148-151	*G.ruber+G.sacculifer*	7800 ± 30	8286.5	84.5	39.2

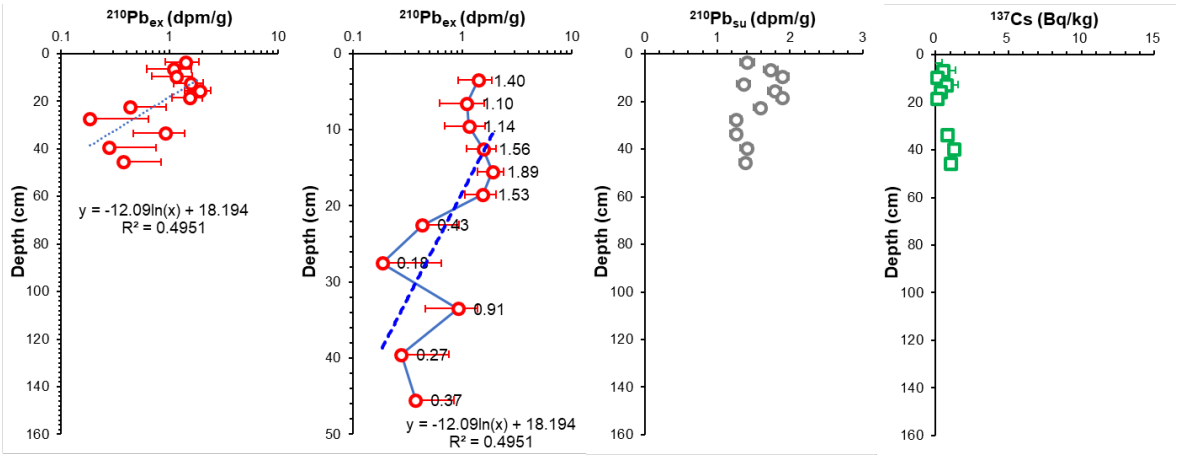

Fig. 3.2 ^{210}Pb dating characteristics of the 0-50 cm section of core ST13

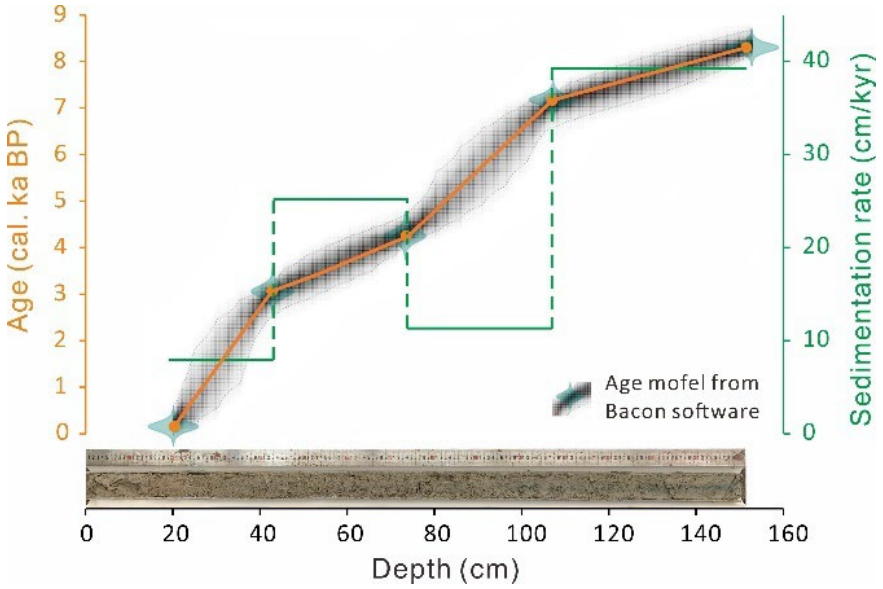

Fig. 3.3 Lithological characteristics and chronological model of core ST13

3.1.3 Introduction and chronological framework of core 18288 of the slope

Core 18288-2 (5°44.388′ N, 110°44.324′ E) is located in the eastern slope of the Sunda shelf, southern SCS. The water depth is 788 m and the core length is 6.8 m (Fig. 3.4). The core was collected by gravity sampler during the German SONNE 115 SUNDAFLUT cruise from December 1996 to January 1997 (Stattegger et al., 1997). The lithology of the core is mainly olive gray, dark green silty clay and clay. Black organic matter strips can be seen at the bottom 1 m. Continuous deposition from bottom to top, no obvious sedimentary discontinuity is observed. The sampling interval is 10 cm, and a total of 69 samples were obtained, which were stored in a constant temperature environment of 4℃ in polyethylene sealed bags. The data were corrected to the local carbon reservoir age (-15±38) (Southon et al., 2002) using the Marine 20

dataset in Calib Rev 8.1.0 software (Heaton et al., 2020), and then the chronological framework was established using linear interpolation and extrapolation.

The chronological framework of core 18288-2 is established by foraminifer AMS^{14}C dating. Eight samples were selected for AMS^{14}C dating. Complete planktonic foraminifera *G. ruber* (*Globianerinoides ruber*) and *G. sacculifer* (*Globigerinoides sacculifer*) were selected. Each dating sample selected 600-800 shells or greater than or equal to 8 mg, The AMS^{14}C analysis was performed by Beta Laboratory in the United States (Table 3.2). Since there were not enough planktonic foraminifera from the sediments at the bottom of the core for AMS^{14}C analysis, other cores with similar ages adjacent to 18288-2 were selected for comparison (Fig. 3.4A). As can be seen from Fig. 3.4A, the cores located in the eastern slope of the Sunda Shelf all show an increase in sedimentation rate after 15 ka. The AMS^{14}C dating data of the 18288-2 core were compared with core 18287-3 (Fig. 3.4B) and analyzed with the results of the simulation of the Calib Rev 7.0.4 software. The comprehensive analysis indicates that the bottom age of the core 18288-2 was about 18.5 ka BP. The age analysis results of all samples did not show a reversal phenomenon, indicating that the core sediments were not affected by the later dynamic transformation and had a complete and continuous sedimentation record. The sedimentation rate of 2-7 m is about 50-70 cm/kyr, which is 3-4 times that of the upper part of the core, indicating that the sedimentation rate in the study area during the deglaciation period is much higher than that in the Holocene (Table 3.2, Fig. 3.4).

Table 3.2 AMS^{14}C data for chronology in core 18288-2

No.	Depth (cm)	Dating materials	Conventional AMS^{14}C age (yr BP)	Calendar age (cal yr BP)	sedimentation rate (cm/kyr)
1	0-1	*G.ruber+G.sacculifer*	220 ± 30	18(-64-120)	—
2	55-56	*G.ruber+G.sacculifer*	3410 ± 30	3215(2911-3485)	17.2
3	125-126	*G.ruber+G.sacculifer*	6260 ± 30	6614 (6324-6922)	20.6
4	175-176	*G.ruber+G.sacculifer*	8540 ± 30	9072(8731-9336)	20.3
5	225-226	*G.ruber+G.sacculifer*	10080 ± 30	10974(10302-11247)	26.3
6	375-376	*G.ruber+G.sacculifer*	12740 ± 30	13817(13099-14455)	52.8
7	505-506	*G.ruber+G.sacculifer*	13270 ± 30	15608(15185-16659)	72.6
8	625-626	*G.ruber+G.sacculifer*	Too few samples to get result		

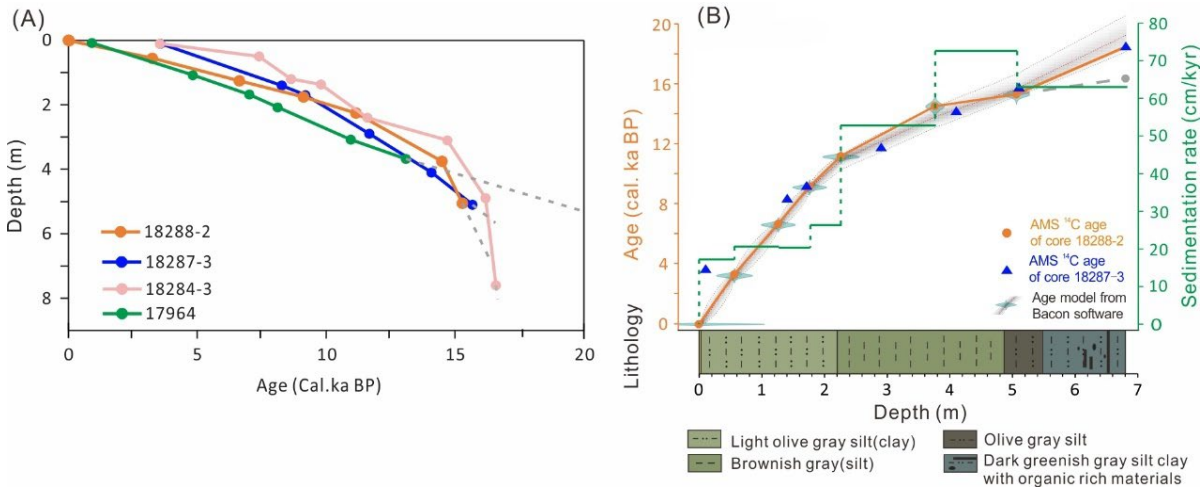

Fig. 3.4 (A) Comparison of the chronological model of core 18288-2 and other surrounding boreholes. (B) Lithological characteristics and chronological model of core 18288-2

3.2 Methods

The scientific question of this study focusses on provenance conversion and weathering history, the bulk and less than 50 μm components of river, sea floor and core sediments were selected for measurements. Carbonate content, major, trace element and Sr-Nd isotope analyse of bulk sediments were completed at the Centre de Recherches Pétrographiques et Géochimiques, France (CRPG-CNRS-UL) (December 2021 to February 2024). Grain size, major, trace element and Sr-Nd-U isotope analysis of less than 50 μm components were carried out at the State Key Laboratory of Marine Geology, Tongji University, China (September 2020 to November 2021).

3.2.1 Experiments of bulk sediments

3.2.1.1 Chemical pretreatment

The samples were uniformly selected and grounded to less than 200 mesh using an agate grinder. The chemical pretreatment of bulk sediments mainly includes two steps.

(1) Removal of exchangeable components (salts, etc.). Take about 1g sample and place it in a 50 mL centrifuge tube, add 30-35 mL Milli-Q water, shake for 5 minutes, let stand for 6 hours, centrifuge and discard the supernatant, repeat 3-4 times.

(2) Removal carbonate components. Add 30-35 mL 20% (v/v) acetic acid, shake at room temperature, let stand for at least 30 minutes until there are no obvious bubbles, centrifuge and discard the supernatant, repeat this step twice. Then add 30-35 mL Milli-Q water, shake and centrifuge, discard the supernatant,

repeat this step until the supernatant is neutral. Use a freeze dryer to freeze the sample, take an appropriate amount and add anhydrous phosphoric acid to test the $CaCO_3$ content using a mass spectrometer. If the $CaCO_3$ wt% is less than 0.1%, it means that the treatment process meets the experimental requirements. Otherwise, repeat the step of removing carbonate components until the $CaCO_3$ wt% is less than 0.1%.

3.2.1.2 Carbonate stable isotope analysis

The bulk sediment was ground to less than 200 mesh using an agate mortar. An appropriate amount of the sample was weighed and placed in a 10 mL headspace tube. Helium (He, purity 99.999%) was introduced to drive out the air in the tube. 0.1-0.2 mL of anhydrous phosphoric acid (H_3PO_4, purity 100%) was injected and allowed to react in Gas Bench II at 70°C for at least 24 hours. The generated CO_2 was extracted by an automatic sampler and entered into a gas chromatographic separation and then passed into a stable isotope mass spectrometer (Thermo Fisher MAT 253) to obtain its oxygen isotope and carbon isotope composition relative to the standard gas. "Thonon" and "Contrex" and synthetic calcium carbonate (Merck) were used as internal calibration and QC standards and calibrated according to international standards. The measured values were calibrated to the V-PDB standard, and the accuracy was always better than 0.5‰ (e.g. Emberson et al., 2018).

3.2.1.3 Digestion and element analysis

An appropriate number of samples was taken and put it into a platinum (Pt) crucible, and then put it into a muffle furnace and burn it at 600℃ for more than 12 hours to further remove the residual organic matter after chemical leaching. Studies have shown that excessive low-concentration H_2O_2 can effectively remove organic matter bonded between particles by fully reacting with sediments, but it cannot remove organic molecular fragments between mineral layers (Cai et al., 2007). For example, organic matter in smectite crystals can only be completely decomposed at a high temperature greater than 350℃ (Cai et al., 2007). During the process, the sediment needs to be accurately weighed before and after burning to calculate the loss on ignition (LOI) of the sediment.

Lithium metaborate ($LiBO_2$) alkali melting method is used for sediment digestion. Take an appropriate amount of sediment and place it in a graphite crucible, add $LiBO_2$ and mix evenly, put the crucible into a 1000℃ high-temperature furnace to melt for 15 minutes, then take out the crucible and pour the melt into a large beaker of 5% HNO_3,

immediately place the beaker on a vibrating table or ultrasonic machine to dissolve the melt into the acid, then transfer it to a constant volume bottle, dilute it with 5% HNO_3, and wait for testing. Prepare different types of standard samples and blank samples in the same way as the samples.

The major elements are analyzed by Inductively Coupled Plasma Optical Emission Spectroscopy (ICP-OES), and the trace elements are analyzed by Inductively Coupled Plasma Mass Spectrometry (ICP-MS). The long-term analytical accuracy of the CRPG laboratory is better than the analytical accuracy of 5%.

3.2.1.4 Analysis of Sr and Nd isotopes

The digestion process of isotope analysis is different from that of elemental analysis. Weigh about 50 mg samples and put them into the PFA beaker, add 1.5 mL of concentrated pure HNO_3 and concentrated pure HF in turn, cover the lid tightly, ultrasonicate for 1 hour, and heat on a hot plate at 120℃ for more than 72 hours. Evaporate on a hot plate at 80℃, add 3 ml of 6N HCl, cover the lid tightly, ultrasonicate for 1 hour, and heat on a hot plate at 120℃ for more than 48 hours, and evaporate on a hot plate at 80℃.

Sr element purification mainly uses Sr specific resin, and the specific purification steps are as follows:

(1) Use 6 N HCl and 0.05 N HNO_3 to wash and activate Sr specific resin, and then use 2 N HNO_3 to balance the resin. Add an appropriate amount of sediment sample dissolved in 2 N HNO_3.
(2) Use 2 N HNO_3, 7 N HNO_3 and 3 N HNO_3 to remove non-target element impurities.
(3) Use 0.05 N HNO_3 to elute the Sr specific resin to obtain the Sr isotope test solution, store it in a PFA beaker, and evaporate it for testing.

Nd element purification is divided into two steps, using Tru resin and Ln resin for purification respectively. The specific steps are as follows:

(1) Use 1 N HCl+0.5 N HF, 2N HNO_3 and Milli-Q ultrapure water to wash and activate Tru resin, and then use 2 N HNO_3 to balance the resin. Add an appropriate amount of sediment sample dissolved in 2 N HNO_3.
(2) Use 2 N HNO_3 to remove impurities other than non-target elements.
(3) Place the Tur resin column on the primary Ln resin column and add Milli-Q ultrapure water to remove impurities other than non-target elements.
(4) Add 6 N HCl to the primary Ln resin column, elute the obtained REEs

solution, store it in a PFA beaker, and evaporate it.

(5) Dissolve the REEs sample in 0.27 N HCl for later use.

(6) Use 0.27 N HCl to wash, activate, and balance the secondary Ln resin column, and add an appropriate amount of sample dissolved in 0.27 N HCl.

(7) Use 0.27 N HCl to elute the secondary Ln resin column to obtain the Nd isotope test solution, store it in a PFA beaker, and evaporate it for testing.

Sr isotopes were measured by Triton PlusTM thermal ionization mass spectrometer. The $^{87}Sr/^{86}Sr$ test value was corrected with $^{86}Sr/^{88}Sr$ =0.1194, and the measurement process was monitored using NBS987 standard solution (recommended value 0.710248 ± 0.000020). The average test value of NBS987 in this experiment was 0.710234 ± 18 (n=102). Nd isotopes were measured using NEPTUNE Plus MC-ICP-MS (multi-acceptor inductively coupled plasma mass spectrometer, Thermo Fisher Scientific). The $^{143}Nd/^{144}Nd$ value was calibrated using $^{146}Nd/^{144}Nd$ = 0.7219 (Wasserburg et al., 1981). JNdi-1 standard was used to monitoring data (recommended value 0.512114 ± 0.000010) (Tanaka et al., 2000). The average test value of JNdi-1 was 0.512115 ± 12 (n=68), which met the test requirements for Nd isotopes. The test results of Nd isotopes are given in the form of εNd, $\varepsilon Nd = [(^{143}Nd/^{144}Nd_{sample}/(^{143}Nd/^{144}Nd)_{CHUR})-1] \times 10^4$, where the $^{143}Nd/^{144}Nd$ value of CHUR is 0.512638 (Jacobsen and Wasserburg, 1980).

3.2.2 Experiments of less than 50 μm components

3.2.2.1 Grain size analysis

First, the wet sieving method was used to extract the 50 μm components from the bulk sediments. The bulk sediments were placed in a 50 μm electroforming sieve, and a large amount of Milli-Q ultrapure water was added to rinse until there were no particles in the outflowing water. The sediment smaller than 50 μm received by the crucible was placed in an oven and dried at 40°C for storage.

Before grain size analysis, it is necessary to remove the organic matter and carbonate components in the sediment. The first step is to remove organic matter. Put some samples in a 50 mL tube. Add 10 ml of 30% H_2O_2, shake it slightly, and place it in a water bath heater at 60°C for 6 hours until no obvious bubbles are generated in the tube. Pour out the supernatant, add 30 mL Milli-Q ultrapure water and centrifuge it. Repeat this step until the supernatant is neutral. The second step is to remove the carbonate component. Add 30 mL of 0.5% HCl to the tube, shake it, and place it in a water bath heater at 60°C for 6 hours. When no obvious bubbles are generated in the

centrifuge tube, pour out the supernatant, add 30 mL of Milli-Q ultrapure water and centrifuge it. Repeat this step until the supernatant is neutral. Before testing, add 10-15mL of Milli-Q ultrapure water to the centrifuge tube, shake it thoroughly to disperse the sediment completely, and add 5mL of 10% sodium hexametaphosphate $(NaPO_3)_6$ dispersant to fully disperse the particles. The Mastersizer 2000 automatic laser grain size analyzer is used for grain size testing, with the opacity (concentration) controlled at 8-12%, the grain size test range of 0.02-2000 microns, the analysis accuracy better than 1%, and the repeated measurement error less than 2%.

3.2.1.2 Chemical pretreatment

Whether river or marine sediments, they are composed of terrigenous debris components, authigenic carbonate components, authigenic oxide components, and organic matter. This study mainly focuses on the geological information preserved in the terrigenous debris components, so it is necessary to remove the authigenic components such as carbonates and oxides formed during the erosion, transportation and deposition of sediments. The chemical pretreatment method mainly refers to the experimental steps proposed by (Francke et al., 2018; Martin et al., 2015), which mainly includes four steps (Table 3.3):

(1) Removal of water-soluble components (e.g. salt, etc.). Take about 1 g sample in a 50 mL tube, add 30 mL Milli-Q ultrapure water, shake for 5 minutes, let stand for 20 minutes, centrifuge and pour off the supernatant, and repeat 3 times.

(2) Removal of acid-soluble components (e.g. carbonates, etc.). Add 10 mL 1M NaOAc/AcOH (pH=5), ultrasonicate at room temperature for 5 min, and repeat 3 times. After the reaction is completed, centrifuge and transfer the supernatant to a pre-weighed solution bottle. After centrifugation, add about 30 mL of Milli-Q ultrapure water and centrifuge again until the clear solution is neutral.

(3) Remove reducible components (e.g. Fe-Mn oxides, etc.). Add 20 mL of 0.1M $NH_2OH{\cdot}HCL$/AcOH (pH=2), ultrasonicate at 80℃ for 6 min twice, and shake by hand each time. After the reaction is completed, centrifuge and transfer the supernatant to a pre-weighed solution bottle. After centrifugation, add about 30 ml of Milli-Q ultrapure water and centrifuge again until the clear solution is neutral.

(4) Remove oxidizable components. Add 10 ml of 15% H_2O_2 and 3 mL of 0.02 M HNO_3 (pH=2) and ultrasonicate at 80℃ for 3 min, repeat 5 times. Shake by hand each time until the sample stops bubbling. After the reaction is completed,

centrifuge, add about 20 mL of Milli-Q ultrapure water and centrifuge again until the supernatant is neutral. Add 5 mL of 3.2M NH_4OAc of 20% v/v HNO_3 to the tube, and manually shake for 1 min at room temperature. After the reaction is completed, centrifuge, add about 20 mL of Milli-Q ultrapure water and centrifuge again until the supernatant is neutral. After all operations are completed, centrifuge and pour off the supernatant, dry at 40°C for use.

Table 3.3 Sequence chemical leaching (sediment < 50 μm) (modified after Francke et al., 2018; Martin et al., 2015)

Target fraction	Reagent	Conditions
water-soluble (NaCl)	200mL Milli-Q H_2O	1 day static settlement
acid-soluble (carbonate)	10 ml 1 M CH_3COONa at ~pH = 5, adjusted with CH_3COOH	3×5 min at room temperature in ultrasonic bath
Reducible (Fe-Mn oxyhydroxides)	10 mL 0.1 M NH_2OH•Hcl at ~pH = 5, adjusted with CH_3COOH	2×6 min at 80 ℃ in ultrasonic bath
Oxidizable (organic matter)	10 mL 15 % H_2O_2 and 3 mL of 0.02 M HNO_3 at ~pH = 2	5×3 min at 80 ℃ in ultrasonic bath
	5mL 3.2 M CH_3COONH_4, adjusted with CH_3COOH	manually agitated for 1 min at room temperatures

3.2.1.3 Digestion and element analysis

Weigh 100 mg sample after burning and put it into a Teflon digestion tank, add 1.5 mL of secondary distilled pure HNO_3 and pure HF in turn, put the Teflon crucible into a steel sleeve, tighten and put it at oven set190 ± 5℃ for more than 72h. After cooling, take out the Teflon crucible, open the lid and place it on a hot plate (115℃) to evaporate to dryness, add 2 mL of secondary distilled pure HNO_3, and evaporate to dryness again. Add 4 mL 30% HNO_3 to the beaker, put the Teflon crucible into a steel sleeve again, tighten and put it in an oven set 190 ± 5℃ for 12h. After cooling, transfer the solution into a 15 ml PFA beaker and check whether the solution has been clarified. If the solution is clear and does not contain any precipitation, it indicates that the sample has been completely digested and evaporate to dryness. Add 2mL of 30% v/v HNO_3 into the hot plate at 80℃ and heat for 2h to completely dissolve the sample. The sample was diluted 2000 times for testing elements. A 15 mL centrifuge tube was taken, 100 μL of sample was added, 2% v/v HNO_3 was added to 10 mL using a wash bottle, and the weight was recorded to test the element. The remaining sample was stored in a PFA

beaker and evaporate it.

Trace elements were analyzed using the Agilent 7900 Inductively Coupled Plasma Mass Spectrometer (ICP-MS) produced by Agilent, USA. The long-term analysis accuracy was better than the analysis accuracy was better than 5%, and the analysis error was less than 10%. The major elements were analyzed by IRIS Advantage Inductively Coupled Atomic Emission Spectrometer (ICP-AES) produced by Thermo, USA. The test accuracy was better than 5%, and the analysis error was less than 10%. During the rest process, blank samples and rock and sediment standards of different series (GSD-9, BHVO-2, BCR-2) were treated with same methods for data monitoring.

3.2.1.4 Analysis of Sr, Nd and U isotopes

In order to save samples and improve work efficiency, this study used the Sr-Nd-U joint separation and purification method. The three resins were connected in series, and the resins were balanced with the same medium acid to add the sample. Then the resins were separated and the three resins were eluted with a specific type and concentration of acid to purify the three elements Sr, Nd and U respectively (Luo et al., 2022). The specific steps are as follows:

(1) Use 3N HNO_3, 3N HCl and 1M HCl to wash and activate the UTEVA specific resin column (purify U), use 3N HNO_3 and Milli-Q ultrapure water to wash and activate the Sr specific resin column (purify Sr), and use 6N HCl to wash and activate the AG50W-X8 resin column (purify REEs).

(2) After washing and activation, combine the UTEVA specific resin column, Sr specfic resin column and AG50W-X8 resin column from top to bottom, add 3M HNO_3 to balance the resin, then add an appropriate amount of sample, and continue to add 3N HNO_3 to clean impurities.

(3) Then separate the three columns in turn, and continue to use different concentrations acid to remove non-target element impurities. The UTEVA specific resin column was eluted with 1 N HCl to obtain the U isotope solution, the Sr specific resin was eluted with Milli-Q ultrapure water to obtain the Sr isotope solution, and the cationic resin was eluted with 6 N HCl to obtain the rare earth elements. The received solution was evaporated to dryness to further separate the Nd element. Except for the Sr solution, the Nd and U test solutions were stored in PFA beakers and evaporated them.

(4) Ln resin was used to separate the Nd element from REEs. 6M HCl and Milli-Q ultrapure water were added in sequence to wash the Ln resin, and then 0.25

M HCl was added to balance the resin. The centrifuged solution was aspirated and loaded, and 0.25 N HCl was added to wash the impurities and receive the purified Nd isotope test solution. The sample was then stored in a PFA beaker and evaporated it.

Then, an appropriate solution was taken to dilute the test concentration with 2% HNO_3 according to the element content. All three isotopes are tested by NEPTUNE Plus MC-ICP-MS (multi-acceptor inductively coupled plasma mass spectrometer, Thermo Fisher Scientific). The $^{87}Sr/^{86}Sr$ test value is corrected by $^{86}Sr/^{88}Sr$ =0.1194, and the NBS987 standard solution is used to monitor the test process (recommended value 0.710248 ± 0.000020) throughout the test process. The average value of NBS987 in this experiment is 0.710253±17 (n=28, 2SD). The $^{143}Nd/^{144}Nd$ test value was calibrated using $^{146}Nd/^{144}Nd$ = 0.7219 (Wasserburg et al., 1981). The test process used JNdi-1 monitoring data (recommended value 0.512114 ± 0.000010) (Tanaka et al., 2000) . The average test value of JNdi-1 was 0.512117±13 (n=28, 2SD), which met the test requirements for Nd isotopes. The test results of Nd isotopes are given in the form of εNd, $\varepsilon Nd = [(^{143}Nd/^{144}Nd_{sample}/(^{143}Nd/^{144}Nd)_{CHUR})-1]\times10^4$, where the $^{143}Nd/^{144}Nd$ value of CHUR is 0.512638 (Jacobsen and Wasserburg, 1980). The test value of $^{234}U/^{238}U$ was corrected with $^{238}U/^{235}U$ = 137.88 (Steiger and Jäger, 1977). CRM112-A was used to monitor data quality during the test (recommended value 5.2841± 0.0082 ×10-5) (Mathew et al., 2012). The activity ratio of ^{234}U and ^{238}U was expressed as ($^{234}U/^{238}U$). The recommended value of ($^{234}U/^{238}U$) of the standard solution CRM112-A was 0.9629±0.0015. The average value of ($^{234}U/^{238}U$) of CRM112-A tested in this study was 0.9627±0.0013 (n=22, 2SD), which met the test requirements. The international rock standard BCR-2 was used for monitoring the entire test process. The average BCR-2 test values of $^{87}Sr/^{86}Sr$, $^{143}Nd/^{144}Nd$ and ($^{234}U/^{238}U$) were 0.705010 ±18 (n=4) (recommended value 0.705000±11, (Jweda et al. (2015)), 0.512641±16 (2SD) (recommended value 0.512637±13, Jweda et al. (2015)) and 1.001 ± 0.002 (2SD) (recommended value 1.002±0.004, Koornneef et al. (2010)), which met the experimental requirements.

Chapter 4 Geochemical characteristics of river and sea floor sediments surrounding the Southern SCS

4.1 Geochemical characteristics of river and sea floor sediments

4.1.1 Element and isotope composition of river sediments

Comparing the elements of bulk components and the residual components (after leaching by acid) of the river sediments (Appendix Table 1-3), elements contents such as SiO_2, Al_2O_3, Fe_2O_3, K_2O, TiO_2, MgO, REEs (La-Lu), Rb, Sc, and Th are relatively stable and very few proportions are leached out by acid. Among them, the loss of leaching of elements such as SiO_2, Al_2O_3, Fe_2O_3, K_2O, TiO_2, REEs (La-Lu), Rb, Sc, and Th is less than 15%, and those elements can exist relatively stable in the residual components. The loss proportion of leaching elements such as MnO, CaO, Na_2O, and Co is relatively high beacuse activity of these elements is relatively strong. For example, the residue/UCC value of MnO and CaO is only about 30% (Fig. 4.1). It is worth noting that in these river samples, the contents of MgO and CaO are low in both residue and bulk components. From high to low latitudes of the study rivers, the average contents of MgO in the bulk and residue of the Mekong River sediments are 1.58% and 1.33% respectively; 0.61% and 0.54% respectively, for Pahang River sediments; 0.54% and 0.52%, respectively, for Kelantan River sediments; and 0.79% and 0.75%, respectively, for Rajang River sediments; The average contents of CaO in the bulk and residue of the Mekong River sediments are 0.77% and 0.24% respectively; 0.33% and 0.08%, respectively, for Pahang River sediments; 0.24% and 0.13%, respectively, for Kelantan River sediments; and 0.14% and 0.04%, respectively, for Rajang River sediments. The result indicates that in the bulk samples, the contents of MgO and CaO gradually decrease with decreasing latitudes. Notably, the CaO content, which is generally less than 1%. Despite the study area having more or less carbonate rocks or carbonate rock fragments in the Quaternary soft sediments, the contents of MgO and CaO in modern river sediments are low. It is speculated that active hydrothermal exchange, high temperatures and frequent precipitation in the tropical areas lead to strong weathering, and almost all soluble elements migrate from rocks to rivers and other media.

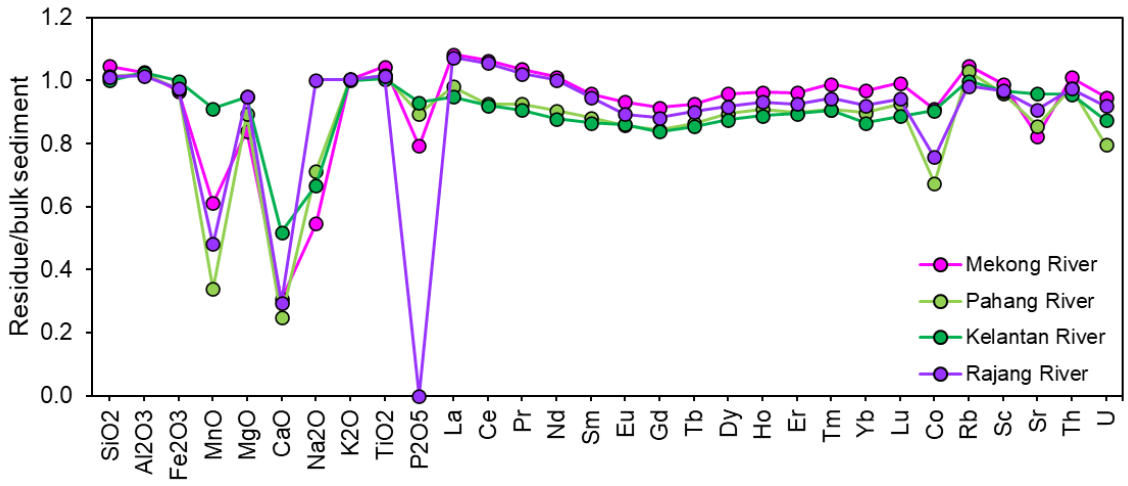

Fig. 4.1 Illustration of element ratios of river sediment residue/bulk component

Because the object of the study is to study the environmental information recorded in the terrigenous debris, the geochemical composition of residue after acid leaching was used for the following research. Overall, SiO_2, Al_2O_3, and Fe_2O_3, account for 75%-90% of all element compositions of the terrigenous debris components of river sediments, while the contents of MnO, MgO, NaO, and CaO are relatively low, such as the MnO content of the Rajang River is 0.02-0.03%, and the CaO content of the Kelantan River is 0.03-0.16%. The contents of MgO, NaO, and CaO in the sediment samples of the Mekong River are relatively high compared to other rivers (MgO 1.10-1.67%, NaO t 0.60-0.87%, CaO 0.18-0.34%) (Appendix Table 1).

In order to better distinguish the geochemical characteristics of different river sediments, the major elements and trace elements are normalized by the element composition of the upper continental crust (UCC) (Fig. 4.2). In the residue of river sediments, the content of SiO_2, Al_2O_3, Fe_2O_3, TiO_2, light rare earth elements (LREE), Rb, Sc, and Th is close to that of UCC. Some easily soluble elements are depleted compared with UCC, such as MnO, MgO, NaO, K_2O, CaO, Sr. Some heavy rare earth elements (HREE) such as Tm, Yb, Lu and Th and U are enriched compared with UCC. The element distribution patterns of all river sediments are almost the same, except that the MnO concentration of the Kelantan River on the Malay Peninsula shows a significant difference. For REEs, we should not only pay attention to their concentration, but more importantly, their distribution pattern. After UCC normalization, REEs pattern shows a right-end upturned pattern, HREE is more enriched, and the distribution patterns of these river sediments are basically the same. Since the source area materials travel over long times and through a large area from source to sink, they usually mix

extensively with UCC materials. Therefore, the elemental composition of clastic materials is highly similar to that of the UCC (Appendix Table 2 and 3).

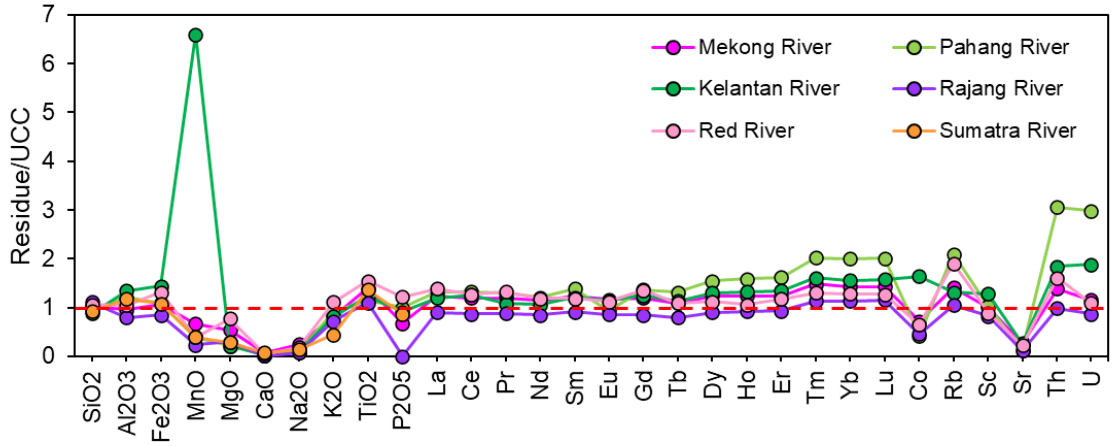

Fig. 4.2 Element ratios of river sediment residue/UCC

$^{87}Sr/^{86}Sr$ and εNd isotopes of sediments or rock are usually used as proxies of sediments provenance (e.g. Colin et al., 2006; Goldstein and O'Nions, 1981; McLennan et al., 1993; Wan et al., 2017). $^{87}Sr/^{86}Sr$ and εNd values of residue show significant difference of the study rivers around the SCS (Appendix Table 6, Fig. 4.3). The $^{87}Sr/^{86}Sr$ value of Red River sediments is 0.730230-0.734568, and the εNd value is -12.48 ~ -11.89; the $^{87}Sr/^{86}Sr$ value of Mekong River sediments is 0.719749~ 0.723118, and the εNd value is -10.62~ -9.99; the $^{87}Sr/^{86}Sr$ value of Rajang River sediments is 0.718332~ 0.719797, and the εNd value is -7.59~ -6.91; The $^{87}Sr/^{86}Sr$ value of Sumatra river sediments is 0.71158~ 0.71053, and the εNd value is -4.47~ -4.64; the $^{87}Sr/^{86}Sr$ value of Kelantan River sediments is 0.715340-0.725300, and the εNd value is -9.90~ -5.27; the $^{87}Sr/^{86}Sr$ value of Pahang River sediments is 0.731202-0.744089, and the εNd value is -11.67~ -7.79 (Appendix Table 6). As can be seen from Fig. 4.3, the $^{87}Sr/^{86}Sr$ and εNd values of the Red River, Mekong River, Rajang River and Sumatra rivers sediments vary relatively little, but the Kelantan River and Pahang River located in the Malay Peninsula show great variations, for example, the εNd value of the Kelantan River sediments varies from -9.90 to -5.27.

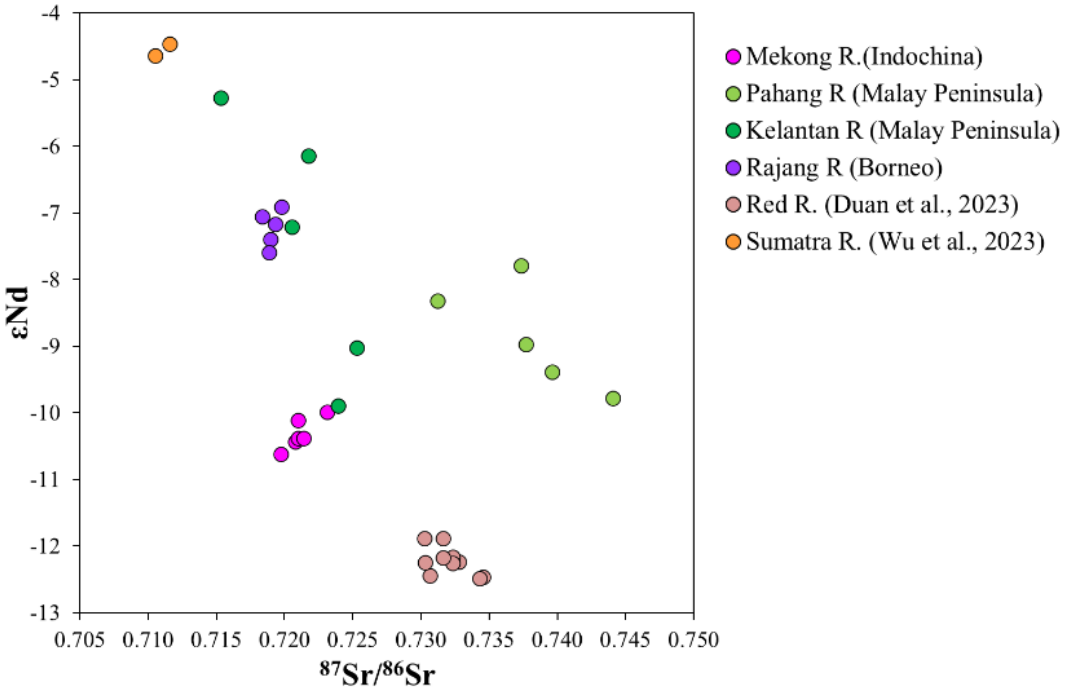

Fig. 4.3 Sr-Nd diagram of river sediments around the SCS

4.1.2 Element and isotope compositions of marine sediments

Focus on the whole SCS, floor sediment geochemistry data were collected and analyzed, and divided into 6 regions based on current data and geographical location, Red River estuary - Gulf of Beibuwan, Mekong River estuary-offshore Indochina Peninsula, offshore Borneo, offshore Malay Peninsula-Western Sunda Shelf, Central-Eastern Sunda Shelf, South China Sea Basin (Li et al., 2003; Wei et al., 2012). The element and isotope composition of the residues after acid leaching were analyzed. The main major elements are SiO_2, Al_2O_3, and Fe_2O_3, accounting for about 80% of the residues, and their concentration in different regions does not change significantly (Appendix Table 4 and 5).

The elements were normalized by UCC to constrain the differences among the different sedimentary regions (Fig. 4.4). The major elements and most trace elements are depleted compared with UCC, and only SiO_2, TiO_2, Rb and Th are relatively enriched compared with that of the UCC. Other elements, such as Fe_2O_3, MnO, Tm, Yb, Lu and U, show different enrichment or loss in different region sediments. Except for the eastern Sunda Shelf, the REE patterns in other regions are the right-end upturned pattern, which means HREE enrichment. While the REE pattern of sediments in the eastern Sunda Shelf presents a straight line, and the concentrations are lower than that of other regions, the concentrations of elements in the eastern shelf are depleted

compared with the UCC.

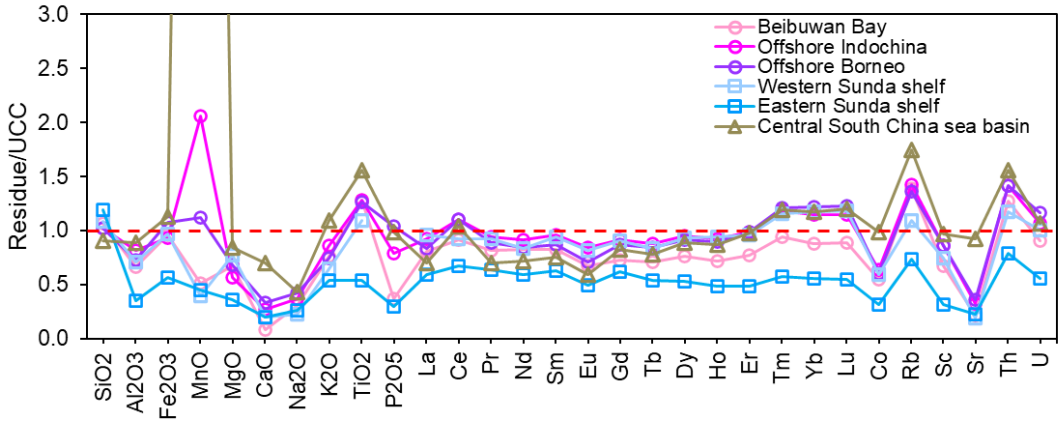

Fig. 4.4 Illustration of element ratios of river sediment residue/UCC

Unlike river sediments, the $^{87}Sr/^{86}Sr$ and εNd values of seafloor sediments show more significant variation (Fig. 4.5, Appendix Table 6). The $^{87}Sr/^{86}Sr$ value of Gulf of Beibuwan sediments is 0.720986~ 0.723118, and the εNd value is -11.55~ -10.17; the $^{87}Sr/^{86}Sr$ value of Indochina Peninsula offshore sediments is 0.715053~ 0.723118, and the εNd value is -10.62~ -9.99; the $^{87}Sr/^{86}Sr$ value of Borneo offshore sediments is 0.715360~ 0.720602, εNd value -8.76~ -8.23; $^{87}Sr/^{86}Sr$ value of sediments in the western Sunda shelf is 0.718748~ 0.723918, εNd value -12.28~ -8.82; $^{87}Sr/^{86}Sr$ value of sediments in the eastern Sunda shelf is 0.719230~ 0.720555, εNd value -11.63~ -9.93; $^{87}Sr/^{86}Sr$ value of sediments in the South China Sea basin is 0.709235~ 0.726755, εNd value -11.30~ -6.93 (Appendix Table 6). Near river estuary, the $^{87}Sr/^{86}Sr$ and εNd values of marine sediments are close to those of river sediments, indicating that river-transported terrigenous debris are the primary source of marine sediments. However, the offshore marine sediments still exhibit a wider range of $^{87}Sr/^{86}Sr$ and εNd values compared to river sediments. This variability may be due to the mixing with other materials after terrigenous debris entering the marine, which will affect the geochemical composition of marine sediments, such as offshore Borneo and the Red River estuary-Gulf of Beibuwan. The $^{87}Sr/^{86}Sr$ and εNd values of shelf and SCS basin sediments show a larger variation, indicating a more complex mixing process from nearshore to deep sea. This mixing complicates the analysis of sediment provenance in a multi-sourced marginal sea (Fig. 4.5).

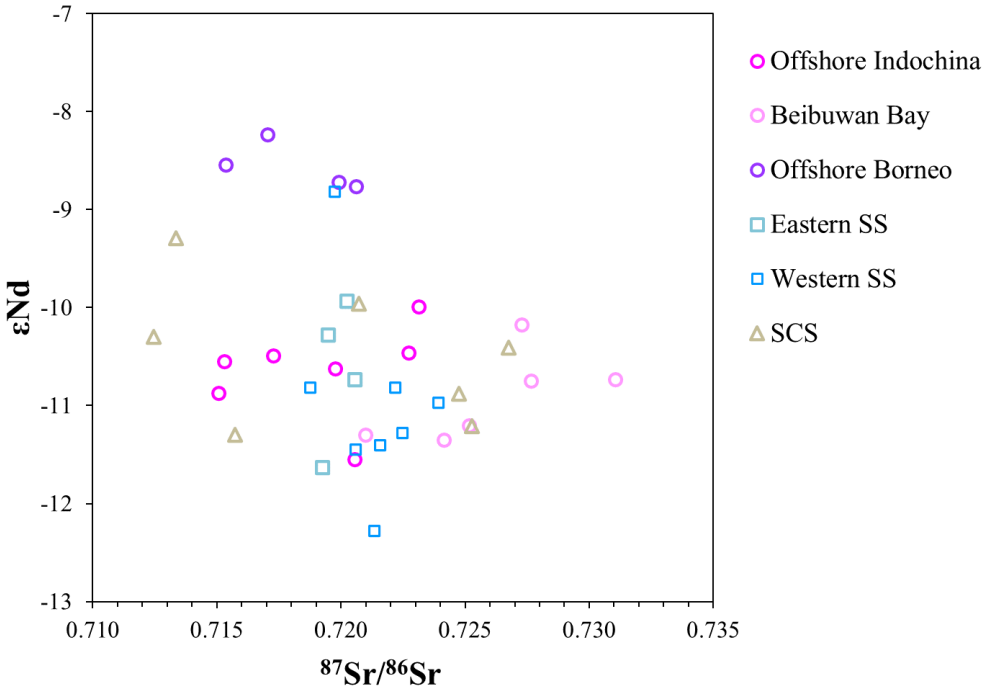

Fig. 4.5 Sr-Nd diagram of sea floor sediments of the South China Sea

4.1.3 ($^{234}U/^{238}U$) characteristic between river and marine sediments

There is little variation of the concentration of U in the Red River sediments, Mekong River sediments, and Rajang River sediments, with an average content of 2.34-3.27 μg/g. Kelantan and Pahang Rivers sediments on the Malay Peninsula have significantly different U concentrations despite being on the same island. Kelantan River sediments have a U concentration around 5.10 μg/g, while Pahang River sediments range from 5.51 to 13.42 μg/g, with one sample reaching 13.42 μg/g, 2-3 times higher than others. The U concentration in the western Sunda Shelf sediments range from 2.28 to 4.09 μg/g, which was within the range of river sediments (Fig. 4.6). The value of the ($^{234}U/^{238}U$) activity ratio is more sensitive to environments than the U concentration. The range of the Red River sediments is 0.923-0.945, the Mekong River sediments are 0.945-0.964, the Pahang River sediments are 0.984-1.031, the Kelantan River sediments are 0.966-0.996, the Rajang River sediments are 0.937-0.952, and the western Sunda Shelf sediments are 0.945-0.967 (Fig. 4.6, Appendix Table 6). As can be seen from the Fig. 4.6, the ($^{234}U/^{238}U$) values of western Sunda Shelf sediments are similar to those of Mekong River sediments but differ significantly from those of Malay Peninsula sediments. This suggests that the sediments on the Sunda Shelf primarily originate from the Mekong River, with less contributions from Malay Peninsula rivers. Wu et al. (2020) analyzed rare earth elements in the surface sediments of the Sunda Shelf and concluded that the Malay Peninsula rivers contribute minimally to the

sedimentation of the Sunda Shelf, and the large rivers are the main source of the sediments in the Sunda Shelf, which is consistent with the conclusion of this U isotope study.

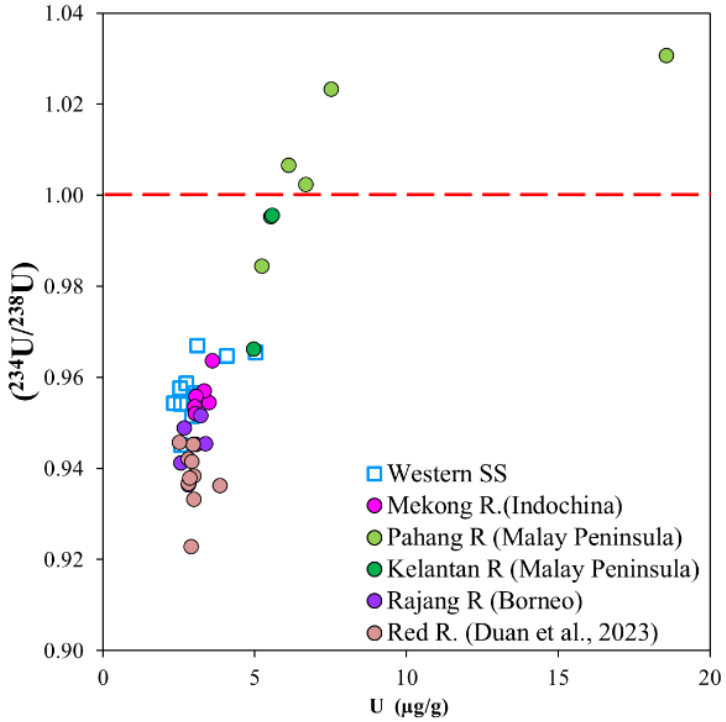

Fig. 4.6 U concentration and ($^{234}U/^{238}U$) distribution in river sediments and sea floor sediments

The U concentration in UCC is 2.7 μg/g, and ideally, the ($^{234}U/^{238}U$) ratio in rocks at secular equilibrium is 1. However, current research indicates that even deeply buried rocks often develop fractures due to various factors, causing the ($^{234}U/^{238}U$) ratio to typically be less than 1 (Ng et al., 2023). The U concentration of river sediments around the Sunda Shelf, except for the rivers in the Malay Peninsula, is about 2.9 μg/g, which is close to the UCC value. This observation suggests that these river sediments are typically mixed from various lithological source rocks, resembling geochemical characteristics of UCC. The average U concentrations of the Pahang River and Kelantan River sediments are 10.10 and 5.84 μg/g, respectively, 2-4 times higher than the UCC. The U concentration of granite is 4.8 μg/g (Taylor, 1964), and the U concentration of Kelantan River sediments is much higher than granite. Additionally, the values of ($^{234}U/^{238}U$) from the Pahang River and Kelantan River sediments are close to 1, higher than those in other river sediments. The values of ($^{234}U/^{238}U$) in some Kelantan River sediments are even higher than 1, warranting further study.

4.2 Controls of sediment geochemical composition

4.2.1 Different lithologies between the southern and northern land of Sunda Shelf and their impact on the geochemical composition of river sediments

The tectonic evolution and lithological characteristics of the land around the Sunda Shelf have been discussed in detail in the Chapter 2 (Fig. 2.4 and 2.5). The Sunda Shelf is located in the southeast of the Eurasian Plate. Its northern part is connected to the Eurasian Plate, its southern and western parts are connected to the Australian-Indian Plate, and its eastern part is connected to the Philippine-Pacific Plate (Bird, 2003). The northern side of the shelf is mainly the South China Block and the Indochina Block, the western part is the Malay Block, the southern part is the West Sumatra Block, and the southeast part is the Banda Block. The South China Block and the Indochina Block in the northern shelf are relatively stable as parts of Eurasian continent. In contrast, the southern Sumatra Block and the Indonesian Archipelago are closer to the plate subduction zones and thus more tectonically active, with many volcanic eruptions and earthquakes during the Holocene (Fig. 2.2 and 4.7). The Red River is developed in the Red River Fault Zone at the junction of the South China Block and the Indochina Block. The exposed rocks are mainly Mesozoic and Paleozoic sedimentary rocks, with low grade metamorphic rocks and intermediate metamorphic rocks distributed along the fault zone. The downstream area is mainly composed of Quaternary deposits. The Mekong River catchment has a large area with complex lithology in the upper reaches, featuring both magmatic rocks and metamorphic rocks. The middle reaches predominantly expose Mesozoic sedimentary rocks, while the vast floodplains in the lower reaches are mainly composed of Quaternary deposits. The Malay Peninsula is dominated by Felsic plutonic rocks and low-grade metamorphic rocks. The southwestern Sumatra is mainly composed of intermediate-mafic volcanic rocks, with active volcanic activities continuing since the Holocene. The northeastern plains are mainly Paleogene-Neogene sedimentary rocks and Quaternary deposits. In Borneo, except for the much felsic plutonic rocks exposed in the southwestern area of Banda Block region, the rest of the island is composed of Mesozoic and Cenozoic sedimentary rocks and Quaternary deposits.

By summarizing the $^{87}Sr/^{86}Sr$ and εNd values of the SCS and surrounding lands (Fig. 4.8 and 4.9), the $^{87}Sr/^{86}Sr$ value increases from the southwest to the northeast of the Sunda Shelf, while the εNd value decreases from the southern to the northern SCS. The age of rocks can be calculated from the ratios of radioactive isotopes in minerals,

determining the relative ages of rocks or minerals and distinguishing their sources. The decay law of radioactive isotopes is the theoretical foundation of isotope geochronology. The most used are the Rb-Sr and the Sm-Nd systems. ^{85}Rb and ^{87}Rb are the two isotopes of Rb, and Sr has four isotopes: ^{84}Sr, ^{86}Sr, ^{87}Sr, and ^{88}Sr. During Earth's evolution, Rb is entered into minerals during rock crystallization. Following the radioactive decay laws, ^{87}Rb continuously decays over time while ^{87}Sr increases. Thus, the atomic numbers of ^{87}Rb and ^{87}Sr in minerals can be used to calculate the crystallization age (Dickin, 2018). Over time, from mantle material to crustal material, the value of $^{87}Sr/^{86}Sr$ increased. It is generally believed that the initial $(^{87}Sr/^{86}Sr)_0$ of present-day continental crust is 0.719 (Faure, 1972). The Sm has seven isotopes, including three radioactive isotopes: ^{147}Sm, ^{148}Sm, ^{149}Sm, and the Nd also has seven isotopes, including two radioactive isotopes: ^{144}Nd and ^{145}Nd. The Sm-Nd dating method is similar to the Rb-Sr system. Nd isotope geochemical tracing is mainly based on the initial ratio $(^{143}Nd/^{144}Nd)_0$. Because the $^{143}Nd/^{144}Nd$ value is very small over geological history, the εNd parameter is used to represent the Nd isotope values in minerals. Generally, the εNd value in crustal materials is smaller, usually less than 0, while it is usually larger than 0 in depleted mantle materials. The $^{87}Sr/^{86}Sr$ and εNd are usually used together when studying the crust and mantle system.

From the variation of $^{87}Sr/^{86}Sr$ and εNd values of rivers and marine sediments and the tectonic evolution of the SCS, the Red River and Mekong River basins in the northern part are located in relatively stable blocks, with the main rock types being sedimentary rocks and deposits. The geochemical characteristics of river sediments are similar to those of the UCC, with larger $^{87}Sr/^{86}Sr$ values and smaller εNd values. In contrast, the river sediments of Borneo and Sumatra, located in the southern part of the shelf, have smaller $^{87}Sr/^{86}Sr$ values and larger εNd values (Fig. 4.5, 4.8 and 4.9).

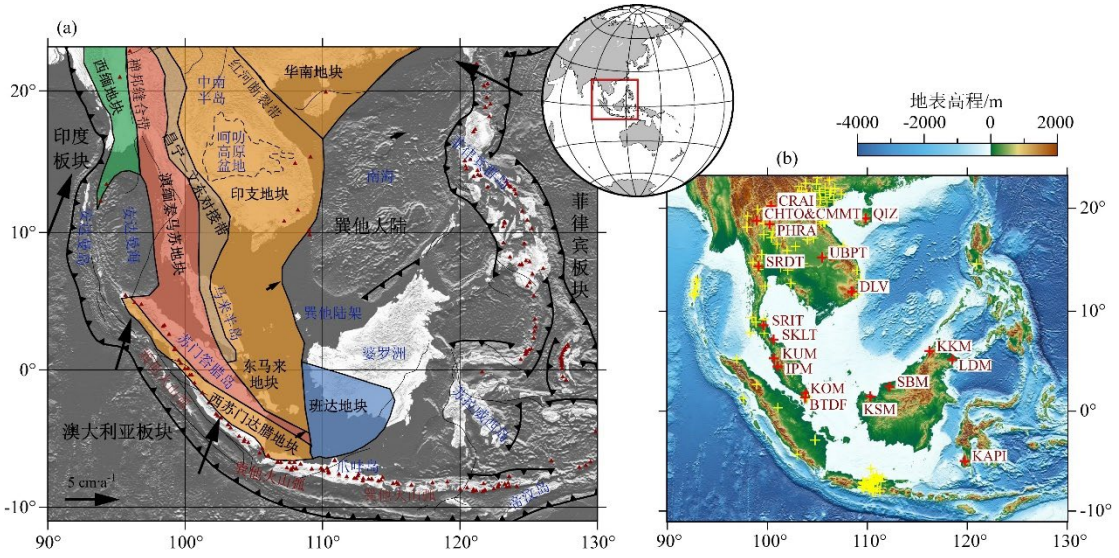

Fig. 4.7 The tectonic division of the Sunda Shelf and surrounding areas. The dark red triangles in (a) represent active volcanoes since the Holocene (Feng et al., 2021).

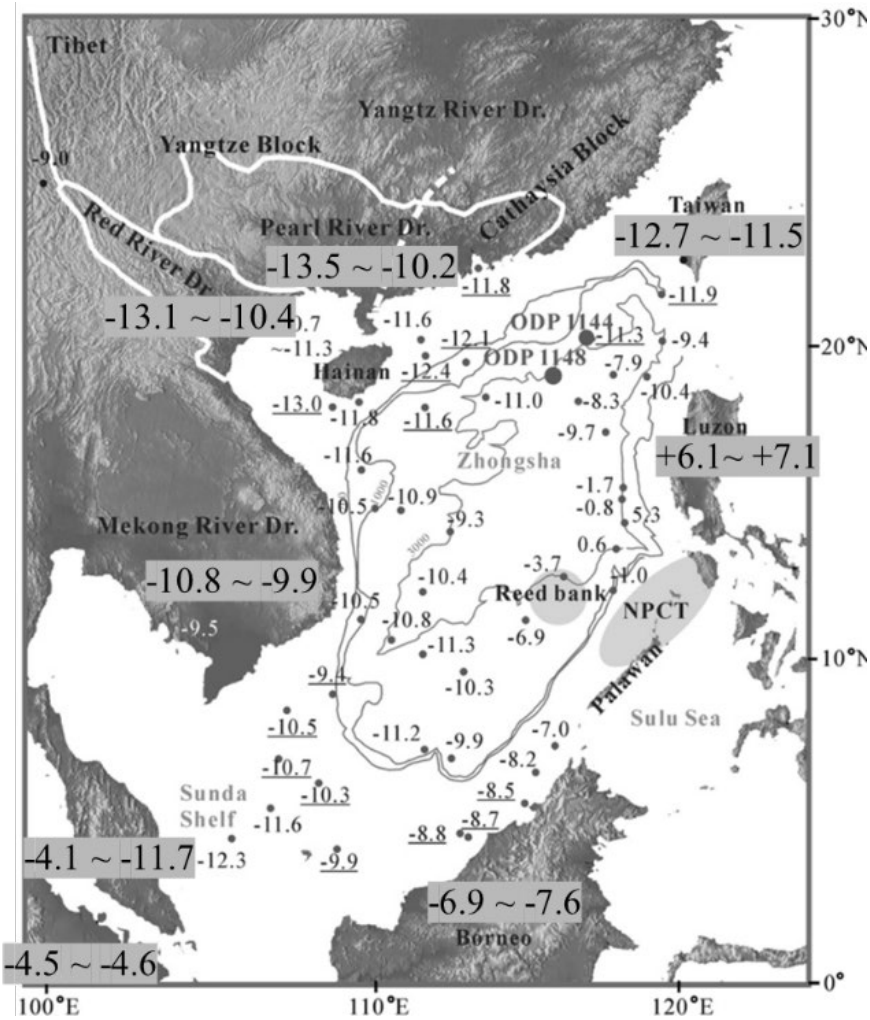

Fig. 4.8 Maps shows εNd distribution of the of SCS and surrounding lands (Wei et al., 2012). The thin lines represent the 200 m, 100 m and 3000 m isobath. The εNd values of the land are the average values of the river sediments.

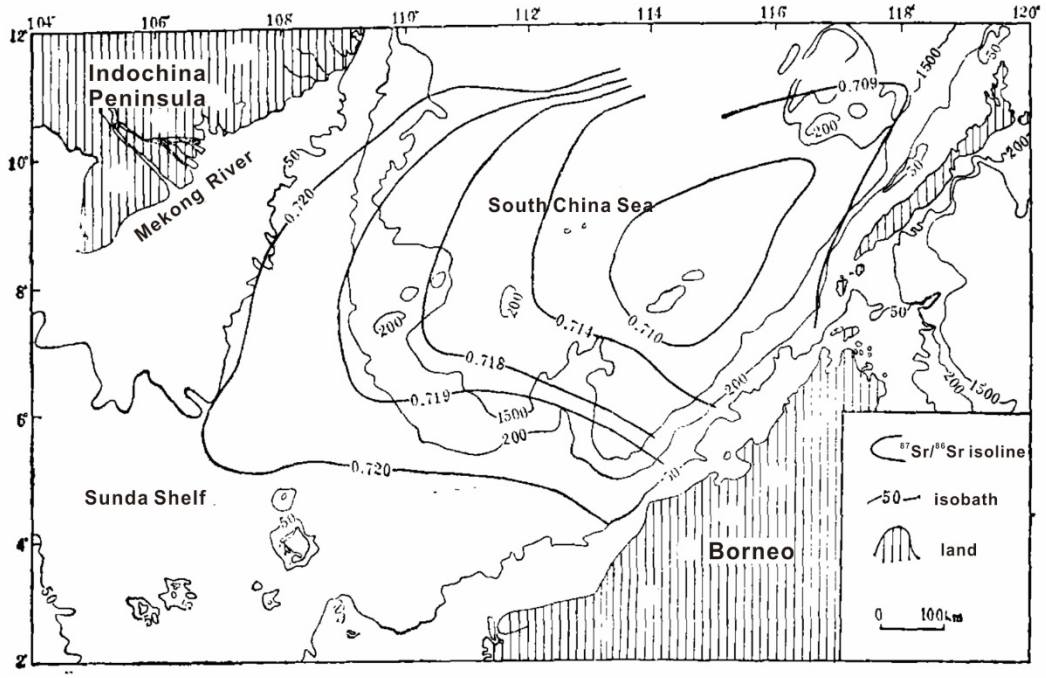

Fig. 4.9 Map shows the $^{87}Sr/^{86}Sr$ ratio distribution of SCS and surrounding lands (Gui et al., 1993). Thin lines represent isobaths, and thick lines represent $^{87}Sr/^{86}Sr$ changes.

4.2.2 Geochemical differences between marine and river sediments

The characteristics of major elements, trace elements and Sr-Nd isotopes between the marine and river sediments around the SCS were compared.

(1) Major elements

River sediments are often a mixture of different source rocks, as mentioned above, and their geochemical composition is highly similar to that of the UCC. This study selected stable landophilic elements, Ti and Al, along with K, Na, Ca, and Mg that are easily lost during weathering, as the main comparison elements (Fig. 4.10). To eliminate the grain size effect, Al/Si is used as the horizontal axis. Al is typically enriched in fine-grained minerals like clay minerals, while Si is usually enriched in coarse-grained materials such as quartz. Therefore, Al/Si is usually used to indicate the grain size change of sediments. Low Al/Si values indicate larger grain sizes, and high Al/Si values indicate smaller grain sizes (Hein et al., 2017). The Ti element is generally found in terrestrial stable minerals and has low concentration in seawater. Generally, the Ti concentration of terrestrial river sediments is positively correlated with grain size, meaning that coarser minerals contain more Ti (Sun et al., 2008). In contrast, the correlation between Ti and grain size in marine sediments is less pronounced. There are more Ti in the marine sediments, especially in Gulf of Beibuwan and offshore Indochina Peninsula (Fig. 4.4, Appendix Table 3 and 5). Conversely, Ti concentrations

of the sediments from Sunda Shelf and SCS Basin are relatively lower (Fig. 4.4, Appendix Table 3 and 5). This indicates that during the sediment transportation process, coarse sediments or large density minerals are preferentially deposited at the estuary or near shore affected by hydrodynamic sorting. These minerals accumulate in the marine, resulting in the Ti concentration in marine sediments being higher than that in river sediments (Fig. 4.10).

The concentrations of K, Na, Ca, and Mg in marine sediments are higher than those in river sediments, which is a very interesting point, but there is no definite explanation for this phenomenon. The terrigenous debris components in marine sediments come from the input of surrounding land rivers. Typically, sediments that have just undergone physical breakdown and erosion have higher concentrations of K, Na, Ca, and Mg. However, after prolonged transport or deposition in river floodplains, these elements are easily to be leached out. Consequently, the terrestrial detrital material deposited in the marine should have lower concentrations of these soluble elements compared to river sediments. Contrary to this expectation, our study reveals higher concentrations of these elements, particularly Mg, in marine sediments (Fig. 4.10). Reverse weathering refers to a reverse chemical weathering process, usually the process of forming new clay minerals by combining of soluble cations and alkaline compounds, resulting in increased concentrations of elements like Mg and K. Studies in regions such as the Amazon River delta have investigated this process (Mackenzie and Garrels, 1966; Mackenzie and Kump, 1995). However, reverse weathering primarily produces fine-grained clay minerals. As shown in Fig. 4.10, marine sediments with high concentrations of K, Na, Ca, and Mg usually have low Al/Si ratios, which is opposite with the reverse weathering processes. Thus, the impact of reverse weathering can be ruled out. This question is not the focus of this study, so its causes are not explored in detail here.

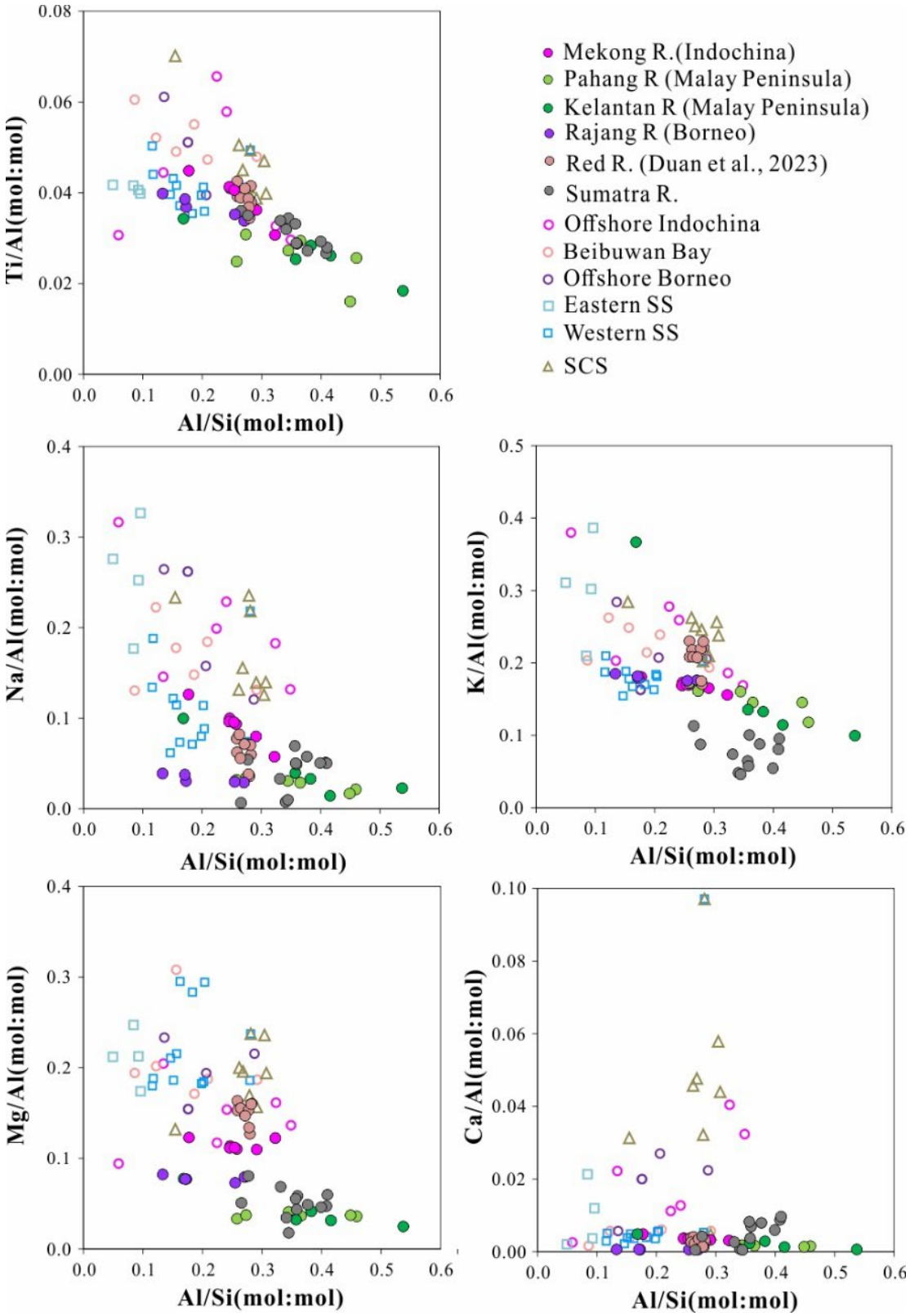

Fig. 4.10 Relationship between the ratios of major elements in river and sea floor sediments. SS: Sunda Shelf.

(2) Trace elements

REEs and some trace elements with poor mobility are more stable than major

elements during rock erosion, weathering and transportation, and are less affected by chemical weathering. These elements widely used in stud of provenance of marine sediment (e.g., Bi et al., 2017; He et al., 2015; Yang et al., 2006). For example, the concentrations of Sc and Co in mafic magmatite are higher than those in felsic magmatite, while the concentrations of La, Th and REEs in felsic magmatite are higher than those in mafic magmatite and their weathering products. This study selected the La-Th-Sc triangle diagram, Th/Sc vs. Zr/Sc and $(Gd/Yb)_N$ vs. δEu correlation are used to distinguish the main source rock types of marine and river sediments.

From Fig. 4.11, except for the sediments of the Pahang River and Kelantan River in the Malay Peninsula, the La, Th and Sc concentrations of the sediments of other rivers are relatively concentrated, which are close to the value of UCC. The La, Th and Sc concentrations in the Malay Peninsula river sediments show significant variation, and the trend of change is roughly parallel to the La-Th line. In particular, the Th content of sediments is higher than that of other rivers. The La, Th and Sc concentrations of marine sediments are clearly divided into different regions. The value of estuary sediments is close to that of adjacent river sediments. Sediments in the eastern or western Sunda Shelf are close to those in the Mekong River, which is also consistent with the ($^{234}U/^{238}U$) characteristic. In addition, sediments in the SCS Basin contain less La.

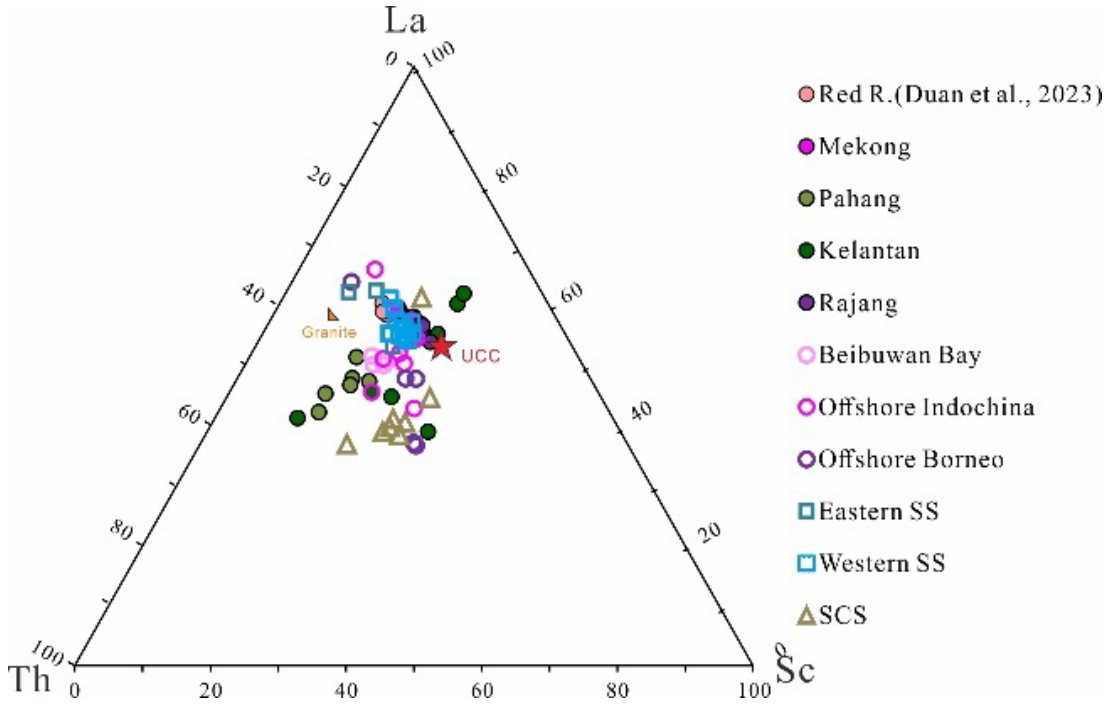

Fig. 4.11 Triangle Diagram of La-Th-Sc element composition in river and seafloor sediments (SS: Sunda Shelf).

The Th/Sc vs. Zr/Sc diagram was proposed to distinguish the composition changes of clastic sediments during the sedimentary process, so as to compare the sources of sediments. Fig. 4.12 shows the magmatic differentiation line of the first cycle (black dashed line) and the sediment recycling process (red dashed line) (McLennan et al., 1993). As Sc is a coexisting element in magmatic rocks, and Th is a very typical incompatible element, the Th/Sc ratio can be used to indicate the changes in chemical composition during magmatic differentiation and the changes in the provenance of clastic rocks. The source is usually distinguished based on the balance of Th/Sc. When Th/Sc=1, it indicates that it comes from UCC. When Th/Sc<1, it indicates that the sediments come from young undifferentiated arcs. When Th/Sc≥1, it indicates material from recycled sedimentary rocks (Taylor and McLennan, 1985). Zr usually exists in zircon and is relatively stable during the sediment transportation process. Generally, in the Th/Sc vs. Zr/Sc diagram, as the values of Th/Sc and Zr/Sc increase, the sediments have experienced a longer transportation time. The Th/Sc and Zr/Sc ratio of river samples are similar to the pattern of the La-Th-Sc triangle diagram, except for the river sediments in the Malay Peninsula. The Th/Sc and Zr/Sc ratios of other river sediments are equal to or slightly larger than that of the UCC, while the ratios of some samples from Pahang River and Kelantan River sediments are parallel to the magmatic differentiation line and close to average values of the granite. The result is consistent with the lithology distribution characteristics of the felsic plutonic rocks in the Malay Peninsula, indicating that the lithology has a significant impact on the geochemical composition of small river sediments. The Th/Sc and Zr/Sc ratios of marine sediments show a strong sedimentary re-cycling, indicating that the marine surface sediments have undergone a more complex transportation process and may be affected by the re-cycling materials from the floodplain of large rivers or the sediments stored on the shelf (Fig. 4.12).

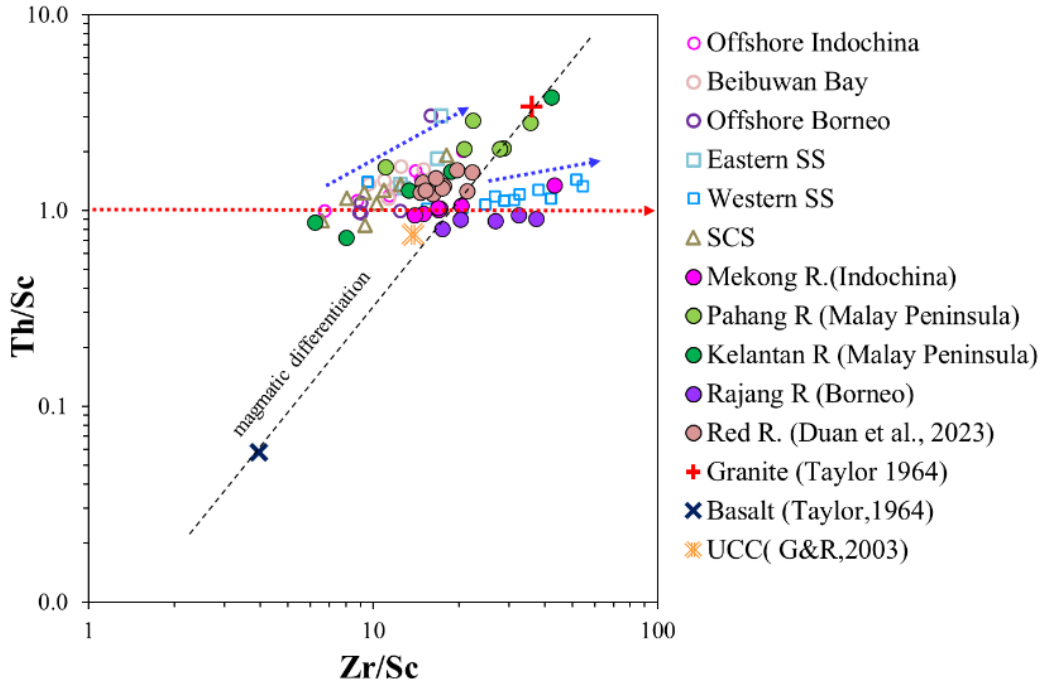

Fig. 4.12 Diagram of Th/Sc vs. Zr/Sc in river and seafloor sediments (note, SS: Sunda Shelf).

The REEs were normalized with chondrites to obtain the $(Gd/Yb)_N$ vs. δEu diagram (Fig. 4.13). Gd/Yb ratio represents the differentiation characteristics of REE. The concentration of Gd in minerals decreases with fractionation, so it can reflect the time in the sedimentation process. δEu represents the degree of the separation of Eu relative to other REEs. Generally, positive Eu anomaly usually happen in metamorphic rocks and sediments, indicating that these rocks are derived from terrigenous materials. Negative Eu anomaly is common in igneous rocks, indicating that the materials are derived from the mantle. Both river and marine sediments show different degrees of negative Eu anomalies. Except for river sediments in the Malay Peninsula, the $(Gd/Yb)_N$ and δEu values of other river sediments is relatively concentrated, while the δEu value anomaly of the Pahang River and Kelantan River sediments has a larger variation, and the negative anomaly is more obvious, which is similar to the analysis of other elements earlier, and is consistent with its lithology characteristics.

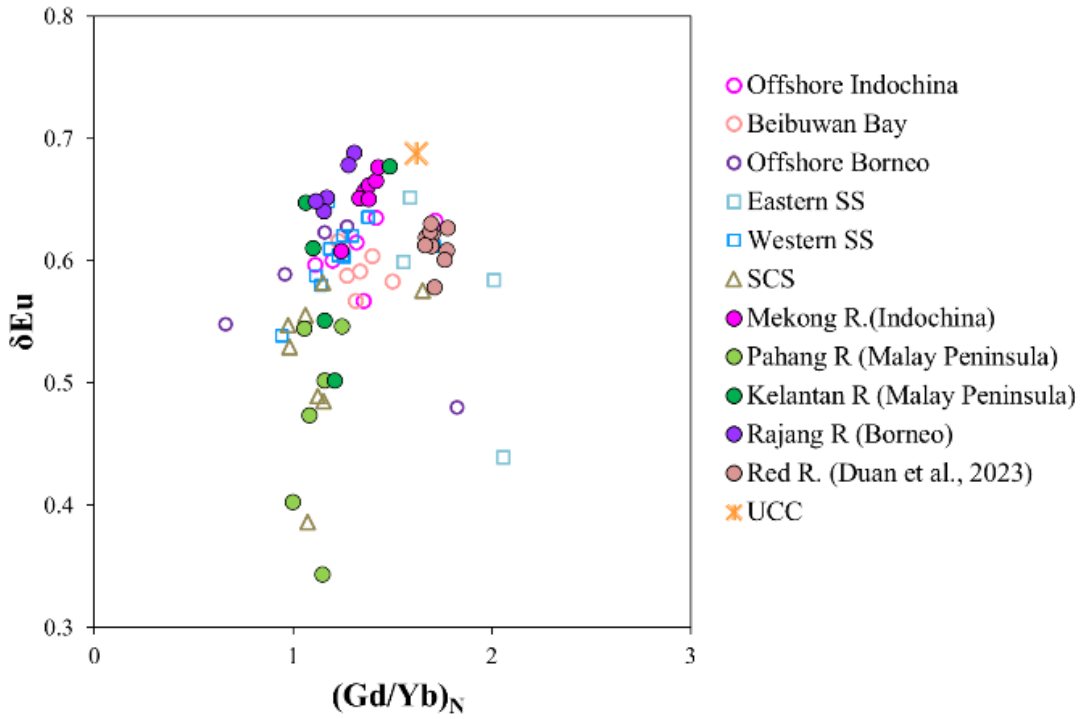

Fig. 4.13 Diagram of $(Gd/Yb)_N$ vs. δEu in river and seafloor sediments (note, SS: Sunda Shelf)

(3) Sr and Nd isotopes

$^{87}Sr/^{86}Sr$ and εNd isotopes are one of the most widely used sediment provenance proxies (e.g., Colin et al., 2006; Goldstein and O'Nions, 1981; McLennan et al., 1993; Wan et al., 2017). Compared with elements, minerals or other proxies, isotopes can more accurately reflect the properties of the source rock and have greater advantages in sediment source tracing. However, whatever it is river or marine sediments, in addition to the detrital components, there are also authigenic components and biological components (e.g., Wilson et al., 2013), which will interfere with the identification of terrigenous signals. Therefore, in this study, the chemical sequence leaching method has been used to remove the non-detrital components (see Chapter 3 for details). Due to the mineral characteristics and formation age, $^{87}Sr/^{86}Sr$ ratio is more sensitive to grain size than εNd (Feng et al., 2009; Tütken et al., 2002). Generally, fine-grained sediments contain higher radioactive Sr concentration as fine-grained sediments contain more micas (including biotite and muscovite) with high Rb/Sr ratios (Feng et al., 2009; Meyer et al., 2011). In addition, incongruent weathering of Sr-containing minerals during weathering will lead to an increase in the $^{87}Sr/^{86}Sr$ ratio (Borg and Banner, 1996). Therefore, caution should be taken when using $^{87}Sr/^{86}Sr$ to trace the source of sediments. Nd isotope values are less affected by changes in sediment grain size and are mainly affected by fractionation during mantle differentiation. There are less changes of Nd

isotope values during sediment erosion, weathering, transportation and accumulation. Therefore, the differences between the marine and river sediments of the SCS are compared based on both Sr and Nd isotopes (Fig. 4.14).

The $^{87}Sr/^{86}Sr$ and εNd of river sediments in the southern islands have obvious mantle-derived characteristics, which are related to the volcanic activity that still active during the Holocene, while the $^{87}Sr/^{86}Sr$ and εNd of river sediments in the northern lands indicate that they are greatly affected by crustal materials. The variation of $^{87}Sr/^{86}Sr$ and εNd of marine sediments are mainly within the range limited by the Mekong River and the Red River sediments. It is understandable that the marine sediments in the northern SCS are mainly from the input of the northern rivers, such as the Pearl River, the Red River, and the Mekong River, because of the closer distance (e.g., Liu et al., 2007b; Liu et al., 2003; Sang et al., 2022; Wang et al., 2021). However, marine sediments located on the Sunda Shelf and the southern SCS do not show obvious characteristics of the mantle source from southern islands but are very close to the range of $^{87}Sr/^{86}Sr$ and εNd of the Mekong River sediments. Therefore, we speculate that in addition to the distance between the river and the ocean, the flux and transportation path of the sediments are also major factors controlling the source of marine sediments, so the present-day marine sediments of the SCS do not show trend of the transition from mantle-derived materials to crust-derived materials from the south to the north like the river sediments (Fig. 4.8 and 4.9). However, the materials depositing at the estuary or near shore are still controlled by the corresponding rivers, such as the sediments of the Rajang River and sediments at the offshore of Borneo, the Mekong River and the sediments of the offshore Indochina Peninsula (Fig. 4.14).

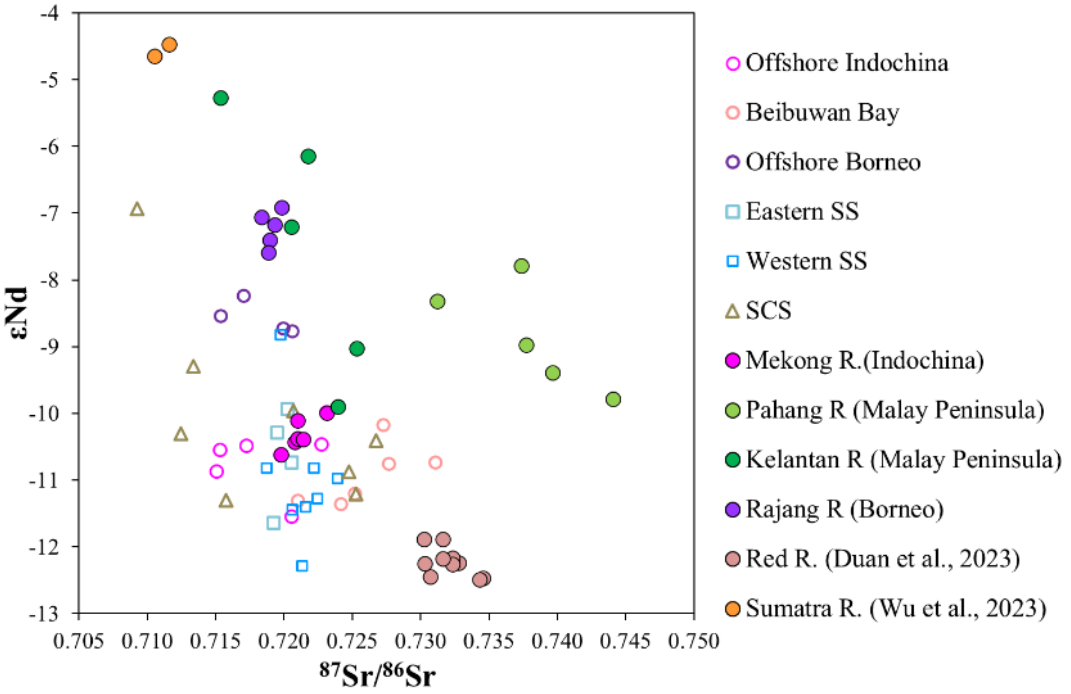

Fig. 4.14 Comparison of Sr-Nd isotopes between river sediments and seafloor sediments (note, SS: Sunda Shelf).

4.3 Is it correct to use river sediments as an end member for tracing marine sediment provenance?

The terrigenous clastic components in marine sediments mainly come from river input. Therefore, when tracing the source of marine terrigenous clastics, river sediments from potential source areas are often selected for comparison. Research methods mainly include two categories, sedimentological methods and geochemical methods. Specifically, (1) grain size. Wang et al., (2014a) studied the grain size characteristics of the core sediments on the inner shelf of the East China Sea, revealed that the flood outbreak in the Yangtze River Basin changed the source of sediments on a millennium scale. (2) Mineralogical method. Both single minerals or mineral assemblages are used to compare the differences between source and sink. Garzanti et al., (2021) studied sandstone petrology and heavy mineral to reveal the sediment source of the Pearl River in South China. Liu et al., (2010) used clay minerals in the Luzon Arc, Pearl River and Taiwan River sediments to analyze the provenance of sediments from northeastern SCS, reveled transportation path of fine-grained clastic sediments in the northeastern SCS. Qiao et al., (2015) used different association types of heavy minerals and clay minerals to determine the provenance of sediments in the northern Gulf of Thailand. (3) Elemental geochemical method. Variation trend of rare earth elements and stable trace

elements in sediments are usually used to reveal the changes in the source. Liu et al., (2016a and 2019) compared major and trace elements of the marine sediments in the Gulf of Thailand with the sediments of four main rivers flowing into the Gulf of Thailand, and the different sources and transportation processes of the sediments in the Gulf of Thailand were distinguished. (4) Isotope method. The isotope method mainly uses the different decay periods of radioactive elements and their mutual relationship to determine the source of sediments. Compared with other methods, it is a more accurate and popular method. For example, the source of the sediments were determined by analyzing the U-Pb isotopes of some minerals containing U in sediments (such as zircon, etc.) and/or comparing the age difference of river and marine sediment samples (Choi et al., 2013; Kosler et al., 2002). Furthermore, the Sr-Nd isotope diagram is widely used to determine the source of sediments (e.g., An and Jian, 2009; Awasthi et al., 2018; Singh et al., 2008; Wei et al., 2012; Yang et al., 2007).

However, there are some problems with current provenance analysis, (1) most studies only use one method, and these methods have more or less defects. For example, mineral is controlled by hydrodynamic sorting. Coarse particles are usually deposited near the source area, while fine particles can be transported farther. If just using clay mineral assemblage, only the source of fine-grained sediments can be distinguished. (2) Scientists pay more attention to the applicability and improvement of provenance analysis methods, but often ignore the subject of comparison: river samples and marine samples. Although terrigenous debris in marine sediments comes from river sediments, the marine core sediments were deposited during the geological history, that is, the sedimentation age of marine sediments and river sediments is different, can we still compare the sedimentological or geochemical proxies measured from river and marine core sediments directly? This is worthy of doubt and consideration.

In this study, Sr and Nd isotopes can better distinguish the difference between river samples and marine samples, and indicate the source of marine sediments. However, when we focus on major elements (Fig. 4.10), we mentioned above that the concentrations of K, Na, Ca and Mg concentration in river terrigenous debris components should be equal to or higher than those in marine terrigenous debris components, but the result is opposite. Therefore, the provenance indicated by Sr and Nd isotopes may not be completely correct, and further exploration is needed. It is speculated that the river sediments may represent environmental information at the time of collection and are not representative, while marine surface sediments may have been

deposited for a period of time (the time can be very long, such as hundreds of years), so when using river sediments as end members to trace the source of marine sediments, we should be cautious, especially when studying the source evolution of marine core sediments.

4.4 Summary

Potential sources in the southern part of the SCS mainly include the Red River in South China, the Mekong River in Indochina Peninsula, the rivers in the Malay Peninsula, Sumatra, and Borneo. These river systems can be divided into two categories: large rivers represented by the Mekong River in the north and small rivers in the southern islands like Pahang River in the Malay Peninsula and the Rajang River in Borneo. These rivers are controlled by different topography and climate that caused different flux into the ocean. The lands of northern SCS are located at stable continental block, and the river catchment contains large mid- and lower-reaches floodplain, mainly characterized by mixed crustal materials, while the islands of southern SCS are located at the active plate boundary zone. For instance, Sumatra still has active volcanic activities during the Holocene, so in addition to sedimentary rocks, there are also widely distributed mantle materials. The difference in lithology between the southern and northern lands controls the geochemical characteristics of river sediments, especially Sr and Nd isotopes composition. The northern land river sediments have lower εNd values and higher $^{87}Sr/^{86}Sr$ values, while the southern island river sediments show larger εNd values and lower $^{87}Sr/^{86}Sr$ values. The nearshore marine sediments are mainly affected by the adjacent rivers, while the sediments at the Sunda shelf or in the deep sea are mainly affected by the Mekong River and the Red River, and a small amount is affected by the sediments from the Borneo. Therefore, large rivers with large fluxes dominate the source of marine sediments. However, we also found that the major element compositions of river sediments and marine sediments do not correspond well, indicating that the river sediments selected as end-member are not representative enough when analyzing provenance. Therefore, cautious is needed when using river sediments as end members to trace the source of marine sediments.

Chapter 5 Sediment “source to sink” process and controlling factors in the southern SCS since the last deglaciation

The southern SCS includes the southern part of the SCS and the Sunda Shelf. The sediment provenance is complex due to multiple potential sources around the area. Previous studies mainly focused on the northern SCS (e.g., Liu et al., 2007b; Liu et al., 2003; Sang et al., 2022; Wang et al., 2021) and the research on the southern SCS is still very limited. Only a few studies pay attention to the sediment provenance of the southern SCS using clay minerals and major elements (Huang et al., 2021; Jiwarungrueangkul and Liu, 2021; Jiwarungrueangkul et al., 2019; Liu et al., 2011; Liu et al., 2012; Liu et al., 2016b). However, single proxy has various limitations, and clay minerals are affected by hydrodynamic sorting, meaning that the fine-grained components cannot fully represent the overall information of terrigenous debris (Garzanti et al., 2010). The SCS is located in the low-latitude tropical region, with active hydrothermal cycles. It is the second largest shallow continental shelf in the world, highly sensitive to sea level changes. During the lowstand of the glacial period, the Sunda Shelf was exposed as the Sunda Continent, potentially forming a new tropical rainforest in the low-latitude tropical region, significantly impacting the global carbon cycle (Wang, 2017). Therefore, it is necessary to conduct more comprehensive research on the provenance of sediments in the southern SCS to enable further in-depth geological and environmental studies. This chapter uses the elements, Sr-Nd isotope data of the core ST13 on the Sunda Shelf and the core 18288-2 on the continental slope in the southern SCS, with multiple proxies to determine the source of terrigenous debris in the southern SCS, and reconstruct the "source to sink" process since the last deglaciation.

5.1 Geochemical composition of clastic sediments

5.1.1 Geochemical composition of shelf sediments since 9 ka

The core ST13 is located in the middle of the Sunda Shelf and records environmental information since 9 ka. Overall, the terrigenous clastic components of bulk sediments of core ST13 are mainly composed of SiO_2, Al_2O_3, and Fe_2O_3, accounting for more than 85%. Since 9 ka, the major elements composition of the sediments has shown little variation, except for significant fluctuations around 4 ka and

8 ka. The average SiO_2 content is 65%, and the average Al_2O_3 content is 15%, with these two elements exhibiting opposite trends. The change of CaO element shows a two-stage pattern. The content before 4 ka is lower than that after 4 ka, with an average content difference of 15%, while other major elements do not show this trend. The change of Ti element is smaller, and its behavior is conservative in the earth surface environment. The trends of Fe_2O_3, MgO, and K_2O are consistent with that of Al_2O_3, while Na_2O shows an opposite trend, indicating that different controlling factors may be at play (Fig. 5.1, Appendix Table 7).

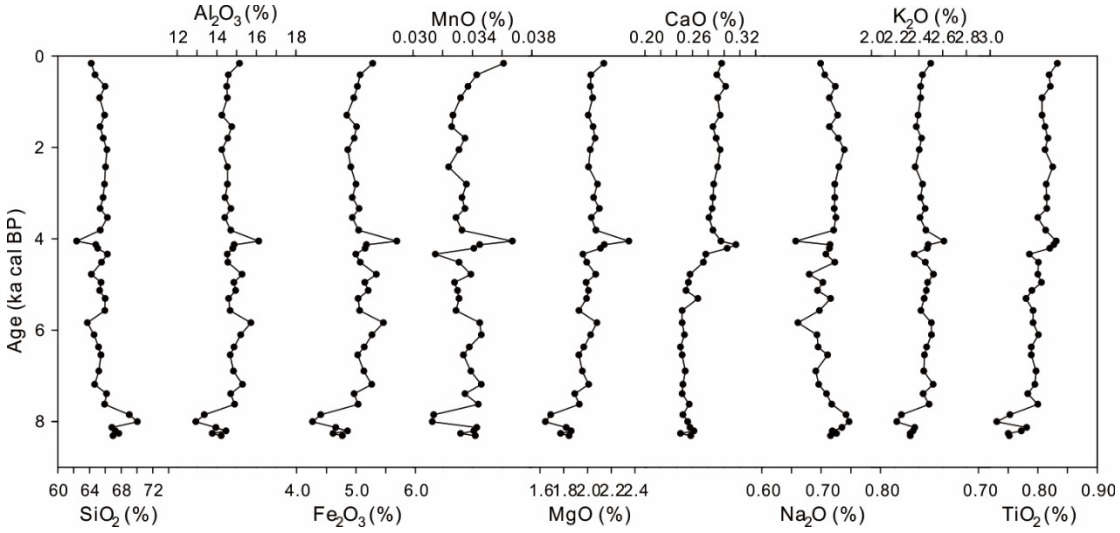

Fig. 5.1 Major elements composition in terrigenous clastic components of core ST13 sediments

The variation of Rb, Sc and Th are consistent with those of Al/Si, indicating that these three elements are greatly affected by grain size. The larger the grain size, the less the content. Rb usually exists in clay minerals and is easily weathered. Th and Sc are High field strength elements (HFSE). Th is mostly enriched in acidic rocks, while Sc is mostly enriched in basic rocks. The variation trends of the two are the same as the grain size, indicating that sediments rich in Th and Sc are greatly affected by hydrodynamic sorting during transportation. Th and U elements show a trend of decreasing content with increasing sedimentation age. The trends of REEs are generally consistent, with a wider range of variation compared to other trace elements. Unlike the major elements, the REEs concentrations exhibit significant fluctuations around 8 ka (Fig. 5.2, Appendix Table 8).

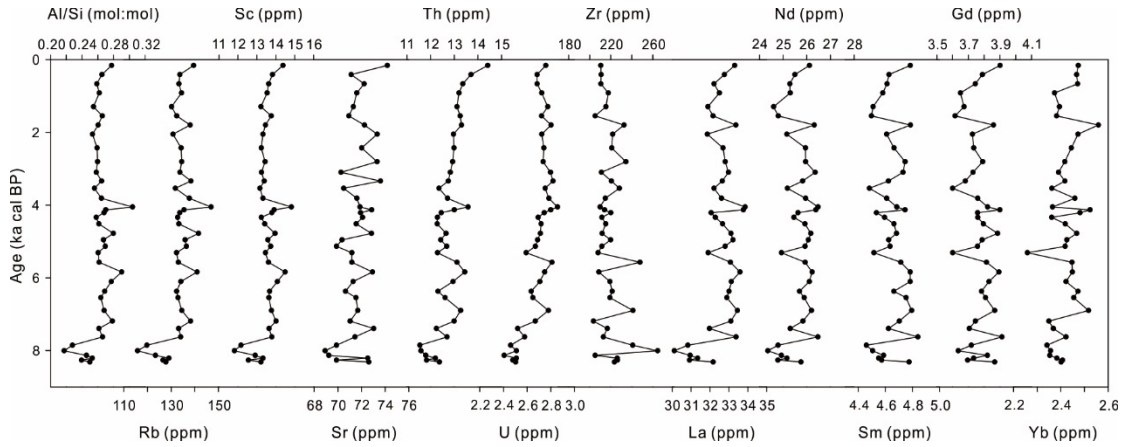

Fig. 5.2 Trace elements composition in terrigenous clastic components of core ST13 sediments

The $^{87}Sr/^{86}Sr$ ratio of core ST13 sediments varies from 0.72251 to 0.72415, with an average of 0.723437; the εNd value varies from -11.45 to 10.78, with an average of -11.06 (Fig. 5.3, Appendix Table 9). Similar to elemental variations, the $^{87}Sr/^{86}Sr$ values show significant fluctuations at around 4 ka and 8 ka, consistent with the trend of the Al/Si. This indicates that the $^{87}Sr/^{86}Sr$ isotopes are greatly influenced by grain size. The plot of $^{87}Sr/^{86}Sr$ versus Al/Si also demonstrates a good correlation; the larger the grain size, the lower the $^{87}Sr/^{86}Sr$ ratio (Fig. 5.4). The εNd value in the core sediments shows minimal variation, the difference between the maximum and minimum values is less than 1. Its poor correlation with the Al/Si ratio indicates that the εNd value is unaffected by grain size (Fig. 5.3 and 5.4). The $CaCO_3$ content in bulk sediment shows significant variation. From 0-4 ka, the average content is around 30%, but it decreases to about 10% after 4 ka. In contrast, the values of $\delta^{18}O$ and $\delta^{13}C$ do not show a decreasing trend from 4 ka. The $\delta^{13}C$ values start to decline from 7 ka, with the average value being greater than 0 between 0-7 ka and less than 0 after 7 ka.

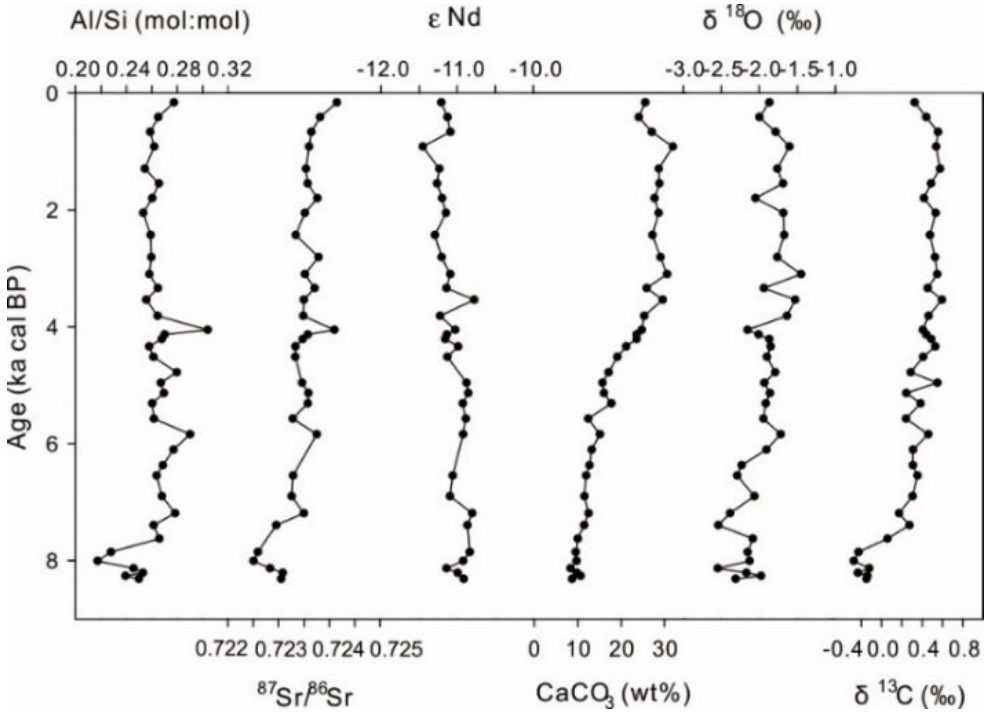

Fig. 5.3 isotopes composition of terrigenous clastic components and $CaCO_3$ content of the bulk sediments of core ST13 sediments

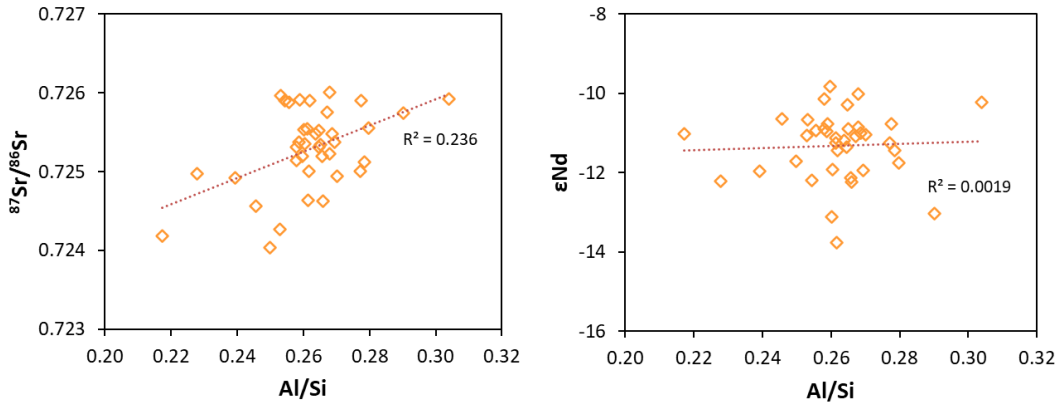

Fig. 5.4 Relationship between $^{87}Sr/^{86}Sr$, εNd and Al/Si in terrigenous clastic components of core ST13 sediments

5.1.2 Geochemical composition of slope sediments since 18.5 ka

The core 18288-2, located in the eastern slope of the Sunda Shelf, serves as a link between the Sunda Shelf and the southern SCS, recording environmental changes over the past 18.5 ka. Overall, the terrigenous clastic components are primarily composed of SiO_2, Al_2O_3, and Fe_2O_3, accounting for over 85% of the total content. As sediment age increases, SiO_2 and Al_2O_3 exhibit opposite trends, both showing changes around 15 ka. From 0-15 ka, SiO_2 content increases continuously, then decreases from 15-18.5 ka. Al_2O_3 shows the opposite trend. These two elements can serve as proxies for grain size,

indicating changes in hydrodynamic sorting. The stable element Ti remains conservative from 0 to15 ka with almost no change in content. However, after 16.5 ka, its content rapidly decreases, showing a trend nearly identical to that of Al_2O_3. The trends of the soluble elements MgO, CaO, Na_2O, and K_2O are almost consistent, displaying different amplitudes of fluctuation at different times (Fig. 5.5, Appendix Table 7).

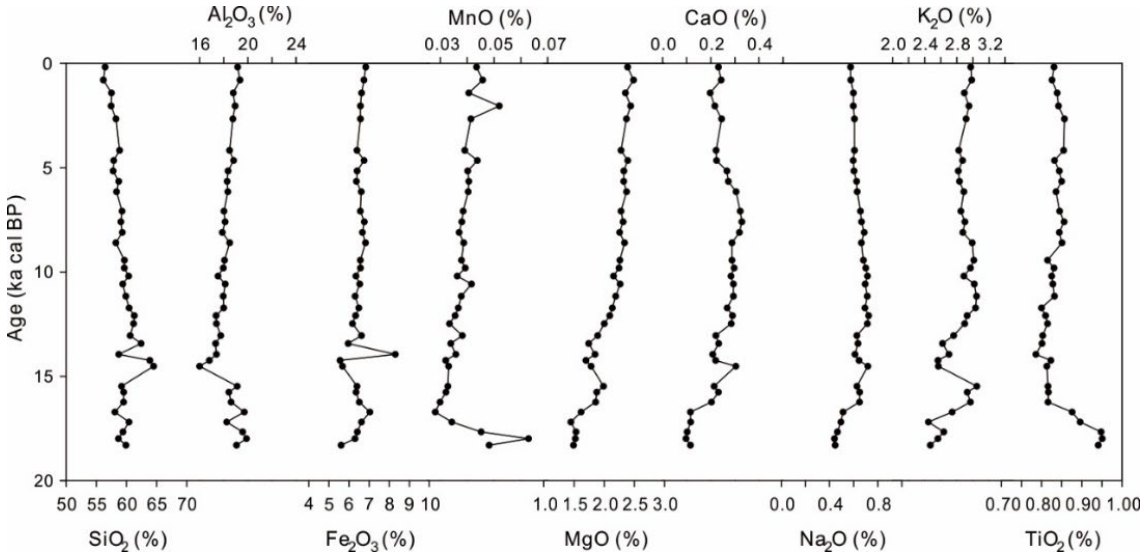

Fig. 5.5 Major elements composition in terrigenous clastic components of core 18288-2 sediments.

The variation of Sc and Th is consistent with that of Al/Si, indicating that these two elements are greatly affected by grain size. The coarser the grain size, the less the content. The variation of the two is the same as the grain size, indicating that sediments rich in Th and Sc are greatly affected by hydrodynamic sorting during transportation. The variation of Th and U elements is inconsistent. The variation of Th is consistent with the grain size, while the U content does decrease with the sedimentation age. The Zr content fluctuates significantly between 10-15 ka, remaining relatively stable during other periods. The trends of REEs are generally consistent with a small range of variation, showing fluctuations only during the 16.5-18.5 ka period (Fig. 5.5, Appendix Table 8).

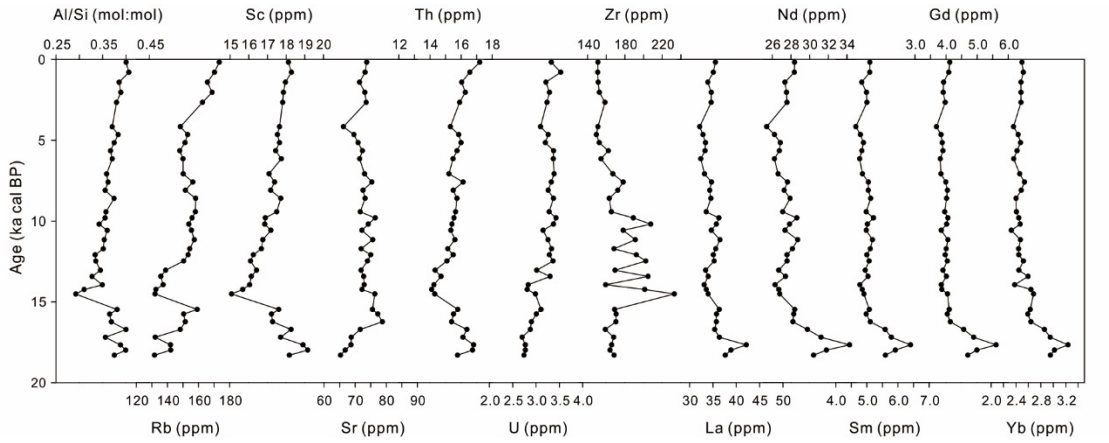

Fig. 5.6 Trace elements composition in terrigenous clastic components of core 18288-2 sediments

The $^{87}Sr/^{86}Sr$ ratio in the core 18288-2 sediment ranges from 0.721098 to 0.726394, with an average of 0.724302; εNd values range from -11.24to -8.70, averaging -10.42 (Fig. 5.7, Appendix Table 9). Figs. 5.7 and 5.8 show that both $^{87}Sr/^{86}Sr$ and εNd values have poor correlation with the Al/Si ratio, indicating that grain size has little impact on isotopic compositions. This is likely because the core 18288-2 is located on the continental slope, far from land. The sediments, having been transported for a long time, are well-mixed, fine, and uniform (after wet sieving, the mass of particles smaller than 50 microns accounts for more than 85% of the bulk sediment). Therefore, grain size effects on $^{87}Sr/^{86}Sr$ and εNd isotopes can be ignored. According to the variations in $^{87}Sr/^{86}Sr$, εNd, and elemental composition shown in Fig. 5.7, the overall trend since 18.5 ka is an increasing $^{87}Sr/^{86}Sr$ ratio and a decreasing εNd value. Both $^{87}Sr/^{86}Sr$ and εNd exhibit distinct segmentation, allowing the core to be divided into three stages from bottom to top. The first stage, from 18.5 to 16.5 ka, corresponds to the late LGM to the early Last Deglaciation, with stable $^{87}Sr/^{86}Sr$ and εNd values averaging 0.721506 and -8.99, respectively. The second stage, from 16.5 to 12.5 ka, marks the late Last Deglaciation. During this period, both grain size and $^{87}Sr/^{86}Sr$ values show significant fluctuations, with average $^{87}Sr/^{86}Sr$ and εNd values of 0.722974 and -10.23, respectively. The third stage, from 12.5 to 0 ka, encompasses the entire Holocene. During this period, $^{87}Sr/^{86}Sr$ and εNd values remain stable, averaging 0.725457 and -10.88, respectively.

The carbonate fraction in the bulk clastic sediments exhibits a distinct pattern: as sediment age increases, the carbonate ($CaCO_3$) content steadily decreases from approximately 20% to nearly 0%. Concurrently, $\delta^{13}C$ values also decrease, with a sharp drop to -20‰ during the third stage. The $\delta^{18}O$ values fluctuate significantly and do not show a clear decreasing trend with sediment age. However, similar to $\delta^{13}C$, there is a

sudden decrease to approximately -15‰ during the third stage, corresponding to the late Last Glacial Period to early deglaciation. There are two possible causes for these changes: (1) During the late LGM to early last deglaciation, shelf exposed as land due to lowstand and allowing large river systems to develop (Alqahtani, 2017; Hanebuth et al., 2011). The location of core 18288-2 at the paleo-river estuary increased terrestrial input, diluting the carbonate content and causing a rapid decrease in $CaCO_3$ and a negative shift in $\delta^{18}O$ values. (2) Measurement errors, as the $CaCO_3$ content in the third stage is less than 0.1‰ (PDB), causing $\delta^{13}C$ and $\delta^{18}O$ values susceptible to system errors and inaccuracies. Therefore, the carbonate composition needs to be further studied in combination with the actual geological conditions in the southern SCS.

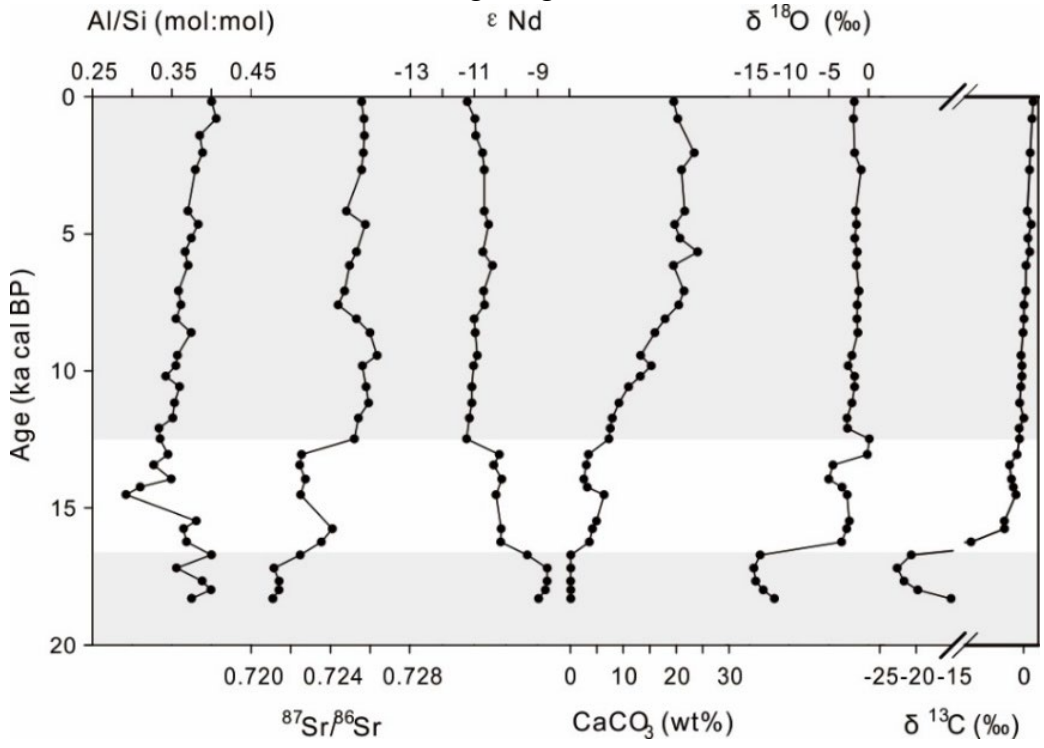

Fig. 5.7 isotopes composition of terrigenous clastic components, $CaCO_3$ content, $\delta^{18}O$ and $\delta^{13}C$ of the bulk sediments of core 18288-2 sediments.

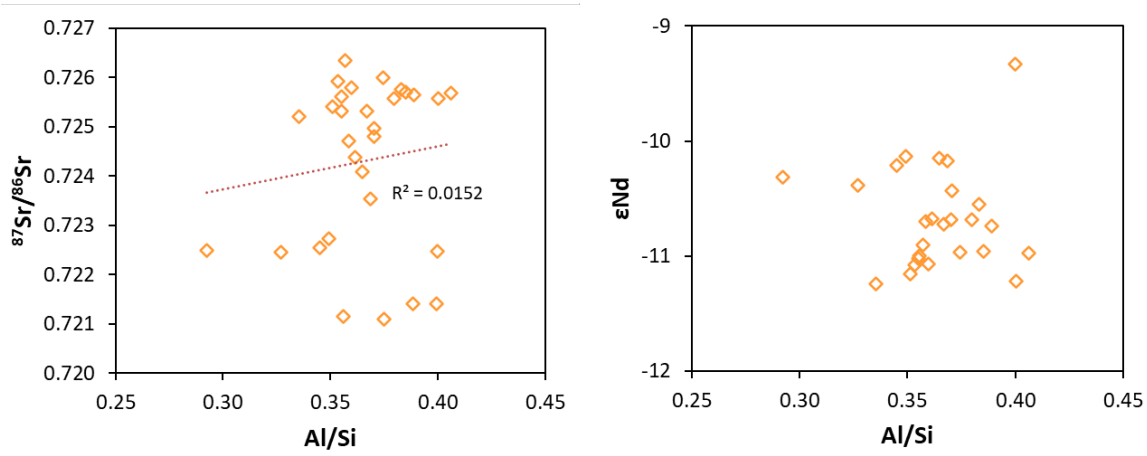

Fig. 5.8 Relationship between $^{87}Sr/^{86}Sr$, εNd and Al/Si in terrigenous clastic components of core 18288-2 sediments.

5.2 Sediments provenance of southern SCS since the last deglaciation

5.2.1 Potential source areas of sediments in the southern SCS

The terrigenous clastic debris of the SCS are primarily derived from surrounding river inputs, with aeolian contributions being minimal (Huang and Wang, 2006). Potential sediment sources in the southern SCS include the Mekong River, Thailand rivers, Malay Peninsula rivers, Sumatran rivers, Bornean rivers, and the Philippine island arc (Fig. 5.9). Current studies on the sediment provenance of the SCS are primarily focused on the northern region (e.g., Liu et al., 2007b; Liu et al., 2010; Liu et al., 2003; Sang et al., 2022; Wang et al., 2021). In contrast, research on the characteristics of terrestrial rivers and marine sediments in the southern region is limited, particularly comprehensive studies on geochemical composition. Current research on the provenance of sediments in the southern SCS primarily relies on comparing clay minerals in river and marine sediments. Clay minerals, as typical weathering products of the earth's surface, can indicate chemical weathering processes and semi-quantitatively assess the transport processes of river sediment (Huang et al., 2021; Liu et al., 2016b; Steinke et al., 2008). The Red River and Mekong River sediments of the Indochina Peninsula have high contents of illite and kaolinite, comprising about 70% of all clay minerals. Thailand river sediments are rich in smectite (42%) and kaolinite (32%). Malay Peninsula and Sumatran rivers sediments are dominated by kaolinite (78% and 57%, respectively). Different regions of Borneo show varied clay mineral compositions, with northern Borneo dominated by illite (~ 60%) and western and eastern Borneo by kaolinite (~ 45%). Smectite dominates river

sediments from the Luzon Arc (87%) (Fig. 5.10A). By comparing clay mineral types and contents in surface sediments of the SCS (Fig. 5.10B) (Liu et al., 2016b), the transport processes and sources of clay minerals in different regions of the southern SCS are inferred. Research on the sources of sediments in the southern SCS during geological periods is more limited due to sample constraints, as detailed in Chapter 1. Preliminary conclusions suggest that the Mekong River is the main sediment source for the southern SCS, with some materials from Borneo and Sumatra. However, the contributions from Thailand and Malay Peninsula rivers are disputed, and it is unclear whether the Red River in the north can transport sediments to the southern SCS. Nonetheless, all these regions are potential sediment sources (Huang et al., 2021; Jiwarungrueangkul and Liu, 2021; Qiao et al., 2015; Wu et al., 2023).

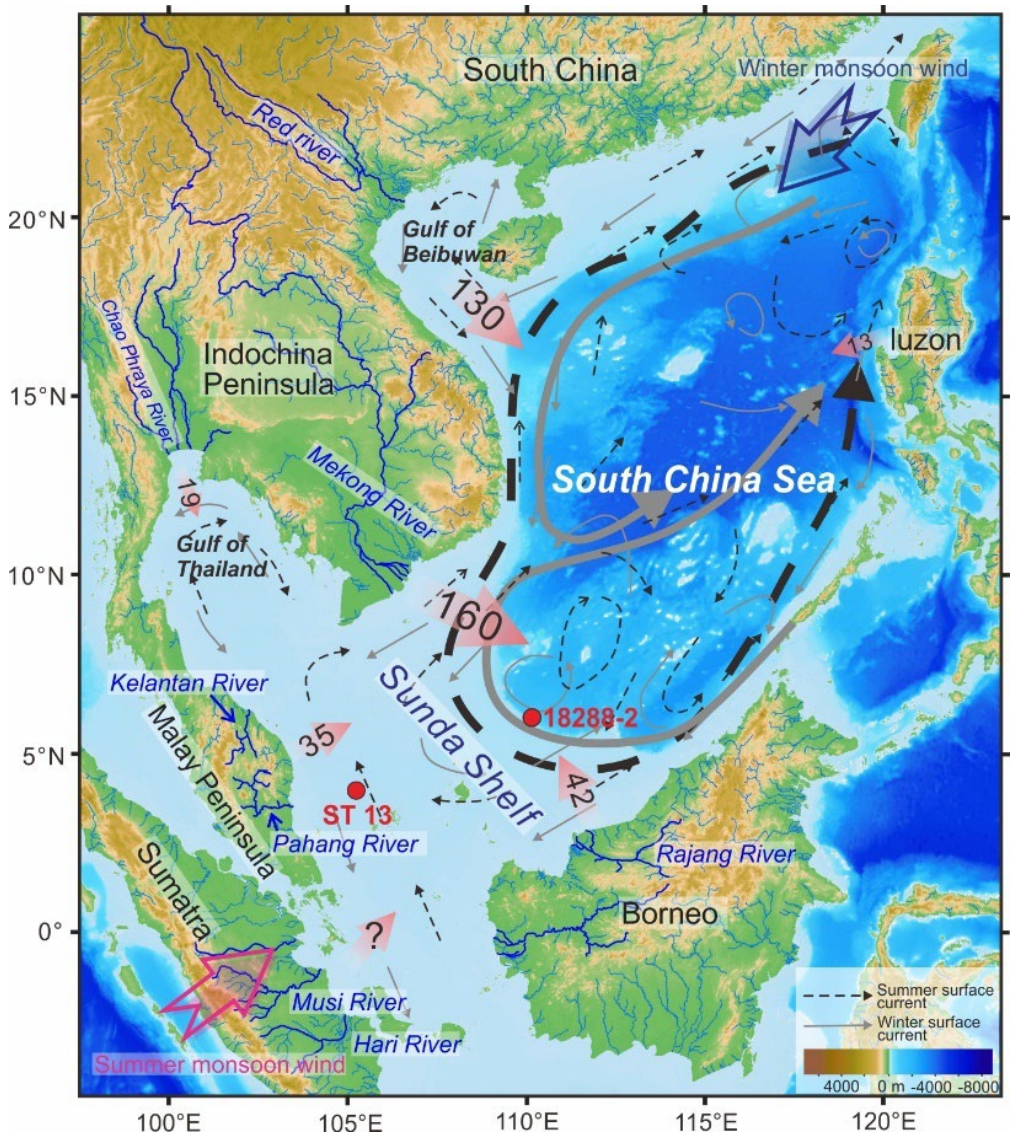

Fig. 5.9 Diagram of the land-sea pattern and surface current distribution in the SCS

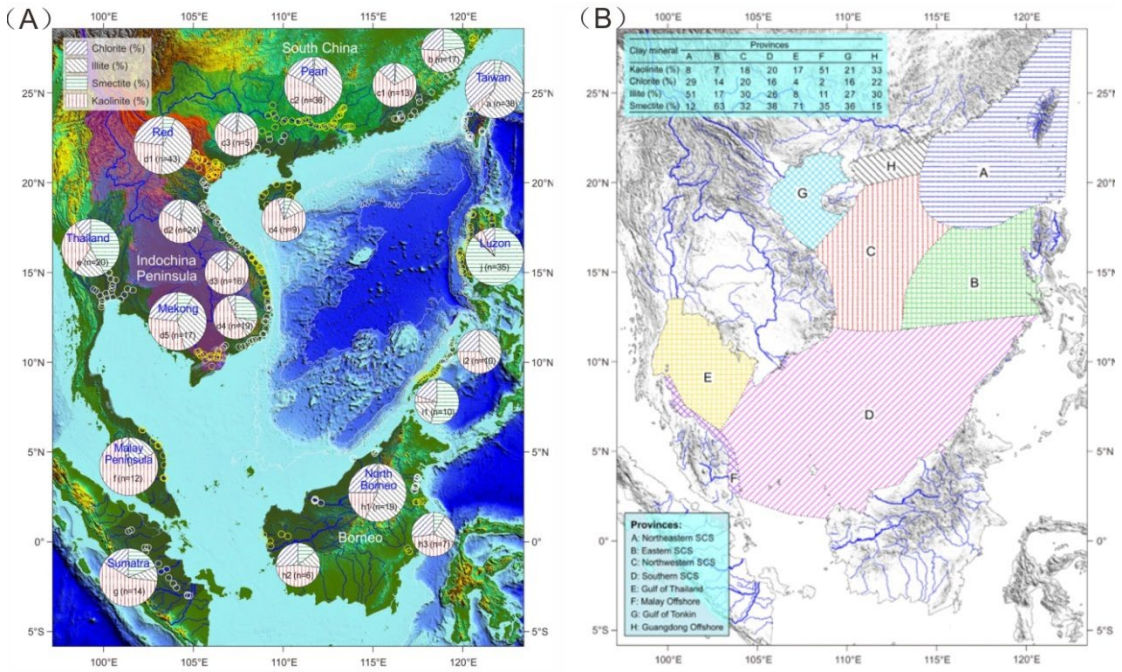

Fig. 5.10 (A) Distribution of clay minerals of river sediments surrounding the SCS. (B)Distribution of clay mineral assemblage provinces (A–H) in seafloor surface sediments of the SCS (Liu et al., 2016b).

5.2.2 Elements proxies

Elements are widely used to constrain the provenance of sediments. Different elements in minerals represent distinct geochemical characteristics, so appropriate elements must be selected for tracing sediment sources based on the geological background of different study areas (Taylor and McLennan, 1985). Generally, it is important to consider whether the element can effectively reflect the properties and geochemical composition of widely exposed rocks in the potential source area, whether it can be distinguished from other elements as an independent comparative end-member, and whether it can maintain stable properties during sediment erosion and transport to record the most complete source rock characteristics. Moreover, as previously mentioned, it is important to take care when selecting end-member values for provenance analysis. This study compares core sediments with both river sediments and marine sediments separately, aiming to more accurately trace the sources of marine sediments during geological periods.

According to different geochemical characteristics, trace elements can be divided into (1) high field-strength elements (HFSE), such as Nb, Ta, Zr, Hf, P, Th, HREE, etc. These elements are relatively stable during rock erosion, weathering and transportation. (2) large ion lithophile elements (LILE), such as Rb, Cs, Ba, Sr, etc. These elements are so active that are easily dissolved into water during catchment weathering and sediment

transportation. La and Th elements are usually found in felsic igneous rocks, while Sc is usually found in mafic igneous rocks. The La-Th-Sc triangle diagram is usually used to compare the sources of sediments (Bhatia and Crook, 1986) (Fig. 5.11). The distribution of core ST13 and 18288-2 sediments in the La-Th-Sc triangle diagram is relatively concentrated, mainly distributed in the area of the continental island arc. Except for the river sediments in the Malay Peninsula, which are distributed paralleling to the La and Th lines, the distribution of other river sediments is concentrated within the range of the continental island arc (Fig. 5.11A). Felsic plutonic rocks exposed in the Malay Peninsula caused river sediments to distribute parallel to the La-Th line. The distribution range of marine sea floor sediments is relatively wide. In addition to being distributed in the continental island arc, some samples are distributed in the active/passive continental margin feature area of the diagram (Fig. 5.11B). The SCS is located on the passive continental margin of East Asia. The sediments come both from stable continental blocks (such as South China) and relatively active islands block (such as Sumatra, Palawan, etc.). The marine sediments are fully mixed with sediments from different sources, so the geochemical composition will be more uniform than the river unit. Therefore, the marine surface sediments are distributed more widely in the La-Th-Sc triangle diagram, and the zoning characteristics of different regions will not be as clear as river sediments (Fig. 5.11B). As shown in Fig. 5.11 (A), the sediments of the two cores are affected by the Mekong River, the Red River and the Rajang River, while the influence of the rivers of the Malay Peninsula is relatively small. As shown in Fig. 5.11 (B), the sediments of the two cores overlap with the sediments of the offshore Indochina Peninsula and the offshore Borneo. However, it is difficult to clearly distinguish whether the source of the sediments of 18288-2 has changed since the last deglaciation period.

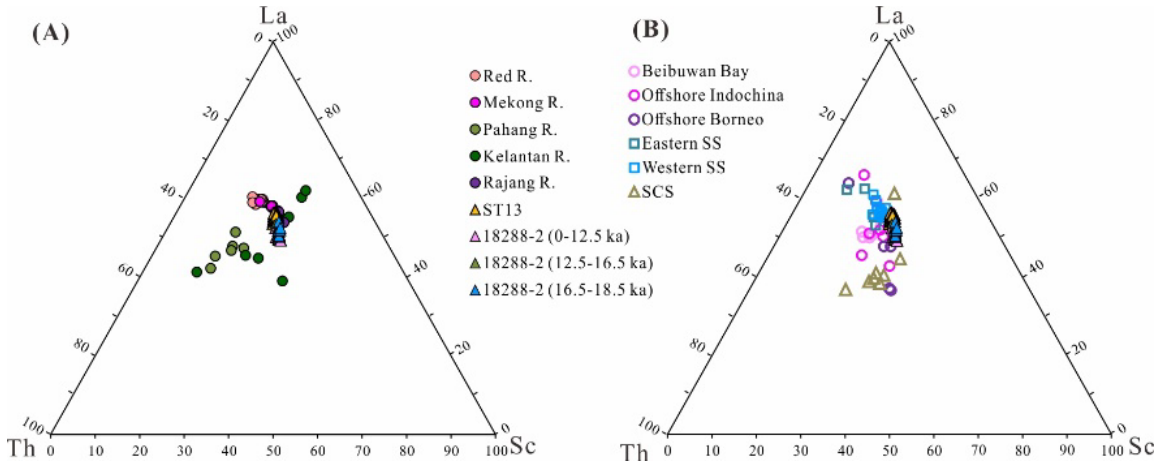

Fig. 5.11 Triangle diagram shows distribution characteristics of the La-Sc-Th of river, marine and core sediments

Th/Sc vs. Zr/Sc diagrams are often used to distinguish the compositional changes of clastic sediments during the deposition process and thus compare the sources of sediments. The diagram shows the magma differentiation line of the first cycle (black dashed line) and the sediment recycling process (red dashed line) (McLennan et al., 1993). The values of core ST13 sediments and core 18288-2 sediments are basically distributed along the red dashed line, indicating that the sediments deposited in the marine have undergone a sediment recycling process during the surface process on the continent, which is similar to the distribution characteristics of sedimentary rocks. The value of core sediments is close to the distribution characteristics of Mekong River and Borneo river sediments. In the core 18288-2, as the sedimentation age increases, the Zr/Sc value decreases. Zr is generally present in zircon, and it can also indicate that the coarse particles have a higher content of material, which is consistent with the grain size distribution characteristics indicated by the Al/Si ratio.

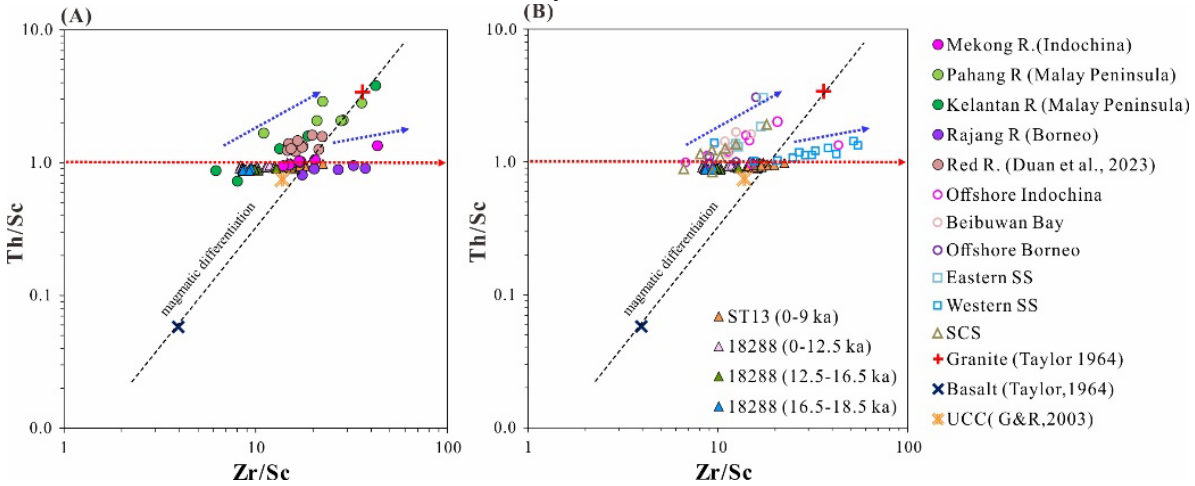

Fig. 5.12 Th/Sc vs. Zr/Sc characteristics of river, marine sea floor sediments and core sediments

Rare earth elements have stable chemical properties and undergo minimal fractionation during weathering and diagenesis. Their content is primarily controlled by the characteristics of the parent rock (McLennan et al., 1989). When using REEs to trace sediment sources, normalization is necessary. Typically, Upper Continental Crust (UCC), chondrites, or Post-Archean Australian Shale (PAAS) are used for normalization. This study uses chondrites for normalization, two main reasons: (1) to eliminate the sawtooth pattern in REE distribution curves caused by the odd-even effect of atomic numbers, allowing for a clearer representation of the separation degree between different elements, and (2) to facilitate the direct comparison of sample compositions relative to the early Earth or chondrites, thus better distinguishing parent rocks. δEu represents the europium anomaly, which in sediments typically reflects the characteristics of the source rock. The calculation of δEu is as follows: $\delta Eu=2\times(Eu)_N/[(Sm)_N+(Gd)_N]$, where the elements are normalised to chondrite values. Generally, $\delta Eu < 1$ indicates a negative anomaly, while $\delta Eu > 1$ indicates a positive anomaly. $(Gd/Yb)_N$ denotes the enrichment or depletion of HREEs, with higher values indicating greater depletion of HREEs. As shown in Fig. 5.13, the δEu values of sediments from the core ST13 and the 18288-2 are all less than 1, indicating a negative anomaly. The distribution of δEu values in the core ST13 sediments is similar to that of the stage Ⅰ of the Holocene in the core 18288-2. As the sediment age decreases in the core 18288-2, the degree of negative δEu anomaly increases, while the range of $(Gd/Yb)_N$ values remains relatively small. Comparing the distribution characteristics of river and surface sediments, the Holocene samples are similar to the sediments from the Mekong River, Borneo, and the offshore Indo-China Peninsula and the offshore Borneo. As the sedimentation age increases in the core 18288-2, the sediment distribution becomes more similar to that of Borneo river and its offshore sediments. Due to current research limitations, there is insufficient trace element data for the river sediments of Sumatra, making comparison difficult.

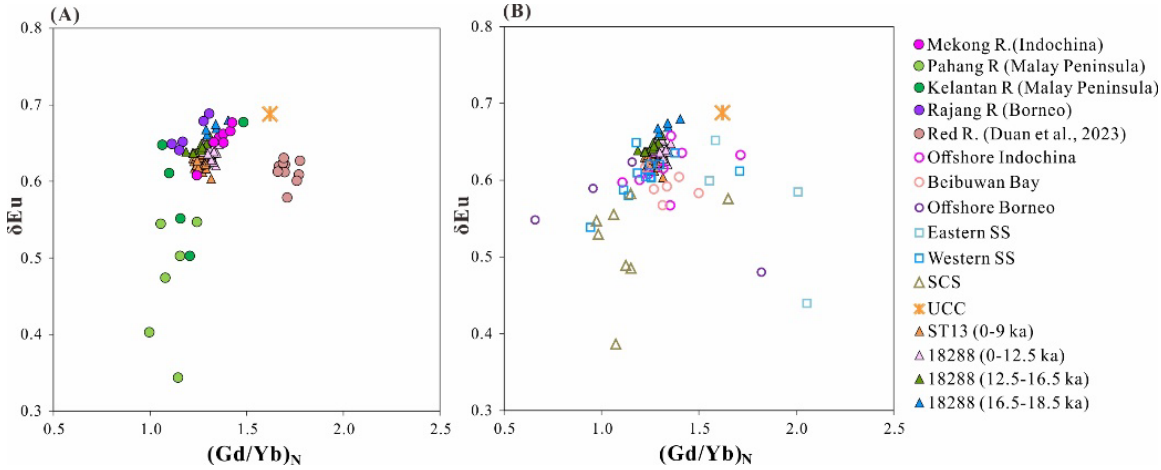

Fig. 5.13 δEu vs. $(Gd/Yb)_N$ characteristics of river, marine sea floor sediments and core sediments

5.2.3 Isotope proxies

It can be seen from Fig. 5.14 that the sediments from core 18288-2 are clearly divided into three stages from core bottom to top, consistent with the analysis in the vertical element variations. (1) Stage I (18.5-16.5 ka), Late LGM to early last deglaciation. (2) Stage II (16.5-12.5 ka), late last deglaciation. (3) Stage III (12.5 – 0 ka), the Holocene. From Stage I to Stage III, from the last deglaciation to the Holocene, the $^{87}Sr/^{86}Sr$ values decrease while the εNd values increase (Fig. 5.12). In Stage I, the $^{87}Sr/^{86}Sr$ and εNd values of core 18288-2 sediments fall within the range constrained by Sumatra, Borneo, the Kelantan River, and the Mekong River. In Stage II, these values are very close to those of Mekong River sediments and overlap with some Thailand river sediments. In Stage III, the $^{87}Sr/^{86}Sr$ and εNd values fall between the ranges of Mekong and Red River sediments and some Thailand river sediments (Fig. 5.14 A). Although from the Sr-Nd isotopes, the Kelantan River on the Malay Peninsula appears to be a source of core 18288-2 sediments, the sediment flux is very small of these island rivers. Additionally, coastal currents (Fig. 5.9) make it difficult for these sediments to transport to the slope, with most being deposited at the offshore Malay Peninsula (Wu et al., 2019). Although Thailand rivers have limited catchment areas, the variation of their Sr-Nd isotopes is wide. Currently, no definitive studies explain this phenomenon, but it is speculated that lithological differences and human activities affecting estuarine sediments may be the cause. However, the sediment flux of the four main Thailand rivers is very small, and the Gulf of Thailand is far from the slope. The Gulf of Thailand, a depression on the Sunda Shelf, receives most Thailand river sediments in its central and northern parts, while its southern part is influenced by Mekong River sediments (Liu et al., 2016a). Therefore, when analyzing sediment

sources on the Slope and the southern SCS during highstand, the contributions from Malay Peninsula and Thailand are very limited and can be considered negligible.

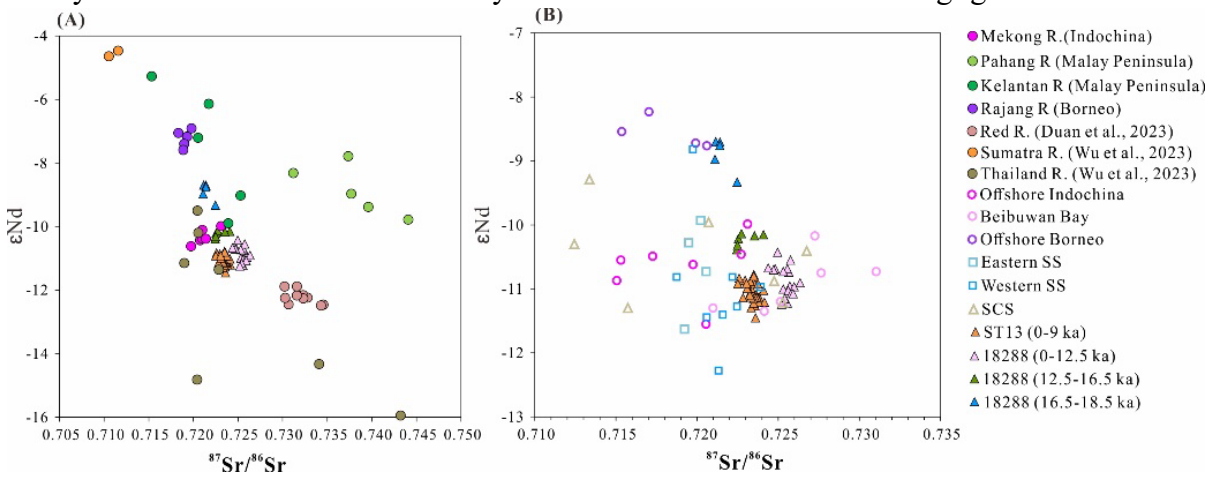

Fig. 5.14 $^{87}Sr/^{86}Sr$ and εNd isotope characteristics of river, sea floor sediments and core sediments

The Red River sediments in the southern land of South China, the Mekong River sediments in the Indochina Peninsula and the Thailand river sediments from the northern shelf generally have high $^{87}Sr/^{86}Sr$ values and low εNd values, while the Borneo and Sumatra river sediments at the southern shelf have low $^{87}Sr/^{86}Sr$ values and high εNd values, which are consistent with the results of previous studies (Figs. 4.8 and 4.9) (Li et al., 2003; Wei et al., 2012; Gui et al., 1993). It shows a transition from the mantle-derived characteristics of the terrestrial sediments in the southern Shelf to the crust-derived characteristics of the sediments in the northern Shelf, which is also consistent with the changes in $^{87}Sr/^{86}Sr$ and εNd values of the core 18288-2 sediments from the last deglaciation to the Holocene. Combined with the element composition characteristics of the sediments, the results indicating that the Mekong River, the world-class river, is the main source of sediments in the southern SCS. Specifically, During the Stage III (Holocene), it was also affected by sediments from the Red River in the northern shelf. In Stage II (late last deglaciation), it was also affected by materials from Borneo, which diluted the influence of materials from the Red River, so that the $^{87}Sr/^{86}Sr$ and εNd values of sediments in this period overlapped with those of Mekong materials. In Stage I (from late LGM to early last deglaciation), in addition to sediments from the Mekong River, the supply of sediments from southern islands (such as Sumatra and Borneo) increased, making the $^{87}Sr/^{86}Sr$ and εNd values of sediments in this period show mantle-derived characteristics (Fig. 5.14A).

The sedimentation age of the core ST13 sediments ranges from 9 to 0 ka, belonging to the Holocene. The variation range of Sr-Nd isotope values is generally

consistent with that of the Stage I samples of the core 18288-2. The difference in the average εNd isotope values of the two groups of samples is ΔεNd=0.64 (the average εNd_{ST13} value is -11.06, and the average $\varepsilon Nd_{18288\text{-}2}$ value is -10.42). The $^{87}Sr/^{86}Sr$ value of the core ST13 sediments is smaller than that of the Stage I sediments of the core 18288-2 ($\Delta^{87}Sr/^{86}Sr = 0.000865$), so the sources of the Sunda Shelf and slope sediments during the Holocene are generally the same. However, due to the numerous land and islands surrounding the southern SCS, the sediments source is complex, leading to varying influences from adjacent landmasses in different regions. Consequently, the difference of shelf provenance from the slope is that the source of most areas of the Sunda Shelf in the Holocene was dominated by the Mekong River. Nearshore areas of the shelf, close to the landmasses, are affected by sediment accumulation from smaller rivers such as those in Thailand and the Malay Peninsula, with only a small portion being transported to distant place by ocean currents.

Similarly, we compared the $^{87}Sr/^{86}Sr$ and εNd values of the core ST13 and 18288-2 sediments with those of the marine sea floor sediments to solve the problem of insufficient representativeness of river sediment sampling (Fig. 5.14B). As described above, marine sediments are more homogeneous mixed than river sediments due to long time transportation and recycling. The $^{87}Sr/^{86}Sr$ and εNd values of the core 18288-2 stage I sediments and the core ST13 sediments mainly distribute at the range of that of the Gulf of Beibuwan, Sunda Shelf and offshore Indochina Peninsula sediments. The $^{87}Sr/^{86}Sr$ and εNd values of the core 18288-2 stage II sediments mainly overlap with the offshore Indochina Peninsula sediments. The isotope composition of core 18288-2 stage III sediments are close to the isotope distribution range of offshore Borneo sediments. Unlike river sediments, there are no published data on the $^{87}Sr/^{86}Sr$ and εNd values from offshore Sumatra sediments. However, based on the geological background and lithology of the Sumatra, it can be inferred that its offshore sediments might have low $^{87}Sr/^{86}Sr$ and high εNd values, indicative of fresh mantle material. As most of these sea floor sediments come from the nearest rivers, by comparing the $^{87}Sr/^{86}Sr$ and εNd characteristics of core sediments and sear floor sediments, the similar conclusions about the provenance of cores as the comparison of river sediments can be got.

In summary, despite the limited basic geological surveys and published geochemical studies of the southern SCS and its surrounding regions, our comprehensive analysis of geochemical compositions of sediments suggest that during the Holocene highstand, the primary source of sediments for the Sunda Shelf and

southern SCS was the Mekong River. Sources also came from the Red River and the recycled material from the Gulf of Beibuwan and Sunda Shelf. Conversely, during the LGM and last deglaciation with low sea levels, while the Mekong River continued to supply sediments, there was an increasing contribution from southern islands rivers such as Sumatra and Borneo.

5.3 Transition of sediment “source to sink” processes during glacial cycles and its controlling factors

5.3.1 Sea level changes and sedimentation patterns in the southern SCS since the LGM

The Sunda Shelf, along with the surrounding Malay Peninsula, Sumatra, and Borneo, forms the Sunda Continent, which has been tectonocally stable duringe the Quaternary (Tjia and Kuala, 1980; Tjia and Liew, 1996). The Sunda Shelf is the submerged part of the Sunda Continent, with an average water depth of 70-80 meters and a slope of less than 0.03°. To the east, the shelf transitions into a steeper continental slope that connects with the SCS basin (Steinke et al., 2003).

The Sunda Shelf is a natural laboratory to study the sea level changes since the modern shelf is shallow and has a small slope. In recent years, the sea level research on the Sunda Shelf and its surrounding areas since the LGM has gradually increased (Bird et al., 2007; Geyh et al., 1979; Hanebuth et al., 2000; Hanebuth et al., 2009; Hesp et al., 1998). Shallow seismic profiles, AMS^{14}C dating of foraminifera and wood chip residues in core sediments were used to study the evolution history of the sea level changes since the LGM (Fig. 5.1) and the paleocoastline evolution map in the SCS (Fig. 5.16) (Sathiamurthy and Voris, 2006). The results show that during the LGM (~20-24 ka), the sea level dropped by about 120 m, and the Sunda Shelf was exposed as flat land. Around 19.6 ka, the sea level experienced its first pulse-like rise, and then around 14.5 ka, the second pulse-like rise occurred. Until 9 ka, the sea level rose at its maximum rate during this period. Around 5-6 ka, the sea level reached its highest point, about 5 m above the current sea level. Since 2 ka, the sea level has been stable at the current level (Hanebuth et al., 2000; Hanebuth et al., 2011; Tjia, 1996). Combined with the time scale of this study, the sea-land pattern maps of the Sunda Shelf at several key time points were selected: 21 ka, about 116 m below the modern sea level; 18.02 ka, about 110 m below the modern sea level; 16.8 ka, about 105 m below the modern sea level; 12.75 ka, about 60 m below the modern sea level; 8.38 ka, about -10 m below the

modern sea level; 4.2 ka, about 5 m above the modern sea level. These maps show the complete process of the Sunda Shelf from exposure to being submerged by seawater. Overall, before the early Holocene, most areas of the shelf were submerged, with an average water depth of 50 m (Fig. 5.16).

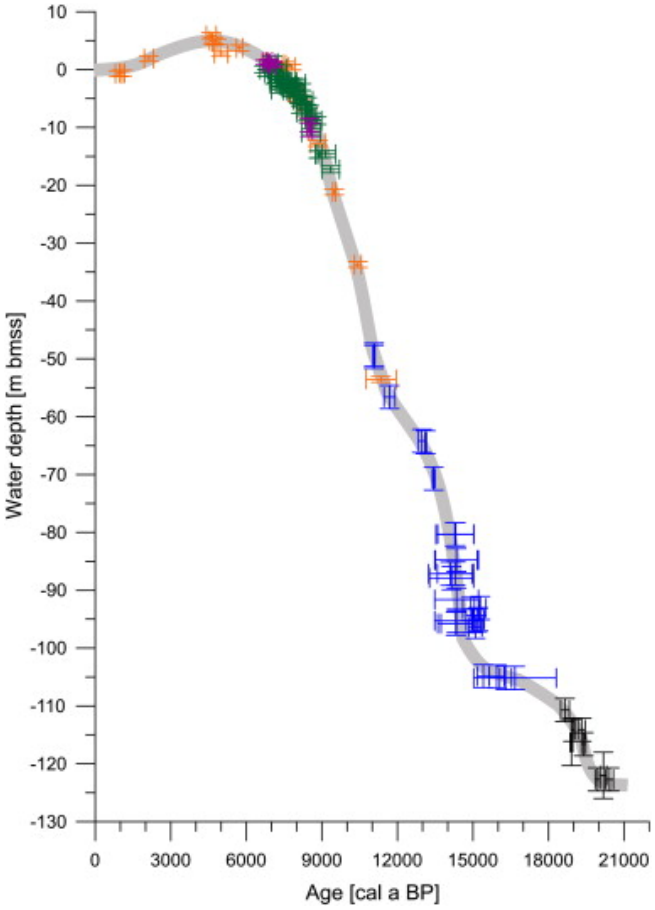

Fig. 5.15 Sea level evolution history of the Sunda Shelf and its surrounding area over the past 21 ka, black data are from the Sunda Shelf (Hanebuth et al., 2009), blue data are from the Sunda Shelf (Hanebuth et al., 2000), orange data are from the Strait of Malacca (Geyh et al., 1979), green data are from the Singapore (Bird et al., 2007), and purple data are from the Singapore (Geyh et al., 1979; Hesp et al., 1998).

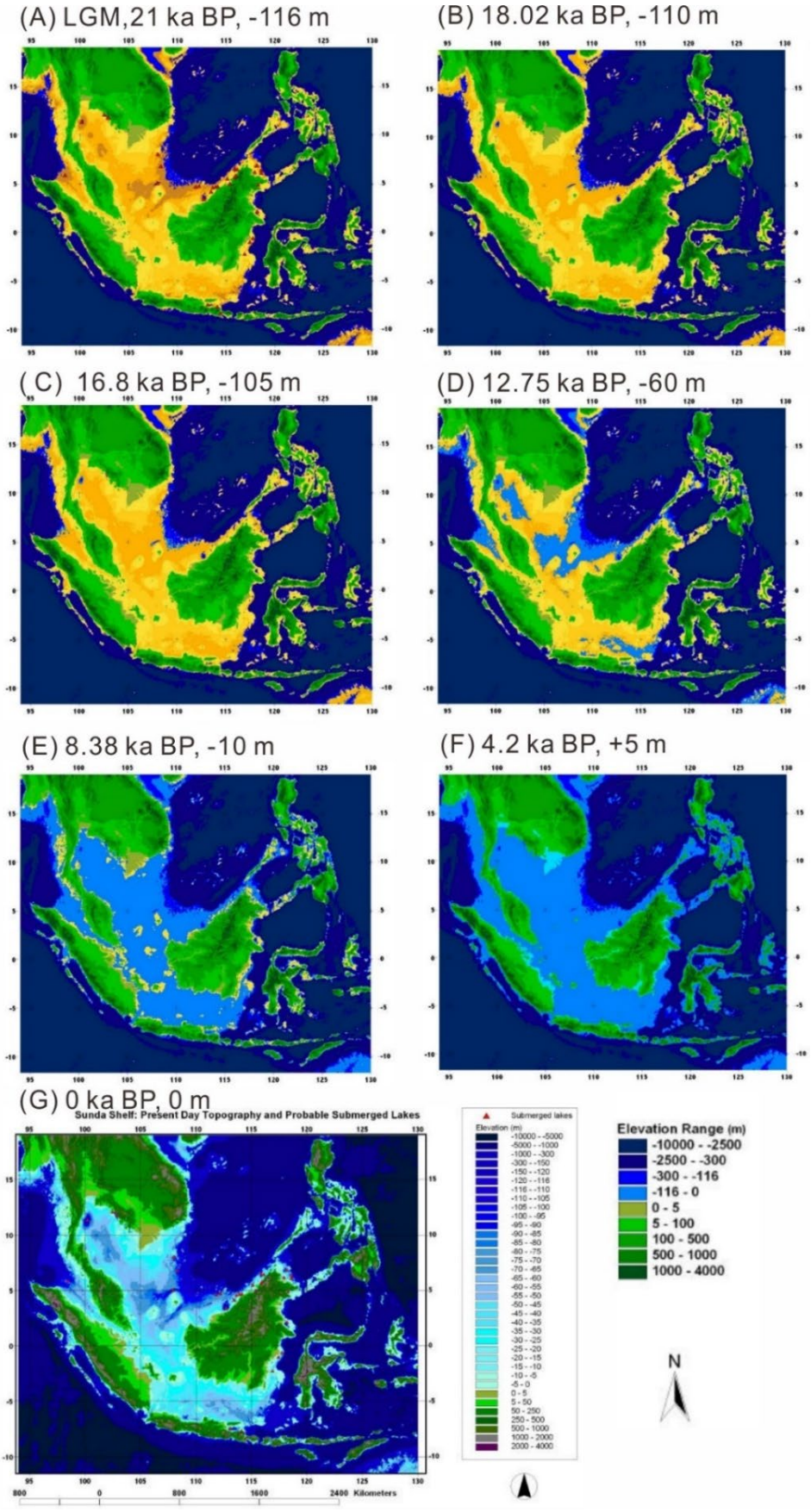

Fig. 5.16 Distribution of land-sea patterns in the Sunda Shelf and surrounding areas at different periods since the LGM (Sathiamurthy and Voris, 2006).

Based on current core sediment records, the sedimentary processes on the Sunda Shelf and Slope can be divided into several stages (Steinke et al., 2003): (1) 20-16.5 ka: during the low sea level and gradual rise period, the sedimentary record on the shelf edge and continental slope is characterized by fine-grained siliciclastic sediments and high accumulation rates of terrigenous organic matter as a result of shelf erosion and fluvial transport. (2) 16.5-14.5 ka: during the continued slow rise in sea level, estuary of paleo-river began to retreat. Clay mineral and organic matter content start to decrease in sediments, while carbonate content increased. The depocenter shifted from the slope to the shelf. (3) 14.5-14 ka: sediment supply to the continental slope decreased, with no significant change in shelf sedimentation. (4) 14-8.5 ka: during the rapid sea level rise, paleo-river systems in the central shelf were submerged, further reducing sediment supply of the slope. (5) 8.5-3 ka: during the Holocene highstand, most of the shelf was submerged, the coastline reached its present position, and the modern sedimentary patterns were established.

During the lowstand, the Sunda Shelf was exposed as a broad, flat land. The study area of the Sunda Shelf features three major paleo-river systems from north to south: the Paleo-Mekong River, the Siam River system, and the North Sunda River system (Fig. 5.17B). The Paleo-Mekong River developed mainly on the shelf of the Indochina Peninsula and connected with the Mekong and its delta. Due to the narrow shelf, this paleo-river system was relatively short. The Siam River system connected the Chao Phraya River in Thailand with rivers on the Malay Peninsula. The upper reaches river channels were covered by fine sediments due to the depression in the Gulf of Thailand. The North Sunda River system is the largest paleo-river system at the exposed Sunda Shelf and is recognized as such in current research. It connected rivers of Sumatra and western Borneo to the slope (Solihuddin, 2014; Voris, 2000).

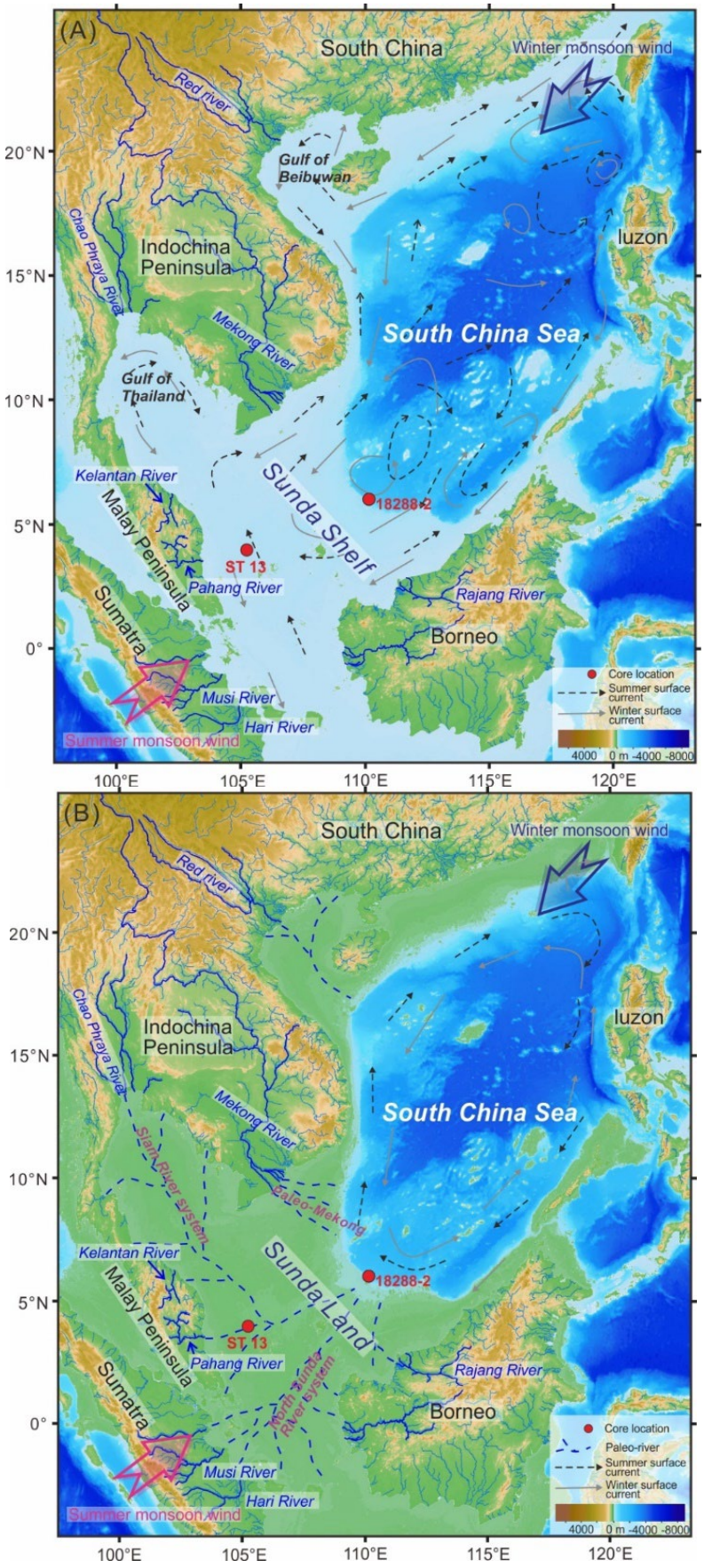

Fig. 5.17 Schematic diagram of the sea-land pattern during the highstand (A) and lowstand (B) in the SCS. The paleo-rivers shown in (B) is modified from Voris (2000).

5.3.2 Source to sink process and pattern changes during the glacial and inter glacial cycle

From Fig. 5.16, it is evident that since the LGM, rising sea levels have caused river estuary to retreat, gradually submerging the Sunda continent and expanding the Sunda Shelf. During low sea level periods, the shelf was exposed, allowing paleo-river systems to develop. These rivers transported eroded or remobilized materials from surrounding lands and the shelf directly to the slope and the southern SCS, resulting in terrigenous input during glacial periods being five times higher than during interglacial periods (Schönfeld and Kudrass, 1993; Wang, 1999). The sedimentation rates calculated by AMS^{14}C dating of core 18288-2 sediments during the lowstand were 3-4 times higher than during highsrtand (Fig. 3.4B). Other studies in the southern SCS have the similar results (Huang et al., 2016; Zhao et al., 2023). As sea levels rose, paleo-river estuary retreated, and the depocenter shifted from the slope and shelf break to the inner shelf and offshore regions (Steinke et al., 2003). Sediment transport to the slope changed from direct river delivery to marine surface current transport, resulting in a gradual decrease in sediment supply. During the transition of the Sunda Shelf from exposure to submergence, its role in the sedimentary process in the SCS shifted from a "source" to a "sink." This shift from source to sink complicates the study of sediment recycling and weathering processes.

5.3.3 Controlling factors of the “source to sink” process in the southern SCS since the last deglaciation

According to the analysis of geochemical proxies, during glacial period with lowstand, the sediments of the slope and the southern SCS were supplied by the Mekong River and the rivers of islands in the southern shelf. As the sea level continued to rise and the continental shelf was submerged, the supply of the island rivers in the southern shelf gradually decreased, and the supply of materials from the large rivers in the northern shelf increased. During the interglacial period with highstand, the Mekong River was the main source of the Sunda shelf and southern SCS, and the sediments from the surrounding islands could only deposit near the coast. The slope and deep sea were also supplied with sediments from the Red River and/or Gulf of Beibuwan in the northern SCS.

After comprehensive analysis, it is believed that the following four factors control the sediments provenance changes of high and low sea levels:

(1) Sea level changes. Since the LGM, rising sea levels have altered the land-sea

configuration of the Sunda Shelf and southern SCS. During low sea level periods, the Sunda Shelf was exposed as a vast plain, developing numerous paleo-river systems. These rivers transported eroded materials from islands in the southern SCS and the shelf directly to the slope and deep sea, with the depocenter mainly located at the shelf edge-slope. As sea levels rose, marine transgression caused river estuary to retreat, shifting the depocenter inward to the shelf. Due to the gentle slope of the Sunda Shelf, less than 0.03°, only relatively fine particles could be suspended and transported to the slope and deepwater areas through surface current during this period. Consequently, sediment on the slope decreased, while sediment on the shelf increased. During high sea level periods, rivers transported sediment to estuary, where most of it accumulated nearshore. A smaller portion was transported over long distances by ocean currents, allowing material from large rivers like the Mekong and Red Rivers to be deposited on the slope and in deepwater areas.

(2) River flux and transportation distance. Currently, research on sediment flux from rivers in the northern SCS flowing into the SCS is extensive, whereas studies on southern island rivers are relatively sparse. According to Table 2.1, the annual sediment flux of the Mekong River is 150 Mt/yr, dominating potential sources around the southern SCS. The Red River follows with 110 Mt/yr. However, due to its greater distance from the Sunda Shelf and southern SCS, and the influence of hydrodynamic sorting, most Red river sediment is not transported far in the ocean. Only a small fraction of fine particles from the Red River or Gulf of Beibuwan reaches the southern SCS. Compared to the Mekong and Red Rivers, sediment fluxes from other island rivers are very small, making it difficult for them to supply sediment to the slope and deepwater areas. Research indicates that sediment from small island rivers, such as Malay Peninsula, primarily accumulates nearshore along the coast (Wu et al., 2019), and is not transported over long distances. Therefore, during high sea level periods, large rivers like the Mekong River are the main sources of material for the Sunda Shelf and southern SCS.

(3) Ocean currents. The SCS is located in the southeast Asian monsoon region. The ocean surface currents are affected by the monsoon with seasonal differences. The southwest monsoon prevails in summer, forming a clockwise ocean current system on the surface of the SCS, while the northeast monsoon

prevails in winter, forming a counterclockwise surface ocean current system. Both the summer and winter monsoons form a strong western boundary current at the boundary of the western SCS close to the land, thus transporting sediments from the Red River and recycled materials from the floor of the shelf to the slope and deep sea.

(4) Climate change. At present, the SCS is located in a low-latitude tropical region and is influenced by monsoon, which results in generally high temperatures and abundant rainfall. Heavy rainfall intensifies the erosion and weathering of source rocks, leading to increased sediment supply from major river basins. During glacial periods, global temperatures decrease, and precipitation patterns change. Current research indicates that because the southern SCS is near the equator and close to the source of the southwest monsoon, areas of Sumatra and Borneo still supported tropical rainforests during glacial periods. In contrast, central part in exposed shelf areas and Indochina Peninsula mainly developed savannas (Sun et al., 2000; Wang et al., 2009). This suggests that during glacial periods, precipitation in the southern shelf was higher than in the northern land areas. Consequently, during glacial periods, the southern islands experienced intense physical erosion due to abundant rainfall. Surface rock and sediments were eroded, providing substantial sediment input into the sea. Well-developed paleo-river systems transported these sediments to the continental slope. Additionally, 5°-30°N is prone to tropical storms, which will cause hurricanes and strong tidal currents, disturbing or remobilizing the surface sediments in shallow waters. Given the average shelf depth of 50-70m, surface sediments in the Gulf of Beibuwan, the offshore shelf of the Indochina Peninsula, and the northern Sunda Shelf are re-mobilized during storm seasons. These remobilization materials are fine-grained sediments, which can be transported long distances by ocean currents. Current research shows that about 30-50% of the fine-grained sediments deposited in the Yangtze River estuary and submerged delta are re-mobilized by diluted water and tidal currents, and transported to the East China Sea shelf and Okinawa trough (Liu et al., 2007a; Xu et al., 2012).

5.4 Summary

According to geochemical analyses, the evolution of sediment provenance in the

southern SCS since the last deglaciation has been revealed. From the late LGM to the early last deglaciation period with lowsatnd, sediments deposited in the slope and southern deep-water regions were primarily from the Mekong River and rivers from islands in the southern shelf. As sea levels rose, the shelf gradually submerged, reducing sediment input from island in the southern shelf and increasing supply from large rivers in the northern shelf. During the high sea levels of the Holocene, the Mekong River became the primary source of shelf sediment, while materials from surrounding islands just accumulated mainly near the shore. The slope and deep-water areas were also influenced by sediments from the Red River and the Gulf of Beibuwan in the northern SCS. Sea level changes primarily influenced provenance and depocenter. During low sea levels, the shelf was exposed, where paleo-river systems developed, and materials from islands were directly transported to the slope by rivers. More sediments transported to the slope due to abundant rainfall in equatorial regions during glacial periods led to erosion of island surface materials, resulting in higher sedimentation rates on the slope than highstand. As sea levels rose, material from islands in the southern shelf gradually decreased, while contributions from large rivers in the northern shelf increased. During high sea levels, sediment flux from large rivers was 5-10 times greater than from island rivers, making the Mekong River the dominant source. Additionally, reworked seafloor sediments from the Sunda Shelf and sediments from the Red River and Gulf of Beibuwan were also transported to the southern SCS by ocean currents. Sea level changes are the primary factor influencing the sediment source variation in the southern SCS since the last deglaciation. Additionally, climate, ocean currents, and sediment flux collectively impact the sediment sources. However, due to limited study materials on the southern SCS, there are no definitive conclusions about the evolution of sediment sources, necessitating further in-depth studies.

Chapter 6 Uranium-series disequilibrium reveals erosion of islands in the southern Sunda Shelf during the lowstand

6.1 Overview and development of the principles of the U-series disequilibrium method

Uranium (U) is a natural element widely found in rocks, soil, and water on Earth. Its atomic number is 92, making it one of the heaviest elements. In the natural environment, uranium usually contains three types of radioactive isotopes, namely ^{238}U (abundance is 99.28%), ^{235}U (0.71%), and ^{234}U (0.0054%). ^{238}U undergoes 14 consecutive α decays and β decays to eventually form a stable isotope ^{206}Pb, which is called uranium series decay (Fig. 6.1). The decay period lengths of each parent and daughter in uranium series decay are different. Therefore, the radioactive isotope dating method developed using this characteristic has been used in different types of rocks, sediments, and geological processes of different time scales, promoting the great development of earth science (Andersen et al., 2017).

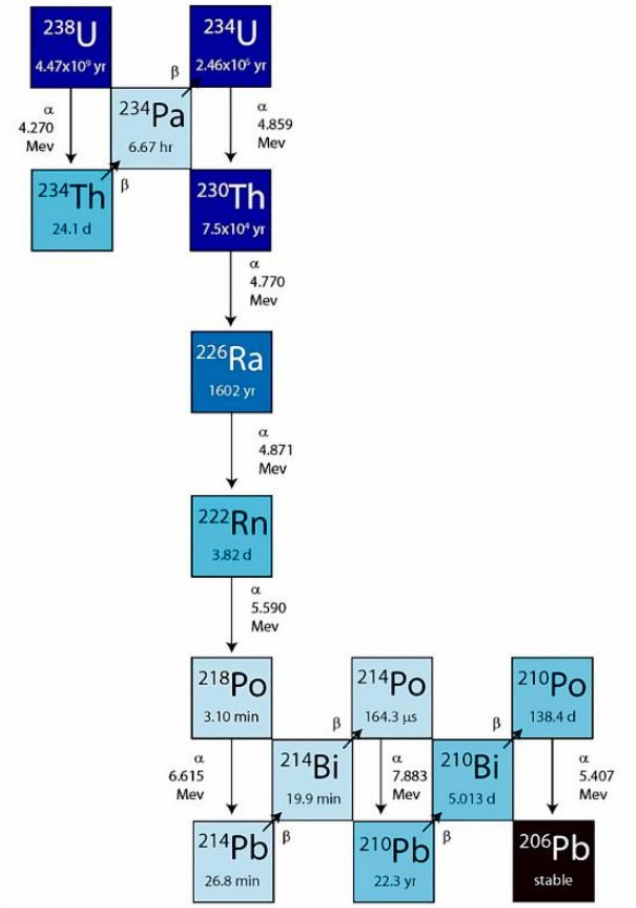

Fig. 6.1 Uranium-238 decay chain

Uranium isotope radiometric dating has been extensively used in the study of Earth's rock evolution. However, the uranium series disequilibrium method differs from traditional uranium isotope dating. It refers to the change in the ($^{234}U/^{238}U$) activity ratio of fine-grained materials caused by α-decay recoil. This ratio is controlled solely by the time of rock fragmentation and is independent of the type and formation time of the source rock, making it a simple method for tracing time (DePaolo et al., 2006). The half-life of ^{238}U is very long. Over time, the number of ^{234}U, ^{230}Th, and ^{226}Ra atoms initially increases exponentially and then stabilizes after approximately 1 Myr. In a closed system, if the half-life of the parent isotope is much longer than that of the daughter isotope, after several daughter isotope half-lives, the production rate of the daughter isotope matches its decay rate. Consequently, the parent-to-daughter radioactive activity ratio no longer changes with time, reaching "secular equilibrium", where the activity ratio (parent/daughter) equals 1.

^{238}U in rocks undergoes one α decay and two β decays to form ^{234}U, which is specifically manifested as ^{238}U decaying into ^{234}Th through α decay, with a half-life of 4.47 billion years. ^{234}Th decays into ^{234}U through two β decays. The half-lives of these two decays are very short, 24.1 days and 6.7 hours respectively. ^{234}U is usually unstable and decays into ^{230}Th through α decay, with a half-life of 246,000 years (Cheng et al., 2013). After 1Myr, ^{238}U and ^{234}U reach secular equilibrium, that is, ($^{234}U/^{238}U$) = 1,

$$\lambda_{238} \times {}^{238}U = \lambda_{234} \times {}^{234}U\lambda \quad (6.1)$$

Among them, λ is the decay constant, ^{238}U and ^{234}U are the atomic numbers of the two nuclides.

Since the absolute value of $^{234}U/^{238}U$ is very small, $^{234}U/^{238}U$ is usually expressed by the radioactivity ratio at equilibrium ($^{234}U/^{238}U$), that is:

$$\left(\frac{^{234}U}{^{238}U}\right) = \frac{^{234}U}{^{238}U}\frac{\lambda_{234}}{\lambda_{238}} \quad (6.2)$$

That is, usual secular equilibrium, ($^{234}U/^{238}U$) = 1.

In earth surface environments, various geological processes can disrupt this closed system, causing the production and decay rates of nuclides to become inconsistent and break the secular equilibrium.

After the equilibrium is disrupted, and in the absence of other geological factors, the system will return to equilibrium after 5-6 half-lives of the daughter nuclide (Bourdon et al., 2003). When ^{238}U decays to ^{234}Th, it releases an α-particle. Due to recoil, ^{234}Th gains kinetic energy and is displaced, a process known as "α recoil" (Fig.

6.2). When rock is fragmented to a small particle (generally considered to be 50 μm) or the specific surface area increases significantly, α-recoil causes the loss of ^{234}U. This results in the accumulation rate of ^{234}U within particles being lower than the production rate, thus secular equilibrium is broken. Over time, the ($^{234}U/^{238}U$) activity ratio of the particles decreases until forming a new equilibrium. Based on this principle, by measuring the ($^{234}U/^{238}U$) activity ratio in geological samples such as rocks, soils, or sediments, to evaluate the timing of various geological processes to establish the method of U-series disequilibrium dating (DePaolo et al., 2012; DePaolo et al., 2006; Dosseto et al., 2008).

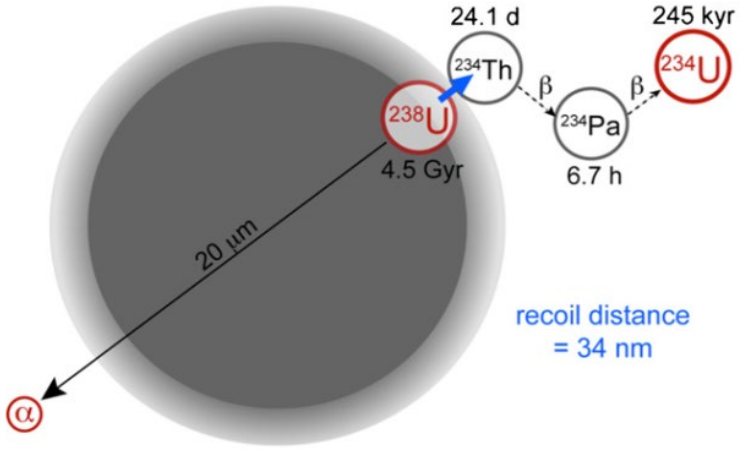

Fig. 6.2 Conceptual model of α-recoil effects (DePaolo et al., 2012).

It is generally believed that the degree of ($^{234}U/^{238}U$) disequilibrium of a particle depends on (1) the time it takes for the particle to break, which is usually measured from the time the particle breaks to less than 50 μm, recorded as t_{com}, called it *Comminution Age*. (2) The proportion of ^{234}Th recoiled from the particle during α recoil is related to factors such as particle morphology and surface properties, which is called the recoil loss factor ($f\alpha$) (DePaolo et al., 2012). Therefore, using the measurement value of the particle ($^{234}U/^{238}U$) (can be represented by A_{means}), we can get:

$$A_{means} = (1 - f_\alpha) + [A_0 - (1 - f_\alpha)]e^{-\lambda_{234} t_{com}} \quad (6.3)$$

Where A_0 is initial ($^{234}U/^{238}U$) value of the rock, and it is usually assumed that $A_0 = 1$. λ_{234} is the decay constant of ^{234}U (unit: yr^{-1}), and t_{com} can be further written as:

$$t_{com} = -\frac{1}{\lambda_{234}} \ln\left[\frac{A_{meas} - (1 - f_\alpha)}{A_0 - (1 - f_\alpha)}\right] \quad (6.4)$$

From equation (6.4), $f\alpha$ is an important parameter. There are many ways to calculate f_α. Different methods of calculating f_α may lead to large deviations in t_{com} (Handley et al., 2013a; Handley et al., 2013b). This study mainly uses a method based on grain size distribution of sediments to calculate $f\alpha$ (DePaolo et al., 2006)

$$f_\alpha = \int_{\frac{L}{2}}^{r_{max}} X(r)\beta(r)\lambda_s(r)\frac{3}{4}\left(\frac{L}{r} - \frac{L^3}{12r^3}\right)dr \qquad (6.5)$$

where L is the ^{234}Th α-recoil length and is assumed to be 0.03 μm, r is the grain radius (in μm). X(r) is the volume fraction of grains with radius r. β(r) is the aspect ratio of the grain and λs is the surface roughness factor. Assumptions are required for the aspect ratio (β), surface roughness (λs). The aspect ratio (β) is previously assumed to range between 1 for the largest grain and 10 for the smallest grain (DePaolo et al., 2012; Dosseto et al., 2010), while surface roughness factor (λ_s) is expected to be 10 for the largest grains and 1 for the smallest grains (Handley et al., 2013a). Combining Eq. (6.4) and Eq. (6.5), and using the measured ($^{234}U/^{238}U$), the communication age can be calculated.

The application of U-series disequilibrium methods in geology began in the 1960s, driven by advancements in instrumentation and analytical techniques. Initial α-spectrometry methods evolved into high-precision low-concentration uranium analysis with the development of mass spectrometry and element purification techniques in the 1990s. This progress significantly advanced the use of U-series disequilibrium in geoscience (Bourdon et al., 2003). High-precision uranium isotope testing can be conducted using multi-collector inductively coupled plasma mass spectrometry (MC-ICP-MS) and thermal ionization mass spectrometry (TIMS). Current techniques require only 10-100 ng of uranium per sample, with an accuracy of 1-3‰ (2σ). U-series disequilibrium methods has been effectively applied to sediment source tracing (DePaolo et al., 2012; DePaolo et al., 2006; Li et al., 2016; Li et al., 2015; Li et al., 2018; Li et al., 2023), soil production rates and ages (Dosseto et al., 2008), and catchment erosion and chemical weathering (Chen et al., 2024; Dosseto et al., 2014; Dosseto et al., 2010; Francke et al., 2019). However, since its inception, only a few research teams have conducted systematic studies. The method is still in the exploratory stage and has several limitations that require further validation and research.

6.2 Application of U-series disequilibrium methods in catchment erosion

Erosion on the earth surface not only shapes the topography and landforms, but also determines the exposure of rock debris in the soils, and therefore controls chemical weathering, atmospheric CO_2 consumption, and regolith development (Clift et al., 2008; France-Lanord and Derry, 1997; Hein et al., 2017; Riebe et al., 2017; West et al., 2005). Studying the mechanism and controlling factors of erosion in catchments provide

insights on the evolution of landform and enhancing understanding of long-term climate change and earth habitability (Dosseto et al., 2010; Heimsath et al., 1997; Plotzki et al., 2015). Currently, various methods are used to study catchment erosion, including monitoring sediment flux at hydrological stations, extracting and comparing remote sensing data, thermochronology, and quartz ^{10}Be analysis. This study selected U-series disequilibrium method to investigate catchment erosion over million-year timescales. The (^{234}U/^{238}U) ratio in rocks or sediments is independent of rock properties and is controlled solely by the time since the rock last fractured and formed a surface. This is the primary advantage of this method over others.

The theoretical model for using (^{234}U/^{238}U) to trace catchment erosion relies on the principle that (^{234}U/^{238}U) increases with depth in weathering profiles (Dosseto et al., 2008; Suresh et al., 2013). Dosseto et al. (2010) analyzed the (^{234}U/^{238}U) values in river sediments with average rainfall, temperature, atmospheric CO_2 concentration, and vegetation, revealing the erosion patterns and different controlling factors during glacial and interglacial periods, marking one of the earliest uses of U-series disequilibrium to trace catchment erosion. Rothacker et al. (2018) used (^{234}U/^{238}U) and lithium isotopes in lake core sediments to reveal soil erosion processes in the catchment since the Holocene. The study concluded that climate change and human activities jointly control soil formation and erosion in catchment. Francke et al. (2019) studied the soil erosion depths between the glacial and Holocene periods by testing the (^{234}U/^{238}U) values in lake core sediments. It is showed that climate and vegetation play different leading roles in catchment erosion during glacial and interglacial periods. Li et al. (2017) tested the (^{234}U/^{238}U) values in river sediments from small catchments on the Tibetan Plateau and quantitatively calculated the erosion rates, which shows a good correlation with erosion rates calculated using in-situ ^{10}Be, suggesting that U-series disequilibrium has great potential for quantitatively tracing catchment erosion. Previous studies mainly focused on small catchments with simple geological backgrounds. Recently, our work in Changjiang catchment, Chen et al. (2024) analyzed (^{234}U/^{238}U) values from core samples at the Changjiang estuary to study erosion in the Changjiang catchment over the past 14 ka. It is revealed that climate change primarily controls catchment erosion. This study applied the U-series disequilibrium method to a worldwide large river catchment, demonstrating its reliability in tracing catchment erosion.

6.3 Characteristics of the paleo-catchment in the southern SCS during the low sea level period and its comparison with the Changjiang catchment

6.3.1 Characteristics and erosion history of the Changjiang catchment

The Changjiang originates from the Tibet Plateau and drains into the west Pacific. It is the longest river in East Asia and its catchment covers a total area of about 1.8×10^6 km^2 (Fig. 6.3 A). The long-term average sediment flux of the Changjiang is 470 Mt/yr (Milliman and Farnsworth, 2011). These sediments are mostly trapped in the estuary to form a large delta and the rest are transported to the East China Sea (ECS) and Okinawa Trough (Fig. 6.3 B), making the largest sediment contribution to the ECS and even the west Pacific.

Changjiang is divided into three sections (Fig. 6.3A). The upper reach is from the source to Yichang and corresponds to high-elevation plateau and/or mountains. The upper Changjiang reach contributed more than 70% of the annual sediment flux before the three Gorges Dam was built in 2003 (Yang et al., 2006). The middle reach is from Yichang to Hukou bears two large lakes (Dongting Lake and Poyang Lake), which play an important role in regulating the sediment flux to the sea. The lower reach is from Hukou to the river estuary, with well-developed lakes and large lowland plain. The estuary is characterized by a large delta system with the largest alluvial island, the Chongming Island, covering an area of about 1.2×10^3 km^2 (Fig. 6.3B)(Chen et al., 2024).

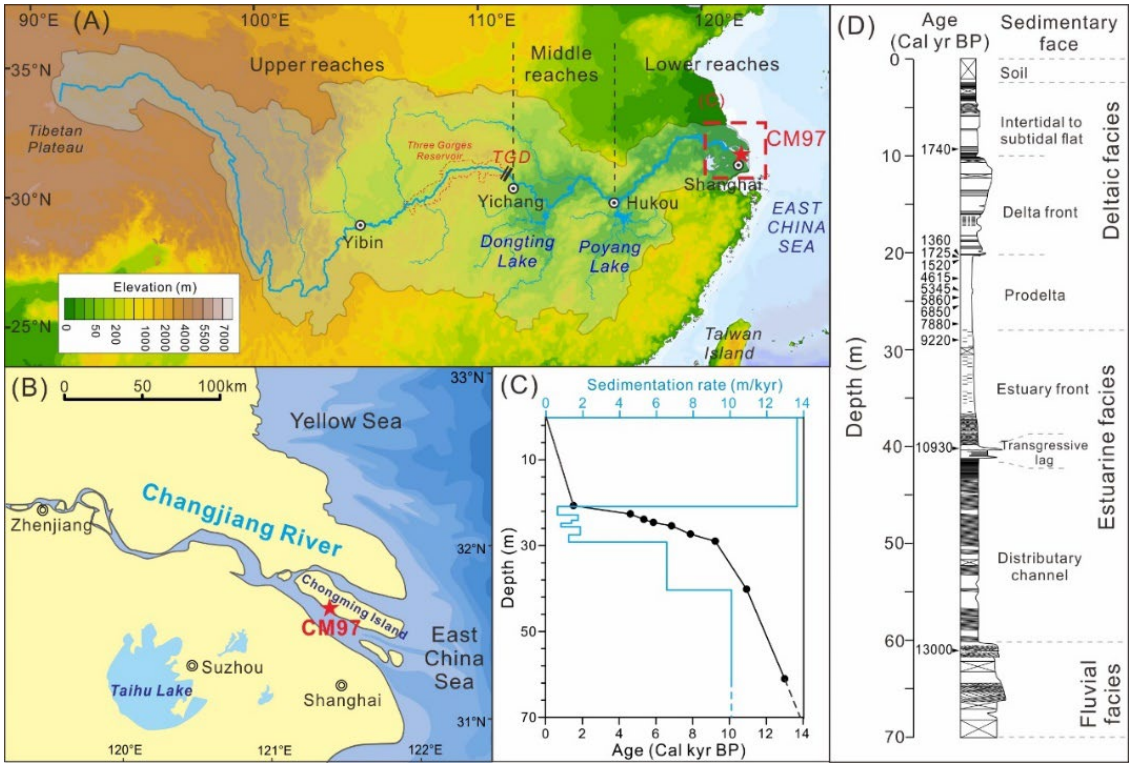

Fig. 6.3 (A) location of Changjiang Basin; (B) the river system and lakes of the deltaic part of the Changjiang catchment and the location of the core CM97; (C) the age model and the sedimentation rate of core CM97 (Hori et al., 2001a, b). (D) the lithology and sedimentary facies of core CM97 (Hori et al., 2001a, b).

The core CM97 on Chongming Island at the Changjiang estuary were selected as samples (Fig. 6.3C and D), systematically analyzed Sr-Nd-U isotopes in terrigenous detrital components smaller than 50 μm. The erosion history over the past 14 ka combined with published data on temperature, precipitation, pollen, and human activity in the Changjiang catchment. Sr and Nd isotope results indicate that since 14 ka, sediments at the Changjiang estuary mainly originated from upper reaches erosion zones, and some contributions from middle and lower reaches floodplains since 4 ka. The *Comminution Age* (t_{com}) calculated from ($^{234}U/^{238}U$) shows a significant correlation with temperature, precipitation, evergreen vegetation pollen, and human activity proxies (Fig. 6.4). The study reveals that from the Bølling–Allerød period to the mid-Holocene, climate changes controlled the erosion processes in the Changjiang catchment, with sediment t_{com} showing a cyclic pattern of younger and older values. During cold and dry periods, with scarce precipitation, older sediment t_{com} value recorded shallower, weaker catchment erosion and slower sediment transport processes. In contrast, during warm and wet periods, abundant precipitation resulted in younger sediment t_{com} values, indicating stronger and deeper catchment erosion and faster sediment transport processes (Fig. 6.5). During the late Holocene, frequent precipitation

has led to middle and lower reaches river flooding, causing the local erosion of older floodplain materials due to river migration. Furthermore, in the past 2 ka, rapid human activities (e.g., deforestation, agriculture) have resulted in local anthropogenic erosion of floodplain soils. These processes have altered the natural erosion patterns of the catchment, reflected in the irregular changes in sediment t_{com} values (Fig. 6.4 A and F) (Chen et al., 2024).

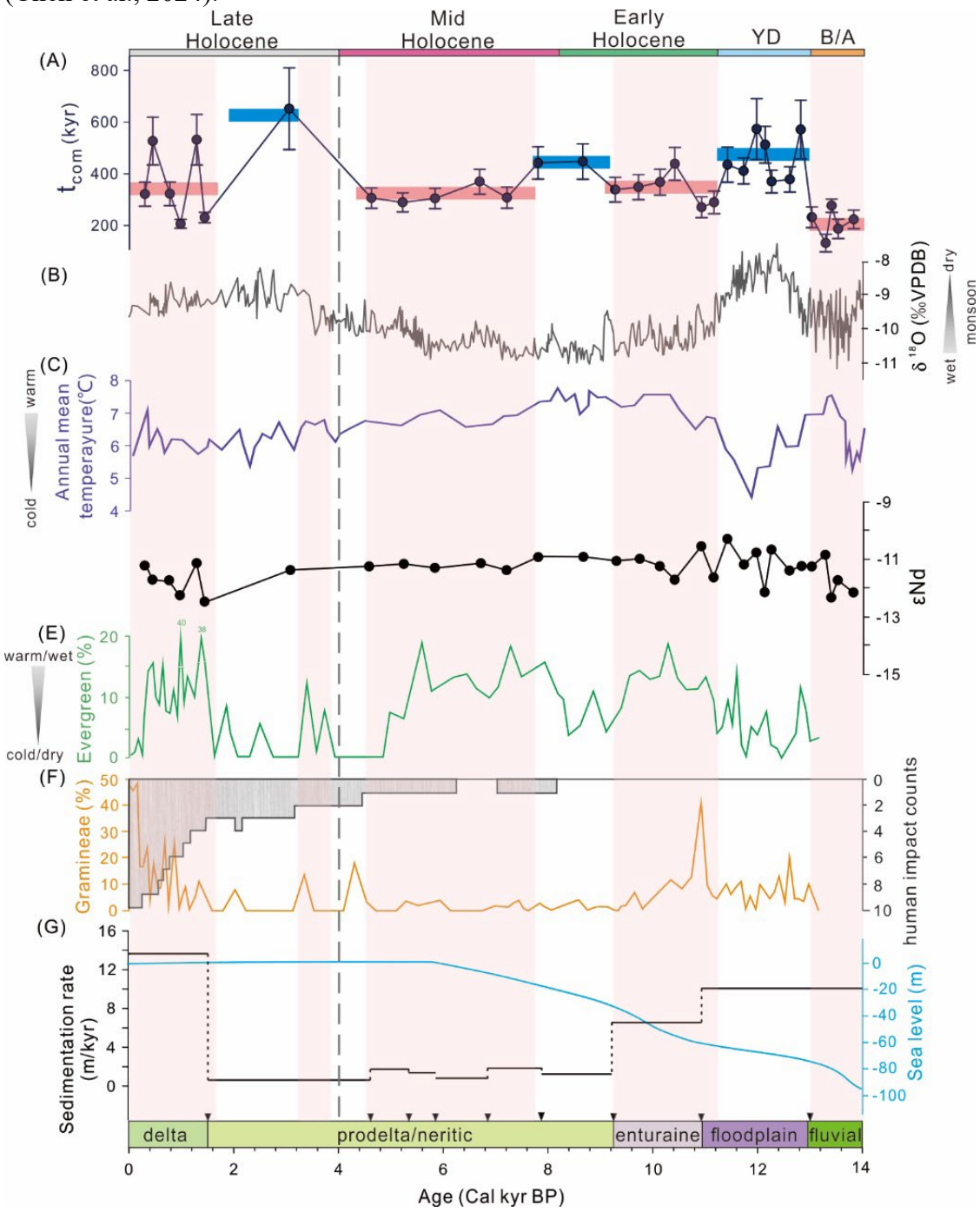

Fig.6 Temporal variations of (A) t_{com}, the blue and red bars represent the average value of t_{com} during the cold and warm periods, respectively. (B) stalagmite $\delta^{18}O$ of Sanbao Cave (Cheng et al., 2016), (C) Annual mean temperature in the middle reaches of the Changjiang catchment (Zhu et al., 2008), (D) εNd, (E) Evergreen pollen content and climate periods from pollen data (pink strips represent

warm and wet periods) (Yi et al., 2003), (F) Gramineae pollen content (Yi et al., 2003) and human impact factor (Wang et al., 2010). (G) the sedimentation rate and sedimentary facies of core CM97, and the sea level of east China sea since 14 ka. The black triangles represent AMS^{14}C dating points.

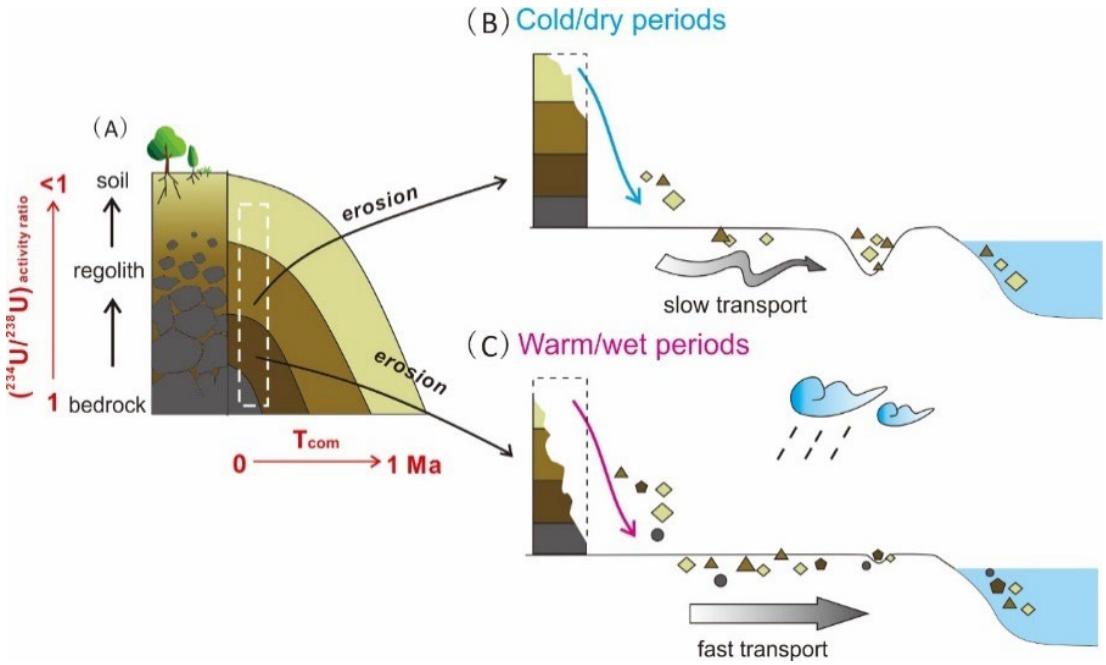

Fig. 6.5 (A) shows the principle of U-series comminution age and its application to weathering profiles. (B) and (C) respectively show the catchment erosion and sediment transport process in the large catchment during the cold/dry and warm/wet environment. Specifically, in (B), during the cold/dry periods, sediments transported slowly and trapped in the plain; in (C), sediments transported faster by strong hydrodynamic force during the warm/wet periods.

6.3.2 Comparison of paleo-catchment in the southern SCS during the low sea level period and modern Changjiang catchment

During the LGM, the sea level in the SCS was 120 meters lower than today, exposing the Sunda Shelf as a vast, flat land. This connected the Sunda Shelf with the Indochina Peninsula, Malay Peninsula, Sumatra, and Borneo, forming the Sunda Land (Fig. 5.17B). On the Sunda Land, two large paleo-river systems (Siam River system and the North Sunda River system) developed, connecting with rivers from the Indochina Peninsula, Malay Peninsula, Sumatra, and Borneo, which flowed into the southern SCS (Fig. 5.17B). Therefore, the low sea level period exhibited a typical large river "source-to-sink" system, with the Malay Peninsula, Sumatra, and Borneo as the sources, and the flat Sunda land as the middle and lower reaches floodplain. The source areas are island mountains with active tectonics, where broken rock fragments and sediments accumulate in weathering profiles. In contrast, the flat, exposed shelf areas may experience remobilization and transport of earlier deposited materials. The

Changjiang catchment has a unique topography, with a drop of approximately 5000 m from source to mouth. The source and upper reaches are located in high-altitude plateaus and/or mountainous areas, while the middle and lower reaches are broad, flat floodplains. Therefore, the geomorphology of the southern SCS during the low sea level period is almost identical to the present-day Changjiang catchment. Secondly, although the low sea level period was a glacial period, the islands of the southern SCS remained humid, while the central and northern exposed shelf were relatively dry (Sun et al., 2000; Wang et al., 2009). This indicates that during the glacial period, the precipitation intense of Sumatra and Borneo is similar to or slightly lower than interglacial periods. Consequently, surface materials can be extensively eroded and transported by paleo-rivers to the slope. Studies show that sediment accumulation on the slope during the glacial was five times greater than during interglacial periods (Schönfeld and Kudrass, 1993; Wang, 1999). During the lowstand, most of the sediments on the slope originated from the islands of the southern SCS, analogous to the upper reaches erosion zones of paleo-rivers. This is similar to the conclusion that sediments at the modern Changjiang estuary mainly come from upper reaches erosion zones. Combining these two reasons, the erosion processes of the tropical islands in the southern SCS during the lowstand can be traced using uranium series disequilibrium methods, similar to those used in the Changjiang catchment (Chen et al., 2024).

6.4 ($^{234}U/^{238}U$) of marine core sediments reveals that tropical island erosion was still active during the glacial period

6.4.1 U isotopes composition of core 18288-2 sediments

The ($^{234}U/^{238}U$) of the terrigenous detrital components of the core 18288-2 sediments was analyzed, and the t_{com} was calculated according to Eqs. (6.4) and (6.5) (Fig. 6.6). ($^{234}U/^{238}U$) of the samples range from 0.9017 to 0.9390, with an average value of 0.9289. The t_{com} values range from 170 to 244 kyr, with an average value of 207 ka. From the vertical distribution of the core, as the sedimentary age decreases, the ($^{234}U/^{238}U$) value increases and the t_{com} value decreases, especially in stage III of the core 18288-2, the ($^{234}U/^{238}U$) value decreases significantly, which means that the t_{com} at the bottom of the core is older, that is, the glacial sediments experienced a longer time of erosion, retention and transportation (Fig. 6.6A and B). The t_{com} value at the bottom of the core is larger than that at the top, while the variation range is smaller than

that of ($^{234}U/^{238}U$). There are two possible factors. (1) The sources of core 18288-2 sediment in Chapter 5. During high sea levels, the main sources are the Mekong River, Red River, and remobilized materials from the Sunda Shelf. During low sea levels, sources include the Mekong River, sediments from Sumatra and Borneo of southern SCS, and re-eroded materials from the Sunda land. Additionally, the influx of materials from the islands of the southern SCS and remobilized materials from the Sunda land increases (Fig. 6.6I). Therefore, during highstand, there are also remobilized shelf sediments transported to the study area, which are record older t_{com}, along with younger materials from the Mekong and Red Rivers. This results in the core 18288-2 sediments appearing older during high sea levels, thus reducing the difference in t_{com} values between high and lowstand. (2) Limitations of the calculation method of t_{com}. As noted in Section 6.1, the accuracy of t_{com} calculations heavily depends on the precision of the f_α. Different methods of calculating f_α can yield significantly varying values. In this study, the grain size distribution of samples is used to calculate f_α. However, uneven grain size distribution and measurement errors can lead to inaccuracies in f_α calculation, resulting in incorrect t_{com} values. Future research will further explore methods for calculating f_α.

Fig. 6.4 shows that the t_{com} of the CM97 core sediment at the Changjiang estuary ranges from 200-600 kyr. In comparison, the t_{com} values of the 18288-2 core sediment are generally smaller. This can be attributed to two main reasons. (1) While the geomorphology of the southern SCS during the glacial period can be compared to the present-day Changjiang, there are significant differences. The Changjiang is 6,500 km long with a drainage area of about 1.8×10^6 km², whereas the widest part of the Sunda Shelf is 800 km and paleo-river channels are no longer than 1,000 km. Therefore, the transportation distance of slope sediments is shorter. In addition, the upper reaches of the paleo-rivers, being islands, is much smaller than the upper reaches of the Changjiang on the Tibetan Plateau. Consequently, the residence time in the source area is relatively shorter for slope sediments in the Southern SCS. (2) Changjiang is in a subtropical-temperate monsoon region characterized by significant seasonal temperature and precipitation variations. In contrast, the southern SCS is in an equatorial tropical region, controlled by tropical monsoon climate with annual precipitation exceeding 1,500 mm and mean temperatures above 20°C. Consequently, the islands in the southern SCS experience stronger precipitation and higher temperatures, leading to more intense erosion and weathering. This results in shorter

residence and faster transportation times for sediments, thus explaining the younger t_{com} for the core 18288-2 sediments.

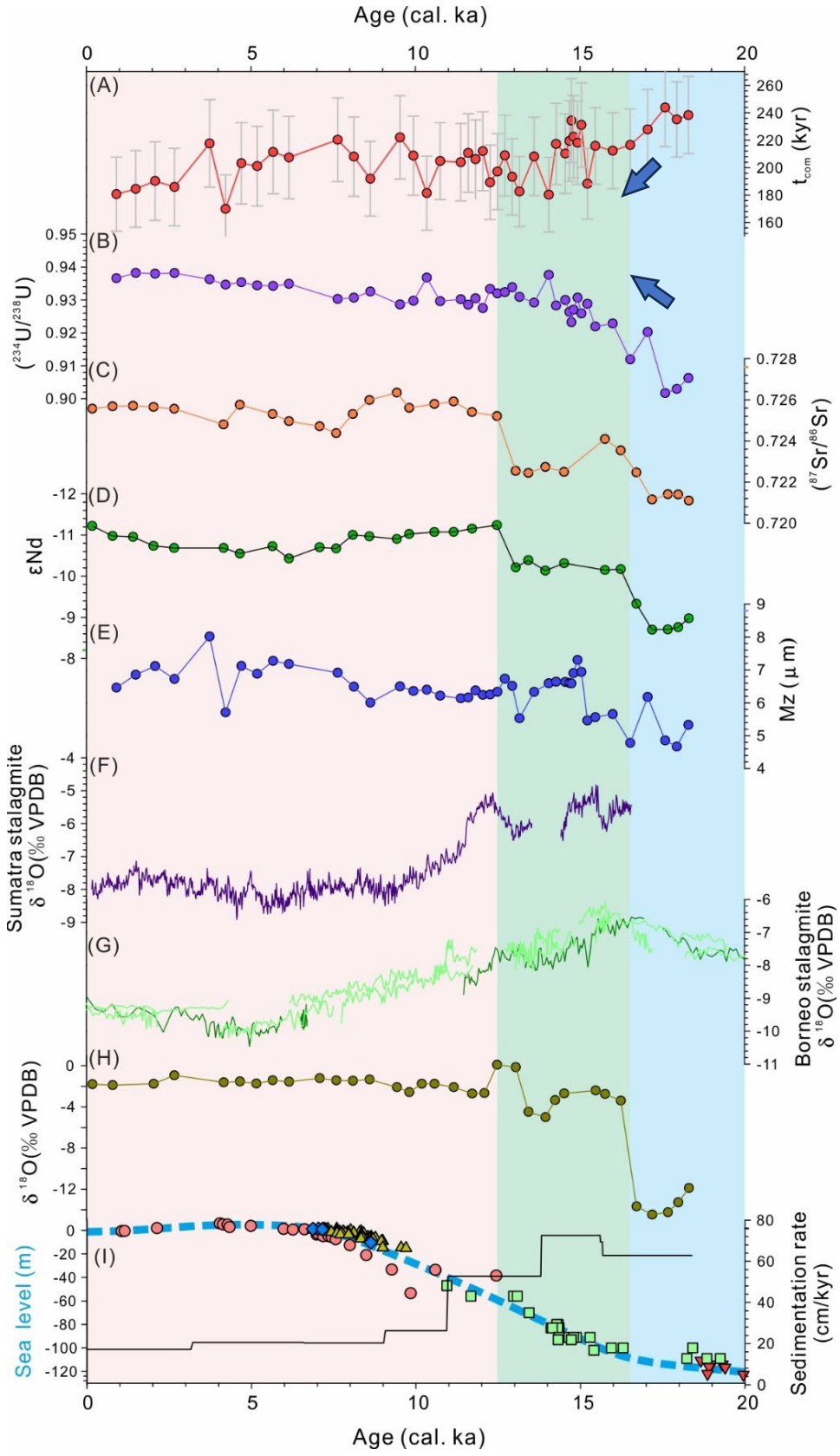

Fig. 6.6 Core 18288-2（A）Comminution Age (t_{com}), (B) ($^{234}U/^{238}U$),(C)$^{87}Sr/^{86}Sr$ ratio, (D) εNd

value (E) median grain size of components less than 50μm, (F) $\delta^{18}O$ value of Tangga Cave stalagmites in Sumatra (Wurtzel et al., 2018), (G) $\delta^{18}O$ value of cave stalagmites in Gunung Buda National Park in northern Borneo (Partin et al., 2007), (H) $\delta^{18}O$ value of carbonate in bulk sediments of the core 18288-2, (I) sea level changes in the SCS since 20 ka (Bird et al., 2007; Geyh et al., 1979; Hanebuth et al., 2000; Hanebuth et al., 2009; Hesp et al., 1998) and sedimentation rate of the core 18288-2. (The blue area represents Stage I, the green area represents Stage II, the pink area represents Stage III).

6.4.2 Precipitation in the southern SCS during the glacial low sea level period

Research on precipitation characteristics during glacial periods with lowstand in the southern SCS mainly relies on speleothem oxygen isotopes and paleo-vegetation distribution. Studies of $\delta^{18}O$ from caves stalagmite in Sumatra and Borneo (Fig. 6.6 F and G) show that, $\delta^{18}O$ is more enriched during glacial periods and more depleted during interglacial periods, though the differences between glacial and interglacial periods are not significant. Sumatra and Borneo are in the low-latitude tropical region of the Indo-Pacific Warm Pool (IPWP). The response of these regions to millennial-scale climate events, as indicated by stalagmite $\delta^{18}O$ from mid- to high-latitude caves, remains unclear. For instance, during the Younger Dryas (YD) event, $\delta^{18}O$ from Sumatra is more enriched, whereas Borneo shows no response. Compared to mid- to high-latitude cave speleothem in the Northern Hemisphere, the range of $\delta^{18}O$ variation in these two studies is smaller, especially during glacial periods. Stalagmite $\delta^{18}O$ values from low-latitude caves are more depleted than those from mid- to high-latitude caves (Partin et al., 2007; Wurtzel et al., 2018). Compared to mid- to high-latitude cave speleothem in the Northern Hemisphere, the range of $\delta^{18}O$ variation in Sumatra and Borneo is smaller, especially during glacial periods. Speleothem $\delta^{18}O$ values from low-latitude are more depleted than those from mid- to high-latitude caves. Additionally, stalagmite $\delta^{18}O$ in Borneo shows a depletion trend from 16 ka to 20 ka, suggesting a slight increase in precipitation. Thus, based on stalagmite $\delta^{18}O$ values, it can be inferred that precipitation during the glacial periods with lowstand in the southern SCS was only slightly weaker than present-day.

During the glacial periods, exposed Sunda shelf connected many Southeast Asian islands, forming Sunda Land. Bird et al. (2005) shows that tropical rainforests still developed in most of Sumatra and central-eastern Borneo, while the interior of the exposed shelf and southwestern Borneo were dominated by savanna (Fig. 6.7). Palynological studies of sediment cores from the southern SCS show that during the low sea levels of glacial periods, exposed shelf and most islands of the southern SCS

were predominantly covered by tropical rainforests. The phytolith content, indicative of humid climates, was almost the same as during highstand interglacial periods, suggesting a slight decrease in humidity during the glacial period but not aridity overall (Wang et al., 2009; Yang et al., 2020). Vegetation proxies such as n-alkane ACL and lipid monomer carbon isotopes from core 18288-2 also suggest that during the glacial period and early deglaciation, tropical rainforests were primarily found on equatorial islands and exposed Sunda shelf, while areas farther from the equator were dominated by herbaceous vegetation (Yu, 2022). Thus, during the glacial period, the climate on islands of the southern SCS (e.g., Sumatra, Borneo) remained humid, with precipitation levels similar to or slightly lower than the present-day.

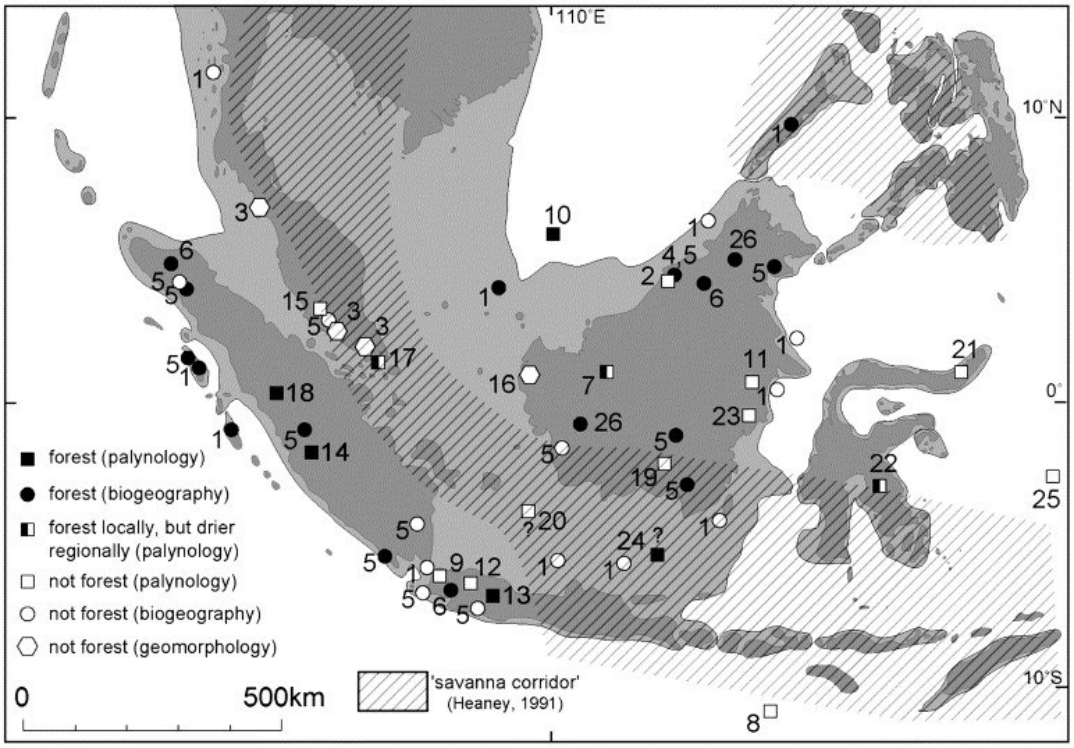

Fig. 6.7 Distribution of vegetation types on the exposed Sunda shelf and surrounding lands during the glacial period (Bird et al., 2005)

6.4.3 Erosion process of the southern SCS during glacial period revealed by uranium series disequilibrium methods

Glacial period sediments of Core 18288-2 records older t_{com} (Fig. 6.6A and B), with sedimentation rates on the slope during glacial periods being 3-4 times higher than those during interglacial periods (Fig. 6.6I). Combined with analysis of sediment sources in the southern SCS during glacial periods (Fig. 6.6C and D), it can be concluded that large amounts of older sediments were transported by paleo-rivers from Sumatra and Borneo to the slope during glacial periods. The theoretical model of using

U-series disequilibrium to trace erosion is based on the weathering profile, where surface sediments break down first and experience longer residence times than deeper fresh rocks, resulting in smaller ($^{234}U/^{238}U$) values. Deeper sediments, closer to bedrock, are relatively fresh and less eroded, showing larger ($^{234}U/^{238}U$) values closer to 1 (Fig. 6.8) (Dosseto et al., 2008; Suresh et al., 2013). Therefore, during glacial period with lowstand, the tropical islands in the southern SCS scoured by rainfall which is similar to or slightly weaker than the Holocene. Early eroded or long-residence materials from the surface or weathering profiles were mobilized and transported by paleo-river to the slope. Additionally, earlier sediments deposited on the exposed shelf were locally remobilized by river flows and/or migration of the channel, which were also transported to the slope by paleo-river. This explains why the glacial period sediments in slope core show older t_{com}, revealing that the tropical islands in the southern SCS still experience active erosion during glacial periods.

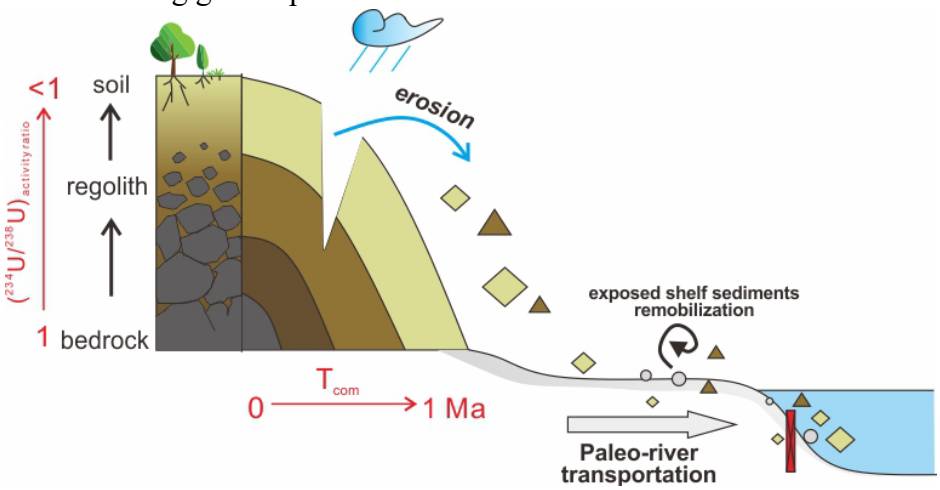

Fig. 6.8 Theoretical model of uranium series disequilibrium tracer erosion and erosion-transport process in the southern South China Sea during glacial periods

6.5 Summary

In this study, the ($^{234}U/^{238}U$) values in the core sediment from the slope of the eastern Sunda Shelf were analyzed and t_{com} were calculated. Combined with provenance analysis and precipitation conditions in the southern SCS during the glacial period, this study indicated the erosion history in the southern SCS. The precipitation intensity was similar to or slightly weaker than that during the Holocene, leading to early-eroded or long-residence materials at the island being mobilized and transported by paleo-river to the slope. Additionally, earlier sediments deposited on the exposed shelf were locally remobilized by river flows and/or channel migration, which were

also transported to the slope. Consequently, sediments record older t_{com} that deposited in slope during the glacial periods, indicating that tropical islands in the southern SCS still experienced active erosion during the glacial period. Thus, the U-series disequilibrium method provides an effective indicator for studying millennial-scale catchment erosion.

Chapter 7 Silicate weathering and CO_2 consumption records in the southern SCS since the last deglaciation

Chemical weathering is a crucial surface process that links various spheres of the Earth's surface, playing a significant role in shaping landforms, climate evolution, and global material cycles (Berner, 1992b; Tipper et al., 2006; West et al., 2005). In nature, the weathering of silicate and carbonate minerals serves as a significant carbon sink by absorbing CO_2, which is crucial for the evolution of the global carbon cycle. Consequently, weathering processes have garnered considerable attention in Earth system research (Berner, 1992b; Berner and Kothavala, 1983; Bufe et al., 2021; Gaillardet et al., 1999a; Ludwig et al., 1999; Penman et al., 2020; Raymo and Ruddiman, 1992). In contrast to the study of modern weathering processes, the study of weathering in geological history primarily relies on two methods: (1) estimating terrestrial river inputs using the geochemical composition of seawater (Misra and Froelich, 2012), and (2) calculating erosion rates and weathering intensity based on the geochemical composition of weathering products (Frings, 2019). The southern SCS, located in the low-latitude tropical region on the edge of the Southeast Asian continent, preserves sedimentary records of erosion, weathering, and climate from different tectonic backgrounds and depositional histories. Particularly, during low sea level periods, the exposure of the Sunda Shelf created tropical rainforest regions comparable to the Amazon and Congo basins, which are significant for the global carbon cycle (Wang, 2017). However, due to the short research history and lack of material in the southern SCS, studies on weathering processes since the LGM are still very limited. This chapter reconstructs the weathering history of the southern SCS since the last deglaciation by analyzing the geochemical composition of sediment cores from the eastern slope of the Sunda Shelf. It also quantitatively calculates the amount of CO_2 consumed during silicate weathering and explores the factors controlling silicate weathering and CO_2 consumption rate in the region since the last deglaciation.

7.1 Reconstruction of weathering history since the last deglaciation

7.1.1 Interpretation of silicate weathering signals recorded in the core 18288-2

Silicate chemical weathering often involves the dissolution of primary minerals

and the formation of secondary minerals, with weathering intensity assessable through mineral composition and elemental content. Following the sequence of elemental mobility, early weathering of igneous rocks leads to the leaching of Ca and Na, with unstable minerals like plagioclase and mica gradually dissolving, causing an increase in illite content. This is followed by the K-leaching stage, where moderately mobile elements (such as K, Mn, Fe) are leached, and illite loses K to form kaolinite, with Al beginning to accumulate. Finally, in the most intense weathering stage, Si may also be leached (Nesbitt et al., 1980). Therefore, soluble elements in terrigenous clastic components (e.g., Ca, Mg, K, Na) are often used to trace weathering intensity. To eliminate the influence of grain size, the ratio of soluble elements to immobile elements is typically used (Gaillardet et al., 1999a). Al is usually selected as the immobile element, with a smaller X/Al ratio indicating greater loss of mobile element X and higher chemical weathering intensity. Additionally, weathering parameters calculated from multiple elements can be used to assess weathering intensity, such as the Chemical Index of Alteration (CIA) (Nesbitt and Young, 1982) and the Weathering Index of Parker (WIP) (Parker, 1970). The most representative indicator of weathering intensity, CIA, is calculated using the following formula:

$$CIA=[Al_2O_3/(CaO^*+Na_2O+K_2O+Al_2O_3)]\times 100$$

Where, CaO* refers to the Ca concentration in silicate minerals, excluding Ca bound to minerals such as carbonates and phosphates. Generally, the larger the CIA value, the stronger the intensity of weathering. The CIA value of unweathered fresh rocks is generally less than 55, and the CIA value of kaolinite is 100 (Nesbitt et al., 1980).

The soluble element ratios (Na/Al, K/Al, Mg/Al, Ca/Al) and CIA values of the terrigenous clastic components of the core 18288-2 sediments are shown in Figure 7.1 (I)-(N). The result exhibits that all weathering proxies show consistent variation trends over time, that is, the weathering intensity of the LGM-last deglaciation period is generally higher than that of the Holocene, which is basically consistent with the trend of grain size indicated by Al/Si. It can be divided into three stages: the Stage I, from the late LGM to early last deglaciation (18.5-16.5 ka), with strongest weathering intensity shown by the weathering proxies. The Stage II, the late last deglaciation period (16.5-12.5 ka), the weathering intensity weakened, and proxies indicated the weakest weathering intensity around 15.5 ka. The Stage III, the Holocene (12.5-0 ka), the weathering intensity is the weakest, and the weathering proxies change steadily.

The silicate chemical weathering is influenced by various factors including

precipitation, temperature, tectonics, geomorphology, lithology, and surface processes (Raymo and Ruddiman, 1992; Riebe et al., 2001; White, 2003; White and Blum, 1995). Climate is the primary control on chemical weathering. Typically, a 1°C increase in temperature results in a 4-14% rise in chemical weathering flux (Gislason et al., 2009), Deng et al. (2022) conducted a global analysis of CIA values in fine-grained sediments and found that silicate weathering intensity decreases with increasing latitude, with temperature regulating the dissolution of minerals such as feldspar. Fig. 7.1 indicates an enhancement of silicate chemical weathering during the glacial period. However, it is generally recognized that higher temperatures and humidity intensify chemical weathering (West et al., 2005; White and Blum, 1995). Consequently, weathering rates are expected to be lower during cold and dry glacial periods compared to warm and humid interglacial periods (Lupker et al., 2013). Our findings contradict this conventional understanding. Similar conclusions were obtained by Wan et al. (2017) and Xu et al. (2018), who found that during glacial periods, lower sea levels exposed continental shelves, revealing silicate sediments and providing more reactive material for chemical weathering, potentially increasing weathering flux. The net effect of these opposing controls on silicate weathering fluxes at the global scale remains uncertain. Although some models suggest that exposed continental shelf enhance chemical weathering, these assumptions lack substantial geological evidence (Ludwig et al., 1999; Munhoven and François, 1996). Fig. 7.1 shows that along with changes in weathering intensity, the sea level in the southern SCS has fluctuated since the last deglaciation (Fig. 7.1A). Proxies, such as Sr and Nd isotopes, also varied across the three stages of weathering intensity (Fig. 7.1G and H), with SST and precipitation exhibiting different degrees of change between glacial and interglacial periods (Fig. 7.1B-F). This raises the question: do the element ratios and CIA values truly reflect an increase in silicate chemical weathering intensity during the glacial period, or are they influenced by other environmental signals, therefore indicating different information?

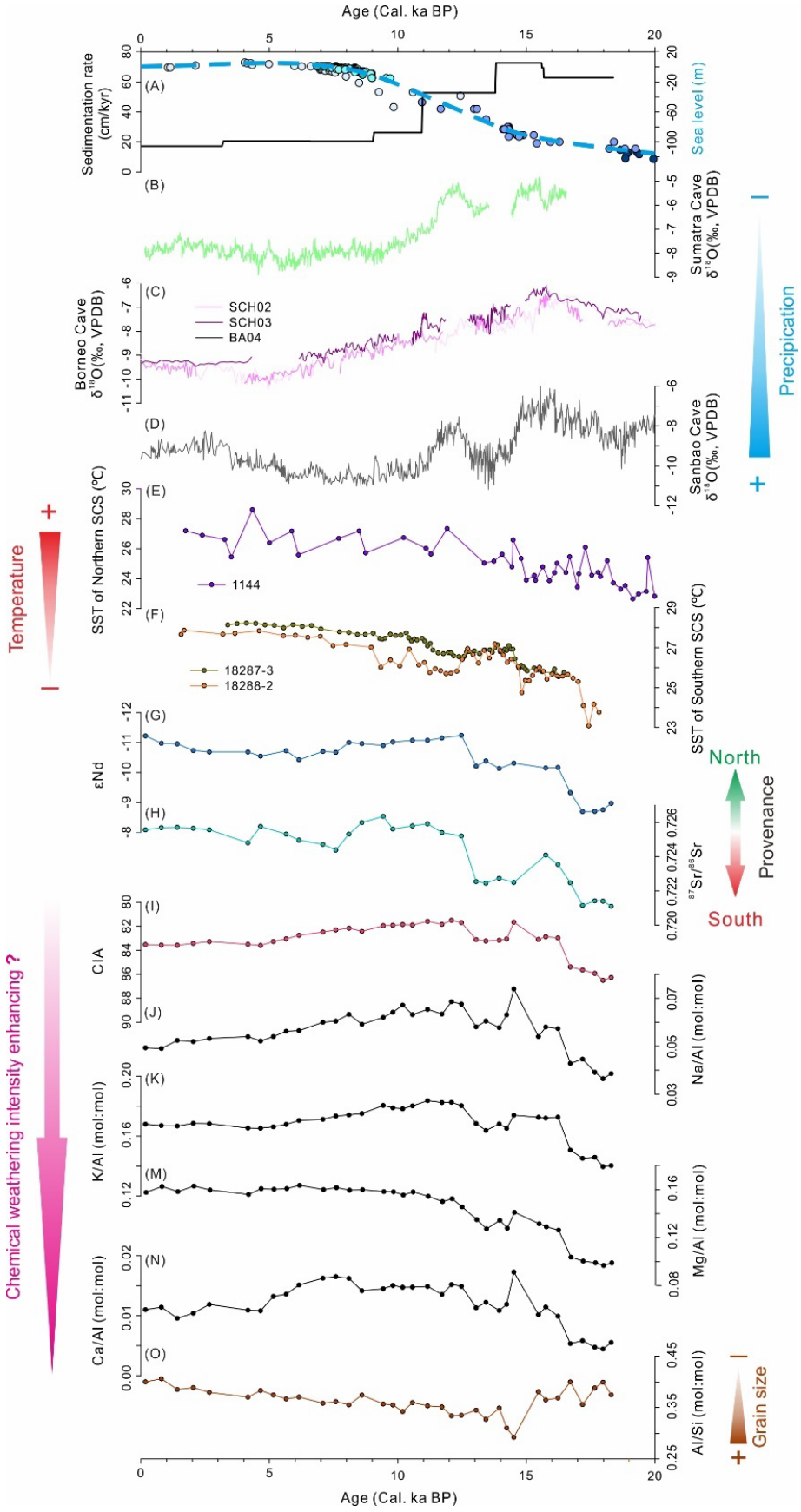

Fig. 7.1 (A) Sea level changes since 20 ka in the SCS (Bird et al., 2007; Geyh et al., 1979; Hanebuth et al., 2000; Hanebuth et al., 2009; Hesp et al., 1998) and sedimentation rate of the core 18288-2,

(B) $\delta^{18}O$ values of stalagmites from Tangga Cave, Sumatra (Wurtzel et al., 2018). (C) $\delta^{18}O$ values of stalagmites from Gunung Buda National Park, northern Borneo (Partin et al., 2007). (D) $\delta^{18}O$ values of stalagmites from Sanbao Cave, Shengnongjia Mountain in the middle reaches of Changjiang, China (Cheng et al., 2016). (E) STT of core 1144 in the northern SCS. (F) STT of core 18287-3 (Steinke et al., 2001) and core 18288-2 in the northern SCS. (G)εNd, (H)$^{87}Sr/^{86}Sr$, (I) CIA, (J) Na/Al, (K) K/Al, (M) Mg/Al, (N) Ca/Al, (O) Al/Si ratio values.

7.1.2 Relative changes of weathering intensity since the last deglaciation

To calculate weathering intensity changes recorded by core sediments from different geological periods, the contributions of various sources (endmembers) are first determined through provenance analysis. A specific element X, indicative of weathering intensity, is selected. The contribution of each endmember to element X is calculated, yielding the theoretical value of element X in the core sediment (X_{mix}). The difference between the measured value of element X in the core (X_{core}) and the mixing value (X_{mix}) is marked as $\Delta X = X_{core} - X_{mix}$. If $\Delta X > 0$, it suggests actual weaker weathering intensity compared to the theoretical mixing value; if $\Delta X < 0$, it indicates stronger weathering intensity; and if $\Delta X = 0$, the weathering intensity is comparable to the theoretical mixing value. By comparing ΔX values across different periods, changes in weathering intensity over time can be inferred. We use the X/Al ratio in calculations to eliminate the grain size effect, resulting in the value $\Delta X/Al$.

Based on the previous analysis of the core, this study calculates the relative weathering intensity for the three stages of the core 18288-2: the Stage I (late LGM to early last deglaciation, the Stage II (late last deglaciation), and Stage III (the Holocene). The complexity of sediment sources during the Holocene highstand, combined with current limitations in verifying the contributions of the Mekong and Red Rivers, prevented the calculation of absolute weathering intensity. However, during the lowstand, the sediments deposited at the slope have a certain proportion originated from Sumatra and Borneo is reliable. Therefore, the Holocene stage in the core was used as an endmember, mixed with contributions from Sumatra and/or Borneo sediments, to calculate weathering intensity changes during the Stage I and Stage II relative to the Stage III.

First, the proportion of different endmembers were quantitatively calculated using the Sr-Nd isotope mixing model. As outlined earlier, three end-members were selected: the Stage I of the core 18288-2, offshore Borneo, and Sumatra. This results in three possible end-member combinations: Possibility (1), 18288-2 (0-12.5 ka) + offshore Borneo; Possibility (2), 18288-2 (0-12.5 ka) + Sumatra; and Possibility (3), 18288-2 (0-12.5 ka) + offshore Borneo + Sumatra (Table 7.1). The end-member proportions

calculated by Sr and Nd concentrations and isotopes through Sr-Nd isotope mixing model. Monte Carlo simulation was then used to perform 10,000 simulations, resulting in the proportions for different end-member combinations (Table 7.1). The model calculation formula is as follows (modified from Singh et al. (2008) and Awasthi et al. (2018)):

$$\left(\frac{^{87}Sr}{^{86}Sr}\right)_{mix} = \frac{\sum_{i=1}^{n} f_i C_i^{Sr} \left(\frac{^{87}Sr}{^{86}Sr}\right)_i}{\sum_{i=1}^{n} f_i C_i^{Sr}} \quad \cdots\cdots\cdots\cdots(7.1)$$

$$C_{mix}^{Sr} = \frac{\sum_{i=1}^{n} f_i \left(c_i^{Sr}\right)^2}{\sum_{i=1}^{n} f_i C_i^{Sr}} \quad \cdots\cdots\cdots\cdots(7.2)$$

$$(\varepsilon Nd)_{mix} = \frac{\sum_{i=1}^{n} f_i C_i^{Nd} \varepsilon Nd_i}{\sum_{i=1}^{n} f_i C_i^{Nd}} \quad \cdots\cdots\cdots\cdots(7.3)$$

$$C_{mix}^{Nd} = \frac{\sum_{i=1}^{n} f_i \left(c_i^{Nd}\right)^2}{\sum_{i=1}^{n} f_i C_i^{Nd}} \quad \cdots\cdots\cdots\cdots(7.4)$$

Where, n is the number of potential end-member i, f is the proportion of end-member I, and C represents the concentration of end-member i (ppm). The results after Monte Carlo simulation are shown in Table 7.1.

Table 7.1 Three end-member possible modes and element mixing line equations

end-member		Possibility 1		Possibility 2		Possibility 3	
		core 18288-2 (12.5-16.5 ka)	core 18288-2 (16.5-18.5 ka)	core 18288-2 (12.5-16.5 ka)	core 18288-2 (16.5-18.5 ka)	core 18288-2 (12.5-16.5 ka)	core 18288-2 (16.5-18.5 ka)
core 18288-2 (0-12.5 ka)		70%	13%	90%	68%	77%	68%
Offshore Borneo		30%	87%	/	/	19%	1%
Sumatra		/	/	10%	32%	4%	31%
Element mixing line by end-member proportion according to the correction between X/Al and Al/Si	Ca/Al	y = -0.0274x + 0.0533	y = 0.0752x + 0.072	y = -0.0622x + 0.0365	y = -0.0201x + 0.0214	y = -0.042x + 0.046	y = -0.0191x + 0.0221
	Mg/Al	y = 0.1326x + 0.1239	y = 0.0996x + 0.1633	y = 0.1259x + 0.1011	y = 0.073x + 0.0966	y = 0.1296x + 0.1149	y = 0.0739x + 0.0983
	K/Al	y = -0.2547x + 0.2643	y = -0.2354x + 0.2527	y = -0.2504x + 0.2552	y = -0.2186x + 0.2217	y = -0.2545x + 0.262	y = -0.2209x + 0.2242
	Na/Al	y = -0.5442x + 0.2487	y = -0.9917x + 0.3947	y = -0.2565x + 0.1513	y = -0.1416x + 0.1058	y = -0.4191x + 0.2068	y = -0.1526x + 0.1101

Theoretical mixing lines for Ca/Al, Mg/Al, K/Al, and Na/Al were calculated according to the proportions of each endmember (Fig. 7.2). The differences between the measured value of Ca/Al, Mg/Al, K/Al, and Na/Al in the core sediments and their respective theoretical mixing lines were calculated to obtain ΔCa/Al, ΔMg/Al, ΔK/Al,

and ΔNa/Al. This analysis revealed the differences between Stage II and Stage III relative to the Stage I (Fig. 7.3). From Fig. 7.3, Possibility (1) (blue hollow circles) shows that ΔCa/Al, ΔMg/Al, and ΔK/Al, ΔNa/Al exhibiting opposite trends between the Stage I and Stage II, which contradicts the elements dissolution theory of weathering process, thus ruling out Possibility (1). In Possibility (2) (red hollow triangles), the differences for all four elements ratio in the first stage are around or slightly above zero, indicating that the weathering intensity in the Stage I is comparable to or slightly stronger than in the Stage III. ΔK/Al and ΔNa/Al in the Stage II shows less significant varation than those in ΔCa/Al and ΔMg/Al, with ΔCa/Al and ΔMg/Al showing significant negative values. This suggests weaker weathering intensity in the Stage II compared to the Stage III. The values for ΔK/Al and ΔNa/Al are slightly below or around zero, supporting the same conclusion as for ΔCa/Al and ΔMg/Al, making Stage II a possible explanation. In Possibility (3) (green hollow squares), the values of ΔCa/Al, ΔMg/Al, ΔK/Al, and ΔNa/Al show little variation between the Stage I and II, and are close to zero, indicating similar weathering intensity in the Stage I and Stage II as in the Stage III. Therefore, Possibility (3) is also a possible model. In summary, this study selects end-member models from Possibility (2) and (3) for the subsequent calculation of CO_2 consumption rates.

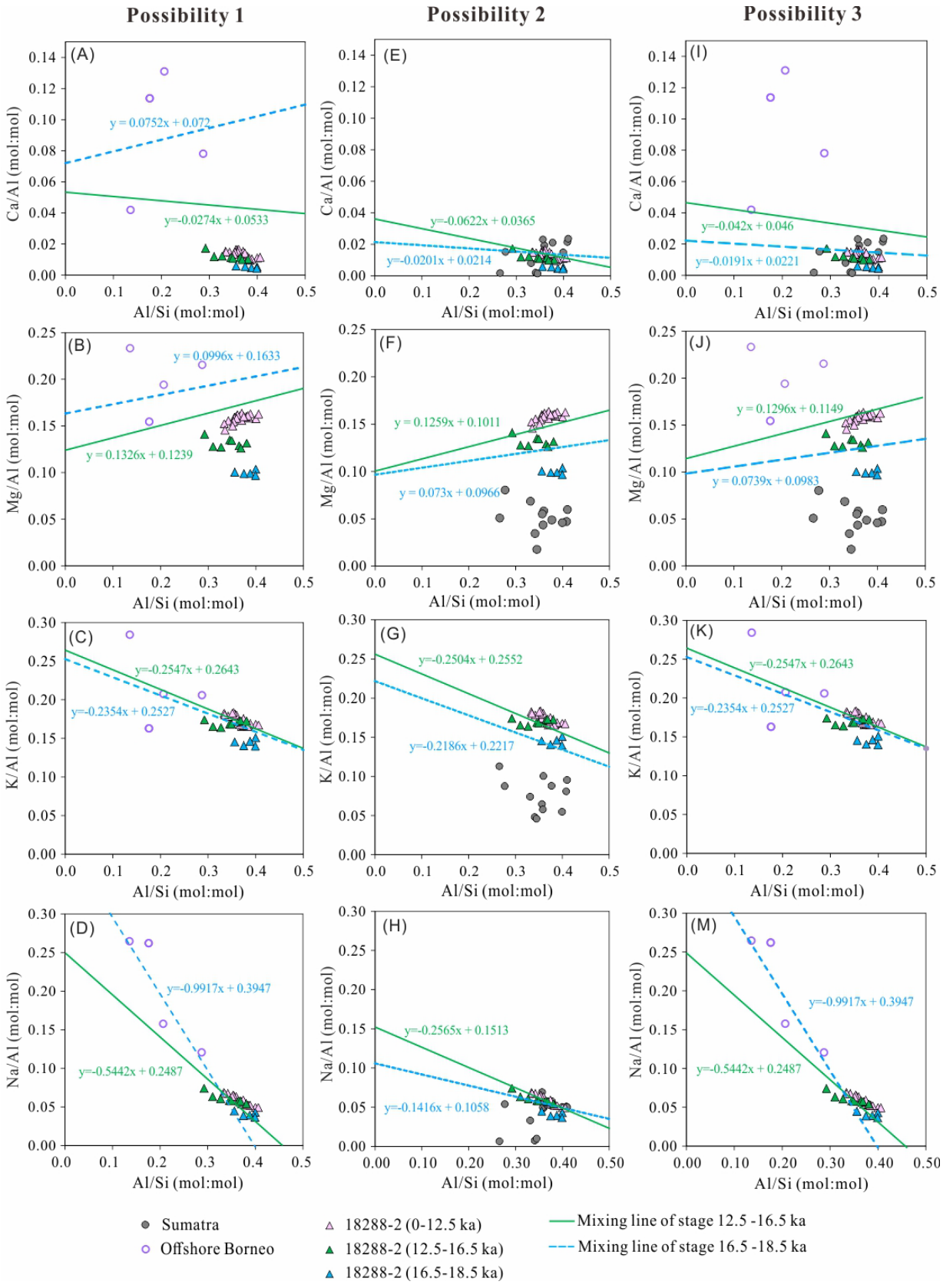

Fig. 7.2 Three end-member combination models of weathering element mixing models

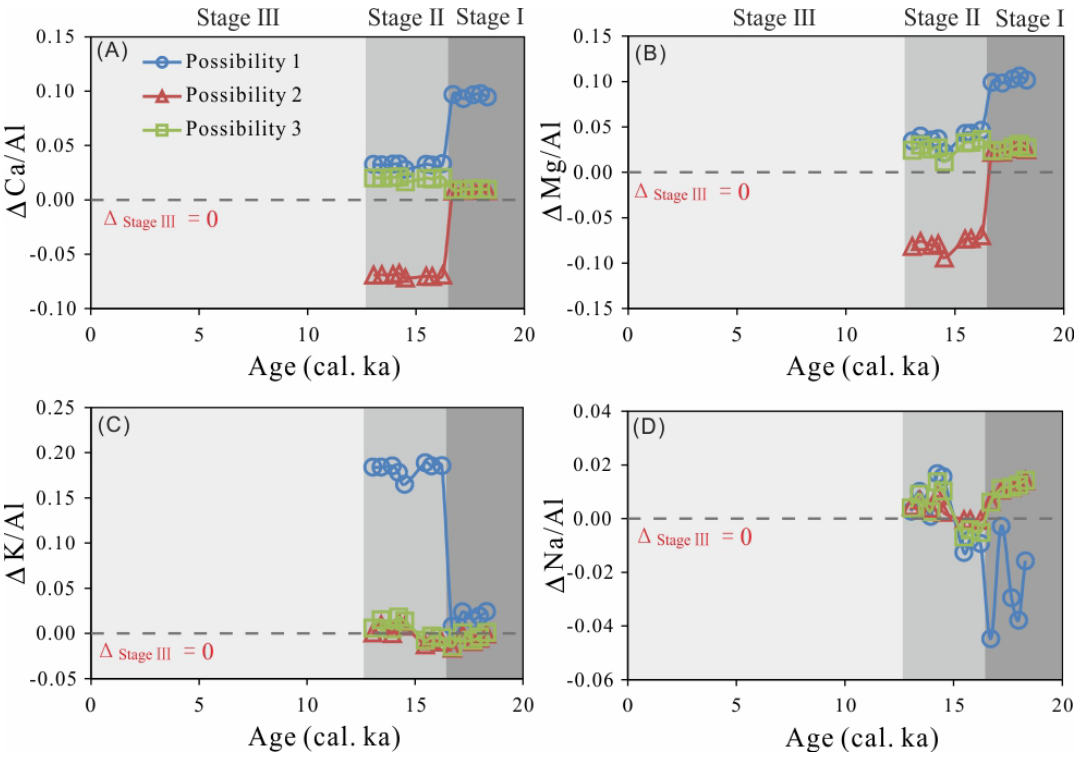

Fig. 7.3 Differences between element ratio and theoretical mixing lines at different stages of the core 18288-2 sediments.

7.2 History of atmosphere CO_2 consumption by silicate weathering in the southern SCS since the last deglaciation

In order to further analyze the differences in CO_2 consumption by silicate weathering during the glacial period and the Holocene, the CO_2 consumption rate was quantitatively calculated based on the differences in weathering intensity calculated in Section 7.1 at Stage I, II and III, combined with the flux of silicate components in the sediments into the sea and the changes in the exposed shelf area since the last deglaciation.

We refined the method proposed by France-Lanord and Derry (1997) to calculate the CO_2 consumption by silicate chemical weathering during the glaciation period. By using the molar ratio differences between mobile elements and Al (ΔCa/Al, ΔMg/Al, ΔK/Al, ΔNa/Al) from the deglaciation and Holocene periods, along with the mass accumulation rates (MAR) of terrigenous sediments, we estimated the loss of moblie elements (ΔX) during the low sea level periods. This approach eliminates the precise knowledge of sediment sources, their contribution proportions, or the chemical weathering loss of bedrock and fluvial sediments on land. We only focus on the weathering that occurred after the fluvially derived sediments accumulated on the study

area during the Holocene highstand and maybe eroded and transferred to the slope during later glacial lowstand. We assumed that the Mg^{2+} and Ca^{2+} lost during silicate weathering were entirely forming marine carbonates. Due to limited research on the fraction of K and Na involved in cation exchange reactions with sediments or the oceanic crust (Berner and Berner, 2012; Sayles and Mangelsdorf Jr, 1977), we conservatively estimate that 30% of K^+ and 20% of Na^+ lost during silicate weathering were exchanged with Ca and Mg to form carbonates (France-Lanord and Derry, 1997). Considering charge balance, the CO_2 consumption can be estimated according to the loss of base cations during chemical weathering. The formula is:

$$\Delta CO_2 = \Delta Ca + \Delta Mg + 0.10\Delta K + 0.15\Delta Na \cdots\cdots\cdots\cdots (7.5)$$

Based on this principle, we calculated the relative CO_2 consumption difference between the Stage I (Late LGM to early deglaciation), the Stage II (late deglaciation), and Stage III (Holocene) in the core 18288-2 (Appendix Table 10). Based on the two different end-member combination models, Overall, in both Possibility (2) and (3), the changes between the Stage I and Stage III were minimal, with differences of 1.56×10^9 mol/yr and 1.70×10^9 mol/yr, respectively. This indicates that CO_2 consumption by silicate weathering in these two stages was nearly identical. For the Stage II, CO_2 consumption in Possibility (2) and (3) was -43.97×10^9 mol/yr and 14.44×10^9 mol/yr, respectively (Appendix Table 10). The results suggest that in Possibility (2), the Stage II consumed less CO_2 than the Stage III, indicating weaker weathering intensity. In Possibility (3), the Stage II consumed more CO_2 than Stage III, indicating stronger weathering, with the CO_2 consumption being larger than difference between Stage I and Stage III. Gaillardet et al. (1999b) reported that CO_2 consumption by silicate weathering during the Holocene was approximately $11{,}700\times10^9$ mol/yr. This study calculated CO_2 consumption difference for different stages is about 200 times lower than this, indicating that the variation in CO_2 consumption by silicate weathering in different stages since the last deglaciation is negligible in the core 18288-2 records. Thus, there has been no significant change in CO_2 consumption by silicate weathering in the southern SCS since the Late LGM. However, Wan et al. (2017) suggested that during the glacial period with lowstand exposed the Sunda Shelf, increasing the availability of weatherable material, and consequently, chemical weathering was stronger during the glacial period than during the interglacial period.

To further assess whether there were significant changes in CO_2 consumption by silicate weathering during glacial and interglacial periods, we collected previously

published data on terrestrial weathering rates around the SCS and the area of potential sediment sources in this study, and calculated the absolute CO_2 consumption concentration by silicate weathering on the land (Appendix Table 10, Fig. 7.4E). Assuming an average CO_2 consumption rate of 191×10^3 mol/km^2/yr during the Holocene (Stage III) (Li et al., 2014), with an average weatherable land area of 1.76×10^6 km^2 in the study area, we estimated the average CO_2 consumption during the Holocene to be 336×10^9 mol/yr. The CO_2 consumption during Stage I and Stage II was calculated to be 300-350×10^9 mol/yr, with minimal differences between stages, suggesting that CO_2 consumption by silicate weathering in the southern SCS has remained relatively constant since the late LGM. However, considering the substantial changes in sea level, climate, and land area in the SCS since the LGM, it is important to consider whether these factors might have influenced CO_2 consumption through silicate weathering.

To specifically analyze the impact of sea level changes on silicate weathering due to the exposure of the Sunda Shelf, we further calculated the CO_2 consumption rate recorded in core 18288-2 since the late LGM (Appendix Table 10). The present-day area of the Sunda Shelf is 2.37×10^6 km^2 (Sathiamurthy and Voris, 2006). At the oldest age covered by core 18288-2, 18.3 ka, the exposed shelf area was approximately 2.35×10^6 km^2, leaving about 0.02×10^6 km^2 still submerged. The area of potential sediment source regions surrounding the Sunda Shelf was derived from Milliman and Farnsworth (2011), allowing us to estimate the area contributing silicate weathering material at different stages (Fig. 7.4C). As shown in Appendix Table 10, the average CO_2 consumption rate during Stage I is 97×10^3 mol/km^2/yr. In Stage II, the CO_2 consumption rate was 90×10^3 mol/km^2/yr and 108×10^3mol/km^2/yr for possibilities (2) and (3), respectively, with an average of 99×10^3 mol/km^2/yr. Thus, the CO_2 consumption rates during Stages I and II are comparable and roughly half that of Stage III (Fig. 7.4F).

Focusing on the impact of exposed shelf on silicate weathering, when sea level was at lowest during the glacial period, the exposed shelf area was at its maximum (Fig. 7.4B). At this time, the CO_2 consumed by weathering on the exposed shelf accounted for approximately 70% of the total CO_2 consumption by silicate weathering. As sea levels rose and the exposed shelf area decreased, the proportion of CO_2 consumption from shelf sediments weathering relative to total terrestrial CO_2 consumption also decreased (Fig. 7.4G). In this study, the land area used to calculate silicate weathering includes both the land area surrounding the Sunda Shelf and the exposed shelf area.

Since Southeast Asia and the SCS have remained tectonically stable during the Quaternary, we assume that the land area around the Sunda Shelf has remained unchanged since the LGM. The exposed shelf area varied with sea level changes, from a fully exposed area of 2.37×10^6 km^2 during the LGM to 0 km^2 approximately 6 ka, when sea levels reached their current height (Fig. 7.4B), means a continuous decreasing in exposed shelf area since the LGM (Sathiamurthy and Voris, 2006). Our calculations indicate that since the late LGM, the total CO_2 consumption by silicate weathering has not changed significantly, despite an increase in total land area. The CO_2 consumption rate during low sea level periods was about half of that during high sea level periods. If there were no additional weatherable materials caused by exposed shelf during the glacial period, CO_2 consumption would have reduced by approximately 70% (around 230×10^9 mol/yr). Applying this result to the entire tropical region (with a shelf area of approximately 8.6×10^6 km^2 between 23ºN and 23ºS), it suggests that around 834×10^9 mol/yr of CO_2 would be consumed, accounting for about 7% of the global CO_2 consumption from weathering during the Holocene ($11{,}700\times10^9$ mol/yr). This result is comparable to the 4-20% (average 12%) CO_2 consumption by silicate weathering of exposed tropical shelf sediments during low sea level periods from Wan et al. (2017). Considering the reduction in atmospheric CO_2 concentrations due to carbonate compensation during glacial-interglacial cycles (Petit et al., 1999), the CO_2 consumed by silicate weathering of exposed shelf during low sea levels in glacial periods accounted for 3-15% (average 9%) of total CO_2 consumption (Wan et al., 2017), a figure similar to our calculated 7%. Our study thus highlights the potential importance of chemical weathering of exposed tropical shelf sediments during glacial periods in influencing atmospheric CO_2 concentrations. That is, during glacial lowstand, the silicate weathering on exposed shelf significantly consumed atmospheric CO_2, likely exacerbated glacial cycles. This suggests that the driving force behind global climate change on glacial-interglacial timescales may have been the low-latitude tropics rather than high-latitude regions, a hypothesis that may indeed be valid (Wang, 2021).

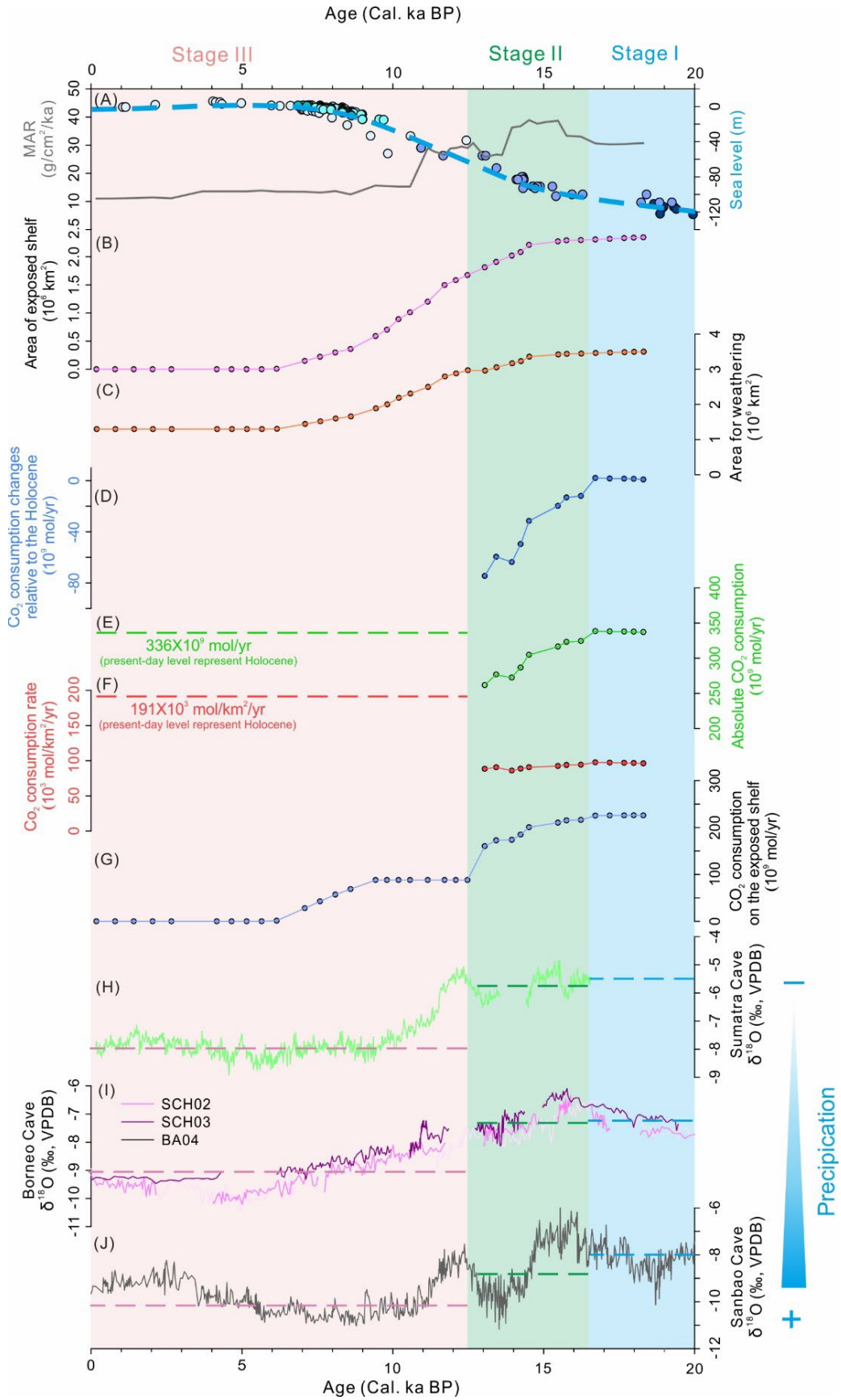

Fig. 7.4 The graph shows the silicate weathering and CO_2 consumption records of the core 18288-2 since the last deglaciation.(A) Sediment mass accumulation rate (MAR) and the sea level change

since 20 ka BP (Bird et al., 2007; Geyh et al., 1979; Hanebuth et al., 2000; Hanebuth et al., 2009; Hesp et al., 1998)；(B) Area of exposed shelf since the last deglaciation (Sathiamurthy and Voris, 2006)；(C) Total land area for weathering reaction since the last deglaciation (both land and exposed shelf) (Milliman and Farnsworth, 2011; Sathiamurthy and Voris, 2006).(D) Difference in CO_2 consumption by silicate weathering in Stage I and II relative to Stage III. (E) Absolute CO_2 consumption by silicate weathering since the last deglaciation, Stage I (the Holocene) is 336×10^9 mol/yr calculated by the rate in (F). (F) CO_2 consumption rate by silicate weathering since the last deglaciation, the rate of Stage I is 119×10^3 mol/km^2/yr (Li et al., 2014).(G) CO_2 consumption by silicate weathering on the exposed shelf since the last deglaciation. (H) $\delta^{18}O$ values of stalagmites from Tangga Cave, Sumatra (Wurtzel et al., 2018). (I) $\delta^{18}O$ values of stalagmites from Gunung Buda National Park, northern Borneo (Partin et al., 2007). (J) $\delta^{18}O$ values of stalagmites from Sanbao Cave, Shengnongjia Mountain in the middle reaches of Changjiang, China (Cheng et al., 2016).

7.3 Factors control atmospheric CO_2 consumption rate by silicate weathering during glacial and interglacial periods

7.3.1 Lithology and mineral composition

The fundamental factors controlling chemical weathering are mineral composition and lithology (Gaillardet et al., 1999a). Silicate weathering is typically regarded as a ligand-exchange process with the metal ions bonded in the mineral structure. The weathering rates depend on the relative strengths of coordinated metal ions in the mineral structure compared to the strength of the metal–ligand bond (White and Buss, 2014). Generally, amphibole and pyroxene are expected to weather faster than feldspar, which in turn weathers faster than quartz. Field work indicates that volcanic glass weathers an order of magnitude faster than crystalline minerals with similar compositions. Previous analysis indicates that the potential sediment sources in this study are characterized by "large area, wide source, and complex lithology", especially during high sea level period. Geochemical composition suggests that slope sediments are primarily supplied by large rivers like the Mekong and Red Rivers, and there is also input from remobilized submarine shelf sediments. These sediments are often mixtures of weathered terrestrial rock products, making their lithology relatively uniform yet complex, and thus making it difficult to accurately determine the lithology of the source areas. In contrast, during low sea level period, the slope sediments show an increased proportions from Sumatra, which is located at a plate boundary and has experienced volcanic eruptions until the Holocene (Feng et al., 2021). These fresh materials from the mantle are more susceptible to weathering and hydrolysis, potentially leading to higher weathering rates recorded in the core sediments. However, this contradicts the data from the core 18288-2, suggesting that the influence of lithology on chemical weathering rates may have been neutralized or altered by other factors in the study area.

7.3.2 Temperature

Temperature shows a strong positive correlation with chemical weathering rate, and temperature can promote the dissolution of minerals and the migration of elements (Deng et al., 2022). In the SCS, the average sea surface temperature (SST) during the LGM and Holocene were 28°C and 23°C, respectively (Fig. 7.1F) (Steinke et al., 2001). The land surface temperature (LST) differed by only 2.5-3.5°C (Shakun and Carlson, 2010), indicating minimal temperature variation in the study area since the LGM. This is primarily because the region is located in the low-latitude tropics, where glacial cooling effects are more pronounced in higher latitudes. Temperature is influenced not only by latitude but also by elevation, typically decreasing by 0.6°C for every 100 meters of altitude gain. During the low sea level period, the weatherable land in the study area included surrounding islands, the continent, and exposed shelf, with an average elevation of approximately 250 meters. In contrast, during high sea level period, only islands and the continent contributed to weathering, with an average elevation of about 900 meters. By combining the calculated CO_2 consumption rates from the three stages of the core 18288-2 with the corresponding SST, we can infer the weathering reaction temperature required in the weathering zones. Calculations indicate that the weathering reaction temperature in the study area has not varied significantly since the LGM. In fact, due to elevation effects, the weathering reaction temperature during high sea level period may have been lower than that during low sea level period, despite an overall increase in temperatures since the LGM. Thus, further evidence is needed to determine whether temperature has controlled the relative CO_2 consumption rates by silicate weathering during glacial and interglacial periods in the tropical areas.

7.3.3 Precipitation and runoff

Numerous studies have demonstrated a strong linear correlation between precipitation or runoff and chemical weathering rates (Gaillardet et al., 1999b; Gislason et al., 2009). Precipitation increases the moisture content of the weathering layer and the wetness of mineral surfaces, thereby enhancing chemical weathering. Additionally, water flow can transport dissolved CO_2 or organic acids into minerals, facilitating chemical weathering (White and Buss, 2014). Precipitation also increases river runoff, dissolving more materials and transporting them into the ocean (Gaillardet et al., 1999a). Stalagmites in karst caves primarily form through the deposition caused by the degassing of CO_2 from dripping water, which mainly originates from atmospheric

precipitation. Therefore, stalagmites can record the stable isotope signals of atmospheric precipitation (Cheng et al., 2016; Partin et al., 2007; Wang et al., 2001). A more negative $\delta^{18}O$ value in stalagmites indicates higher precipitation. $\delta^{18}O$ isotope records from two stalagmites in Sumatra and Borneo on the southern Sunda Shelf, as well as one record from the Sanbao Cave in northern shelf, indicate changes in precipitation since the late LGM in both the southern and northern regions of the shelf (Fig. 7.4H, I, J). The $\delta^{18}O$ values from Sumatra cave and Sanbao Cave show similar trends and respond well to the Younger Dryas (YD) and Bølling–Allerød (B-A) events. In contrast, the $\delta^{18}O$ from Borneo cave does not show a strong response to the YD event, the reasons for which are not elaborated here. Our focus is on the changes in $\delta^{18}O$ values since the LGM. The three stalagmites $\delta^{18}O$ values were divided into three stages corresponding to the sedimentary records of core 18288-2. The average values for each stage are presented in Table 7.2 (Fig. 7.4H, I, J). Overall, the $\delta^{18}O$ values of the stalagmites decrease from the Stage I to III, indicating a general increase in precipitation from the LGM to the Holocene. Strong precipitation enhanced the dissolution of minerals in terrestrial sediments, thereby accelerating chemical weathering rates.

Table 7.2 Average $\delta^{18}O$ values in stalagmites of land caves around the study area at different periods

Area	Stage III (0-12.5 ka) (‰ VPDB)	Stage II (12.5-16.5 ka) (‰ VPDB)	Stage I (16.5-18.5 ka) (‰ VPDB)
Sanbao Cave	-9.79	-8.66	-7.99
Sumatra Cave	-7.71	-5.78	-5.54
Borneo Cave	-8.39	-7.46	-7.14

7.3.4 Buffering of carbonate system

The silicate weathering kinetics can be strongly regulated by the pH of the solution. For every unit of pH change, weathering kinetics can increase by an order of magnitude whether due to increased acidity (pH <5–6) or alkalinity (pH >8–9) (Gudbrandsson et al., 2014; Lasaga, 1984). Such changes can even counteract the potential effects of temperature or runoff on silicate chemical weathering. However, when the solution environment is near circumneutral pH (~6–8), the dissolution rate of feldspar is minimal and relatively insensitive to pH changes (Bufe et al., 2021). When carbonates on the

land surface dissolve, they neutralize the solution's pH, thereby inhibiting the dissolution of silicates. During low sea level period, the carbonate formed in the marine were exposed with the shelf exposure. These carbonates dissolved by contacting with the rain and/or groundwater, which adjusts the solution's pH to circumneutral values (~pH 6-8), thereby inhibiting the rate of silicate chemical weathering. During high sea level periods, the shelf is submerged, and the surrounding land becomes the primary weathering source. As mentioned earlier, the bedrock of surrounding land is characterized by complex lithology. While sedimentary rocks are less extensive on the Malay Peninsula, they are widespread in Indochina Peninsula, Sumatra, and Borneo. Current field work indicates the presence of carbonate rocks in these sedimentary formations. However, due to a lack of detailed knowledge about their distribution and content, it is challenging to assess whether the dissolution of carbonates significantly regulates pH during silicate weathering. Therefore, this controlling factor requires further investigation and may be more applicable to studies in smaller, more homogenous catchments, such as rivers in Taiwan (Bufe et al., 2021).

7.4 Summary

We reconstructed the silicate chemical weathering processes and CO_2 consumption history in the southern SCS since the last deglaciation through sediment records from the core 18288-2 on the eastern slope of the Sunda Shelf. By analyzing the ratios of soluble to stable elements (Ca/Al, Mg/Al, K/Al, Na/Al), we observed that the sediment records from the southern SCS indicate stronger weathering intensity during the glacial period. To assess the preservation and transmission of weathering signals from source to sink, we calculated the relative weathering intensity since the last deglaciation. Based on the geochemical composition of the core 18288-2, we computed the relative changes in silicate weathering intensity in three stages: Stage I (the late LGM to early last deglaciation), Stage II (the late last deglaciation), and Stage III (the Holocene). The results show that the CO_2 consumption concentration by silicate weathering was similar across these three stages, indicating that the weathering intensity did not vary significantly. Sea level changes led to the exposure of the Sunda Shelf during the glacial period, resulting in significant differences in the weatherable area between glacial and interglacial periods. By calculating the CO_2 consumption rates by silicate weathering in different stages, we assessed the impact of shelf exposure on atmospheric CO_2 consumption during the glacial period. The results indicate that CO_2

consumption rates during the Stage I and II (late LGM to last deglaciation) were only half of those in the Stage III (the Holocene), although the total CO_2 consumption content by silicate weathering across the three stages was similar. During the glacial lowstand, the exposure of the Sunda Shelf increased the weatherable land area by approximately a factor of two. Calculations indicate that the CO_2 consumption by silicate weathering of exposed shelf sediments accounted for about 7% of the global CO_2 consumption during the Holocene. This study highlights the potential significance of weathering on tropical exposed shelves during glacial periods on atmospheric CO_2 concentration. During glacial lowstand, silicate weathering on the exposed shelf led to significant CO_2 consumption, likely exacerbated glacial cycles. This suggests that low-latitude tropical regions, rather than high-latitude regions, could be key drivers of global climate change on glacial-interglacial time scales. Additionally, we investigated the factors controlling the variations in CO_2 consumption rates between the glaciation and the Holocene. It was found that precipitation and runoff are the primary factors controlling CO_2 consumption rates by silicate weathering in the study area. The effects of bedrock lithology, mineral composition, and carbonate system buffering on silicate weathering require further investigation. Temperature appears to have had no significant impact on CO_2 consumption rates by silicate weathering in the low-latitude tropical regions since the LGM.

Chapter 8 Conclusions and future work

8.1 Conclusions

This study focuses on the southern SCS, particularly the Sunda Shelf and surrounding land areas. Main river sediments in potential source regions, seafloor sediments, and core ST13 from the Sunda Shelf and core 18288-2 from the slope were selected as samples. Geochemical methods, including elemental and isotopic analyses, were employed to investigate the sedimentary source evolution since the Last deglaciation and the transition of the Sunda Shelf's "source-sink" role during high and low sea levels. The study also revealed the relative changes in silicate weathering intensity between glacial and interglacial periods, calculated the atmospheric CO_2 consumption rate by silicate weathering in the southern SCS since the Last deglaciation, and indicated the factors controlling this process. The main conclusions are as follows:

(1) The potential source regions in the southern SCS are complex, primarily consisting of large rivers in South China and the Indochina Peninsula in the northern part of the SCS, as well as smaller island rivers from Sumatra and Borneo in southern part of the SCS. Isotopic proxies show that river sediments around the SCS exhibit increasing $^{87}Sr/^{86}Sr$ ratios and decreasing εNd values from southern to northern lands, indicating mantle-derived control in the south and crustal-derived control in the north. Nearshore sediments have a chemical composition similar to that of nearby river sediments. Central shelf and deep see sediments are geochemically closer to crustal materials. This suggests that modern seafloor sediments are primarily influenced by rivers with high sediment discharge into the sea. However, the elemental composition of river sediments does not always correspond well with that of marine sediments, indicating the need for caution when using river sediments as end-members to trace marine sediment sources.

(2) The evolution of sediment sources since the LGM. From the late LGM to early last deglaciation, with low sea levels, sediment on the slope and in the southern deep-water areas primarily supplied by the Mekong River and southern island rivers. As sea levels rose, the shelf was gradually submerged, leading to a decrease in material from southern island rivers and an increase in sediment supply from large rivers in the northern shelf. During the high sea levels of the Holocene, the Mekong River became the primary source of

sediment for the shelf, with material from surrounding islands accumulating only nearshore. The slope and deep-water areas were also influenced by sediment from the Red River and the Gulf of Beibuwan in the northern SCS. We indicated that sea level changes have primarily driven changes in accommodation space and deposition centers, which have been the dominant factor influencing sediment source variations in the southern SCS since the last deglaciation, climate, ocean currents, and sediment fluxes have also played significant roles.

(3) By analyzing the ($^{234}U/^{238}U$) ratios and Comminution Ages (t_{com}) of 18288-2 core sediments from the slope of the eastern Sunda Shelf, combined with provenance analysis and glacial climate conditions in the southern SCS, it was determined that during the low sea levels of the glacial period, precipitation intensity on the tropical islands of the southern SCS was slightly weaker than that of the Holocene. Material that was either eroded early or retained on the profile for long time was flushed out and transported by paleo-rivers to the slope for deposition. This study reveals that erosion on tropical islands in the southern SCS remained active during the glacial period. The use of uranium-series disequilibrium offers an effective method for studying millennial-scale tropical catchment erosion.

(4) The relative silicate weathering intensity and atmospheric CO_2 consumption rates during glacial and interglacial periods were calculated using major element analysis of core sediments. The results indicate that since the Last deglaciation, the atmospheric CO_2 consumption flux in the southern SCS has remained nearly constant. While the CO_2 consumption rate by silicate weathering during the glacial period was only half that of the Holocene. We found that, compared to the high sea levels of the Holocene, the low sea levels of the glacial period exposed approximately 60-70% more land area of the southern SCS. This increased area available for weathering reactions during the glacial period compensated for the reduced rate of silicate chemical weathering, thereby maintaining the long-term balance of atmospheric CO_2 consumption by silicate weathering. Thus, we must reassess the impact of tropical low-latitude shelf exposure during glacial periods on atmospheric CO_2 concentrations. This could potentially provide strong evidence for the hypothesis that low-latitude tropical regions drive global climate change on

glacial-interglacial timescales. Our study also revealed that the primary factor controlling variations of silicate weathering and atmospheric CO_2 consumption rate is precipitation. The influence of temperature and lithology requires further evidence for confirmation.

8.2 Shortage and prospect

Although this study has provided some insights and conclusions regarding the sediment sources, silicate weathering processes, and CO_2 consumption history of the Sunda Shelf and southern SCS since the Last deglaciation, there are still many work that require further research due to the limitations of the current study and my professional expertise.

(1) **Samples**. Given the limitations of sediment samples in the geological timescale of the southern SCS, we should increase the cruises for ocean drilling, formulate a systematic and comprehensive drilling plan, and conduct systematic sampling from the Sunda shelf-slope-Southern deep sea. The time scale if the drilling should also span as many glacial-interglacial cycles as possible, so as to systematically study the impact of several exposures of the Sunda Shelf since the Quaternary on the sediment "source-sink" process and the impact on the long-term terrestrial silicate weathering consumption of atmospheric CO_2.

(2) **Provenance tracing end members and proxies.** Effectively clarifying the source of sediments is the basis for studying paleoenvironmental changes, so more detailed and accurate provenance tracing research is needed. First, clarifying the accuracy of traditional river sediments as a comparing end member. Can offshore surface sediments be used as another set of comparison end members for deep-sea sediment sources? In terms of proxies, on the basis of fully analyzing sedimentological proxies, the applicability of geochemical proxies should be further analyzed.

(3) **Proxies of weathering signals.** The terrestrial chemical weathering signals is recorded in the sea area, which requires reliable interpretation proxies. From the source area, floodplain to estuary and then to the shelf, the intermediate process of environmental signal generation, transmission and transformation is very complex and requires systematic research. This study mainly used major element to trace the silicate chemical weathering intensity and the rate of atmospheric CO_2 consumption since the last deglaciation. With the development

of isotope analysis technology, many non-traditional stable isotope proxies (such as Li, Mg, K isotopes, etc.) have begun to be used to study continental weathering. Therefore, we can try to use more proxies to jointly analyze the weathering history and make up for the shortcomings of a single proxy. And combined with big data and models, we can further explore the control factors of weathering in low-latitude tropical regions at different time scales.

Reference

[1] Allen, P.A. Fundamentals of the Earth Surface System, Earth Surface Processe, 1997. pp. 1-50.

[2] Allen, P.A., From landscapes into geological history. Nature. 2008, 451, 274-276.

[3] Alqahtani, F., Jackson, C.A.-L., Johnson, H.D., Som, M.R., Fluvial Reservoir Analogues in the Malay Basin: Analysis of Shallow 3D Seismic Data of Pleistocene Rivers on the Sunda Shelf. Journal of Sedimentary Research. 2017, 87, 17-40.

[4] An, Y., Jian, Z., Pulleniatina Minimum Event during the last deglaciation in the southern South China Sea. Science Bulletin. 2009, 54, 4514-4519.

[5] Andersen, M.B., Stirling, C.H., Weyer, S., Uranium isotope fractionation. Reviews in Mineralogy and Geochemistry. 2018, 82, 799-850.

[6] Anthony, E.J., Julian, M., Source-to-sink sediment transfers, environmental engineering and hazard mitigation in the steep Var River catchment, French Riviera, southeastern France. Geomorphology. 1999, 31, 337-354.

[7] Awasthi, N., Ray, E., Paul, D., Sr and Nd isotope compositions of alluvial sediments from the Ganga Basin and their use as potential proxies for source identification and apportionment. Chemical Geology.2018, 476, 327-339.

[8] Ayliffe, L.K., Gagan, M.K., Zhao, J.-x., et al., Rapid interhemispheric climate links via the Australasian monsoon during the last deglaciation. Nature Communications.2013, 4.

[9] Berner, E.K., Berner, R.A., Global environment: water, air, and geochemical cycles. Princeton University Press. 2012

[10] Berner, R.A., Palaeo-CO_2 and climate. Nature. 1992a, 358.

[11] Berner, R.A., Weathering, plants, and the long-term carbon cycle. Geochimica et Cosmochimica Acta 1992b, 56, 3225-3231.

[12] Berner, R.A., Kothavala, Z., The carbonate-silicate geochemical cycle and its effects on atmospheric carbon dioxide over the past 100 million years. Am J Sci. 1983, 283, 641-683.

[13] Berner, R.A., Lasaga, A.C., Garrels, R.M., Carbonate-silicate geochemical cycle and its effect on atmospheric carbon dioxide over the past 100 million years.1983, 283:7.

[14] Bi, L., Yang, S.Y., Zhao, Y., et al., Provenance study of the Holocene sediments in the Changjiang (Yangtze River) estuary and inner shelf of the East China sea. Quatern Int. 2017, 441, 147-161.

[15] Bird, M.I., Fifield, L.K., Teh, T.S., et al., An inflection in the rate of early mid-Holocene eustatic sea-level rise: A new sea-level curve from Singapore. Estuarine, Coastal and Shelf Science. 2007, 71, 523-536.

[16] Bird, M.I., Taylor, D., Hunt, C., Palaeoenvironments of insular Southeast Asia during the Last Glacial Period: a savanna corridor in Sundaland? Quaternary Science Reviews. 2005, 24, 2228-2242.

[17] Bird, P., An updated digital model of plate boundaries. Geochemistry, Geophysics, Geosystems. 2003, 4, 1027.

[18] Borg, L.E., Banner, J.L., Neodymium and strontium isotopic constraints on soil sources in Barbados, West Indies. Geochimica et Cosmochimica Acta. 1996, 60, 4193-4206.

[19] Bourdon, B., Turner, S., Henderson, G.M., Lundstrom, C.C., Introduction to U-series

Geochemistry. Reviews in Mineralogy and Geochemistry. 2003, 52, 1-21.

[20] Bufe, A., Hovius, N., Emberson, R., Rugenstein, J.K.C., Galy, A., Hassenruck-Gudipati, H.J., Chang, J.-M., Co-variation of silicate, carbonate and sulfide weathering drives CO_2 release with erosion. Nature Geoscience. 2021, 14, 211-216.

[21] Camanni, G., Ye, Q., The significance of fault reactivation on the Wilson cycle undergone by the northern South China Sea area in the last 60 Myr. Earth-Science Reviews. 2022, 225.

[22] Carter, L., Orpin, A.R., Kuehl, S.A., From mountain source to ocean sink - the passage of sediment across an active margin, Waipaoa Sedimentary System, New Zealand. Marine Geology. 2010, 270, 1-10.

[23] Chen, J., Li, C., Galy, A., et al., Uranium-series comminution ages constrain large catchment erosion and its response to climate change: A case study from the Changjiang. Earth and Planetary Science Letters. 2024, 625.

[24] Cheng, H., Edwards, R.L., Sinha, A., et al., The Asian monsoon over the past 640,000 years and ice age terminations. Nature. 2016, 534, 640-646.

[25] Cheng, H., Lawrence Edwards, R., Shen, C.-C., et al., Improvements in ^{230}Th dating, ^{230}Th and ^{234}U half-life values, and U–Th isotopic measurements by multi-collector inductively coupled plasma mass spectrometry. Earth and Planetary Science Letters. 2013, 371-372, 82-91.

[26] Cheng, Z., Wu, J., Luo, C., et al., Coexistence of savanna and rainforest on the ice-age Sunda Shelf revealed by pollen records from southern South China Sea. Quaternary Science Reviews. 2023, 301.

[27] Choi, T., Lee, Y.I., Orihashi, Y., Yi, H.-I., The provenance of the southeastern Yellow Sea sediments constrained by detrital zircon U–Pb age. Marine Geology. 2013, 337, 182-194.

[28] Clift, P.D., Giosan, L., Blusztajn, J., et al., Holocene erosion of the Lesser Himalaya triggered by intensified summer monsoon. Geology. 2008, 36, 79-86.

[29] Colin, C., Turpin, L., Blamart, D., et al., Evolution of weathering patterns in the Himalayas and Indo-Burman ranges over the last 280 kyr : effects of sediment provenance on ^{87}Sr/^{86}Sr ratios tracers. Geochemistry, Geophysics, Geosystems. 2006, 7, 1-6.

[30] Deng, K., Yang, S., Guo, Y., A global temperature control of silicate weathering intensity. Nature Communications. 2022, 13.

[31] DePaolo, D.J., Lee, V.E., Christensen, J.N., Maher, K., Uranium comminution ages: Sediment transport and deposition time scales. Comptes Rendus Geoscience. 2012, 344, 678-687.

[32] DePaolo, D.J., Maher, K., Christensen, J.N., et al., Sediment transport time measured with U-series isotopes: Results from ODP North Atlantic drift site 984. Earth and Planetary Science Letters. 2006, 248, 394-410.

[33] Dickin, A.P., Radiogenic Isotope Geology, Third Edition ed. Cambridge University Press, United Kingdom. 2018.

[34] Dosseto, A., Buss, H.L., Chabaux, F., Age and weathering rate of sediments in small catchments: The role of hillslope erosion. Geochimica et Cosmochimica Acta. 2014, 132, 238-258.

[35] Dosseto, A., Hesse, P.P., Maher, K., Fryirs, K., Turner, S., Climatic and vegetation control on sediment dynamics during the last glacial cycle. Geology, 2010, 38, 395-398.

[36] Dosseto, A., Turner, S.P., Chappell, J., The evolution of weathering profiles through time: New insights from uranium-series isotopes. Earth and Planetary Science Letters. 2008. 274, 359-

371.

[37] Duan, Z., Li, C., Guo, Y., et al., Sr-Nd isotopic fingerprints of Red River sediments and its implication for provenance discrimination in the South China Sea. Marine Geology. 2023, 457.

[38] Duc, D.M., Nhuan, M.T., Ngoi, C.V., Nghi, T., Tien, D.M., van Weering, T.C.E., van den Bergh, G.D., Sediment distribution and transport at the nearshore zone of the Red River delta, Northern Vietnam. Journal of Asian Earth Sciences. 2007, 29, 558-565.

[39] Dürr, H.H., Meybeck, M., Dürr, S.H., Lithologic composition of the Earth's continental surfaces derived from a new digital map emphasizing riverine material transfer. Global Biogeochem Cy. 2009, 19.

[40] Emberson, R., Galy, A., Hovius, N., Weathering of Reactive Mineral Phases in Landslides Acts as a Source of Carbon Dioxide in Mountain Belts. Journal of Geophysical Research: Earth Surface. 2018, 123, 2695-2713.

[41] Fang, G., Fang, W., Fang, Y., Wang, K., A survey of studies on the South China Sea upper ocean circulation. Acta Oceanographica Taiwanica. 1998, 37, 1-16.

[42] Feng, J., Zhu, L., Zhen, X., Hu, Z., Grain size effect on Sr and Nd isotopic compositions in eolian dust: Implications for tracing dust provenance and Nd model age. Gechemical Journal. 2009, 43, 123-131.

[43] France-Lanord, C., Derry, L.A., Organic carbon burial forcing of the carbon cycle from Himalayan erosio. Nature. 1997, 390, 65-67.

[44] Francke, A., Carney, S., Wilcox, P., Dosseto, A., Sample preparation for determination of comminution ages in lacustrine and marine sediments. Chemical Geology. 2018, 479, 123-135.

[45] Francke, A., Dosseto, A., Panagiotopoulos, K., Leicher, N., Lacey, J.H., Kyrikou, S., Wagner, B., Zanchetta, G., Kouli, K., Leng, M.J., Sediment residence time reveals Holocene shift from climatic to vegetation control on catchment erosion in the Balkans. Global and Planetary Change. 2019, 177, 186-200.

[46] Franke, D., Savva, D., Pubellier, M., Steuer, S., Mouly, B., Auxietre, J.-L., Meresse, F., Chamot-Rooke, N., The final rifting evolution in the South China Sea. Marine and Petroleum Geology. 2014, 58, 704-720.

[47] Frings, P.J., Palaeoweathering: How Do Weathering Rates Vary with Climate? Elements. 2019, 15, 259-265.

[48] Frings, P.J., Buss, H.L., The Central Role of Weathering in the Geosciences. Elements. 2019, 15, 229-234.

[49] Gaillardet, J., Dupré, B., Allègre, C.J., Geochemistry of large river suspended sediments: silicate weathering or recycling tracer? Geochimica et Cosmochimica Acta. 1999a, 63, 4037-4051.

[50] Gaillardet, J., Dupre, B., Louvat, P., Allegre, C.J., Global silicate weathering and CO2 consumption rates deduced from the chemistry of large rivers. Chemical Geology. 1999b, 159, 3-30.

[51] Ganopolski, A., Winkelmann, R., Schellnhuber, H.J., Critical insolation-CO2 relation for diagnosing past and future glacial inception. Nature. 2016, 534, S19-S20.

[52] Garzanti, E., Andò, S., France-Lanord, C., et al., Mineralogical and chemical variability of fluvial sediments1. Bedload sand (Ganga–Brahmaputra, Bangladesh). Earth and Planetary Science Letters. 2010, 299, 368-381.

[53] Garzanti, E., He, J., Barbarano, M., et al., Provenance versus weathering control on sediment composition in tropical monsoonal climate (South China) - 2. Sand petrology and heavy minerals. Chemical Geology., 2021, 564.

[54] Geyh, M.A., Kudrass, H.R., Streif, H., Sea-level changes during the late Pleistocene and Holocene in the Strait of Malacca. Nature. 1979, 278, 441-443.

[55] Gibbs, R.J., Clay mineral segregation in the marine environment. J Sediment Res. 1977, 47, 237-243.

[56] Gislason, S.R., Oelkers, E.H., Eiriksdottir, E.S., Kardjilov, M.I., Gisladottir, G., Sigfusson, B., Snorrason, A., Elefsen, S., Hardardottir, J., Torssander, P., Oskarsson, N., Direct evidence of the feedback between climate and weathering. Earth and Planetary Science Letters. 2009, 277, 213-222.

[57] Goldstein, S.L., O'Nions, R.K., 1981. Nd and Sr isotopic relationships in pelagic clays and ferromanganese deposits. Nature. 1981, 292, 324-327.

[58] Gudbrandsson, S., Wolff-Boenisch, D., Gislason, S.R., Oelkers, E.H., Experimental determination of plagioclase dissolution rates as a function of its composition and pH at 22°C. Geochimica et Cosmochimica Acta. 2014, 139, 154-172.

[59] Handley, H.K., Turner, S., Afonso, J.C., et al., Sediment residence times constrained by uranium-series isotopes: A critical appraisal of the comminution approach. Geochimica et Cosmochimica Acta. 2013a, 103, 245-262.

[60] Handley, H.K., Turner, S.P., Dosseto, A., et al., Considerations for U-series dating of sediments: Insights from the Flinders Ranges, South Australia. Chemical Geology. 2013b, 340, 40-48.

[61] Hanebuth, T., Stattegger, K., Grootes, P.M., 2000. Rapid flooding of the Sunda Shelf: A late-glacial sea-level record. Science. 2000, 288, 1033-1035.

[62] Hanebuth, T.J.J., Stattegger, K., Bojanowski, A., Termination of the Last Glacial Maximum sea-level lowstand: The Sunda-Shelf data revisited. Global and Planetary Change. 2009, 66, 76-84.

[63] Hanebuth, T.J.J., Stattegger, K., Schimanski, A., Lüdmann, T., Wong, H.K., Late Pleistocene forced-regressive deposits on the Sunda Shelf (Southeast Asia). Marine Geology. 2003, 199, 139-157.

[64] Hanebuth, T.J.J., Voris, H.K., Yokoyama, Y., et al., Formation and fate of sedimentary depocentres on Southeast Asia's Sunda Shelf over the past sea-level cycle and biogeographic implications. Earth-Science Reviews. 2011, 104, 92-110.

[65] Hartmann, J., Jansen, N., Dürr, H.H., Kempe, S., Köhler, P., Global CO2-consumption by chemical weathering: What is the contribution of highly active weathering regions? Global and Planetary Change. 2009, 69, 185-194.

[66] Hartmann, J., Moosdorf, N., The new global lithological map database GLiM A representation of rock. Geochemisty, Geophics, Geosystems. 2012, 13.

[67] He, M., Zheng, H., Clift, P.D., et al., Geochemistry of fine-grained sediments in the Yangtze River and the implications for provenance and chemical weathering in East Asia. Progress in Earth and Planetary Science. 2015, 2, 1-20.

[68] Heaton, T.J., Köhler, P., Butzin, M., Bard, E., Reimer, R.W., Austin, W.E.N., Bronk Ramsey, C., Grootes, P.M., Hughen, K.A., Kromer, B., Reimer, P.J., Adkins, J., Burke, A., Cook, M.S., Olsen, J., Skinner, L.C., Marine20—The Marine Radiocarbon Age Calibration Curve (0–

55,000 cal BP). Radiocarbon. 2020, 62, 779-820.

[69] Heimsath, A.M., Dietrich, W.E., Nishiizumi, K., Finkel, R.C., The soil production function and landscape equilibrium. Nature. 1997, 388, 358-361.

[70] Hein, C.J., Galy, V., Galy, A., et al., Post-glacial climate forcing of surface processes in the Ganges-Brahmaputra river basin and implications for carbon sequestration. Earth and Planetary Science Letters. 2017, 478, 89-101.

[71] Hesp, P.A., Hung, C.C., Hilton, M., Ming, C.L., M, I., Turner, S., A First Tentative Holocene Sea-Level Curve for Singapore. Journal of Coastal Research. 1998, 14, 308-314.

[72] Hori, K., Saito, Y., Zhao, Q.H., et al., Sedimentary facies and Holocene progradation rates of the Changjiang (Yangtze) delta, China. Geomorphology. 2001a, 41, 233-248.

[73] Hori, K., Saito, Y., Zhao, Q.H., et al., Sedimentary facies of the tide-dominated paleo-Changjiang (Yangtze) estuary during the last transgression. Marine Geology. 2001b, 177, 331-351.

[74] Huang, J., Jiang, F., Wan, S., et al., Terrigenous supplies variability over the past 22,000yr in the southern South China Sea slope: Relation to sea level and monsoon rainfall changes. Journal of Asian Earth Sciences. 2016, 117, 317-327.

[75] Huang, J., Jiao, W., Liu, J., et al., Sediment distribution and dispersal in the southern South China Sea: Evidence from clay minerals and magnetic properties. Marine Geology. 2021, 439.

[76] Huang, W., Wang, P., Sediment mass and distribution in the South China Sea since the Oligocene. Science in China Series D: Earth Sciences. 2006, 49, 1147-1155.

[77] Hutchison, C.S., Dating Tectonism in the Indosinian–Thai–Malayan Orogen by Thermoluminescence. GSA Bulletin. 1968, 79, 375-386.

[78] Hutchison, C.S., Geology of North-West Borneo_ Sarawak, Brunei and Sabah. Elsevier Science, Amsterdam. 2005.

[79] Jacobsen, S.B., Wasserburg, G.J., Sm-Nd isotopic evolution of chondrites. Earth and Planetary Science Letters. 1980, 50, 139-155.

[80] Jiwarungrueangkul, T., Liu, Z., East Asian monsoon and sea-level controls on clay mineral variations in the southern South China Sea since the Last Glacial Maximum. Quatern Int. 2021, 592, 1-11.

[81] Jiwarungrueangkul, T., Liu, Z., Zhao, Y., Terrigenous sediment input responding to sea level change and East Asian monsoon evolution since the last deglaciation in the southern South China Sea. Global and Planetary Change. 2019, 174, 127-137.

[82] Jweda, J., Bolge, L., Class, C., Goldstein, S.L., High Precision Sr-Nd-Hf-Pb Isotopic Compositions of USGS Reference Material BCR-2. Geostand Geoanal Res. 2015, 40, 101-115.

[83] Kasting, J.F., The Goldilocks Planet? How Silicate Weathering Maintains Earth “Just Right”. Elements. 2019, 15, 235-240.

[84] Koornneef, J.M., Stracke, A., Aciego, S., Reubi, O., Bourdon, B., A new method for U–Th–Pa–Ra separation and accurate measurement of ^{234}U–^{230}Th–^{231}Pa–^{226}Ra disequilibria in volcanic rocks by MC-ICPMS. Chemical Geology. 2010, 277, 30-41.

[85] Kosler, J., Fonneland, H., Sylvester, P., Pedersen, R.-B., U–Pb dating of detrital zircons for sediment provenance studies —a comparison of laser ablation ICPMS and SIMS techniques. Chemical Geology. 2002, 182, 605-618.

[86] Kump, L.R., Brantley, S.L., Arthur, M.A., Chemical Weathering, Atmospheric CO2, and

Climate. Annual Review of Earth and Planetary Sciences. 2000, 28, 611-667.

[87] Lasaga, A.C., Chemical Kinetics of Water-Rock Interactions. Journal of Geophyscial Research. 1984, 89, 4009-4025.

[88] Li, C., Francois, R., Yang, S.Y., et al., Constraining the transport time of lithogenic sediments to the Okinawa Trough (East China Sea). Chemical Geology. 2016, 445, 199-207.

[89] Li, C., Yang, S., Lian, E., et al., A review of comminution age method and its potential application in the East China Sea to constrain the time scale of sediment source-to-sink process. Journal of Ocean University of China. 2015, 14, 399-406.

[90] Li, L., Chen, J., Chen, Y., Hedding, D.W., Li, T., Li, L., Liu, X., Zeng, F., Wu, W., Zhao, L., Li, G., Uranium isotopic constraints on the provenance of dust on the Chinese Loess Plateau. Geology. 2018, 46, 747-750.

[91] Li, L., Li, G.K., Li, T., Yi, S., Lu, H., Hedding, D.W., Chen, J., Li, G., Tracking the Provenance of Aeolian Loess in Northeastern China by Uranium Isotopes. Geochemistry, Geophysics, Geosystems. 2023, 24.

[92] Li, L., Li, L., Li, G., Uranium comminution age responds to erosion rate semi-quantitatively. Acta Geochim. 2017, 36, 426-428.

[93] Li, S., Lu, X.X., Bush, R.T., Chemical weathering and CO_2 consumption in the Lower Mekong River. Sci Total Environ. 2014, 472, 162-177.

[94] Li, X.-h., Wei, G., Shao, L., et al., Geochemical and Nd isotopic variations in sediments of the South China Sea: a response to Cenozoic tectonism in SE Asia. Earth and Planetary Science Letters. 2003, 211, 207-220.

[95] Li, X., Wang, Z., Yong-jian, Y., et al., Formation and evolution of the South China Sea since the Late Mesozoic: A review. China Geology. 2022, 5, 1-14.

[96] Liu, J., Chen, M., Xiang, R., et al., Abrupt change of sediment records in the southern South China Sea during the last glacial period and its environment significance. Quatern Int. 2011, 237, 109-122.

[97] Liu, J.P., Xu, K.H., Li, A.C., et al., Flux and fate of Yangtze River sediment delivered to the East China Sea. Geomorphology. 2007a, 85, 208-224.

[98] Liu, S., Shi, X., Yang, G., et al., Distribution of major and trace elements in surface sediments of the western Gulf of Thailand: Implications to modern sedimentation. Cont Shelf Res. 2016a, 117, 81-91.

[99] Liu, S.F., Zhang, H., Zhu, A.M., et al., Distribution of rare earth elements in surface sediments of the western Gulf of Thailand: Constraints from sedimentology and mineralogy. Quatern Int. 2019, 527, 52-63.

[100] Liu, Z., Colin, C., Huang, W., et al., Clay minerals in surface sediments of the Pearl River drainage basin and their contribution to the South China Sea. Chinese Science Bulletin. 2007b, 52, 1101-1111.

[101] Liu, Z., Colin, C., Li, X., et al., Clay mineral distribution in surface sediments of the northeastern South China Sea and surrounding fluvial drainage basins: Source and transport. Marine Geology. 2010, 277, 48-60.

[102] Liu, Z., Trentesaux, A., Clemens, S.C., et al., Clay mineral assemblages in the northern South China Sea: implications for East Asian monsoon evolution over the past 2 million years. Marine Geology. 2003. 201, 133-146.

[103] Liu, Z., Wang, H., Hantoro, W.S., et al., Climatic and tectonic controls on chemical weathering in tropical Southeast Asia (Malay Peninsula, Borneo, and Sumatra). Chemical Geology. 2012, 291, 1-12.

[104] Liu, Z.F., Zhao, Y.L., Colin, C., et al., Chemical weathering in Luzon, Philippines from clay mineralogy and major-element geochemistry of river sediments. Appl Geochem. 2009, 24, 2195-2205.

[105] Liu, Z.F., Zhao, Y.L., Colin, C., et al., Source-to-sink transport processes of fluvial sediments in the South China Sea. Earth-Science Reviews. 2016b, 153, 238-273.

[106] Ludwig, W., Amiotte-Suchet, P., Probst, J.-L., Enhanced chemical weathering of rocks during the last glacial maximum: a sink for atmospheric CO_2 ? Chemical Geology. 1999, 159.

[107] Lupker, M., France-Lanord, C., Galy, V., et al., Increasing chemical weathering in the Himalayan system since the Last Glacial Maximum. Earth and Planetary Science Letters. 2013, 365, 243-252.

[108] Luthi, D., Le Floch, M., Bereiter, B., et al., High-resolution carbon dioxide concentration record 650,000-800,000 years before present. Nature. 2008, 453, 379-382.

[109] Mackenzie, F.T., Garrels, R.M., Chemical mass balance between rivers and oceans. Am J Sci. 1966, 264, 507-525.

[110] Mackenzie, F.T., Kump, L.R., Reverse Weathering, Clay Mineral Formation, and Oceanic Element Cycles. Science. 1995, 270, 586-586.

[111] Martin, A.N., Dosseto, A., Kinsley, L.P.J., Evaluating the removal of non-detrital matter from soils and sediment using uranium isotopes. Chemical Geology. 2015, 396, 124-133.

[112] Mathew, K., Mason, P., Voeks, A., et al., Uranium isotope abundance ratios in natural uranium metal certified reference material 112-A. International Journal of Mass Spectrometry. 2012, 315, 8-14.

[113] McLennan, S.M., Hemming, S., McDaniel, D., et al., Geochemical approaches to sedimentation, provenance, and tectonics. Special Papers-Geological Society of America.1993, 21-21.

[114] McLennan, S.M., McCulloch, M.T., Taylor, S.R., Maynard, J.B., Effects of sedimentary sorting on neodymium isotopes in deep-sea turbidites. Nature. 1989, 337, 547-549.

[115] Meyer, I., Davies, G.R., Stuut, J.-B.W., Grain size control on Sr-Nd isotope provenance studies and impact on paleoclimate reconstructions: An example from deep-sea sediments offshore NW Africa. Geochemistry, Geophysics, Geosystems. 2011, 12, 1-14.

[116] Milliman, J.D., Farnsworth, K.L., River Discharge to the Coastal Ocean-A Global Synthesis. Cambridge University Press United Kingdom. 2011.

[117] Milliman, J.D., Farnsworth, K.L., Albertin, C.S., Flux and fate of fluvial sediments leaving large islands in the East Indies. J Sea Res. 1999, 41, 97-107.

[118] Misra, S., Froelich, P.N., Lithium isotope history of Cenozoic seawater: changes in silicate weathering and reverse weathering. Science. 2012, 335, 818-823.

[119] Mukul R. Bhatia, Crook, K.A.W., Trace element characteristics of graywackes and tectonic setting discrimination of sedimentary basins. Contrib Mineral Petr. 1986, 92, 181-193.

[120] Munhoven, G., François, L.M., Glacial-interglacial variability of atmospheric CO2due to changing continental silicate rock weathering: A model study. Journal of Geophysical Research: Atmospheres. 1996, 101, 21423-21437.

[121] Nesbitt, H.W., Markovics, G., price, R.C., Chemical processes affecting alkalis and alkaline earths during continental weathering. Geochimica et Cosmochimica Acta. 1980, 44, 1659-1666.

[122] Nesbitt, H.W., Young, G.M., Early Proterozoic climates and plate motions inferred from major element chemistry of lutites. Nature. 1982, 299, 715-717.

[123] Ng, N.C.W., Li, C., Wang, C., Guo, Y., Duan, Z., Su, N., Yang, S., A review of global bedrock (234U/238U) disequilibrium and its controlling factors on earth's surface. Journal of Geochemical Exploration. 2023, 245.

[124] Parker, A., An Index of Weathering for Silicate Rocks. Geological Magazine. 1970, 107, 501-504.

[125] Partin, J.W., Cobb, K.M., Adkins, J.F., Clark, B., Fernandez, D.P., Millennial-scale trends in west Pacific warm pool hydrology since the Last Glacial Maximum. Nature. 2007, 449, 452-455.

[126] Pelejero, C., Kienast, M., Wang, L., O.Grimalt, J., The flooding of Sundaland during the last deglaciation: imprints in hemipelagic sediments from the southern South China Sea. Earth and Planetary Science Letters. 1999, 171, 661-671.

[127] Penman, D.E., Caves Rugenstein, J.K., Ibarra, D.E., Winnick, M.J., Silicate weathering as a feedback and forcing in Earth's climate and carbon cycle. Earth-Science Reviews. 2020, 209.

[128] Petit, J.R., Jouzel, J., Raynaud, D., et al., Climate and atmospheric history of the past 420,000 years from the Vostok ice core, Antarctica. Nature. 1999, 399, 429-436.

[129] Plotzki, A., May, J.H., Preusser, F., Roesti, B., Denier, S., Lombardo, U., Veit, H., Geomorphology and evolution of the late Pleistocene to Holocene fluvial system in the south-eastern Llanos de Moxos, Bolivian Amazon. Catena. 2015, 127, 102-115.

[130] Qiao, S., Shi, X., Fang, X., et al., Heavy metal and clay mineral analyses in the sediments of Upper Gulf of Thailand and their implications on sedimentary provenance and dispersion pattern. Journal of Asian Earth Sciences. 2015, 114, 488-496.

[131] Raymo, M.E., Ruddiman, W.F., Tectonic forcing of late Cenozoic climate. Nature. 1992, 359, 117-122.

[132] Riebe, C.S., Hahm, W.J., Brantley, S.L., Controls on deep critical zone architecture: a historical review and four testable hypotheses. Earth Surface Processes and Landforms. 2017, 42, 128-156.

[133] Riebe, C.S., Kirchner, J.W., Granger, D.E., Finkel, R.C., Strong tectonic and weak climatic control of long-term chemical weathering rates. Geology. 2001, 29, 511-514.

[134] Romans, B.W., Castelltort, S., Covault, J.A., et al., Environmental signal propagation in sedimentary systems across timescales. Earth-Science Reviews. 2016, 153, 7-29.

[135] Rothacker, L., Dosseto, A., Francke, A., et al., Impact of climate change and human activity on soil landscapes over the past 12,300 years. Scientific Reports. 2018, 8, 1-7.

[136] William F.Ruddiman. Earth's Cliamte: Past and Future. New York: W.H.Freeman and Company, 2014: 113.

[137] Sang, P.N., Liu, Z., Colin, C., Chemical Weathering of the Mekong River Basin With Implication for East Asian Monsoon Evolution During the Late Quaternary: Marine Sediment Records in the Southern South China Sea. Frontiers in Earth Science. 2022, 10.

[138] Sathiamurthy, E., Voris, H.K., Maps of Holocene Sea level transgression and submerged lakes on the Sunda Shelf. The Natural History Journal of Chulalongkorn University

Supplement. 2006, 2, 1153-1167.

[139] Sayles, F., Mangelsdorf Jr, P., The equilibration of clay minerals with sea water: exchange reactions. Geochimica et Cosmochimica Acta. 1977, 41, 951-960.

[140] Schönfeld, J., Kudrass, H.-R., Hemipelagic Sediment Accumulation Rates in the South China Sea Related to Late Quaternary Sea-Level Changes. Quaternary Research. 1993, 40, 368-379.

[141] Scientists, E., South China Sea tectonics: opening of the South China Sea and its implications for southeast Asian tectonics, climates, and deep mantle processes since the late Mesozoic. International Ocean Discovery Program Preliminary Report 349. 2014.

[142] Shakun, J.D., Carlson, A.E., A global perspective on Last Glacial Maximum to Holocene climate change. Quaternary Science Reviews 29, 1801-1816. 2010.

[143] Sigman, D.M., Boyle, E.A., Glacial/interglacial variations in atmospheric carbon dioxide. Nature 407, 859-869. 2000.

[144] Singh, S.K., Rai, S.K., Krishnaswami, S., Sr and Nd isotopes in river sediments from the Ganga Basin: Sediment provenance and spatial variability in physical erosion. Journal of Geophysical Research 113. 2008.

[145] Solihuddin, T., A Drowning Sunda Shelf Model during Last Glacial Maximum (LGM) and Holocene: A Review. Indonesian Journal on Geoence. 2014, 1.

[146] Southon, J., Kashgarian, M., Fontugne, M., Metivier, B., Yim, W.W.S., 2002. Marine reservoir corrections for the Indian Ocean and southeast Asia. Radiocarbon 44, 167-180.

[147] Stattegger, K., Kuhnt, W., Wong, H.K., et al., 1997. Cruise Report SONNE 115 SUNDAFLUT. Sequence stratigraphy, late Pleistocene^Holocene sea level £uctuations and high resolution record of the post-Pleistocene transgression on the Sunda Shelf. Berichte-Reports, Geol.-Palaont. Inst. Univ. Kiel, Nr. 86.

[148] Steiger, R.H., Jäger, E., Subcommission on geochronology: Convention on the use of decay constants in geo- and cosmochronology. Earth and Planetary Science Letters. 1977, 36, 359-362.

[149] Steinke, S., Hanebuth, T.J.J., Vogt, C., Stattegger, K., Sea level induced variations in clay mineral composition in the southwestern South China Sea over the past 17,000 yr. Marine Geology.2008, 250, 199-210.

[150] Steinke, S., Kienast, M., Hanebuth, T., On the significance of sea-level variations and shelf paleo-morphology in governing sedimentation in the southern South China Sea during the last deglaciation. Marine Geology. 2003, 201, 179-206.

[151] Steinke, S., Kienast, M., Pflaumann, U., et al., A High-Resolution Sea-Surface Temperature Record from the Tropical South China Sea (16,500–3000 yr B.P.). Quaternary Research. 2001, 55, 352-362.

[152] Sun, X.J., Li, X., Luo, Y.L., Chen, X.D., The vegetation and climate at the last glaciation on the emerged continental shelf of the South China Sea. Palaeogeogr Palaeocl. 2000, 160, 301-316.

[153] Sun, Y., Wu, F., Clemens, S.C., Oppo, D.W., Processes controlling the geochemical composition of the South China Sea sediments during the last climatic cycle. Chemical Geology. 2008, 257, 240-246.

[154] Suresh, P.O., Dosseto, A., Hesse, P.P., Handley, H.K., Soil formation rates determined from

Uranium-series isotope disequilibria in soil profiles from the southeastern Australian highlands. Earth and Planetary Science Letters. 2013, 379, 26-37.

[155] Tanaka, T., Togashi, S., Kamioka, H., et al., JNdi-1: a neodymium isotopic reference in consistency with LaJolla neodymium. Chemical Geology. 2000, 168, 279-281.

[156] Tangang, F.T., Xia, C., Qiao, F., et al., Seasonal circulations in the Malay Peninsula Eastern continental shelf from a wave–tide–circulation coupled model. Ocean Dynamics. 2011, 61, 1317-1328.

[157] Taylor, S.R., Abundance of chemical elements in the continental crust: a new table. Geochimica et Cosmochimica Acta. 1964, 28, 1273-1285.

[158] Taylor, S.R., McLennan, S.M., The continental crust:its composition and evolution. Blackwell, Oxford, United States. 1985.

[159] Tipper, E.T., Bickle, M.J., Galy, A., et al., The short term climatic sensitivity of carbonate and silicate weathering fluxes: Insight from seasonal variations in river chemistry. Geochimica et Cosmochimica Acta. 2006, 70, 2737-2754.

[160] Tjia, H.D., Sea-level changes in the tectonically stable Malay-Thai Peninsula. Quatern Int. 1996, 31, 95-101.

[161] Tjia, H.D., Kuala, L., The Sunda Shelf, Southeast Asia. Zeitschrift für Geomorphologie. 1980, 24, 405-427.

[162] Tjia, H.D., Liew, K.K., Changes in tectonic stress field in northern Sunda Shelf basins. Geological Society, London, Special Publications. 1996, 106, 291 - 306.

[163] Tütken, T., Eisenhauer, A., Wiegand, B., THansen, B., Glacial–interglacial cycles in Sr and Nd isotopic composition of Arctic marine sediments triggered by the Svalbard/Barents Sea ice sheet. Marine Geology. 2002, 182, 351-372.

[164] Voris, H.K., Maps of Pleistocene sea levels in Southeast Asia: shorelines, river systems and time durations. J Biogeogr. 2000, 27, 1153-1167.

[165] Walker, J.C.G., Hays, P.B., Kasting, J.F., A negative feedback mechanism for the long-term stabilization of Earth's surface temperature. Journal of Geophysical Research. 1981, 86.

[166] Wan, S., Clift, P.D., Zhao, D., et al., Enhanced silicate weathering of tropical shelf sediments exposed during glacial lowstands: A sink for atmospheric CO2. Geochimica et Cosmochimica Acta. 2017, 200, 123-144.

[167] Wang, B., Clemens, S.C., Liu, P., Contrasting the Indian and East Asian monsoons: implications on geologic timescales. Marine Geology. 2003, 201, 5-21.

[168] Wang, C., Zeng, L., Lei, Y., et al., Geochemical record of the sediments in the continental shelf of the northwestern South China Sea: Implications for the provenance and sedimentary evolution. Marine Geology. 2021, 440.

[169] Wang, G., Chen, D., Su, J., Generation and life cycle of the dipole in the South China Sea summer circulation. Journal of Geophysical Research: Oceans. 2006, 111.

[170] Wang, K., Zheng, H., Tada, R., et al., Millennial-scale East Asian Summer Monsoon variability recorded in grain size and provenance of mud belt sediments on the inner shelf of the East China Sea during mid-to late Holocene. Quatern Int. 2014a, 349, 79-89.

[171] Wang, P., Response of Western Pacific marginal seas to glacial cycles: paleoceanographic and sedimentological features. Marine Geology. 1999, 156, 5-39.

[172] Wang, P., Low-latitude forcing: A new insight into paleo-climate changes. Innovation

(Camb) 2021, 2, 100145.

[173] Wang, P., Li, Q., Tian, J., Pleistocene paleoceanography of the South China Sea: Progress over the past 20years. Marine Geology. 2014b, 352, 381-396.

[174] Wang, X.M., Sun, X.J., Wang, P.X., Stattegger, K., Vegetation on the Sunda Shelf, South China Sea, during the Last Glacial Maximum. Palaeogeogr Palaeocl. 2009, 278, 88-97.

[175] Wang, Y., Liu, X., Herzschuh, U., Asynchronous evolution of the Indian and East Asian Summer Monsoon indicated by Holocene moisture patterns in monsoonal central Asia. Earth-Science Reviews. 2010, 103, 135-153.

[176] Wang, Y.J., Cheng, H., Edwards, R.L., An, Z.S., Wu, J.Y., Shen, C.-C., Dorale, J.A., A High-Resolution Absolute-Dated Late Pleistocene Monsoon Record from Hulu Cave, China. Science. 2001, 294, 2345-2348.

[177] Wang, Z., Tian, H., Wu, Z., et al., Research status and prospect of surface sediment types in the China-ASEAN seas and adjacent areas. Marine Geology and Quaternary Geology. 2023, 43, 49-60.

[178] Wasserburg, G.J., Jacobsen, S.B., Depaolo, D.J., et al., Precise Determination of Sm/Nd Ratios, Sm and Nd Isotopic Abundances in Standard Solutions. Geochimica Et Cosmochimica Acta. 1981, 45, 2311-2323.

[179] Wei, G.J., Liu, Y., Ma, J.L., et al., Nd, Sr isotopes and elemental geochemistry of surface sediments from the South China Sea: Implications for Provenance Tracing. Marine Geology. 2012, 319, 21-34.

[180] West, A., Galy, A., Bickle, M., Tectonic and climatic controls on silicate weathering. Earth and Planetary Science Letters. 2005, 235, 211-228.

[181] White, A.F., Natural Weathering Rates of Silicate Minerals. Treatise on Geochemistry. 2003, 5, 133-168.

[182] White, A.F., Blum, A.E., Effects of climate on chemical_ weathering in watersheds. Geochimica et Cosmochimica Acta. 1995, 59, 1729-1747.

[183] White, A.F., Buss, H.L., Natural Weathering Rates of Silicate Minerals, Treatise on Geochemistry. 2014, pp. 115-155.

[184] Wilson, D.J., Piotrowski, A.M., Galy, A., Clegg, J.A., Reactivity of neodymium carriers in deep sea sediments: Implications for boundary exchange and paleoceanography. Geochimica et Cosmochimica Acta. 2013, 109, 197-221.

[185] Wu, J., Suppe, J., Lu, R., Kanda, R., Philippine Sea and East Asian plate tectonics since 52 Ma constrained by new subducted slab reconstruction methods. Journal of Geophysical Research: Solid Earth. 2016, 121, 4670-4741.

[186] Wu, K., Liu, S., Kandasamy, S., et al., Grain-size effect on rare earth elements in Pahang River and Kelantan River, Peninsular Malaysia: Implications for sediment provenance in the southern South China Sea. Cont Shelf Res. 2019, 189.

[187] Wu, K., Liu, S., Shi, X., et al., The Impact of Changes in Sea Level and East Asian Monsoon on Sediment Transport on the Sunda Shelf Since the Last Deglaciation. Journal of Geophysical Research: Earth Surface. 2023, 128.

[188] Wu, K.K., Liu, S.F., Shi, X.F., et al., Distribution of rare earth elements in surface sediments of the western Sunda Shelf: Constraints from sedimentology and mineralogy. Cont Shelf Res. 2020, 206.

[189] Wurtzel, J.B., Abram, N.J., Lewis, S.C., Bajo, P., Hellstrom, J.C., Troitzsch, U., Heslop, D., Tropical Indo-Pacific hydroclimate response to North Atlantic forcing during the last deglaciation as recorded by a speleothem from Sumatra, Indonesia. Earth and Planetary Science Letters. 2018, 492, 264-278.

[190] Xu, K., Li, A., Liu, J.P., et al., Provenance, structure, and formation of the mud wedge along inner continental shelf of the East China Sea: A synthesis of the Yangtze dispersal system. Marine Geology. 2012, 291-294, 176-191.

[191] Xu, Z., Li, T., Clift, P.D., et al., Bathyal records of enhanced silicate erosion and weathering on the exposed Luzon shelf during glacial lowstands and their significance for atmospheric CO_2 sink. Chemical Geology. 2018, 476, 302-315.

[192] Yang, S., Jiang, S., Ling, H., et al., Sr-Nd isotopic compositions of the Changjiang sediments: Implications for tracing sediment sources. Science in China Series D: Earth Sciences. 2007, 50, 1556-1565.

[193] Yang, S., Li, C., Yokoyama, K., Elemental compositions and monazite age patterns of core sediments in the Changjiang Delta: Implications for sediment provenance and development history of the Changjiang River. Earth and Planetary Science Letters. 2006, 245, 762-776.

[194] Yi, S., Saito, Y., Zhao, Q.H., et al., Vegetation and climate changes in the Changjiang (Yangtze River) Delta, China, during the past 13,000 years inferred from pollen records. Quaternary Science Reviews. 2003, 22, 1501-1519.

[195] Yu, J., Li, L., Zhang, X., He, J., Jia, G., Kuhnt, W., Mangrove sediment erosion in the Sunda Shelf during meltwater pulses: Insights from biomarker records. Organic Geochemistry. 2023, 175.

[196] Zhao, H., Liu, Z., Zhao, Y., Sea level and East Asian monsoon influenced chemical weathering records in the southern South China Sea over the past 21 ka. Global and Planetary Change. 2024, 232.

[197] Zhao, H., Liu, Z., Zhao, Y., Wu, J., Colin, C., Lunar nodal tidal cycle influences on the input of coarse sediments during the last glaciation in the deep South China Sea. Quaternary Science Reviews. 2023, 310.

[198] Zhu, C., Chen, X., Zhang, G., et al., Spore-pollen-climate factor transfer function and paleoenvironment reconstruction in Dajiuhu, Shennongjia, Central China. Science Bulletin. 2008, 53, 42-49.

(The following references are from Chinese journals)

[199] Cai, J., Bao, Y., Yang, S., Wang, X., Fan, D., Xu, J., Wang, A., The occurrence and enrichment mechanism of organic matter in argillaceous sediments and mudstones. Science China D: Earth Science. 2007, 37, 244-253 (in Chinese).

[200] Feng, M., Chen, L., Wang, X., Wei, S., Wang, X., Crustal structure and its tectonic implications in Sundaland and adjacent areas: Constraints from tele-seismic receiver functions. Chinese Journal of Geophysics. 2021, 64, 4364-4377 (in Chinese with English abstract).

[201] Gui, X., Yu, J., Li, X., Chen, S., Sr-O isotopic composition and paleoenvironment of sediments in Nansha Sea area. Chinese Science Bulletin. 1993, 38, 1786-1790 (in Chinese).

[202] Li, S., Suo, Y., Liu., X., Dai, L., Yu, S., Zhao, S., Ma, Y., Wang, X., Cheng, S., An, H., Xue, Y., Xiong, L., Cao, X., Xu, L., Basin dynamic and basin groups of the South China Sea. Marine

Geology and Quaternary Geology. 2012, 32, 55-78 (in Chinese with English abstract).

[203] Luo, Z., Li, C., Lai, Z., Wang, C., Guo, Y., Duan, Z., Xu, J., Yang, S., Separation of Sr, Nd, and U from geological samples using tandem resin column. Rock and Mineral Analysis. 2022, 41 (in Chinese with English abstract).

[204] Wang, P., The Sunda Shelf—A Submerged Amazon Basin? Advances in Earth Science. 2017, 32, 1119-1125 (in Chinese with English abstract).

[205] Wang, P., Jian, Z., Review and prospect of deep exploration in South China Sea. Science China D: Earth Science. 2019, 49, 1590-1606 (in Chinese).

[206] Yang, Y., Tian, J., Huang, E., Herbaceous vegetation expansion on the north equatorial Sundaland during the last glacial maximum. Marine Geology and Quaternary Geology. 2020, 40, 85-93 (in Chinese with English abstract).

[207] Yao, B., Wan, L., Wu, N., Cenozoic plate tectonic activities in the great South China Sea. China Geology. 2004, 31, 113-121(in Chinese with English abstract).

[208] Yin, X., Wang, H., Han, J., Lü, X., Shen, Z., Chen, J., He, H., Xie, A., Guan, Y., Dong, C., Comparison between the marginal-sea polymetallic nodules in South Chins Sea and ocean polymetallic nodules. Journal of Jilin University (Earth Science Edition) 2019, 49, 59, 261-277 (in Chinese with English abstract).

[209] Yu, J., Paleo-environment and paleo-vegetation changes in the northern part of the Sunda Shelf during the last glacial period. Tongji University, Master thesis, Shanghai, 2022 (in Chinese with English abstract).

[210] Zhang, Z., Pei, J., Li, J., Du, Y., Shi, D., Xiang, Y., Tectonic and sedimentary evolution and its controlling effects on regional petroleum plays in the southern South China Sea. Natural Gas Geoscience. 2021, 32, 657-674 (in Chinese with English abstract).

Appendix I: Tables of geochemical data

Appendix Table 1 Major elements of river bulk and residue (after leaching) of sediment

		Bulk Sediments											Residue (After acid leaching)										
		SiO_2	Al_2O_3	Fe_2O_3	MnO	MgO	CaO	Na_2O	K_2O	TiO_2	P_2O_5	LOI**	SiO_2	Al_2O_3	Fe_2O_3	MnO	MgO	CaO	Na_2O	K_2O	TiO_2	P_2O_5	LOI*	reference
Mekong River (n=7)	min.(%)	57.17	11.33	4.49	0.07	1.41	0.42	1.00	1.93	0.74	0.11	6.34	63.05	11.35	4.14	0.03	1.10	0.18	0.60	1.89	0.80	0.10	3.40	this study
	max.(%)	70.13	16.19	6.15	0.15	2.07	1.99	2.11	2.44	0.91	0.14	10.83	75.31	17.25	5.98	0.09	1.67	0.34	0.87	2.48	0.94	0.11	7.86	
	ave.(%)	65.24	14.35	5.57	0.11	1.58	0.77	1.48	2.28	0.86	0.13	7.13	68.19	14.72	5.38	0.07	1.33	0.24	0.81	2.29	0.90	0.10	5.41	
Pahang River (n=6)	min.(%)	55.38	14.93	4.15	0.06	0.47	0.17	0.23	2.33	0.55	0.11	7.21	55.55	15.27	4.02	0.02	0.40	0.06	0.23	2.32	0.56	0.10	6.02	
	max.(%)	68.37	21.63	7.27	0.18	0.74	0.43	0.81	2.97	0.87	0.31	11.65	69.74	22.32	7.04	0.07	0.66	0.10	0.33	3.00	0.87	0.24	11.12	
	ave.(%)	61.38	18.20	5.63	0.12	0.61	0.33	0.41	2.54	0.72	0.17	9.85	62.21	18.61	5.48	0.04	0.54	0.08	0.30	2.55	0.74	0.15	9.23	
Kelantan River (n=7)	min.(%)	52.18	10.49	2.87	0.05	0.41	0.13	0.18	1.62	0.58	0.11	2.54	53.41	18.62	6.32	0.14	0.48	0.03	0.17	2.13	0.70	0.10	8.12	
	max.(%)	77.98	23.84	9.31	5.31	0.67	0.42	1.18	3.61	0.88	0.28	10.83	61.39	24.37	8.11	1.61	0.64	0.16	0.44	2.40	0.87	0.19	10.02	
	ave.(%)	61.23	17.51	7.11	1.57	0.54	0.24	0.50	2.34	0.75	0.20	7.91	58.04	20.68	7.26	0.66	0.52	0.10	0.34	2.28	0.78	0.14	9.11	
Rajang River (n=5)	min.(%)	66.28	9.53	3.46	0.02	0.65	0.11	0.20	1.66	0.57	0.00	4.48	66.79	9.10	3.18	0.02	0.59	0.04	0.21	1.56	0.57	/**	4.51	
	max.(%)	78.32	14.95	5.50	0.08	1.06	0.18	0.28	2.47	0.80	0.00	8.38	80.41	15.36	5.42	0.03	0.96	0.05	0.27	2.50	0.82	/	7.91	
	ave.(%)	72.81	12.12	4.40	0.05	0.79	0.14	0.24	2.02	0.69	0.00	6.30	73.65	12.31	4.29	0.02	0.75	0.04	0.24	2.03	0.70	/	5.76	
Red River (n=10)	min.(%)	/											68.39	15.40	5.53	0.03	1.71	0.09	0.37	2.68	0.92	0.13	/	Duan et al., 2023
	max.(%)												71.54	16.98	7.49	0.04	2.10	0.27	0.78	3.47	1.06	0.25	/	
	ave.(%)												70.18	16.18	6.59	0.04	1.93	0.18	0.61	3.12	0.99	0.18	/	
Sumatra River (n=12)	min.(%)												56.02	14.95	4.36	0.01	0.26	0.03	0.06	0.79	0.79	0.04	8.48	Liu et al., 2012
	max.(%)												68.42	20.37	6.37	0.10	0.95	0.52	0.76	1.77	1.00	0.20	16.40	
	ave.(%)												60.85	18.10	5.46	0.04	0.72	0.28	0.45	1.26	0.88	0.13	11.84	

Tips: *LOI, loss of ignition. **/, below detection limit or no analysis

Appendix Table 2 Trace elements of river bulk sediment

River		La	Ce	Pr	Nd	Sm	Eu	Gd	Tb	Dy	Ho	Er	Tm	Yb	Lu	Co	Rb	Sc	Sr	Th	U
Mekong River	min.(μg/g)	31.58	61.84	7.25	27.08	5.29	1.02	4.56	0.73	4.52	0.95	2.58	0.40	2.62	0.40	11.08	90.17	10.95	87.28	13.22	3.08
	max.(μg/g)	37.41	75.29	8.66	32.40	6.46	1.36	5.61	0.88	5.37	1.14	3.12	0.48	3.14	0.47	15.50	125.07	15.85	141.50	15.18	3.40
(n=7)	ave.(μg/g)	35.61	71.03	8.22	30.75	6.07	1.25	5.25	0.82	5.04	1.07	2.94	0.45	2.96	0.45	13.76	112.79	14.17	97.91	14.40	3.28
Pahang River	min.(μg/g)	31.44	64.80	7.18	25.97	5.27	0.79	4.70	0.78	5.05	1.09	3.18	0.51	3.40	0.52	7.46	137.00	12.16	28.76	26.04	6.46
	max.(μg/g)	48.52	105.58	11.20	41.09	8.52	1.38	7.36	1.23	7.91	1.71	5.01	0.81	5.47	0.82	15.55	243.40	20.04	60.34	42.94	17.26
(n=6)	ave.(μg/g)	41.76	90.00	9.88	36.16	7.43	1.10	6.46	1.06	6.74	1.45	4.16	0.67	4.45	0.67	10.96	170.91	15.02	49.06	32.86	10.10
Kelantan River	min.(μg/g)	27.88	57.46	6.47	23.17	4.36	0.66	3.55	0.58	3.69	0.80	2.29	0.36	2.52	0.38	7.23	51.43	8.29	63.18	8.23	4.50
	max.(μg/g)	48.35	107.12	10.28	39.93	7.87	1.79	7.35	1.13	7.01	1.47	3.97	0.62	4.14	0.64	194.59	189.87	24.07	130.76	31.30	7.64
(n=7)	ave.(μg/g)	39.11	86.51	8.51	32.67	6.54	1.33	5.96	0.93	5.83	1.24	3.45	0.53	3.58	0.55	66.46	110.33	18.56	87.36	20.23	5.84
Rajang River	min.(μg/g)	20.82	40.33	4.78	17.80	3.39	0.70	2.86	0.46	2.91	0.64	1.80	0.29	1.96	0.30	8.64	71.37	9.19	33.96	8.24	1.97
	max.(μg/g)	30.28	61.56	7.15	27.32	5.47	1.20	4.75	0.75	4.62	0.97	2.72	0.42	2.85	0.44	13.47	110.43	15.01	52.46	12.63	3.25
(n=5)	ave.(μg/g)	25.92	51.93	6.08	22.97	4.52	0.96	3.87	0.61	3.83	0.82	2.31	0.36	2.47	0.38	10.50	90.00	12.02	41.28	10.58	2.54

Appendix Table 3 Trace elements of river leached bulk sediment

River		La	Ce	Pr	Nd	Sm	Eu	Gd	Tb	Dy	Ho	Er	Tm	Yb	Lu	Co	Rb	Sc	Sr	Th	U	reference
Mekong River	min.(μg/g)	36.66	70.78	8.03	28.89	5.42	1.01	4.46	0.70	4.42	0.93	2.58	0.41	2.68	0.42	10.17	95.72	10.76	73.05	13.90	3.01	this study
	max.(μg/g)	39.57	78.13	8.77	32.16	6.04	1.24	5.06	0.80	5.09	1.08	2.94	0.46	2.94	0.47	13.66	135.59	16.14	83.36	15.51	3.27	
(n=7)	ave.(μg/g)	38.58	75.54	8.52	31.11	5.81	1.16	4.80	0.76	4.83	1.03	2.82	0.44	2.86	0.44	12.51	118.25	14.03	80.65	14.56	3.11	
Pahang River	min.(μg/g)	32.08	63.45	7.06	24.99	5.04	0.63	4.21	0.70	4.62	1.03	2.96	0.48	3.17	0.50	5.17	144.07	11.79	24.53	24.62	5.51	
	max.(μg/g)	47.14	100.30	10.85	39.00	7.81	1.19	6.52	1.13	7.59	1.68	4.83	0.80	5.30	0.83	10.94	247.31	19.30	52.45	41.91	13.42	
(n=6)	ave.(μg/g)	41.00	83.28	9.15	32.73	6.55	0.94	5.45	0.92	6.03	1.32	3.73	0.61	4.00	0.62	7.39	175.94	14.41	42.02	32.08	8.05	
Kelantan River	min.(μg/g)	28.11	55.30	5.64	20.17	4.00	0.64	3.35	0.54	3.47	0.76	2.16	0.34	2.25	0.35	6.04	49.11	8.35	59.74	7.88	4.10	
	max.(μg/g)	45.86	105.01	9.12	35.11	7.03	1.63	6.46	1.02	6.39	1.36	3.73	0.56	3.50	0.55	68.89	190.26	23.45	128.99	31.77	6.73	
(n=7)	ave.(μg/g)	37.08	79.63	7.71	28.73	5.66	1.15	5.00	0.80	5.10	1.10	3.09	0.48	3.11	0.49	28.48	110.13	17.93	83.70	19.37	5.10	
Rajang River	min.(μg/g)	20.65	39.70	4.52	16.66	2.99	0.58	2.31	0.38	2.43	0.54	1.53	0.25	1.68	0.26	6.59	63.57	8.37	29.98	7.41	1.76	
	max.(μg/g)	34.74	69.35	7.85	29.36	5.58	1.17	4.53	0.73	4.58	0.99	2.71	0.43	2.81	0.44	9.48	115.73	14.51	46.20	13.01	2.87	
(n=5)	ave.(μg/g)	27.83	54.86	6.21	23.04	4.28	0.86	3.41	0.55	3.52	0.76	2.14	0.34	2.28	0.36	7.96	88.41	11.65	37.46	10.31	2.34	
Red River	min.(μg/g)	36.67	67.93	7.89	26.03	4.81	0.94	4.65	0.66	3.71	0.75	2.25	0.33	2.14	0.33	8.59	129.90	10.56	50.16	15.32	2.50	Duan et al., 2023
	max.(μg/g)	56.03	103.74	12.40	43.80	7.30	1.48	7.13	1.01	5.88	1.19	3.63	0.53	3.47	0.53	14.32	200.72	16.63	102.39	20.93	3.83	
(n=10)	ave.(μg/g)	42.94	79.99	9.40	31.91	5.59	1.12	5.42	0.76	4.38	0.88	2.69	0.39	2.57	0.39	11.11	160.01	12.45	71.86	16.86	2.94	

Appendix Table 4 Major elements of seafloor bulk sediment

		SiO_2	Al_2O_3	Fe_2O_3	MnO	MgO	CaO	Na_2O	K_2O	TiO_2	P_2O_5
Gulf of Beibuwan (n=6)	min.(%)	61.82	5.80	3.29	0.03	0.89	0.12	0.46	1.09	0.55	0.04
	max.(%)	79.22	15.31	7.00	0.08	2.28	0.40	1.36	2.74	1.15	0.09
	ave.(%)	70.88	10.24	4.85	0.05	1.66	0.30	1.02	2.12	0.82	0.06
Offshore Indochina (n=9)	min.(%)	58.24	4.16	1.65	0.02	0.31	0.18	0.60	1.46	0.20	0.03
	max.(%)	83.17	17.25	6.88	0.95	2.07	2.23	1.84	3.27	1.31	0.20
	ave.(%)	68.10	12.58	4.72	0.21	1.40	0.97	1.20	2.42	0.82	0.12
Offshore Borneo (n=5)	min.(%)	62.13	8.46	3.73	0.05	1.25	0.39	1.11	1.54	0.73	0.05
	max.(%)	73.37	15.15	6.29	0.19	2.58	1.70	1.63	2.88	0.87	0.21
	ave.(%)	67.99	11.18	5.41	0.11	1.69	1.19	1.37	2.09	0.81	0.16
Western Sunda shelf * (n=12)	min.(%)	58.47	7.91	3.00	0.02	1.14	0.16	0.36	1.36	0.55	/
	max.(%)	81.67	15.35	7.40	0.11	2.71	5.30	1.85	2.61	1.08	/
	ave.(%)	72.21	10.97	4.90	0.04	1.91	0.71	0.74	1.82	0.70	/
Eastern Sunda shelf (n=4)	min.(%)	76.73	3.52	2.14	0.03	0.59	0.16	0.59	1.01	0.23	0.03
	max.(%)	83.39	6.25	3.46	0.07	1.11	1.58	1.24	2.23	0.39	0.07
	ave.(%)	79.35	5.40	2.85	0.05	0.90	0.72	0.85	1.51	0.35	0.05
Central South China sea basin (n=8)	min.(%)	56.23	9.10	3.27	0.11	0.95	0.28	1.08	2.39	0.92	0.05
	max.(%)	69.40	15.49	7.88	3.03	2.71	5.30	2.04	3.44	1.08	0.20
	ave.(%)	60.60	13.67	5.69	1.86	2.08	2.51	1.40	3.05	1.00	0.15

Tips: data from Wei et al., 2012; *, data from this study and Wei et al., 2012

Appendix Table 5 Trace elements of seafloor leached bulk sediment

		La	Ce	Pr	Nd	Sm	Eu	Gd	Tb	Dy	Ho	Er	Tm	Yb	Lu	Co	Rb	Sc	Sr	Th	U
Gulf of Beibuwan (n=6)	min.(μg/g)	14.00	35.40	3.29	13.10	2.44	0.43	1.88	0.31	1.96	0.40	1.15	0.20	1.14	0.19	6.10	68.00	5.30	36.30	8.30	1.61
	max.(μg/g)	37.40	85.30	8.53	32.10	5.44	0.97	4.09	0.66	3.89	0.77	2.34	0.37	2.37	0.37	14.30	161.00	15.30	87.30	20.90	3.63
	ave.(μg/g)	25.02	57.75	5.78	22.20	3.87	0.68	2.92	0.50	2.97	0.60	1.78	0.28	1.76	0.28	9.46	116.95	9.44	69.40	13.32	2.45
Offshore Indochina (n=9)	min.(μg/g)	14.60	30.20	3.32	12.00	2.28	0.42	1.65	0.25	1.36	0.27	0.73	0.11	0.78	0.12	2.30	53.60	2.49	45.00	5.00	0.89
	max.(μg/g)	37.97	90.10	8.27	30.80	5.63	1.10	4.50	0.78	4.52	0.98	2.70	0.44	2.91	0.47	20.20	161.00	17.90	163.00	20.80	4.65
	ave.(μg/g)	28.74	69.33	6.66	24.71	4.50	0.84	3.67	0.61	3.71	0.76	2.26	0.35	2.29	0.36	10.97	119.93	12.10	105.32	14.88	2.88
Offshore Borneo (n=5)	min.(μg/g)	15.00	58.80	3.50	13.50	2.45	0.44	2.40	0.43	2.91	0.62	1.97	0.32	2.05	0.32	7.70	77.70	6.74	79.80	12.70	2.91
	max.(μg/g)	48.80	100.00	11.67	41.50	7.16	1.02	5.46	0.84	4.29	0.82	2.49	0.43	2.95	0.45	12.70	152.00	15.10	162.00	20.70	3.50
	ave.(μg/g)	25.98	69.18	6.30	22.88	4.09	0.71	3.46	0.59	3.58	0.74	2.28	0.36	2.43	0.38	10.38	114.52	12.01	115.25	14.90	3.14
Western Sunda shelf * (n=12)	min.(μg/g)	24.72	47.51	5.39	19.41	3.58	0.63	2.87	0.45	2.88	0.63	1.82	0.29	2.02	0.31	6.41	63.20	6.97	42.62	9.85	2.28
	max.(μg/g)	41.30	87.70	10.31	27.33	6.82	1.31	6.03	0.99	5.39	1.03	2.98	0.44	2.86	0.45	14.20	134.40	14.32	76.58	19.40	4.09
	ave.(μg/g)	29.67	58.21	6.58	22.52	4.40	0.81	3.61	0.58	3.65	0.78	2.21	0.35	2.34	0.37	10.29	92.14	10.44	61.87	12.35	2.71
Eastern Sunda shelf (n=4)	min.(μg/g)	13.20	31.60	3.21	11.30	2.07	0.37	1.71	0.25	1.30	0.26	0.71	0.11	0.69	0.11	3.67	40.00	2.78	33.90	5.12	0.83
	max.(μg/g)	30.50	66.90	7.45	26.10	4.85	0.65	3.98	0.57	3.07	0.58	1.60	0.24	1.57	0.24	7.45	85.30	5.38	99.40	13.90	2.56
	ave.(μg/g)	18.25	42.18	4.50	15.90	2.96	0.50	2.49	0.38	2.06	0.41	1.12	0.17	1.12	0.17	5.41	61.70	4.47	72.48	8.28	1.51
Central South China sea basin (n=8)	min.(μg/g)	17.40	38.10	4.21	15.90	2.85	0.36	2.78	0.44	3.04	0.61	1.87	0.31	2.03	0.32	14.20	34.80	8.06	75.10	7.15	1.81
	max.(μg/g)	24.20	81.60	5.37	22.50	4.49	0.86	4.56	0.72	4.09	0.83	2.53	0.41	2.72	0.43	22.10	178.00	17.30	1467.00	19.90	4.58
	ave.(μg/g)	21.79	65.31	4.95	19.33	3.53	0.59	3.28	0.55	3.46	0.72	2.25	0.36	2.34	0.37	16.99	146.85	13.61	296.25	16.36	2.88

Tips: data from Wei et al., 2012; *, data from this study and Wei et al., 2012

Appendix Table 6 Isotopes composition of river and sea floor sediments

		$^{87}Sr/^{86}Sr$	2σ	$^{143}Nd/^{144}Nd$	2σ	ε_{Nd}	$^{234}U/^{238}U$	2σ	$(^{234}U/^{238}U)$	2σ
Mekong River (n=7)	min.	0.719749	0.000007	0.512094	0.000007	-10.62	0.000052	4E-08	0.945	0.001
	max.	0.723118	0.000011	0.512126	0.000009	-9.99	0.000053	5E-08	0.964	0.001
	ave.	0.721173	0.000008	0.512109	0.000008	-10.32	0.000052	5E-08	0.955	0.001
Pahang River (n=6)	min.	0.731202	0.000006	0.512040	0.000005	-11.67	0.000054	3E-08	0.984	0.001
	max.	0.744089	0.000014	0.512239	0.000009	-7.79	0.000057	4E-08	1.031	0.001
	ave.	0.737996	0.000010	0.512160	0.000006	-9.32	0.000055	3E-08	1.010	0.001
Kelantan River (n=7)	min.	0.715340	0.000009	0.512131	0.000006	-9.90	0.000053	3E-08	0.966	0.001
	max.	0.725300	0.000013	0.512368	0.000010	-5.27	0.000055	4E-08	0.996	0.001
	ave.	0.721365	0.000010	0.512253	0.000007	-7.51	0.000054	4E-08	0.986	0.001
Rajang River (n=5)	min.	0.718332	0.000007	0.512249	0.000007	-7.59	0.000051	3E-08	0.937	0.001
	max.	0.719797	0.000015	0.512284	0.000008	-6.91	0.000052	8E-08	0.952	0.001
	ave.	0.719059	0.000010	0.512268	0.000007	-7.23	0.000052	5E-08	0.945	0.001
Red River (n=10)	min.	0.730230	0.000007	0.511998	0.000004	-12.48	0.000051	3E-08	0.923	0.000
	max.	0.734568	0.000013	0.512029	0.000006	-11.89	0.000052	1E-06	0.946	0.002
	ave.	0.732071	0.000010	0.512011	0.000005	-12.23	0.000051	1E-06	0.938	0.002
Sumatra River (n=2)	min.	0.711580	0.000010	0.512409	0.000008	-4.47				
	max.	0.710530	0.000010	0.512400	0.000008	-4.64				
	ave.	0.711055	0.000010	0.512405	0.000008	-4.55				
Gulf of Beibuwan (n=6)	min.	0.720986	0.000013	0.512056	0.000010	-11.35			/	
	max.	0.731040	0.000019	0.512117	0.000012	-10.17				
	ave.	0.726038	0.000018	0.512079	0.000012	-10.92				
Offshore Indochina	min.	0.715053	0.000007	0.512046	0.000007	-11.55				
	max.	0.723118	0.000030	0.512155	0.000012	-9.99				

(n=9)	ave.	0.719109	0.000016	0.512100	0.000010	-10.65
Offshore Borneo (n=5)	min.	0.715360	0.000013	0.512189	0.000007	-8.76
	max.	0.720602	0.000056	0.512282	0.000012	-8.23
	ave.	0.718226	0.000024	0.512216	0.000009	-8.56
Western Sunda shelf (n=12)	min.	0.718748	0.000006	0.512009	0.000008	-12.28
	max.	0.723918	0.000040	0.512186	0.000010	-8.82
	ave.	0.721322	0.000013	0.512075	0.000009	-10.98
Eastern Sunda shelf (n=4)	min.	0.719230	0.000017	0.512042	0.000006	-11.63
	max.	0.720555	0.000030	0.512129	0.000008	-9.93
	ave.	0.719872	0.000026	0.512093	0.000007	-10.64
Central South China sea basin (n=8)	min.	0.709235	0.000009	0.512059	0.000011	-11.30
	max.	0.726755	0.000020	0.512283	0.000013	-6.93
	ave.	0.718536	0.000017	0.512124	0.000012	-10.04

Tips: some data from Wei et al., 2012; Wu et al., 2023; Duan et al., 2023

Appendix Table 7 Major elements of core ST13 and 18288-2 sediments

Core		SiO_2	Al_2O_3	Fe_2O_3	MnO	MgO	CaO	Na_2O	K_2O	TiO_2	P_2O_5	LOI*
ST13 (n=38)	min.(%)	62.38	12.94	4.27	0.03	1.65	0.25	0.66	2.21	0.73	0.00	6.70
	max.(%)	70.04	16.12	5.69	0.04	2.35	0.32	0.75	2.61	0.83	0.00	9.05
	ave.(%)	65.72	14.63	5.02	0.03	1.99	0.27	0.71	2.43	0.80	/*	7.79
18288-2 (n=35)	min.(%)	56.15	16.00	5.55	0.03	1.45	0.10	0.44	2.45	0.79	0.10	7.32
	max.(%)	64.50	19.88	8.31	0.06	2.49	0.33	0.72	3.05	0.95	0.13	10.60
	ave.(%)	59.42	18.29	6.49	0.04	2.07	0.24	0.62	2.84	0.84	0.11	8.86

Tips: *LOI, loss of ignition. **/, below detection limit or no analysis

Appendix Table 8 Trace elements of core ST13 and 18288-2 sediments

Core		La	Ce	Pr	Nd	Sm	Eu	Gd	Tb	Dy	Ho	Er	Tm	Yb	Lu	Co	Rb	Sc	Sr	Th	U
ST13 (n=38)	min.(μg/g)	30.11	58.33	6.72	24.35	4.46	0.84	3.60	0.57	3.52	0.75	2.12	0.33	2.26	0.34	11.38	115.79	11.81	68.92	11.54	2.41
	max.(μg/g)	33.85	65.26	7.38	26.47	4.84	0.94	3.91	0.63	4.03	0.87	2.47	0.39	2.56	0.39	14.41	146.87	14.82	74.18	14.41	2.86
	ave.(μg/g)	32.52	62.30	7.13	25.65	4.65	0.88	3.77	0.60	3.82	0.82	2.33	0.36	2.42	0.37	12.63	133.31	13.51	71.59	12.75	2.68
18288-2 (n=35)	min.(μg/g)	32.16	59.13	7.10	25.40	4.64	0.91	3.69	0.59	3.79	0.80	2.22	0.35	2.33	0.35	12.12	131.65	15.07	65.28	14.11	2.70
	max.(μg/g)	42.15	84.07	9.28	34.28	6.40	1.36	5.61	0.91	5.63	1.18	3.24	0.49	3.24	0.49	17.12	173.28	19.15	78.76	17.19	3.53
	ave.(μg/g)	34.96	66.65	7.71	27.98	5.10	1.00	4.11	0.66	4.20	0.88	2.48	0.39	2.56	0.39	14.74	150.83	17.29	72.55	15.61	3.16

Appendix Table 9 Isotope composition of core ST13 and 18288-2

Core		$^{87}Sr/^{86}Sr$	2σ	$^{143}Nd/^{144}Nd$	2σ	ε_{Nd}	$^{234}U/^{238}U$	2σ	$(^{234}U/^{238}U)$	2σ	$f\alpha$	T_{com} (ka)	2σ (ka)
ST13 (n=33)	min.	0.722506	0.000005	0.512051	0.000005	-11.45	0.000051	5E-08	0.9227	0.0010	0.148	112	22
	max.	0.724146	0.000013	0.512086	0.000011	-10.78	0.000052	1E-07	0.9530	0.0019	0.174	245	33
	ave.	0.723437	0.000008	0.512071	0.000007	-11.06	0.000052	7E-08	0.9391	0.0013	0.162	170	27
18288-2 (n=30)	min.	0.721098	0.000006	0.512062	0.000005	-11.24	0.000049	3E-08	0.9017	0.0005	0.139	170	25
	max.	0.726349	0.000015	0.512192	0.000010	-8.70	0.000052	4E-08	0.9390	0.0008	0.200	244	32
	ave.	0.724302	0.000009	0.512104	0.000008	-10.42	0.000051	4E-08	0.9289	0.0007	0.161	207	29

Appendix Table 10 CO_2 consumption by silicate weathering in different possibility model

		Al (mol/g)	MAR ($g/cm^2/ka$)	Al ($g/cm^2/ka$)	ΔCa ($g/cm^2/ka$)	ΔMg ($g/cm^2/ka$)	ΔK ($g/cm^2/ka$)	ΔNa ($g/cm^2/ka$)	ΔCO_2 ($mol/km^2/a$)	Area of exposed Sunda Shelf (10^6 km^2)	Area of submarine Sunda Shelf (10^6 km^2)	CO_2 consumption changes relative to stage III on the continent(10^9 mol/a)	Absolute CO_2 long term consumption on the continent(10^9 mol/a)	Area for weathering (10^6 km2) *	CO_2 consumption rate(10^3 $mol/km^2/a$)	CO_2 consumption by the weathering at the exposed shelf(10^9 mol/a)	CO_2 consumption at the exposed shelf/total continet
Possibility 2	Stage III	0.004	15.897	0.057	/	/	/	/	/	0.46	1.90	/	336 ***	1.76	191 **	88.40	26%
	Stage II	0.003	33.688	0.117	-0.008	-0.009	0.000	0.000	-172325	2.11	0.26	-43.97	292.42	3.26	89.71	189.40	65%
	Stage I	0.004	30.530	0.115	0.001	0.003	-0.001	0.001	39847	2.33	0.04	1.56	337.95	3.48	97.03	225.84	67%
Possibility 3	Stage III	0.004	15.897	0.057	/	/	/	/	/	0.46	1.90	/	336 ***	1.76	191 **	88.40	26%
	Stage II	0.003	33.688	0.117	0.002	0.003	0.001	0.000	56582	2.11	0.26	14.44	350.83	3.26	107.62	227.24	65%
	Stage I	0.004	30.530	0.115	0.001	0.003	-0.001	0.001	43529	2.33	0.04	1.70	338.09	3.48	97.07	225.94	67%

Tips: * Areas can be weatherd through the sea level changes, both continent and exposed shelf area.

**The CO_2 consumption rate of the Stage III (Holocene) is estimated at 191 ($\times 10^3$ $mol/km^2/a$) for silicate weathering at the Mekong River catchment.

*** Stage III absolute CO_2 long term consumption on the continent is calculated according to the rate**.

Appendix II: Publication

Chen, J., Li, C., Galy, A., Wang, H., Yang, C., Yang, S., 2024. Uranium-series comminution ages constrain large catchment erosion and its response to climate change: A case study from the Changjiang. *Earth and Planetary Science Letters* 625.

Earth Planet. Sci. Lett. 625 (2024) 118493

Contents lists available at ScienceDirect

Earth and Planetary Science Letters

journal homepage: www.elsevier.com/locate/epsl

Uranium-series comminution ages constrain large catchment erosion and its response to climate change: A case study from the Changjiang

Junfei Chen [a,b], Chao Li [a,*], Albert Galy [b], Hui Wang [a], Chengfan Yang [a], Shouye Yang [a]

[a] State Key Laboratory of Marine Geology, Tongji University, Shanghai 200092, China
[b] Centre de Recherches Pétrographiques et Géochimiques, UMR7358, CNRS, Université de Lorraine, Vandoeuvre les Nancy 54500, France

ARTICLE INFO

Keywords:
Catchment erosion
Uranium isotope
Comminution age
Climate changes
Changjiang

ABSTRACT

Catchment erosion not only plays an important role on landscape evolution, but also determines the exposure of rock debris in the regolith profile, and therefore impacts the chemical weathering and associated CO_2 absorption and ultimately global climate. But climate also modulates erosion and complex interaction loops, especially at large scale can hamper a clear understanding of these processes. Here we mainly use Uranium-series Comminution Age (t_{com}) of core sediments from Changjiang estuary to reconstruct the catchment erosion, and the relationship with climate changes and human activities during the last 14 kyrs.

Since 14 ka, the sea level has been rising continuously until current highstand system tract in the East China Sea where the Changjiang estuary is located. The sediments in the Changjiang estuary mainly come from the upper reaches erosion zone during this period, but the sediment supply from the middle and lower reaches has gradually increased since the Late Holocene. The period can be divided into two modes. The first mode happens from the Bølling-Allerød period to the Mid-Holocene when the sea level rose rapidly, and the t_{com} of sediment recorded the residence time in the upper reaches erosion zone, with a periodic pattern of t_{com} in a good agreement with climate changes. During the cold and dry periods, the longer t_{com} (average 460 kyrs) is consistent with less precipitation resulting in shallower erosion with transported material mainly coming from the soil with longer residence time. In contrast, during the warm and wet periods, the t_{com} is shorter (average 290 kyrs), with the more abundant precipitations that contribute to deeper erosion in the upper catchment, and more fresh material transported to the estuary through stronger hydrodynamic forces. The second mode is more chaotic and corresponds to 0 to 4 ka, when climate was warm and humid and stable sea level, but t_{com} fluctuated from 200 kyrs to 650 kyrs. The increasing river flooding caused by abundant precipitation leads to lateral migration of the river channel in the middle and lower reaches, and the sediments deposited in the floodplain were eroded and mobilized again. In addition, the rapid development of human activities since 2 ka has accelerated deforestation and agricultural cultivation, leading to localized erosion of the floodplain. These remobilized sediments were transported to the estuary and deposited, resulting in a larger t_{com} value. This study overall indicates that, in the millennial scale, the t_{com} of fine detrital fraction shows a sensitive and quick response to catchment erosion, and provides new insights into quantifying the time scale of sediment source to sink processes and inferring the paleoenvironment accurately climate changes.

1. Introduction

The erosion of continental masses not only shapes the topography and landforms on the earth surface, but also determines the exposure of rock debris in the soils, and therefore controls chemical weathering, atmospheric CO_2 consumption, and regolith development (Clift et al., 2008; France-Lanord and Derry, 1997; Hein et al., 2017; Riebe et al., 2017; West et al., 2005). Studying the mechanism and controlling factors of erosion in catchments provide insights on the evolution of landform, and also a better understanding of long-term climate change and earth habitability (Dosseto et al., 2010; Heimsath et al., 1997; Plotzki et al., 2015). However, a full quantification of the erosion of an entire catchment requires the investigation of a large number of representative soil and bedrock samples from various geomorphic settings (Schaller et al., 2002). Alternatively, the river sediment collected at the outlet of a catchment can be assumed to be an aggregate of grains that

* Corresponding author.
E-mail address: cli@tongji.edu.cn (C. Li).

https://doi.org/10.1016/j.epsl.2023.118493
Received 7 July 2023; Received in revised form 4 November 2023; Accepted 7 November 2023
Available online 23 November 2023

originate from all of upstream areas "let nature do the averaging for us" (Von Blanckenburg, 2005).

The sediments deposited on the estuary document the changes in catchment erosion and transport process through time, thereby reflecting the changes in the catchment climate, hydrology, vegetation and human activities. There have been considerable efforts to constrain erosion processes using geochemical tracers measured in river material, including major and trace elements (Gaillardet et al., 1997), as well as cosmogenic nuclides (Von Blanckenburg, 2005). One of the key issues has been to determine the feedback of erosion to climate variations over orbital timescales (Munhoven and François, 1994). In particular, it is important to assess the response of erosion to environment variations, particularly to abrupt climate forcing, such as during glacial terminations.

Uranium isotopes activity ratio, denoted as ($^{234}U/^{238}U$), in fine-grained sediments have been employed to quantitatively evaluate the catchment erosion as the ($^{234}U/^{238}U$) in sediment grain is sensitive to the comminution process of parent rock (e.g., Dosseto et al., 2010; Dosseto and Schaller, 2016; Francke et al., 2020, 2019; Rothacker et al., 2018). The ongoing depletion of ^{234}U in fine grain sediments (typically < 50 μm) from the soil formation, transportation, recycling to final deposition, combined with the surface properties of sediments allows the estimate of the Comminution Age (t_{com}) that defines the time since physical breakdown of bedrock into a small rock debris particle to deposition after transport (DePaolo et al., 2006). Such time includes the time of catchment erosion and the storage time of sediment in regolith (T1), but also the time of the transport in the river (T2), and the time of temporary storage in the floodplain (T3) (Fig. 1A) (Dosseto et al., 2010). For these complexities, so far the ($^{234}U/^{238}U$) or t_{com} studies on catchment erosion are mainly applied in small river basins or inland lakes (e.g. Dosseto et al., 2014). Most of these study areas have stable provenance, simple lithology, and small climate changes. Here, we apply this method to a large basin that is more sensitive to climate change, such as monsoon modulated by the wandering of the inter-tropical convergence zone (ITCZ), rather than simply local climate (temperature, precipitation).

The Changjiang River is the seventh largest river in the world by water discharge and transports huge amount of sediment to the ocean every year. In this study, we analysed the Sr, Nd, U isotopes in the sediments from the Chongming Island in the Changjiang estuary (core CM97) (Fig. 2). Together with the sediment grain size distribution, we calculate the t_{com} variations since 14 ka. Combined with published pollen data, we propose an integrated explanation of the variations of the erosion in the Changjiang catchment during the past 14 kyrs and its major response to climate changes.

2. Geological background

The Changjiang originates from the Tibet Plateau and drains into the west Pacific. It is the longest river in East Asia and its catchment covers a total area of about 1.8×10^6 km^2 (Fig. 2A). The long-term average sediment flux of the Changjiang is 470 Mt/yr (Milliman and Farnsworth, 2011). These sediments are mostly trapped in the estuary to form a large delta and the rest are transported to the adjacent East China Sea

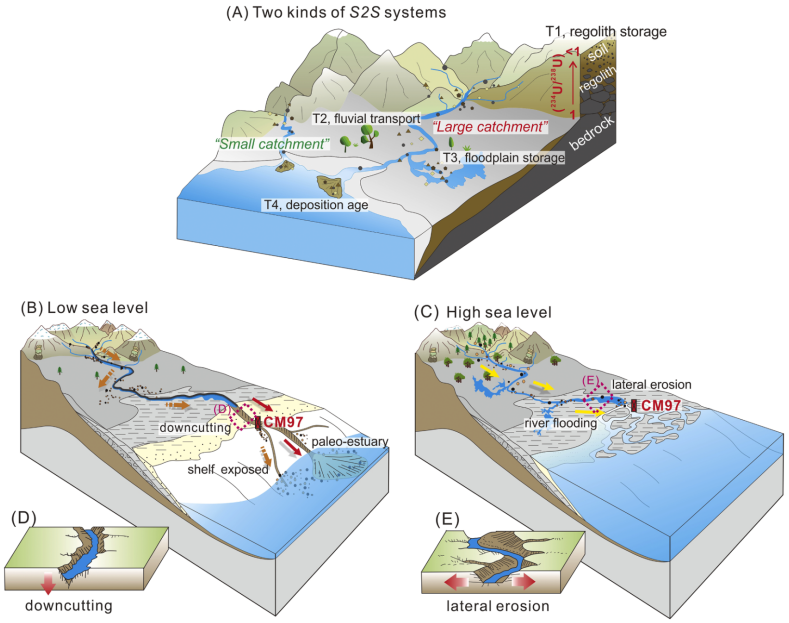

Fig. 1. (A) Conceptual model of different sediment transport process between large catchment and small catchment, and the changes of ($^{238}U/^{234}U$) in the regolith. (B) and (C) respectively show transitions in river geomorphology and "source-sink" processes in large catchment during the low sea level and high sea level periods; in (B), orange arrows indicate sediments from the upper reaches erosion zone, and red arrows indicate sediments from the floodplain in the middle and lower reaches; in (C), yellow arrows indicate sediment from the upper reaches erosion zones dominate the estuary sediments composition during the high sea level periods. (D) and (E) show in detail the channel downcutting during the low sea level period and the lateral erosion during the high sea level period.

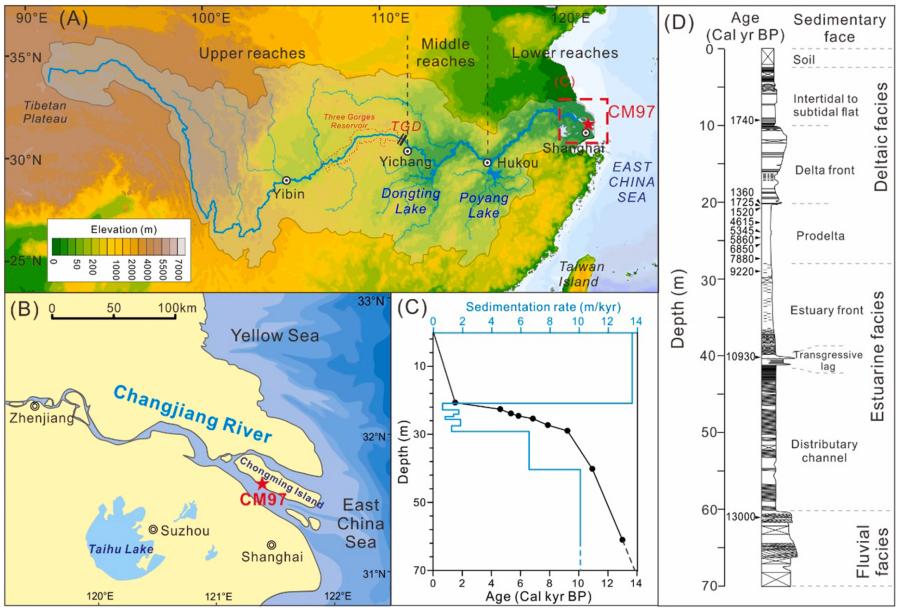

Fig. 2. (A) location of Changjiang Basin; (B) the river system and lakes of the deltaic part of the Changjiang catchment and the location of the core CM97; (C) the age model and the sedimentation rate of core CM97 (Hori et al., 2001a, Hori et al., 2001b). (D) the lithology and sedimentary facies of core CM97 (Hori et al., 2001a, Hori et al., 2001b).

(ECS) (Fig. 2B), making the largest sediment contribution to the ECS.

According to the geomorphic and hydrological characteristics, the Changjiang is divided into three sections (Fig. 2A). The upper reach refers to the section from the source to Yichang, and corresponds to high-elevation plateau and/or mountains. The upper Changjiang reach contributed more than 70% of the annual sediment flux before the three Gorges Dam was built in 2003 (Yang et al., 2006). The middle reach from Yichang to Hukou bears two large lakes (Dongting Lake and Poyang Lake), which play an important role in regulating the sediment flux to the sea. The lower reach is from Hukou to the river mouth, with well-developed lakes and large lowland plain. The estuary is characterized by a large delta system with the largest alluvial island, the Chongming Island, covering an area of about 1.2×10^3 km^2 (Fig. 2B). Given the size of the Changjiang catchment, the lithology is variable. The upper reach mainly includes Paleozoic carbonate rock, Jurassic red sandstone and Mesozoic igneous rocks, while the middle-lower reaches mainly consist of Paleozoic marine rock and Quaternary fluviolacustrine deposits (Chen et al., 2002; Ding et al., 2004). The climate in the Changjiang Basin is dominated by the East-Asian monsoon system, with large seasonal variations from warm and humid in summer to cold and arid in winter.

The Changjiang, provides the largest point delivery of sediments to the ECS (Milliman and Farnsworth, 2011), and sea level changes also affect the transport and accumulation of river sediments in the East Asian continent from source to sink. ECS represents a typical case for large-scale continental shelf response to the global sea level change (Li et al., 2014). Three sedimentary system tracts had been formed in the ECS since the LGM. First is the low-stand system tract corresponding to the LGM (23 - 15.4 ka), when the estuary was onto the shelf (−120 to −100 m). The second is the transgressive system tract corresponding to the last deglaciation (15.4 - 7 ka) and corresponding sea level rise. The third is the high-stand system tract corresponding to the high sea level since 7 ka. The eddy mud, coastal current mud, delta and beach have been accumulating since then. Since the late last deglaciation, the sea level of the East China Sea has risen from about −100 m to the current height. Continuous transgression has transformed the depositional environment of the Changjiang estuary from continental to marine environment (Hori et al., 2001a, b; Li et al., 2014).

3. Materials and methods

3.1. Materials

The Core CM97 (31°37′ N, 121°23′ E) was drilled in Chongming Island in 1997 (Fig. 2B). The core is 70 m in length and its lithology is mainly silt and clay, with only a small amount of sand component at the bottom of the drilled section (Fig. 2D). The core CM97 recorded the transgression period with rising sea level and the highstand system tract period with stable high sea level. From the bottom of the core to top, the sedimentary environments are fluvial facies, estuarine facies and deltaic facies (Hori et al., 2001a, b) (Fig. 2D). The age model for this core is determined by radiocarbon (Δ^{14}C) ages on molluscan shells (Fig. 2C) and the bottom section dated back to ~14 ka (Hori et al., 2001a, b). A total of 32 levels were sampled, for grain size, major and trace elements, and isotope analysis.

3.2. Analytical method

About 0.2 g of <50 μm were separated from the bulk sediment by wet sieving and were treated with an excess of 30% H_2O_2 at 60 °C for 6 h to

remove organic matter and then with 1 N HCl at 60 °C for 6 h to remove carbonates. Then, the residue was washed with ultrapure water until complete removal of H_2O_2 and HCl. The grain size of the <50 μm residue fraction was determined using a Malvern 2000 Mastersizer Particle Size Analyzer with a measurement range of 0.02- 2000 mm.

In order to obtain the sediment detrital fractions, the non-detrital fraction (acid-soluble, reducible and oxidizable fractions) of each sample was chemically leached (Francke et al., 2018; Martin et al., 2015) (Table 1). Then, about 0.05 g freeze-dried leaching residues were digested with ultrapure HNO_3 and HF (1:1) in a Teflon digestion vessel. The major and trace elements were determined by ICP-AES (IRIS Advantage, Thermo) and ICP-MS (Agilent 7900), respectively. The analytical accuracy, monitored by BCR-2, is < 5% for major elements and < 10% for the trace elements.

The Sr, Nd, and U were purified with ionic-exchange resin in clean lab laboratory environments and the isotopic ratios were determined using a MC-ICP-MS Neptune plus. The measured $^{87}Sr/^{86}Sr$ ratios were normalized to $^{88}Sr/^{86}Sr = 0.1192$ and the average value of the $^{87}Sr/^{86}Sr$ of the NBS987 was 0.710253±17 (n = 9, 2SD). The measured $^{143}Nd/^{144}Nd$ ratios were normalized to $^{146}Nd/^{144}Nd = 0.7219$ (Wasserburg et al., 1981) by an exponential law and the average value of JNdi-1 (Tanaka et al., 2000) was 0.521117±13 (n = 9, 2SD). Nd isotopic data are expressed as: $\varepsilon Nd = [(^{143}Nd/^{144}Nd_{sample}/(^{143}Nd/^{144}Nd)_{CHUR}) - 1] \times 10^4$, with the $^{143}Nd/^{144}Nd$ ratio of the CHUR (Chondritic Uniform Reservoir) of 0.512638 (Jacobsen and Wasserburg, 1980). The measured $^{234}U/^{238}U$ ratios were normalized to $^{238}U/^{235}U = 137.88$ (Steiger and Jäger, 1977) by an exponential law and to the CRM112-A (Mathew et al., 2012) by using a true bracketing linear correction (Andersen et al., 2004). The activity ratios of ^{234}U and ^{238}U, denoted as ($^{234}U/^{238}U$), have been calculated using λ_{234} and λ_{238} of 2.82629×10^{-6} a^{-1} (Cheng et al., 2000) and 1.551×10^{-10} a^{-1} (Jaffey et al., 1971), respectively. The average ($^{234}U/^{238}U$) value of the CRM112-A is 0.9627 ±0.0013 (n = 9, 2SD), while the recommended ($^{234}U/^{238}U$) value for the CRM112-A is 0.9629±0.0015 (calculated from the value of $^{234}U/^{238}U$ is $5.2841 \pm 0.0082 \times 10^{-5}$) (Mathew et al., 2012). The total procedural accuracy and repeatability were evaluated by replicate analyses of the international standard BCR-2 during the experiments. The measured $^{87}Sr/^{86}Sr$, $^{143}Nd/^{144}Nd$ and ($^{234}U/^{238}U$) values of BCR-2 are 0.705010 ± 18(n = 4) (reference value is 0.705000±11, Jweda et al., 2015), 0.512641±16 (2SD) (reference value is 0.512637±13, Jweda et al., 2015) and 1.001 ± 0.002 (2SD) (reference value is 1.002±0.004, Koornneef et al., 2010) respectively, which are consistent with the internationally recognized ratio within the error range. All these geochemical measurements were conducted at the State Key Laboratory of Marine Geology, Tongji University.

3.3. Notion of comminution age method

The secular equilibrium is the condition of large fresh rock in a closed system, and is characterized by ($^{234}U/^{238}U$) = 1. It can be disturbed because the decay of ^{238}U produces ^{234}Th, then ^{234}Pa and then ^{234}U, which will be outside the initial crystal lattice position of ^{238}U, and therefore more mobile (Kigoshi, 1971). This process is defined as the α-recoil effect and will lead to depletion in ^{234}U, so a ($^{234}U/^{238}U$) <1. Such α-recoil becomes significant once the grain breaks down into small pieces. Hence, the ($^{234}U/^{238}U$) will decrease with time until a new steady state is reached, and the ($^{234}U/^{238}U$) therefore measures the time since the original large grain was crushed (or comminuted) following,

$$A_{means} = (1 - f_\alpha) + [A_0 - (1 - f_\alpha)]e^{-\lambda_{234} t_{com}} \quad (1)$$

where f_α is the recoil loss factor, the fraction of ^{238}U-decays that result in the daughter isotope being lost from the grains. A_{meas} is the measured ($^{234}U/^{238}U$) of the sediment while A_0 is the initial ($^{234}U/^{238}U$) of the source rock (typically expected to be 1.000). λ_{234} is the ^{234}U decay constant (in yr^{-1}) and t_{com} is the time since rock crushing or comminution. The t_{com} can be expressed following the equation (DePaolo et al., 2006):

$$t_{com} = -\frac{1}{\lambda_{234}} \ln\left[\frac{A_{meas} - (1 - f_\alpha)}{A_0 - (1 - f_\alpha)}\right] \quad (2)$$

As shown in the Eq. (2), f_α is one important parameter for calculating the comminution age, and represents the number of ^{234}U nuclides ejected out of the grain, or on the grain surface and leached since U is soluble, which is affected by the particle grain size and surface roughness (DePaolo et al., 2012, 2006). There are several methods to estimate f_α and the uncertainty of f_α can result in a large variation for comminution age calculation (Handley et al., 2013a, 2013b). In this study, f_α is achieved using the weighted geometric method based on grain size distribution (DePaolo et al., 2006), following:

$$f_\alpha = \int_{\frac{L}{2}}^{r_{max}} X(r)\beta(r)\lambda_s(r)\frac{3}{4}\left(\frac{L}{r} - \frac{L^3}{12r^3}\right)dr \quad (3)$$

where L is the ^{234}Th α-recoil length and is assumed to be 0.03 μm, r is the grain radius (in μm). X(r) is the volume fraction of grains with radius r. β(r) is the aspect ratio of the grain and λs is the surface roughness factor. Assumptions are required for the aspect ratio (β), surface roughness (λs). The aspect ratio (β) is previously assumed to range between 1 for the largest grain and 10 for the smallest grain (DePaolo et al., 2012; Dosseto et al., 2010), while surface roughness factor (λ_s) is expected to be 10 for the largest grains and 1 for the smallest grains (Handley et al., 2013a). Combining Eq. (2) and Eq. (3), and using the measured ($^{234}U/^{238}U$), the communication age can be calculated.

In a typical weathering profile, the fresh rock is in secular equilibrium, so its ($^{234}U/^{238}U$) = 1 and the t_{com}=0. Above the fresh rock, in the different layers of the soil, ($^{234}U/^{238}U$) is expected to decrease upward and t_{com} increased upward in the regolith. As a result, if erosion in the catchment is shallow (e.g. sheet wash), the downstream sediments should be characterized by low ($^{234}U/^{238}U$) and long t_{com} from the surface of the regolith. Instead, when deep erosion (gully, bank mass wasting) dominates the erosional flux in the catchment, will carry sediments with higher ($^{234}U/^{238}U$) and shorter t_{com} (Fig. 1A and 7A) (Dosseto et al., 2014). However, considering the complexity of t_{com} calculation, especially the difficulties to estimate f_α due to the complex grain size, morphology and surface characteristics of natural minerals, the computed t_{com} values should be considered with caution. Clearly the comminution age method is still in its infancy, and our application of uranium-series comminution ages in this study mainly focuses on the relationship between its relative variation and the controlling factors of climate, vegetation, or human activities.

Table 1
Sequence chemical leaching method (modified after Francke et al., 2018; Martin et al., 2015).

Target fraction	Reagent	Conditions
acid-soluble	10 ml 1 M CH_3COONa at ~pH = 5, adjusted with CH_3COOH	3*5 min at room temperature in ultrasonic bath
reducible	10 ml 0.1 M $NH_2OH•HCl$ at ~pH = 5, adjusted with CH_3COOH	2*6 min at 80 °C in ultrasonic bath
oxidizable	10 ml 15 % H_2O_2 and 3 ml of 0.02 M HNO_3 at ~pH = 2	5*3 min at 80 °C in ultrasonic bath
	5 mL 3.2 M CH_3COONH_4, adjusted with CH_3COOH	manually agitated for 1 min at room temperatures

4. Results

4.1. Grain size

The mean grain size (Mz) of the fine fraction (<50 μm) ranges from

6.66 to 28.64 μm, and averages at 15.54 μm (Fig. 3A, Table 2). Irregular fluctuation of Mz was observed from 0 - 2 ka at the top and 11–14 ka at the bottom of the core, while it is relatively constant in the middle of the core, from 2 to 11 ka. The largest Mz appear at 11–14 ka, corresponding to the fluvial and floodplain environment. The Mz gradually becomes finer from the fluvial facies upward to the prodelta/neritic facies characterized by the finest sediments during 2 - 11 ka. The deltaic facies, from 2 to 0 ka, record a return to coarser sediments.

4.2. Sr and Nd isotopic compositions

The $^{87}Sr/^{86}Sr$ and εNd values of the silicate fraction of the fine fraction (< 50 μm) of the core CM97 are listed in Table 2. The $^{87}Sr/^{86}Sr$ ratios range from 0.71684 to 0.72694 and the εNd values range from −12.5 to −10.3 (Fig. 3B and C). The εNd values show no significant variation, except for a slight variation during the 11 - 14 ka and 0 - 2 ka periods. In addition, the $^{87}Sr/^{86}Sr$ is correlated with grain size ($p < 0.001$), while there is no statistically meaningful correlation between εNd and grain size (Fig. 4A and 4B).

4.3. Uranium isotopes and comminution ages

The ($^{234}U/^{238}U$) varies between 0.882 and 0.966, and averages at 0.927 (Fig. 3D, Table 2). According to the Eq. (2) and measured Mz value, the f_α value ranges from 0.079 to 0.155, and averages at 0.118 (Table 2). Assuming that $A_0 = 1$, t_{com}, ranges from 132 to 652 kyrs, with an average value of 360 kyrs (Fig. 3E, Table 2). The largest ($^{234}U/^{238}U$) and smallest t_{com} values are found at 13–14 ka, on the contrary, the smallest ($^{234}U/^{238}U$) and largest t_{com} values correspond to young sediments (~3 ka). It is worth noticing that for the last 2 ka, t_{com} values show severe fluctuation, while before 4 ka, the value of t_{com} is relatively stable.

There is a positive correlation between the ($^{234}U/^{238}U$) value and the grain size ($p < 0.001$) (Fig.4C), indicating that ($^{234}U/^{238}U$) is greatly affected by grain size, so ($^{234}U/^{238}U$) values alone should be considered with caution. However, the influence of grain size can be eliminated to a

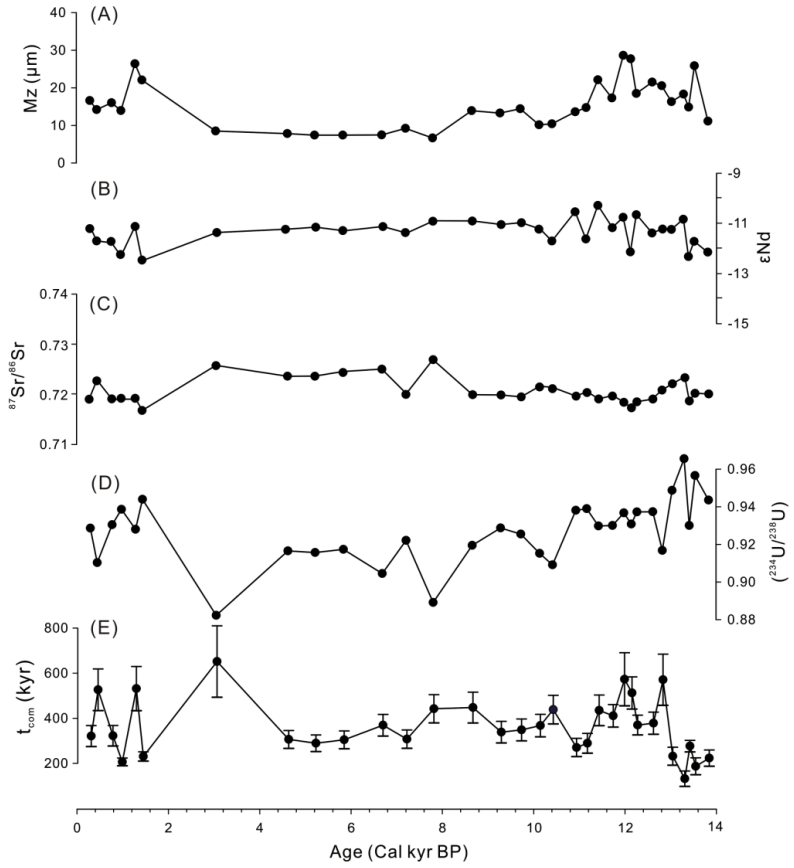

Fig. 3. (A), (B), (C), (D) and (E) are the result of the mean value of grain size (Mz), εNd, $^{87}Sr/^{86}Sr$ ratio, ($^{234}U/^{238}U$) and t_{com} of the fine fraction (<50 μm) versus the sediment deposition age.

Table 2
Grain size, isotopes and t_{com} compositions of sediments from core CM97.

No.	Depth (cm)	Age (cal kyr BP)	Mz (μm)	$^{87}Sr/^{86}Sr$	2σ	$^{143}Nd/^{144}Nd$	2σ	εNd	$(^{234}U/^{238}U)$	2σ	$f\alpha$	t_{com} (kyr)	2σ (kyr)
CM4	4.00	0.29	16.62	0.71916	0.00001	0.512064	0.000004	−11.2	0.9286	0.0019	0.1196	321.20	46.59
CM6.05	6.05	0.44	14.21	0.72273	0.00001	0.512038	0.000006	−11.7	0.9103	0.0007	0.1158	526.46	92.48
CM10.5	10.50	0.77	16.04	0.71915	0.00001	0.512034	0.000004	−11.8	0.9305	0.0007	0.1163	322.60	45.63
CM13.3	13.30	0.98	13.95	0.71924	0.00001	0.512007	0.000007	−12.3	0.9386	0.0008	0.1386	206.55	17.17
CM17.5	17.50	1.28	26.39	0.71923	0.00001	0.512068	0.000004	−11.1	0.9280	0.0007	0.0926	531.70	98.02
CM19.6	19.60	1.44	22.08	0.71684	0.00001	0.511998	0.000007	−12.5	0.9440	0.0012	0.1169	230.56	20.53
CM21.68	21.68	3.05	8.53	0.72578	0.00001	0.512057	0.000004	−11.3	0.8823	0.0012	0.1399	651.85	158.22
CM22.66	22.66	4.62	7.83	0.72365	0.00001	0.512062	0.000006	−11.2	0.9166	0.0007	0.1441	306.11	39.53
CM23.7	23.70	5.22	7.42	0.72367	0.00001	0.512066	0.000003	−11.2	0.9157	0.0006	0.1509	289.39	36.87
CM24.6	24.60	5.84	7.43	0.72456	0.00001	0.512060	0.000004	−11.3	0.9174	0.0008	0.1432	304.57	39.61
CM25.3	25.30	6.69	7.47	0.72501	0.00001	0.512067	0.000004	−11.1	0.9045	0.0006	0.1474	369.32	48.05
CM26.1	26.10	7.21	9.23	0.71997	0.00001	0.512056	0.000004	−11.4	0.9221	0.0006	0.1341	307.53	40.73
CM27.2	27.20	7.80	6.66	0.72694	0.00001	0.512077	0.000004	−10.9	0.8891	0.0008	0.1554	442.39	62.69
CM28.3	28.30	8.66	13.93	0.71983	0.00001	0.512076	0.000004	−11.0	0.9195	0.0009	0.1121	447.52	68.38
CM29.4	29.40	9.28	13.31	0.71980	0.00001	0.512070	0.000004	−11.1	0.9287	0.0009	0.1157	338.54	47.89
CM32.3	32.30	9.73	14.44	0.71954	0.00001	0.512073	0.000003	−11.0	0.9255	0.0008	0.1189	348.53	48.50
CM35	35.00	10.14	10.17	0.72165	0.00001	0.512062	0.000004	−11.2	0.9152	0.0008	0.1311	367.73	49.98
CM36.85	36.85	10.42	10.42	0.72142	0.00001	0.512038	0.000004	−11.7	0.9092	0.0007	0.1279	438.28	63.58
CM40.2	40.20	10.93	13.62	0.71965	0.00001	0.512098	0.000005	−10.5	0.9381	0.0008	0.1157	270.49	40.45
CM42.6	42.60	11.17	14.75	0.72024	0.00001	0.512042	0.000004	−11.6	0.9390	0.0009	0.1092	289.24	43.86
CM45.2	45.20	11.43	22.13	0.71928	0.00001	0.512111	0.000012	−10.3	0.9298	0.0009	0.0992	435.09	67.91
CM48.3	48.30	11.73	17.32	0.71972	0.00001	0.512067	0.000003	−11.1	0.9300	0.0010	0.1018	410.80	49.98
CM50.8	50.80	11.98	28.64	0.71845	0.00001	0.512087	0.000005	−10.8	0.9368	0.0008	0.0789	573.03	117.89
CM52.45	52.45	12.15	27.71	0.71750	0.00001	0.512018	0.000007	−12.1	0.9308	0.0011	0.0904	512.38	71.22
CM53.7	53.70	12.27	18.50	0.71854	0.00001	0.512093	0.000005	−10.6	0.9373	0.0008	0.0967	370.01	43.87
CM57.2	57.20	12.62	21.51	0.71910	0.00001	0.512055	0.000005	−11.4	0.9374	0.0008	0.0954	378.33	49.26
CM59.3	59.30	12.83	20.55	0.72108	0.00001	0.512063	0.000004	−11.2	0.9168	0.0007	0.1039	570.87	113.40
CM61.45	61.45	13.04	16.33	0.72211	0.00001	0.512062	0.000005	−11.2	0.9487	0.0008	0.1067	231.74	39.70
CM64.1	64.10	13.30	18.32	0.72349	0.00001	0.512083	0.000006	−10.8	0.9655	0.0009	0.1107	132.04	34.07
CM62.25	65.25	13.42	14.87	0.71872	0.00001	0.512007	0.000006	−12.3	0.9300	0.0009	0.1289	276.51	25.67
CM66.5	66.50	13.54	25.88	0.72025	0.00001	0.512037	0.000004	−11.7	0.9566	0.0008	0.1057	187.01	37.51
CM69.5	69.50	13.84	11.15	0.72014	0.00001	0.512016	0.000004	−12.1	0.9436	0.0010	0.1205	223.33	35.79

certain extent, after the calculation of the parameter f_α, since t_{com} values are not correlated to Mz (Fig.4D). Therefore, t_{com} instead of $(^{234}U/^{238}U)$ will be discussed to see any relationship between catchment erosion and environment changes.

5. Discussion

5.1. Sea level and sedimentary environment changes

Sea level fluctuation can cause changes in the deltaic and offshore sedimentary environment of large catchments. In the ECS, during the glacial period, the sea level was 90 - 120 m below the current sea level (Li et al., 2014). The Changjiang estuary advanced to the continental shelf due to regression, which caused strong down cutting of the river channel in the middle and lower reaches (Fig. 1B and D). More fluvial deposits of the floodplain could have been mobilized and transported to the estuary, with the material from the upper reaches erosion zone transported downstream and deposited in the floodplain in the middle and lower reaches and some transported to the estuary (Fig. 1B). Therefore, during the low sea level periods, the sediments deposited in the estuary are a mix of upper reaches and middle-low reaches. Since the sediments from floodplain in the middle and lower reaches have stayed in the surface environment for a much longer time than the sediments from the upper reaches, older t_{com} of the estuary sediment are likely to be found during these periods. During the interglacial period, sea level rise caused the estuary to recede. The transgression could have led to a weakening of the channel incision in the middle and lower reaches, and the channel is dominated by deposition. In that case, only the material from the upper reaches erosion zone could have been efficiently transported to the estuary (Fig. 1C). So, during this period, the t_{com} of the estuary sediment was relatively small. However, during the period of highstand systems tract, the channel may have lateral migration in the floodplain, and local floodplain materials are eroded and remobilized due to river diversion (Fig. 1E). Therefore, during this period, sediments from floodplain in the middle and lower reaches of the can also be found in the estuary, and the mixing of these sediments will lead to an increase in the t_{com} of the estuarine sediments.

The time scale of the CM97 core is in the rising and stable period of highstand sea level. The sedimentary environment recorded by the core evolved from the continental fluvial at low sea level to the prodelta/neritic environment at high sea level. However, the sea level has been stable since 7 ka (Li et al., 2014), so the sedimentary environment changed from prodelta/neritic to delta since 2 ka is inconsistent with sea level change. The sedimentation rate has increased rapidly since 2 ka (Fig. 2C and 6G), indicating that more sediments were eroded and transported into the estuary to form the delta during this period, and inconsistent with natural forcing (climate and sea level).

5.2. Sediment provenance since the 14 ka

Sr and Nd isotopic compositions have been widely interpreted to trace the detrital source of silicate (e.g. Colin et al., 2006; Goldstein and O'Nions, 1981; McLennan et al., 1993; Wan et al., 2017). However, in addition to the detrital component, there are authigenic and biological components in the bulk sediment (e.g. Wilson et al., 2013), but they were chemically leached (Francke et al., 2018; Martin et al., 2015) in this study. Moreover, the grain-size can also induce significant differences in the Sr and Nd isotopic compositions of sediments (e.g. Galy et al., 1996; McLennan et al., 1989; Meyer et al., 2011). In this study, the range in grain size is such that, only the $^{87}Sr/^{86}Sr$ ratios are sensitive to grain size (Fig. 4A, 4B). Rb and Sr having significantly different physical and chemical properties, Sr is more readily lost from minerals than Rb by weathering processes (Marques et al., 2004). As a result, during the sediments "source to sink" transport process, chemical weathering

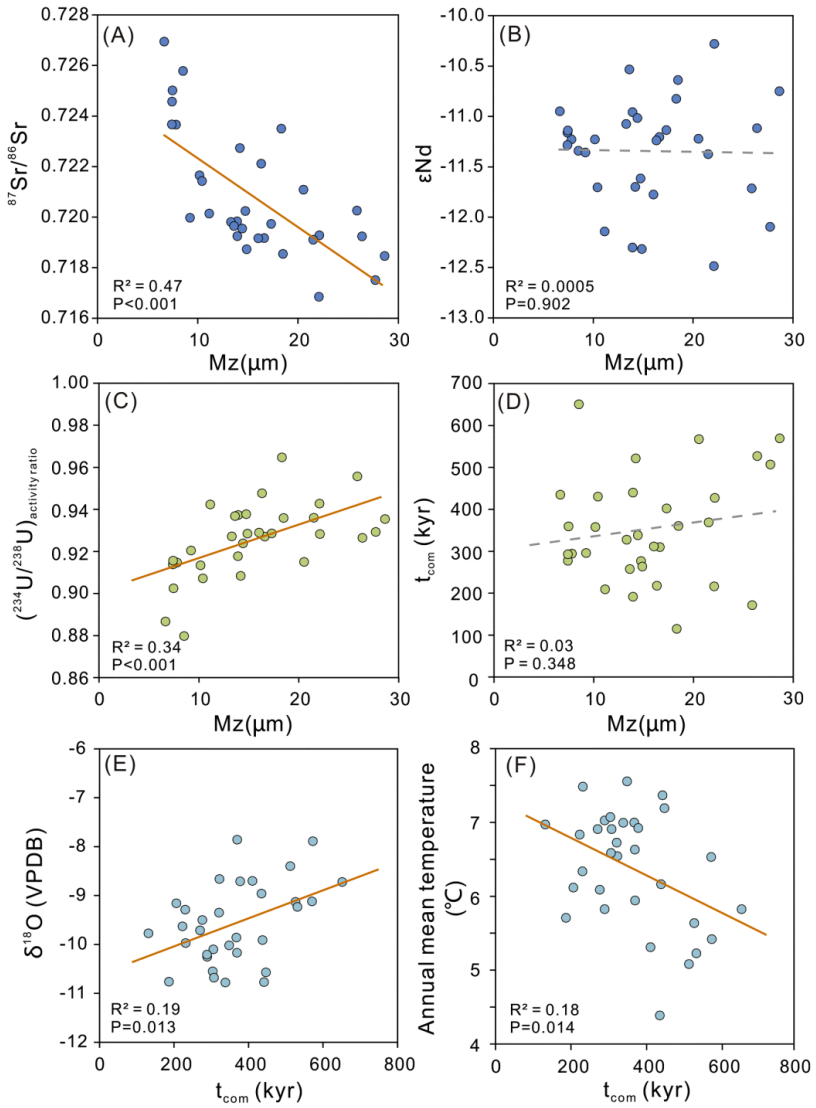

Fig. 4. Correlation diagram between grain size (Mz) and (A) the $^{87}Sr/^{86}Sr$ ratio, (B) the εNd, (C) the ($^{234}U/^{238}U$) and (D) t_{com}. (E) Correlation diagram between t_{com} and $\delta^{18}O$ (Cheng et al., 2016) and (F) Correlation diagram between t_{com} and mean annual temperature in the middle reaches of the Changjiang catchment (Zhu et al., 2008). Solid orange line represents significant linear correlation ($p < 0.05$), and dotted gray line represent non significant linear correlation.

causes the Rb/Sr ratios of minerals to increase, and can also enrich sediments in radiogenic ^{87}Sr. Consequently, the chemical weathering results in $^{87}Sr/^{86}Sr$ ratios increasing significantly as grain sizes decrease further, which maybe more clay and weathered micas (biotite and muscovite) in the finer sediments (e.g. Feng et al., 2009; Meyer et al., 2011). While Sm and Nd have similar geochemical properties, these lead to Sm and Nd behaving similarly during weathering (McCulloch and Wasserburg, 1978). As a result, the Nd isotopic compositions do not vary

significantly with grain size during the sediments transportation (Meyer et al., 2011). Consequently, it is more likely that changes in εNd values document changes in sources provenance. Therefore, the comparison (Fig.5) of Sr and Nd isotopes between the CM97 sediments and river sediments (He et al., 2015; Yang et al., 2007) should mainly consider εNd values. The small range of εNd values in CM97 sediments strongly suggests that the provenance in the estuary has not changed significantly (Fig. 3B) since 14 ka despite the large sedimentological changes and likely represents the whole Changjiang basin. In addition, none of the samples studied for t_{com} have extreme εNd values when compared to the river sources (Fig 5), suggesting that none of these samples are particularly impacted by a specific origin.

As discussed in the previous section, t_{com} is sensitive to sediment transport processes and adds constraints on the source of the material reaching the estuary. In a large catchment like the Changjiang, the sediments of the floodplain of the middle and lower reaches correspond to material from the upper reaches erosion zones that stay in the catchment for a longer time, that is, with older t_{com} when it finally reaches the estuary. The modern Changjiang sediments in the upper reaches have younger t_{com} values (250–350 kyrs, average 300 kyrs), while sediments in the middle and lower reaches have older t_{com} values (300–600 kyrs, average 450 ka) (Li et al., 2016). Thus, older t_{com} in the estuary would be recorded when the supply of middle and lower reaches sediments increases. During the Bølling–Allerød (B/A) period, due to the low sea level, the sediments of floodplain would be eroded and remobilized (Fig, 1E). However, such erosion in the middle and lower reaches floodplain requires a stronger precipitation (because the slope of the channel is never very high in these areas) than erosion in the upper reaches erosion zone, where local relief can be significant. In the core CM97 (Fig. 6), during the strong monsoon periods, t_{com} values are young (~ 150 - 400 kyrs) and similar to those of the modern Changjiang sediments in upper reaches, indicating that although the middle and lower reaches floodplain deposits could have been remobilized, the material from the upper reaches erosion zone dominates the estuarine sediments. During the weak monsoon periods with less precipitation, erosion in the whole catchment is weak, while erosion in the upper reaches erosion zones will be more sensitive to climate changes than that in the middle and lower reaches. Since the B/A period, and for most of the 14 to 4 ka period, the sea level is rising, and the floodplain is more likely to be under active sedimentation rather than downcutting of the river network and significant erosion. Therefore, the estuary sediments mainly come from the upper reaches erosion zone of the Changjiang, and only since the late Holocene, the floodplain sediments remobilization of the middle and lower reaches could have appeared. Therefore,

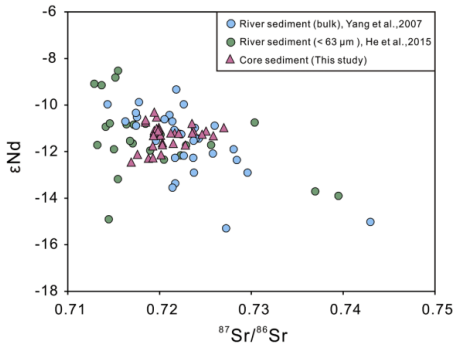

Fig. 5. εNd versus $^{87}Sr/^{86}Sr$ in core CM97 sediments, in comparison with data for the Changjiang river sediments from Yang et al. (2007) and He et al. (2015).

fluctuations in t_{com} are likely to correspond to changes in the erosion processes of the upper reaches of the Changjiang.

5.3. Impact of climate change on catchment erosion

For the last 14 ka, t_{com} varies from 200 to 600 kyrs, with obvious difference in the oldest part and the youngest part of the core. From the B/A period to the Mid-Holocene (14 – 4 ka), t_{com} has a smaller range of variation (200–500 kyrs; average 350 kyrs), and presents a cyclical fluctuation. Since the Late Holocene (4 – 0 ka), t_{com} values are more variable, from 200 to 650 ka, related to the occurrence of $t_{com} > 600$ kyrs (Fig.6A). Combined with the analysis of the sea level change and sediment provenance, the record can be divided into two regimes. First, from the B/A period to Mid-Holocene, the variation of the estuarine sediments t_{com} mainly correspond to the erosion processes of the upper reaches erosion zone of the catchment. second, since the Late Holocene, the severe fluctuation of t_{com} and the occurrence of sediments with the oldest t_{com} (up to ~650 kyrs) are likely recording the episodic mobilization of sediment stored for longer time in the catchment (corresponding to the sediments from the middle and lower floodplain), despite a stable sea level. However, this local short-term erosion process may not be related to natural factors, which will be analysed below.

Prior to 4 ka, t_{com} show alternating periods of relatively old and young values (Fig. 6A), that are roughly coeval with changes in climatic conditions as interpreted from the oxygen isotopes (precipitation, Fig. 6B, Cheng et al., 2016) and spore-pollen (temperature, Fig. 6C, Zhu et al., 2008). In more details, the pollen data from core CM97 further divided the climatic variations of Changjiang catchment into 5 warm and humid sub-periods and 4 cool and dry sub-periods since 14 ka (Fig. 6E, Yi et al., 2003), and t_{com} is older during cool and dry periods, such as Younger Dryas (YD) event, and is younger during warm and wet periods, such as B/A and Holocene Climatic Optimum (HCO) periods (Fig. 6). Such millennial response to climatic conditions while t_{com} values encompass several glacial-interglacial cycles suggest a mechanism at the scale of the Changjiang catchment (or upper reaches of the catchment) rather than at the scale of the regolith.

We propose that during the cold and dry periods (Fig. 7B), shallow erosion of the weathered material with longer residence time due to weak scouring could be more important and bring sediment with older t_{com} to the estuary. Also, weaker hydrodynamic conditions in the rivers lead to a longer storage of the weathered detritus from the regolith in the floodplain before being transferred to the estuary (Fig. 7B). In contract, during the warm and wet periods (Fig. 7C), the erosional processes are more efficient in mobilizing deeper parts of the regolith (via enhanced land-sliding on the steep slopes of the upper reaches), and also a more efficient transport to the distant estuary through stronger hydrodynamic force of the Changjiang in the middle and lower reaches. This could explain the younger t_{com} values recorded by the sediments deposited in the estuary (Fig. 7C). The erosion of upper reaches responds rapidly to climate change, and it can erode the weathered deposits that have remained on the weathering profile or soil for several hundred thousand years in a short time, which is consistent with previous studies in other regions (Rothacker et al., 2018; Dosseto et al., 2010).

5.4. Impact of human activities

Since the Late Holocene (~ 4 ka to now), the change of the t_{com} is still in good accordance with the climatic fluctuations, but during the last warm and humid climate t_{com} values fluctuated greatly, with the occurrence of largest t_{com} values (Fig. 6A). These abnormal large t_{com} values are consistent with the published t_{com} values of river sediments in the middle and lower reaches of the Changjiang (Li et al., 2016). It shows that in addition to the younger sediments that come from the upper reaches erosion zone, the older floodplain sediments in the middle and lower reaches were eroded and mobilized to be transported to the estuary since Late Holocene. In addition, the rapid fluctuation of t_{com}

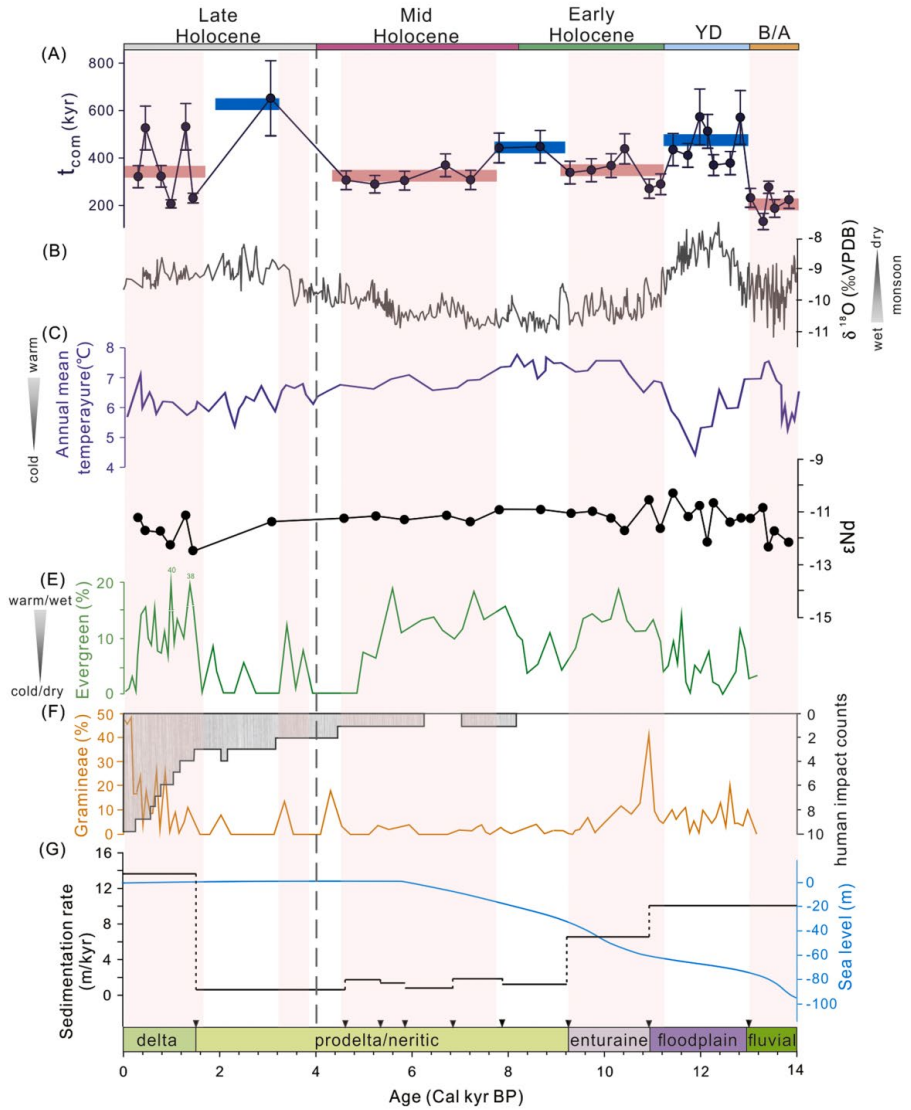

Fig. 6. Temporal variations of (A) t_{com}, the blue and red bars represent the average value of t_{com} during the cold and warm periods, respectively. (B) stalagmite $\delta^{18}O$ of Sanbao Cave (Cheng et al., 2016), (C) Annual mean temperature in the middle reaches of the Changjiang catchment (Zhu et al., 2008), (D) εNd, (E) Evergreen pollen content and climate periods from pollen data (pink strips represent warm and wet periods) (Yi et al., 2003), (F) Gramineae pollen content (Yi et al., 2003) and human impact factor (Wang et al., 2010a). (G) the sedimentation rate and sedimentary facies of core CM97, and the sea level of east China sea since 14 ka. the black triangles represent AMS^{14}C dating points. The age of the Younger Drays (YD) and the Bølling–Allerød interstadial period (B/A) are according to Stuiver et al. (1995).

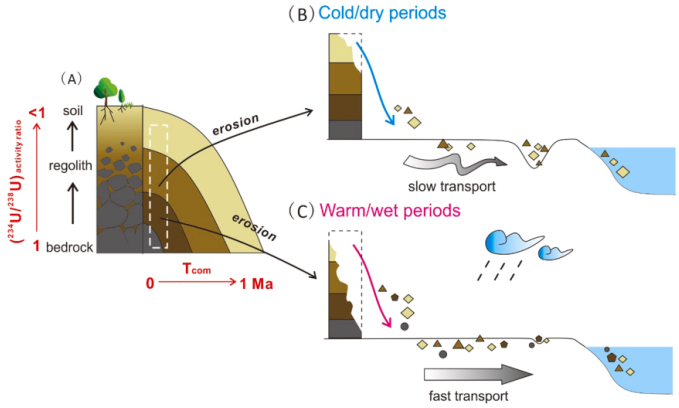

Fig. 7. (A) shows the principle of U-series comminution age and its application to weathering profiles. (B) and (C) respectively show the catchment erosion and sediment transport process in the large catchment during the cold/dry and warm/wet environment. Specifically, in (B), during the cold/dry periods, sediments transported slowly and trapped in the plain; in (C), sediments transported faster by strong hydrodynamic force during the warm/wet periods.

values reveals that the mobilization of floodplain sediments is not continuous. Two processes could explain older t_{com} values. 1) During this highstand system tract, the climate is characterized by warm and steady precipitation. So, frequent flooding of middle and lower reaches of Changjiang can cause the river to divert. Such lateral migration of the channel would result in erosion of the floodplain, causing local old sediments to be mobilized and transported to the estuary (Fig. 1C). 2) The more severe fluctuation of the t_{com} values since 2 ka are associated with an abrupt rise in the sedimentation rate of the Changjiang estuary (around the 14 m/kyrs, Fig. 6G) that could be related to enhanced erosion of the plain by human activities. Human impact (Procrustes analysis based on the results of four principal component analysis (PCA) axes from both pollen and non-pollen records) rapidly increased from 2 to 10 in the last 2 ka (Fig.6F, Wang et al., 2010a). In addition, Gramineae pollen increased in the Changjiang basin since 2 ka (Fig.6F), suggesting that the rice planting had expanded rapidly (Yao et al., 2017; Yi et al., 2003). A significant deforestation and agricultural planting since 2 ka in the middle and lower Changjiang catchment will increase erosion of the floodplain, leading to the mobilization of older sediments and transport to the estuary (Wang et al., 2010b), causing a rise of the t_{com} values.

6. Conclusions

The U-series t_{com} can be interpreted as the time from physical breakdown of bedrock into small particles to deposition after transport. In large catchments, the transport of sediments from the upper reaches erosion zone to the middle and lower reaches of the floodplain add complex processes. In this study, the Nd isotopes, and t_{com} of the sediments from the core CM97 located at the Changjiang estuary were analyzed and combined with the climate and human activity proxies of previous studies, to give some constraints on the catchment erosion of the Changjiang and its response to climate changes and human activities since the B/A period.

Based on the sedimentary environment and t_{com} changes, the last 14 kyrs in the Changjiang can be divided into two regimes. First, from the B/A period to the Mid-Holocene, the sea level rose rapidly, and the t_{com} of estuary sediment mainly recorded the residence time in the upper reaches erosion zones. The stable and cyclical variation of the t_{com} shows coordinated variation with the climate changes. During the cold and dry period, the sediment t_{com} was old as less precipitation resulted in shallower erosion and the erosion material mainly comes from the soil with longer residence time. In addition, these sediments were transported slowly due to weaker hydrodynamic forces, resulting in estuarine sediments characterized by old t_{com} during the cold period. On the contrary, during the warm and wet periods, due to the abundant precipitation, catchment erosion is strong and erosion thickness is relatively large. More fresh sediments are mobilized and quickly transported to the estuary through the strong hydrodynamic forces. Therefore, the estuarine sediments record smaller t_{com} during the warm periods. Second, after the Late Holocene, the climate was still warm and humid with the highstand system tract, but the t_{com} recorded by estuarine sediments fluctuated. The more severe fluctuation of the t_{com} values since 2 ka are associated with an abrupt rise in the sedimentation rate of the Changjiang estuary and human activities that could have enhanced erosion of the middle and lower reaches of the Changjiang. This study reveals that the U-series t_{com} can effectively constrain the catchment-wide erosion on a millennium scale and is sensitive in response to the climate change and human activities.

Overall, on the glacial-interglacial scale, climate plays a leading role in catchment erosion. With the beginning of the Anthropocene, human activities changed the natural processes of erosion at whole catchment scale. This study offers a new proxy, a U-series Comminution Age method, to study environments changes in large catchment on geological time scale, and provides new insights into the use of U-series comminution age in large river basin during the Quaternary.

CRediT authorship contribution statement

Junfei Chen: Writing – review & editing, Writing – original draft, Methodology, Investigation, Funding acquisition, Formal analysis, Data curation, Conceptualization. **Chao Li:** Writing – review & editing, Supervision, Project administration, Funding acquisition, Formal analysis. **Albert Galy:** Writing – review & editing, Supervision, Methodology, Formal analysis, Data curation. **Hui Wang:** Writing – review & editing, Data curation. **Chengfan Yang:** Writing – review & editing, Formal analysis. **Shouye Yang:** Writing – review & editing, Supervision, Project administration, Funding acquisition.

Declaration of Competing Interest

The authors declare that they have no known competing financial interests or personal relationships that could have appeared to influence the work reported in this paper.

Data availability

Data will be made available on request.

Acknowledgement

This work was supported by the National Key Research and Development Program of China (2022YFF0800504), the National Natural Science Foundation of China (41991324, 42273057, 42076063), the Natural Science Foundation of Shanghai (21590712700) and State Key Laboratory of Loess and Quaternary Geology, Institute of Earth Environment, CAS (SKLLQG2222). Junfei Chen was funded by China Scholarship Council (CSC No. 202106260083). The author thanks Juan Xu, Zhifei Duan and Lei Bi for their help in the laboratory and discussion. We thank Andrew Jacobson for editorial handing of the manuscript and Anthony Dosseto and an anonymous reviewer for the helpful comments and suggestions.

References

Andersen, M.B., Stirling, C.H., Potter, E.K., Halliday, A.N., 2004. Toward epsilon levels of measurement precision on $^{234}U/^{238}U$ by using MC-ICPMS. Int. J. Mass spectrom. 237, 107–118.
Chen, J., Wang, F., Xia, X., Zhang, L., 2002. Major element chemistry of the Changjiang (Yangtze River). Chem. Geol. 187, 231–255.
Cheng, H., Edwards, R.L., Hoff, J., Gallup, C.D., Richards, D.A., Asmeromd, Y., 2000. The half-lives of uranium-234 and thorium-230. Chem. Geol. 169, 17–33.
Cheng, H., Edwards, R.L., Sinha, A., Spotl, C., Yi, L., Chen, S., Kelly, M., Kathayat, G., Wang, X., Li, X., Kong, X., Wang, Y., Ning, Y., Zhang, H., 2016. The Asian monsoon over the past 640,000 years and ice age terminations. Nature 534, 640–646.
Clift, P.D., Giosan, L., Blusztajn, J., Campbell, I.H., Allen, C., Pringle, M., Tabrez, A.R., Danish, M., Rabbani, M.M., Alizai, A., Carter, A., Lückge, A., 2008. Holocene erosion of the Lesser Himalaya triggered by intensified summer monsoon. Geology 36, 79–86.
Colin, C., Turpin, L., Blamart, D., Frank, N., Kissel, C., Duchamp, S., 2006. Evolution of weathering patterns in the Himalayas and Indo-Burman ranges over the last 280 kyr: effects of sediment provenance on $^{87}Sr/^{86}Sr$ ratios tracers. Geochem. Geophys. Geosyst. 7, 1–6.
DePaolo, D.J., Lee, V.E., Christensen, J.N., Maher, K., 2012. Uranium comminution ages: sediment transport and deposition time scales. C.R. Geosci. 344, 678–687.
DePaolo, D.J., Maher, K., Christensen, J.N., McManus, J., 2006. Sediment transport time measured with U-series isotopes: results from ODP North Atlantic drift site 984. Earth Planet. Sci. Lett. 248, 394–410.
Ding, T., Wan, D., Wang, C., Zhang, F., 2004. Silicon isotope compositions of dissolved silicon and suspended matter in the Yangtze River, China. Geochim. Cosmochim. Acta 68, 205–216.
Dosseto, A., Buss, H.L., Chabaux, F., 2014. Age and weathering rate of sediments in small catchments: the role of hillslope erosion. Geochim. Cosmochim. Acta 132, 238–258.
Dosseto, A., Hesse, P.P., Maher, K., Fryirs, K., Turner, S., 2010. Climatic and vegetation control on sediment dynamics during the last glacial cycle. Geology 38, 395–398.
Dosseto, A., Schaller, M., 2016. The erosion response to Quaternary climate change quantified using uranium isotopes and in situ - produced cosmogenic nuclides. Earth Sci. Rev. 155, 60–81.
Feng, J., Zhu, L., Zhen, X., Hu, Z., 2009. Grain size effect on Sr and Nd isotopic compositions in eolian dust: implications for tracing dust provenance and Nd model age. Gechemical J. 43, 123–131.
France-Lanord, C., Derry, L.A., 1997. Organic carbon burial forcing of the carbon cycle from Himalayan erosio. Nature 390, 65–67.
Francke, A., Carney, S., Wilcox, P., Dosseto, A., 2018. Sample preparation for determination of comminution ages in lacustrine and marine sediments. Chem. Geol. 479, 123–135.
Francke, A., Dosseto, A., Just, J., Wagner, B., Jones, B.G., 2020. Assessment of the controls on $(^{234}U/^{238}U)$ activity ratios recorded in detrital lacustrine sediments. Chem. Geol. 1.
Francke, A., Dosseto, A., Panagiotopoulos, K., Leicher, N., Lacey, J.H., Kyrikou, S., Wagner, B., Zanchetta, G., Kouli, K., Leng, M.J., 2019. Sediment residence time reveals Holocene shift from climatic to vegetation control on catchment erosion in the Balkans. Glob Planet Change 177, 186–200.
Gaillardet, J., Dupre, B., Allegre, C.J., Negrel, P., 1997. Chemical and physical denudation in the Amazon River Basin. Chem. Geol. 142, 141–173.
Galy, A., France-Lanord, C., Derry, L.A., 1996. The late oligocene-early miocene himalayan belt constraints deduced from isotopic compositions of early miocene turbidites in the bengal fan. Tectonophysics 260, 109–118.
Goldstein, S.L., O'Nions, R.K., 1981. Nd and Sr isotopic relationships in pelagic clays and ferromanganese deposits. Nature 292, 324–327.
Handley, H.K., Turner, S., Afonso, J.C., Dosseto, A., Cohen, T., 2013a. Sediment residence times constrained by uranium-series isotopes: a critical appraisal of the comminution approach. Geochim. Cosmochim. Acta 103, 245–262.
Handley, H.K., Turner, S.P., Dosseto, A., Haberlah, D., Afonso, J.C., 2013b. Considerations for U-series dating of sediments: insights from the Flinders Ranges, South Australia. Chem. Geol. 340, 40–48.
He, M., Zheng, H., Clift, P.D., Tada, R., Wu, W., Luo, C., 2015. Geochemistry of fine-grained sediments in the Yangtze River and the implications for provenance and chemical weathering in East Asia. Prog Earth Planet Sci. 2.
Heimsath, A.M., Dietrich, W.E., Nishiizumi, K., Finkel, R.C., 1997. The soil production function and landscape equilibrium. Nature 388, 358–361.
Hein, C.J., Galy, V., Galy, A., France-Lanord, C., Kudrass, H., Schwenk, T., 2017. Post-glacial climate forcing of surface processes in the Ganges-Brahmaputra river basin and implications for carbon sequestration. Earth Planet. Sci. Lett. 478, 89–101.
Hori, K., Saito, Y., Zhao, Q.H., Cheng, X.R., Wang, P.X., Sato, Y., Li, C.X., 2001a. Sedimentary facies and Holocene progradation rates of the Changjiang (Yangtze) delta, China. Geomorphology 41, 233–248.
Hori, K., Saito, Y., Zhao, Q.H., Cheng, X.R., Wang, P.X., Sato, Y., Li, C.X., 2001b. Sedimentary facies of the tide-dominated paleo-Changjiang (Yangtze) estuary during the last transgression. Mar. Geol. 177, 331–351.
Jacobsen, S.B., Wasserburg, G.J., 1980. Sm-Nd isotopic evolution of chondrites. Earth Planet. Sci. Lett. 50, 139–155.
Jaffey, A.H., Flynn, K.F., Glendenin, L.E., Bentley, W.C., Essling, A.M., 1971. Precision measurement of half-lives and specific activities of $^{235}U$and ^{238}U. Phys Rev C 4, 1889–1906.
Jweda, J., Bolge, L., Class, C., Goldstein, S.L., 2015. High precision Sr-Nd-Hf-Pb isotopic compositions of USGS reference material BCR-2. Geostand. Geoanal. Res. 40, 101–115.
Kigoshi, K., 1971. Alpha-recoil Thorium-234: dissolution into water and the Uranium-234/Uranium-238 disequilibrium in nature. Science 173, 47–48.
Koornneef, J.M., Stracke, A., Aciego, S., Reubi, O., Bourdon, B., 2010. A new method for U–Th–Pa–Ra separation and accurate measurement of ^{234}U–^{230}Th–^{231}Pa–^{226}Ra disequilibria in volcanic rocks by MC-ICPMS. Chem. Geol. 277, 30–41.
Li, C., Yang, S., Zhao, J.X., Dosseto, A., Bi, L., Clark, T.R., 2016. The time scale of river sediment source-to-sink processes in East Asia. Chem. Geol. 446, 138–146.
Li, G., Li, P., Liu, Y., Qiao, L., Ma, Y., Xu, J., Yang, Z., 2014. Sedimentary system response to the global sea level change in the East China Seas since the last glacial maximum. Earth Sci. Rev. 139, 390–405.
Marques, J.J., Schulze, D.G., Curi, N., Mertzman, S.A., 2004. Trace element geochemistry in Brazilian Cerrado soils. Geoderma 121, 31–43.
Martin, A.N., Dosseto, A., Kinsley, L.P.J., 2015. Evaluating the removal of non-detrital matter from soils and sediment using uranium isotopes. Chem. Geol. 396, 124–133.
Mathew, K., Mason, P., Voeks, A., Narayanan, U., 2012. Uranium isotope abundance ratios in natural uranium metal certified reference material 112-A. Int. J. Mass spectrom. 315, 8–14.
McCulloch, M.T., Wasserburg, G.J., 1978. Sm-Nd and Rb-Sr chronology of continental crust formation. Science 200, 1003–1011.
McLennan, S.M, Hemming, S., McDaniel, D., Hanson, G., 1993. Geochemical approaches to sedimentation, provenance, and tectonics. Special Papers-Geological Soc. Am. 21.
McLennan, S.M., McCulloch, M.T., Taylor, S.R., Maynard, J.B., 1989. Effects of sedimentary sorting on neodymium isotopes in deep-sea turbidites. Nature 337, 547–549.
Meyer, I., Davies, G.R., Stuut, J.-B.W., 2011. Grain size control on Sr-Nd isotope provenance studies and impact on paleoclimate reconstructions: an example from deep-sea sediments offshore NW Africa. Geochem. Geophys. Geosyst. 12, 1–14.
Milliman, J.D., Farnsworth, K.L., 2011. River discharge to the coastal ocean-a global synthesis. Cambridge University Press, United Kingdom.
Munhoven, G., François, L.M., 1994. Glacial-interglacial changes in continental weathering: possible implications for atmospheric CO_2. Springer Berlin Heidelberg, Berlin, Heidelberg, pp. 39–58.
Plotzki, A., May, J.H., Preusser, F., Roesti, B., Denier, S., Lombardo, U., Veit, H., 2015. Geomorphology and evolution of the late Pleistocene to Holocene fluvial system in the south-eastern Llanos de Moxos, Bolivian Amazon. Catena 127, 102–115.
Riebe, C.S., Hahm, W.J., Brantley, S.L., 2017. Controls on deep critical zone architecture: a historical review and four testable hypotheses. Earth Surf. Processes Landforms 42, 128–156.
Rothacker, L., Dosseto, A., Francke, A., Chivas, A.R., Vigier, N., Kotarba-Morley, A.M., Menozzi, D., 2018. Impact of climate change and human activity on soil landscapes over the past 12,300 years. Sci. Rep. 8, 1–7.
Schaller, M., von Blanckenburg, F., Veldkamp, A., Tebbens, L.A., Hovius, N., Kubik, P.W., 2002. A 30 000yr record of erosion rates from cosmogenic 10Be in Middle European river terraces. Earth Planet. Sci. Lett. 204, 307–320.
Steiger, R.H., Jäger, E., 1977. Subcommission on geochronology: convention on the use of decay constants in geo- and cosmochronology. Earth Planet. Sci. Lett. 36, 359–362.
Tanaka, T., Togashi, S., Kamioka, H., Amakawa, H., Kagami, H., Hamamoto, T., Yuhara, M., Orihashi, Y., Yoneda, S., Shimizu, H., Kunimaru, T., Takahashi, K., Yanagi, T., Nakano, T., Fujimaki, H., Shinjo, R., Asahara, Y., Tanimizu, M., Dragusanu, C., 2000. JNdi-1: a neodymium isotopic reference in consistency with LaJolla neodymium. Chem. Geol. 168, 279–281.

Von Blanckenburg, F., 2005. The control mechanisms of erosion and weathering at basin scale from cosmogenic nuclides in river sediment. Earth Planet. Sci. Lett. 237, 462–479.
Wan, S., Clift, P.D., Zhao, D., Hovius, N., Munhoven, G., France-Lanord, C., Wang, Y., Xiong, Z., Huang, J., Yu, Z., Zhang, J., Ma, W., Zhang, G., Li, A., Li, T., 2017. Enhanced silicate weathering of tropical shelf sediments exposed during glacial lowstands: a sink for atmospheric CO_2. Geochim. Cosmochim. Acta 200, 123–144.
Wang, Y., Liu, X., Herzschuh, U., 2010a. Asynchronous evolution of the Indian and East Asian Summer Monsoon indicated by Holocene moisture patterns in monsoonal central Asia. Earth Sci. Rev. 103, 135–153.
Wang, Z., Li, M., Zhang, R., Zhuang, C., Liu, Y., Saito, Y., Xie, J., Zhao, B., 2010b. Impacts of human activity on the late-Holocene development of the subaqueous Yangtze delta, China, as shown by magnetic properties and sediment accumulation rates. Holocene 21, 393–407.
Wasserburg, G.J., Jacobsen, S.B., Depaolo, D.J., Mcculloch, M.T., Wen, T., 1981. Precise determination of Sm/Nd ratios, Sm and Nd isotopic abundances in standard solutions. Geochim. Cosmochim. Acta 45, 2311–2323.
West, A., Galy, A., Bickle, M., 2005. Tectonic and climatic controls on silicate weathering. Earth Planet. Sci. Lett. 235, 211–228.
Wilson, D.J., Piotrowski, A.M., Galy, A., Clegg, J.A., 2013. Reactivity of neodymium carriers in deep sea sediments: implications for boundary exchange and paleoceanography. Geochim. Cosmochim. Acta 109, 197–221.
Yang, S., Jiang, S., Ling, H., Xia, X., Sun, M., Wang, D., 2007. Sr-Nd isotopic compositions of the Changjiang sediments: implications for tracing sediment sources. Sci. China C Life Sci. 50, 1556–1565.
Yang, S., Li, C., Yokoyama, K., 2006. Elemental compositions and monazite age patterns of core sediments in the Changjiang Delta: implications for sediment provenance and development history of the Changjiang River. Earth Planet. Sci. Lett. 245, 762–776.
Yao, F., Ma, C., Zhu, C., Li, J., Chen, G., Tang, L., Huang, M., Jia, T., Xu, J., 2017. Holocene climate change in the western part of Taihu Lake region, East China. Palaeogeogr. Palaeoclimatol. Palaeoecol. 485, 963–973.
Yi, S., Saito, Y., Zhao, Q.H., Wang, P.X., 2003. Vegetation and climate changes in the Changjiang (Yangtze River) Delta, China, during the past 13,000 years inferred from pollen records. Quat. Sci. Rev. 22, 1501–1519.
Zhu, C., Chen, X., Zhang, G., Ma, C., Zhu, Q., Li, Z., Xu, W., 2008. Spore-pollen-climate factor transfer function and paleoenvironment reconstruction in Dajiuhu, Shennongjia, Central China. Sci. Bull. 53, 42–49.